# Numerical modeling of damage in heterogeneous materials using strain gradient theory

**Putar, Filip**

**Doctoral thesis / Disertacija**

**2019**

*Degree Grantor / Ustanova koja je dodijelila akademski / stručni stupanj:* **University of Zagreb, Faculty of Mechanical Engineering and Naval Architecture / Sveučilište u Zagrebu, Fakultet strojarstva i brodogradnje**

*Permanent link / Trajna poveznica:* https://urn.nsk.hr/urn:nbn:hr:235:377978

*Rights / Prava:* In copyright / Zaštićeno autorskim pravom.

*Download date / Datum preuzimanja:* **2024-04-20**

*Repository / Repozitorij:*

Repository of Faculty of Mechanical Engineering and Naval Architecture University of Zagreb

University of Zagreb

FACULTY OF MECHANICAL ENGINEERING AND NAVAL ARCHITECTURE

Filip Putar

# NUMERICAL MODELING OF DAMAGE IN HETEROGENEOUS MATERIALS USING STRAIN GRADIENT THEORY

DOCTORAL THESIS

Zagreb, 2018

University of Zagreb

FACULTY OF MECHANICAL ENGINEERING AND NAVAL ARCHITECTURE

Filip Putar

# NUMERICAL MODELING OF DAMAGE IN HETEROGENEOUS MATERIALS USING STRAIN GRADIENT THEORY

DOCTORAL THESIS

Supervisor:

Prof. dr. sc. Jurica Sorić

Zagreb, 2018

Sveučilište u Zagrebu

FAKULTET STROJARSTVA I BRODOGRADNJE

Filip Putar

# NUMERIČKO MODELIRANJE OŠTEĆENJA U HETEROGENIM MATERIJALIMA PRIMJENOM GRADIJENTNE DEFORMACIJSKE TEORIJE

DOKTORSKI RAD

Mentor:

Prof. dr. sc. Jurica Sorić

Zagreb, 2018.

# Bibliography data


| | |
|---|---|
| UDC: | 519.6 : 539.214<br>519.6 : 539.3<br>519.6 : 624.044 |
| Keywords: | quasi-brittle damage, $C^1$ continuity finite element, strain gradient theory, multiscale analysis, RVE, heterogeneous material |
| Scientific area: | Technical Sciences |
| Scientific field: | Mechanical Engineering |
| Institution: | Faculty of Mechanical Engineering and Naval Architecture (FAMENA), University of Zagreb |
| Supervisor: | Dr. sc. Jurica Sorić, Professor, University of Zagreb, Croatia |
| Number of pages: | 132 |
| Number of pages (in total): | 164 |
| Number of pictures: | 86 |
| Number of tables: | 6 |
| Number of references: | 148 |
| Date of oral examination: | 28 January 2019 |
| Committee members: | Dr. sc. Zdenko Tonković, Professor, University of Zagreb, Croatia<br>Dr. sc. Lovre Krstulović-Opara, Professor, University of Split, Croatia<br>Dr. sc. Marko Čanađija, Professor, University of Rijeka, Croatia |
| Archive: | Faculty of Mechanical Engineering and Naval Architecture (FAMENA) |

# Acknowledgements

First of all, I would like to express my gratitude to my thesis advisor, prof. Jurica Sorić, for having accepted me as his PhD student and for the constant support, encouragement and guidance throughout the last four years. I would also like to thank prof. Zdenko Tonković for many valuable discussions and suggestions he generously offered during the research phase.

Furthermore, I would like to thank committee members profs. Lovre-Krstulović Opara and Marko Čanađija, for finding time to read and review this thesis, and for providing the valuable suggestions and comments that ultimately led to its improved version.

A special thanks to Tomislav Lesičar, who was basically my second advisor and a compass for scientific matters. Fruitful and stimulating discussions with him always got me back on track when I encountered challenges in the research.

I would like to express my gratitude to all my friends at the Faculty of Mechanical Engineering and Naval Architecture, particularly to my colleagues from the Institute of Applied Mechanics. I would like to thank the staff members of Laboratory of Numerical Mechanics, prof. Igor Karšaj and assist. profs. Tomislav Jarak and Ivica Skozrit, for all interesting polemics both related and unrelated to science. The pleasant and friendly work atmosphere made my office hours very enjoyable, and the best part of it were definitely cheerful meetings during the coffee and tea breaks which always managed to lift my spirits. A special thanks for that to my dear colleagues Lana Virag, Daria Ćurko, Marija Smoljkić, Boris Jalušić, Karlo Seleš, Ivan Trapić, Joško Frančeski, Matija Novak, Nino Horvat, Ante Jurčević, Josip Živić and Bruno Dogančić (no preferred order).

Finally, my deepest gratitude goes to my parents Jasna and Branko. Thank you for all your patience, understanding, unconditional support and believing in me when I needed it the most.

Thank you!

Filip

Zagreb, November 2018

# Special acknowledgement

I wish to express my sincere gratitude to the Croatian Science Foundation, which financed the research conducted in this thesis through the project “Multiscale numerical Modeling of Material Deformation Responses from Macro- to Nanolevel (2516)”.

Filip Putar

Zagreb, November 2018

# Contents

**BIBLIOGRAPHY DATA** ..... **I**

**ACKNOWLEDGEMENTS** ..... **II**

**SPECIAL ACKNOWLEDGEMENT** ..... **III**

**CONTENTS** ..... **IV**

**LIST OF FIGURES** ..... **VII**

**LIST OF TABLES** ..... **XIII**

**NOMENCLATURE** ..... **XIV**

**ABSTRACT** ..... **XVIII**

**KEY WORDS** ..... **XX**

**KLJUČNE RIJEČI** ..... **XX**

**PROŠIRENI SAŽETAK** ..... **XXI**

**1 INTRODUCTION** ..... **1**

1.1 BACKGROUND AND MOTIVATION ..... 1

1.2 OVERVIEW OF DAMAGE MODELING IN CONTINUUM ..... 3

1.3 MULTISCALE MODELING OF DAMAGE ..... 6

1.4 SCOPE AND OBJECTIVE ..... 9

1.5 OUTLINE OF THE THESIS ..... 11

**2 DAMAGE MODELING IN LINEAR-ELASTIC MATERIALS** ..... **13**

2.1 BASIC THEORY OF CONTINUUM DAMAGE MECHANICS ..... 14

2.2 DAMAGE IN QUASI-BRITTLE MATERIALS ..... 16

2.3 LOCAL APPROACH TO DAMAGE ..... 20

2.4 REGULARIZATION TECHNIQUES ..... 23

**3 HIGHER-ORDER FINITE ELEMENT FOR SOFTENING ANALYSIS** ..... **28**

3.1 $C^1$ CONTINUITY FINITE ELEMENT BASED ON THE SECOND-GRADIENT CONTINUUM THEORY ..... 29

3.1.1 Higher-order continuum theory ..... 29
3.1.2 Formulation of the basic $C^1$ continuity finite element ..... 32
3.2 $C^1$ CONTINUITY FINITE ELEMENT FOR SOFTENING ANALYSIS ..... 34
3.2.1 Weak formulation ..... 34
3.2.2 Calculation of constitutive stiffness matrices ..... 37
3.2.3 Analysis procedure ..... 40
3.3 NUMERICAL EXAMPLES ..... 42
3.3.1 Plate with an imperfect zone subjected to tensile load, homogeneous microstructure ..... 42
3.3.2 Plate with an imperfect zone subjected to tensile load, heterogeneous microstructure ..... 50
3.3.3 Shear band problem ..... 57
3.3.4 Compact tension specimen ..... 64
3.3.5 Gear tooth damage ..... 69
3.3.6 Discussion ..... 71

**4 MULTISCALE ANALYSIS OF QUASI-BRITTLE HETEROGENEOUS MATERIALS UNDERGOING DAMAGE ..... 73**

4.1 $C^1$ CONTINUITY FINITE ELEMENT FOR SOFTENING ANALYSIS OF MICROSTRUCTURE ..... 76
4.1.1 Weak formulation ..... 76
4.1.2 Numerical test ..... 78
4.2 $C^0$-$C^1$ MULTISCALE SCHEME ..... 84
4.2.1 $C^0$-$C^1$ macro-micro scale transition relations ..... 84
4.2.2 Numerical example ..... 92
4.3 $C^1$-$C^1$ MULTISCALE SCHEME ..... 96
4.3.1 $C^1$-$C^1$ macro-micro scale transition relations ..... 96
4.3.2 RVE failure conditions ..... 101
4.3.3 Numerical example ..... 102
4.4 NUMERICAL EXAMPLES ..... 103
4.4.1 Rectangular plate subjected to tensile load ..... 103
4.4.2 Plate with an imperfect zone subjected to tensile load ..... 110
4.4.3 Shear band problem ..... 112
4.4.4 Discussion ..... 116

**5 CONCLUSIONS ..... 119**

**ŽIVOTOPIS ..... 123**

**BIOGRAPHY ..... 124**

**BIBLIOGRAPHY ..... 125**

# List of figures

**Figure 1.1** Homogenization of a heterogeneous material. Based on [60]. ..... 8
**Figure 2.1** Damaged body and RVE of the point *M*..... 15
**Figure 2.2** Distribution of damage in a continuum. Based on [21]. ..... 15
**Figure 2.3** Evolution of the failure process in quasi-brittle materials. Based on [34]..... 16
**Figure 2.4** Damage growth and corresponding uniaxial stress-strain response for (a) linear softening and (b) exponential softening. Based on [6]..... 18
**Figure 2.5** Equivalent strain measurements in principal strain space for (a) Mazars' definition (2.8) and (b) modified von Mises' definition (2.9). Based on [6]..... 19
**Figure 2.6** Qualitative softening responses for different finite element discretizations in the framework of classical continuum mechanics..... 21
**Figure 2.7** Representation of the nonlocal material behavior (top) and weighted averaging for an irregular microstructure (bottom). Based on [104]..... 25
**Figure 3.1** $C^1$ continuity triangular finite element. Based on [11]. ..... 33
**Figure 3.2** Scheme of the damage algorithm..... 42
**Figure 3.3** Geometry and boundary conditions of the plate subjected to tensile load. Based on [45]. ..... 43
**Figure 3.4** Comparison of damage profiles along the horizontal central axis of the plate obtained using the presented FEM damage model to the EFG results from the literature..... 44
**Figure 3.5** The coarsest finite element mesh of the plate under tension ..... 44
**Figure 3.6** Comparison of damage profiles along horizontal central axis of the plate under tension for three different mesh densities ..... 45
**Figure 3.7** Evolution of the equivalent elastic strain $\varepsilon_{eq}$ along horizontal central axis of the plate for different loading levels ..... 46
**Figure 3.8** Evolution of the damage variable *D* along horizontal central axis of the plate for different loading levels..... 46
**Figure 3.9** Distribution of the equivalent elastic strain $\varepsilon_{eq}$ for homogeneous material at failure stage..... 47
**Figure 3.10** Distribution of the damage *D* for homogeneous material at failure stage ..... 47

**Figure 3.11** Distribution of the equivalent stress $\sigma_{eq}$ for homogeneous material at failure stage ..... 48

**Figure 3.12** Distribution of the strain gradient component $\eta_{111}$ for homogeneous material at failure stage ..... 49

**Figure 3.13** Distribution of the double stress component $\mu_{111}$ for homogeneous material at failure stage ..... 49

**Figure 3.14** Deformed shape with the distribution of strain component $\varepsilon_{11}$ for homogeneous material with the internal length scale $l$ = 1.5 mm ..... 50

**Figure 3.15** RVE_0 described by the size $L$ = 5.2 mm ($l$ = 1.5 mm), average hole radius $r_{ave} = 1.118$ mm and porosity $e$ = 0.13 ..... 51

**Figure 3.16** Evolution of the equivalent elastic strain $\varepsilon_{eq}$ along horizontal central axis of the heterogeneous plate for different loading levels ..... 52

**Figure 3.17** Evolution of the damage variable $D$ along horizontal central axis of the heterogeneous plate for different loading levels ..... 52

**Figure 3.18** Distribution of the equivalent elastic strain $\varepsilon_{eq}$ for heterogeneous material represented by RVE_0 at failure stage ..... 53

**Figure 3.19** Distribution of the damage $D$ for heterogeneous material represented by RVE_0 at failure stage ..... 53

**Figure 3.20** Three different-sized samples of the same heterogeneous material: (a) RVE_1 with the size $L$ = 3 mm ($l$ = 0.87 mm), (b) RVE_2 with the size $L$ = 7.5 mm ($l$ = 2.16 mm) and (c) RVE_3 with the size $L$ = 15 mm ($l$ = 4.33 mm) ..... 54

**Figure 3.21** Comparison of damage profiles along horizontal central axis of the plate for heterogeneous material represented by three different-sized RVEs and homogenous material of the corresponding internal length scales ..... 54

**Figure 3.22** Comparison of damage profiles along horizontal central axis of the plate for two heterogeneous materials of the same porosity and corresponding homogenous material ..... 55

**Figure 3.23** RVE_4 described by the size $L$ = 1.73 mm ($l$ = 0.5 mm), average hole radius $r_{ave} = 0.075$ mm and porosity $e$ = 0.27 ..... 56

**Figure 3.24** Comparison of structural responses of the plate under tension for heterogeneous material represented by RVE_4 and homogeneous material of the same internal length scale ..... 56

**Figure 3.25** (a) Geometry and boundary conditions of the plate with an imperfect zone subjected to compressive load ($h$ = 60 mm) and (b) computational model consisting of upper half of the plate and appropriate boundary conditions, with a depicted mesh detail ..... 58
**Figure 3.26** Distribution of the equivalent elastic strain $\varepsilon_{eq}$ through several loading stages for homogeneous material..... 59
**Figure 3.27** Distribution of the equivalent elastic strain $\tilde{e}$ through several loading stages obtained by conventional implicit gradient formulation [33] ..... 59
**Figure 3.28** Distribution of the damage $D$ through several loading stages for homogeneous material..... 60
**Figure 3.29** Distribution of the damage $\omega$ through several loading stages obtained by conventional implicit gradient formulation [33] ..... 60
**Figure 3.30** Comparison of damage distribution $D$ for homogeneous material for two different disretizations consisting of 800 (left) and 3200 (right) triangular finite elements..... 61
**Figure 3.31** Comparison of damage distribution $D$ for homogeneous material defined with the internal length scales $l$ = 1 mm (left) and $l$ = 2 mm (right) ..... 61
**Figure 3.32** Deformed shape with damage distribution $D$ for homogeneous material with the internal length scale $l$ = 2 mm ..... 62
**Figure 3.33** Distribution of the equivalent elastic strain $\varepsilon_{eq}$ through several loading stages for heterogeneous material..... 63
**Figure 3.34** Comparison of structural responses of the plate under compression for heterogeneous material and homogeneous material of the same internal length scale ..... 63
**Figure 3.35** (a) Geometry and boundary conditions of the compact tension specimen ($h$ = 100 mm) and (b) computational model consisting of upper half of the plate and appropriate boundary conditions ..... 64
**Figure 3.36** Damage evolution ahead of the notch tip through several loading stages obtained by (a) conventional implicit gradient damage formulation and (b) localizing gradient damage model with decreasing interactions [34] ..... 65
**Figure 3.37** Damage profiles at different loading stages obtained by conventional implicit gradient damage formulation [34]..... 66
**Figure 3.38** Damage evolution ahead of the notch tip through several loading stages for homogeneous material..... 66
**Figure 3.39** Comparison of damage distribution $D$ for homogeneous material for two different disretizations consisting of 800 (left) and 3200 (right) triangular finite elements..... 67

**Figure 3.40** Comparison of damage distribution $D$ for homogeneous material defined with the internal length scales $l$ = 8 mm (left) and $l$ = 20 mm (right) ..... 67
**Figure 3.41** Deformed shape with damage distribution $D$ for homogeneous material with the internal length scale $l$ = 8 mm ..... 68
**Figure 3.42** Comparison of structural responses of the compact tension specimen for heterogeneous material and homogeneous material of the same internal length scale ..... 69
**Figure 3.43** Computational model of the spur gear with: (a) notch and (b) pre-existing crack ..... 70
**Figure 3.44** Distribution of the equivalent elastic strain $\varepsilon_{eq}$ over the gear model with notch 71
**Figure 3.45** Deformed shape with the distribution of the damage variable $D$ over the gear model with pre-existing crack ..... 71
**Figure 4.1** Homogenization of the localized deformation ..... 75
**Figure 4.2** RVE of the side length of 0.5 mm discretized by 2205 $C^1$ triangular finite elements ..... 79
**Figure 4.3** Tensile loading case: (a) computational model and (b) deformed shape with distribution of damage $D$ in failure stage ..... 80
**Figure 4.4** Compressive loading case: (a) computational model and (b) deformed shape with distribution of damage $D$ in failure stage ..... 80
**Figure 4.5** Shear loading case: (a) computational model and (b) deformed shape with distribution of damage $D$ in failure stage ..... 81
**Figure 4.6** Structural responses for three different RVE loading cases ..... 81
**Figure 4.7** Structural responses for two tensile RVE loading cases with different internal length scale parameters ..... 82
**Figure 4.8** Distribution of the damage $D$ through several loading stages for internal length scale parameter $l$ = 0.01 mm ..... 82
**Figure 4.9** Distribution of the damage $D$ through several loading stages for internal length scale parameter $l$ = 0.02 mm ..... 83
**Figure 4.10** Scheme of $C^0$-$C^1$ multiscale algorithm ..... 85
**Figure 4.11** Representative volume element [17] ..... 86
**Figure 4.12** Geometry and boundary conditions of the plate subjected to tensile load ..... 93
**Figure 4.13** Macrolevel discretization consisting of: (a) 24, (b) 54 and (c) 48 $C^0$ continuity rectangular finite elements (CPE8R) ..... 94
**Figure 4.14** Homogeneous MVE consisting of 32 $C^1$ continuity triangular finite elements ... 94

**Figure 4.15** Load-displacement diagrams obtained by three different macrolevel discretizations used in $C^0$-$C^1$ multiscale scheme and by one-scale damage model ..... 96
**Figure 4.16** Scheme of $C^1$-$C^1$ multiscale algorithm ..... 97
**Figure 4.17** Localization zone inside an RVE..... 101
**Figure 4.18** Macrolevel discretization consisting of: (a) 48 and (b) 96 $C^1$ continuity triangular finite elements ..... 102
**Figure 4.19** Load-displacement diagrams obtained by two different macrolevel discretizations used in $C^1$-$C^1$ multiscale scheme and by one-scale damage model ..... 103
**Figure 4.20** Computational model of rectangular plate subjected to tensile load with $h$ = 10 mm ..... 104
**Figure 4.21** RVE described by the size $L$ = 2.6 mm, average hole radius $r_{\text{ave}} = 0.559$ mm and porosity $e$ = 0.13..... 105
**Figure 4.22** Load-displacement diagram obtained by $C^1$-$C^1$ multiscale analysis for heterogeneous microstructure of internal length scale $l_{\text{micro}} = 0.6608$ mm..... 105
**Figure 4.23** Distribution of damage variable $D$ over some characteristic RVEs for $l_{\text{micro}} = 0.6608$ mm at failure stage ..... 106
**Figure 4.24** Load-displacement diagram obtained by $C^1$-$C^1$ multiscale analysis for heterogeneous microstructure of internal length scale $l_{\text{micro}} = 0.025$ mm..... 107
**Figure 4.25** Distribution of damage variable $D$ over some characteristic RVEs for $l_{\text{micro}} = 0.025$ mm at failure stage ..... 108
**Figure 4.26** Load-displacement diagrams obtained by one-scale damage models and $C^1$-$C^1$ multiscale scheme for materials consisting of homogeneous and heterogeneous microstructures ..... 109
**Figure 4.27** Structural responses of the plate subjected to tensile load obtained by the $C^1$-$C^1$ multiscale scheme for homogeneous and heterogeneous microstructure ..... 111
**Figure 4.28.** Deformed shape with the distribution of strain component $\varepsilon_{11}$ for heterogeneous microstructure with the internal length scale $l_{\text{micro}} = 0.025$ mm at final stage of the analysis ..... 111
**Figure 4.29** Distribution of damage variable $D$ over some characteristic RVEs for $l_{\text{micro}} = 0.025$ mm at final stage of the analysis ..... 112

**Figure 4.30** (a) Geometry and boundary conditions of the plate with an imperfect zone subjected to compressive load ($h$ = 60 mm) and (b) discretization consisting of 96 $C^1$ continuous triangular finite elements ..... 113

**Figure 4.31** Structural responses of the plate subjected to compressive load obtained by the $C^1$-$C^1$ multiscale scheme for homogeneous and heterogeneous microstructure ..... 114

**Figure 4.32** Distribution of the equivalent elastic strain $\varepsilon_{\text{eq}}$ for heterogeneous microstructure with the internal length scale $l_{\text{micro}} = 0.025$ mm at the onset of softening ..... 115

**Figure 4.33** Distribution of damage variable $D$ over some characteristic RVEs for $l_{\text{micro}} = 0.025$ mm at the onset of softening ..... 116

# List of tables

**Table 3.1** Basic relations of the strain gradient continuum [17] ..... 31
**Table 3.2** Basic relations of the second-order homogenization [17] ..... 38
**Table 3.3** Stiffness calculation for microstructurally homogeneous and heterogeneous materials ..... 40
**Table 4.1** Solving algorithm of $C^0$-$C^1$ macro-micro scheme ..... 92
**Table 4.2** Macro-to-micro scale transition relations in $C^1$-$C^1$ multiscale scheme [11] ..... 98
**Table 4.3** Micro-to-macro scale transition relations in $C^1$-$C^1$ multiscale scheme [11] ..... 100

# Nomenclature

## Greek symbols

| | |
|---|---|
| $\alpha$, $\beta$ | exponential softening law parameters |
| $\tilde{\alpha}$ | local variable |
| $\bar{\alpha}$ | nonlocal variable |
| $\boldsymbol{\varepsilon}$ | strain tensor |
| $\varepsilon_1$, $\varepsilon_2$, $\varepsilon_3$ | principal strains |
| $\varepsilon_{\mathrm{eq}}$ | equivalent elastic strain |
| $\tilde{\varepsilon}_{\mathrm{eq}}$ | local equivalent elastic strain |
| $\bar{\varepsilon}_{\mathrm{eq}}$ | nonlocal equivalent elastic strain |
| $\boldsymbol{\varepsilon}_{x_1}$, $\boldsymbol{\varepsilon}_{x_2}$ | strain gradient tensor |
| $\Delta\boldsymbol{\varepsilon}$ | iterative correction of strain tensor |
| $\Delta\boldsymbol{\varepsilon}_{x_1}$, $\Delta\boldsymbol{\varepsilon}_{x_2}$ | iterative correction of strain gradient tensor |
| $\delta\boldsymbol{\varepsilon}$ | strain tensor variation |
| ${}^3\boldsymbol{\eta}$ | second-order strain tensor |
| $\Delta{}^3\boldsymbol{\eta}$ | iterative correction of second-order strain tensor |
| $\delta{}^3\boldsymbol{\eta}$ | second-order strain tensor variation |
| $\vartheta$ | weight function |
| $\kappa$ | history parameter |
| $\kappa_0$ | initial history parameter |
| $\kappa_{\mathrm{u}}$ | ultimate history parameter |
| $\lambda$ | first Lamé's elastic constant |
| ${}^3\boldsymbol{\mu}$, ${}^3\boldsymbol{\mu}_{x_1}$, ${}^3\boldsymbol{\mu}_{x_2}$ | double stress tensor |
| ${}^3\boldsymbol{\mu}^{i-1}$, ${}^3\boldsymbol{\mu}_{x_1}^{i-1}$, ${}^3\boldsymbol{\mu}_{x_2}^{i-1}$ | double stress tensor at the last converged equilibrium state |
| $\Delta{}^3\boldsymbol{\mu}$, $\Delta{}^3\boldsymbol{\mu}_{x_1}$, $\Delta{}^3\boldsymbol{\mu}_{x_2}$ | iterative correction of double stress tensor |

| | |
|---|---|
| $\mu$ | second Lamé's elastic constant |
| $\nabla$ | gradient operator |
| $\nabla^2$ | Laplacian operator |
| $\nu$ | Poisson's ratio |
| $\xi$, $\eta$ | isoparametric coordinates |
| $\boldsymbol{\sigma}$ | Cauchy stress tensor |
| $\boldsymbol{\sigma}^{i-1}$ | Cauchy stress tensor at the last converged equilibrium state |
| $\Delta\boldsymbol{\sigma}$ | iterative correction of Cauchy stress tensor |
| $\tilde{\boldsymbol{\sigma}}$ | effective stress tensor |
| $\sigma_{\mathrm{eq}}$ | equivalent stress |
| $\boldsymbol{\tau}$ | double surface traction tensor |

## Latin symbols

| | |
|---|---|
| $A$ | surface of the body |
| $A_d$ | localization area |
| $a_1$, ..., $a_{21}$ | displacement coefficients |
| $\mathbf{B}_{\varepsilon}$, $\mathbf{B}_{\eta}$, $\mathbf{B}_{\eta_1}$, $\mathbf{B}_{\eta_2}$ | derivatives of the shape functions |
| $\mathbf{C}^{\mathrm{eff}}$ | effective stiffness tensor |
| $\mathbf{C}$ | elastic stiffness tensor |
| ${}^4\mathbf{C}_{\sigma\varepsilon}$, $\mathbf{C}_{\sigma\varepsilon}$ | material matrix relating stress to strain |
| ${}^5\mathbf{C}_{\sigma\eta}$, $\mathbf{C}_{\sigma\eta}$ | material matrix relating stress to second-order strain |
| ${}^5\mathbf{C}_{\mu\varepsilon}$, $\mathbf{C}_{\mu\varepsilon}$ | material matrix relating double stress to strain |
| ${}^6\mathbf{C}_{\mu\eta}$, $\mathbf{C}_{\mu\eta}$ | material matrix relating double stress to second-order strain |
| ${}^4\mathbf{C}_{\sigma\varepsilon}$, ${}^5\mathbf{C}_{\sigma\varepsilon_{x_1}}$, ${}^5\mathbf{C}_{\sigma\varepsilon_{x_2}}$ | generalized Aifantis material matrices |
| ${}^5\mathbf{C}_{\mu_{x_1}\varepsilon}$, ${}^6\mathbf{C}_{\mu_{x_1}\varepsilon_{x_1}}$, ${}^6\mathbf{C}_{\mu_{x_1}\varepsilon_{x_2}}$ | generalized Aifantis material matrices |
| ${}^4\mathbf{C}_{\mu_{x_2}\varepsilon}$, ${}^5\mathbf{C}_{\mu_{x_2}\varepsilon_{x_1}}$, ${}^5\mathbf{C}_{\mu_{x_2}\varepsilon_{x_2}}$ | generalized Aifantis material matrices |

| | |
|---|---|
| $c$, $c_1$, $c_2$ | gradient coefficients |
| $\mathbf{D}$ | coordinate matrix |
| $D$ | damage variable |
| $D^{i-1}$ | damage variable at the last converged equilibrium state |
| $\left(\frac{\mathrm{d}D}{\mathrm{d}\boldsymbol{\varepsilon}}\right)^{i-1}$ | derivative of damage variable over the strain tensor at the last converged equilibrium state |
| $\Delta D$ | iterative correction of damage variable |
| $D$ | normal gradient operator |
| $\bar{d}$ | phase-field parameter |
| $e$ | porosity |
| $E$ | Young's modulus |
| $\mathbf{F}_\mathrm{e}$, $\mathbf{F}_\mathrm{i}$ | external and internal nodal force vectors |
| $\mathbf{f}_\mathrm{b}$ | RVE boundary nodal force vector |
| $G_\mathrm{c}$ | fracture energy |
| $\mathbf{H}_1$, $\mathbf{H}_2$ | coordinate matrices |
| $h$ | degradation function |
| $\mathbf{I}$ | second-order unit tensor |
| $I_1$ | first invariant of strain tensor |
| $J_2$ | second invariant of deviatoric strain tensor |
| $\mathbf{K}$ | finite element stiffness matrix |
| $\tilde{\mathbf{K}}_{bb}$ | condensed RVE stiffness matrix |
| $\mathbf{K}_\mathrm{aa}$, $\mathbf{K}_\mathrm{ab}$, $\mathbf{K}_\mathrm{ba}$, $\mathbf{K}_\mathrm{bb}$ | RVE stiffness submatrices |
| $\mathbf{K}_{\varepsilon\varepsilon}$, $\mathbf{K}_{\varepsilon\eta}$, $\mathbf{K}_{\eta\varepsilon}$, $\mathbf{K}_{\eta\eta}$ | stiffness submatrices |
| $\mathbf{K}_\sigma$, $\mathbf{K}_{\mu_{x_1}}$, $\mathbf{K}_{\mu_{x_2}}$ | stiffness submatrices |
| $k$ | ratio between uniaxial compressive and tensile strength |
| $L$ | RVE side length |
| $l$ | internal length scale parameter |
| $l_\mathrm{micro}$ | internal length scale parameter at microstructural level |
| $\mathbf{N}$ | shape function matrix |

| | |
|---|---|
| $\mathbf{N}$, $\mathbf{n}$ | unit outward normal vector |
| $\mathbf{r}$ | microfluctuation field |
| $s$ | boundary line |
| $\mathbf{T}$ | double traction tensor |
| $\mathbf{t}$ | surface traction vector |
| $\mathbf{u}$ | displacement vector |
| $\mathbf{u}_{\mathrm{b}}$ | RVE boundary displacement vector |
| $\mathbf{u}^{i-1}$ | displacement vector at the last converged equilibrium state |
| $\delta\mathbf{u}$ | displacement vector variation |
| $\Delta\mathbf{u}$ | iterative correction of displacement vector |
| $u$ | displacement field |
| $V$ | volume of body |
| $\mathbf{V}$ | global vector of nodal degrees of freedom |
| $\Delta\mathbf{V}$ | iterative correction of global vector of nodal degrees of freedom |
| $\mathbf{v}$ | vector of nodal degrees of freedom |
| $\delta\mathbf{v}$ | variation of nodal degrees of freedom |
| $\Delta\mathbf{v}$ | iterative correction of nodal degrees of freedom |
| $W$ | strain energy density function, work |
| $\mathbf{x}$, $\mathbf{y}$ | position vector |
| $x$, $y$ | Cartesian coordinates |
| $x_1$, $x_2$ | Cartesian coordinates |

# Abstract

Prevention of the damage phenomenon in the structural components has always been a major criterion for keeping the longest possible working lifetime of the engineering systems and thus the minimization of the financial expenses due to maintenance, as well as for the safety of the people who benefit from such systems. In recent times, the need for keeping the track of the damage is even higher as a demand towards lighter, thinner and smaller designing solutions is rapidly increasing, where the very rigorous reliability and safety requirements need to be satisfied. In addition, new production technologies enable the manufacturing of the novel material solutions that provide exceptional exploitation characteristics, but can be very susceptible to failure due to very complex microstructures, where, from the engineering point of view, the initiation of the damage takes place. In order to reduce the amount of classical experiments to assess the structural integrity, various numerical models for the description of the material degradation are developed to this end. Due to importance of the microstructure in the damage development, multiscale models capable of consideration of such phenomena present an important modeling tool, but still need to be developed more for the commercial use.

Regarding the modeling of damage at one scale only, classical continuum theory cannot be employed due to inconsistencies in the mathematical model that eventually lead to incorrect numerical results. Most of the available damage models take into account the influence of the microstructure by enhancing the constitutive relations with the measurement of the internal length scale, which serves as a strain localization limiter and prevents the dependency of the numerical results on the discretization. Although most of the models based on this, so called nonlocal continuum, can prevent the aforementioned numerical artefacts when damage is considered, there are still some difficulties that can arise when the internal length scale is kept constant, leading to nonphysical or spurious growth of the damage.

Herein, a damage model for quasi-brittle materials embedded into the two dimensional $C^1$ continuity triangular finite element formulation based on the strain gradient continuum theory is considered. The isotropic damage law is applied to the higher-order stress-strain constitutive model, which enables the analysis of both homogeneous and heterogeneous materials. Such softening formulation also ensures a decrease of the intensity of the material nonlocality associated with the damage growth, which is necessary for the correct description of the narrow localized deformation. In order to obtain the required constitutive matrices, the

second-order homogenization procedure is applied to the various representative volume elements in the frame of a multiscale approach. The derived finite element formulation is implemented into the finite element program ABAQUS by means of UEL subroutine. The superior regularization capabilities, as well as the accuracy and efficiency of the proposed higher-order gradient damage model are demonstrated by the standard benchmark examples.

In the multiscale modeling of damage several obstacles are present of which still some have to be resolved, especially when computational homogenization is applied as a method for scale transitioning. Namely, generally a higher-order continuum has to be used at the macrolevel, while in the presence of the sharp localization zones at the microstructural level, macrostructural response is dependent on the size of the RVEs used. Physically, inconsistencies can arise in such conditions between the strain fields of two structural levels, which is known as the violation of the scale separation.

In the thesis, previously developed multiscale scheme which utilizes the higher-order continuum at both structural levels is modified for the consideration of the damage at the microlevel. Effects of the microlevel damage formation can be observed through the degradation of the homogenized tangent stiffness tensors, which then govern the localization at the larger structural level. Finite element based on the Aifantis theory of gradient elasticity is adapted for the softening analysis and its capabilities are tested on the random RVE for several different loading cases. Additionally, in order to prove the necessity for the higher-order continuum at the macroscale, which is in this case generalized Aifantis theory, scale transition methodology where classical continuum is employed at the macrolevel is developed. Therein, rather than strains and strain gradients, only the strain tensors contribute to the formation of the RVE boundary displacements, while the stiffness tensors that carry the nonlocal characteristics cannot be transferred at the macrolevel. Both multiscale schemes are tested on a standard benchmark example and compared with the one-scale damage model solution for the case of the homogenous microstructure, when only a mild and diffused localization is observed. In order to capture the loss of structural integrity of the macrostructural integration point when sharp localization is formed across an RVE, a specific conditions which detect the completely formed localization zone are developed. Finally, the capabilities of the presented $C^1$-$C^1$ multiscale scheme to capture the effects of the sharp localization at microlevel are demonstrated by few benchmark numerical examples.

# Key words

quasi-brittle damage

$C^1$ continuity finite element

strain gradient theory

multiscale analysis

RVE

heterogeneous material

# Ključne riječi

kvazi-krhko oštećenje

konačni element $C^1$ kontinuiteta

gradijentna deformacijska teorija

višerazinska analiza

RVE

heterogeni materijal

# Prošireni sažetak

## Uvod

Novi i sve stroži zahtjevi na pouzdanost i sigurnost konstrukcija, zajedno s primjenom novih materijala i novih proizvodnih tehnologija, mogu jedino biti ostvareni korištenjem naprednih metoda numeričke strukturne analize i što realnijim opisom ponašanja materijala. Budući da u radnom vijeku određene konstrukcijske komponente može doći do pojave oštećenja, potrebno je znati opisati njeno ponašanje sve do potpunog gubitka mehaničkog integriteta, odnosno loma. Većina inženjerskih materijala nakon određene deformacije počinje pokazivati postepeno smanjenje krutosti ili takozvano popuštanje što je direktna posljedica degradacijskih procesa na razini atomske rešetke. Kako je numeričko modeliranje procesa koji se zbivaju na toj razini još uvijek neprikladno sa stajališta računalnog vremena, oštećenje se u odgovarajući numerički algoritam najčešće uvodi kao set kontinuiranih makroskopskih varijabli koje nose informaciju o stanju materijala na nižim prostornim skalama, odnosno u njima je implicitno sadržano stanje mikrostrukture. Popuštanje se može istovremeno odvijati s pojavom plastičnosti što je slučaj kod duktilnih materijala kao što su razni čelici, a u slučaju izostanka plastičnosti govori se o popuštanju kvazi-krhkih materijala poput perlitne matrice u nodularnom lijevu koji se često javlja u mehaničkim konstrukcijama, betona, keramike i nekih vrsta ojačanih kompozita.

Oštećenje je u inženjerskim materijalima izrazito nehomogeno i lokalizirano. Mikropukotine se stvaraju na mjestima koncentracije naprezanja i njihov je naknadni rast u ograničenom području koje je malo u usporedbi sa cijelom konstrukcijskom komponentom. Pojava popuštanja koja nastaje kao posljedica oštećenja uvijek je popraćena velikim gradijentima deformacije na način da se deformacija lokalizira u području gdje se popuštanje odvija. U teoriji klasičnog kontinuuma popuštanje može dovesti do lokalnog gubitka eliptičnosti diferencijalnih jednadžbi koje opisuju proces deformiranja. Matematički gledano, modul materijalne tangentne krutosti pri ulasku u fazu popuštanju prestaje biti pozitivno definitan što rezultira lošom uvjetovanošću cjelokupnog problema, posljedica čega je nemogućnost konvergencije numeričkih rješenja prema fizikalno smislenom rješenju. Pritom se deformacija, promatrano u okviru metode konačnih elemenata, lokalizira u samo jedan konačni element ili najtanji sloj konačnih elemenata, a disipacijska energija teži k nuli.

# Postojeći modeli oštećenja

Očuvanje eliptičnosti diferencijalnih jednadžbi koje opisuju proces deformiranja u fazi popuštanja, ili takozvana regularizacija problema lokalizacije deformacije, moguća je primjenom mehanike kontinuuma višeg reda. Njome se, za razliku od klasične mehanike kontinuuma, preko parametra unutarnje duljinske skale u obzir uzimaju i mikrostrukturne interakcije koje se mogu opisati na više različitih načina. Primjenom mikropolarne teorije ili poznatije Cosseratove teorije, materijalne čestice dobivaju dodatan rotacijski stupanj slobode neovisan o polju pomaka. Time se veoma uspješno rješavaju problemi gdje je smik dominantan način deformiranja tako da pri čistom vlaku pristup ne funkcionira. Viskoplastična teorija u konstitutivni model uključuje ovisnost brzine promjene deformacije, odnosno viskozne efekte, no ona daje dobre rezultate samo ako je lokalizacijska zona unaprijed poznata.

U novije vrijeme sve se češće primjenjuju metode temeljene na nelokalnom ponašanju materijala, tako da naprezanje u nekoj točki kontinuuma ne ovisi samo o deformaciji i ostalim varijablama stanja u toj točki, već i o deformacijama i ostalim varijablama stanja točaka koje ju okružuju. U osnovi razlikuju se dva različita pristupa pri opisivanju nelokalnog modela, integralni i gradijentni pristup. Integralni pristup temeljen je na prostornom osrednjavanju varijabli stanja, najčešće deformacija, u konačnoj blizini određene točke, što naposljetku dovodi do veoma složenih konstitutivnih relacija sastavljenih od integrala konvolucijskog tipa. Gradijentni pristup proširuje konstitutivnu relaciju ili samo gradijentima deformacije ili gradijentima deformacije i njihovim konjugiranim veličinama, što se odnosi na takozvanu punu gradijentnu teoriju. U slučaju proširenja samo gradijentima deformacije, do sada su kod proučavanja lokalizacije i popuštanja najčešće korištene implicitne i nešto rjeđe eksplicitne gradijentne formulacije. Problemi razmatrani u literaturi vezani su za elastično ponašanje materijala, plastično ponašanje materijala, ili se dotiču analize širenja elastičnih valova. Mišljenja su da eksplicitna gradijentna formulacija u model unosi takozvanu slabu nelokalnost budući da je ekvivalentna nelokalna deformacija izražena najčešće samo preko ekvivalentne lokalne deformacije i njenog drugog gradijenta, što proizlazi odbacivanjem viših članova razvoja lokalne ekvivalentne deformacije u Taylorov red. Implicitna formulacija s druge strane unosi takozvanu jaku nelokalnost jer kod nje nelokalna deformacija nije eksplicitno izražena preko članova lokalne deformacije, već je dana kao rješenje problema rubnih vrijednosti čime su zapravo zadržani odbačeni članovi višeg reda u slučaju eksplicitne formulacije. Zbog različitih karaktera dviju gradijentnih formulacija nužan je i različit pristup u numeričkoj

implementaciji, pa tako korištenje eksplicitne formulacije zahtijeva uporabu konačnih elemenata $C^1$ kontinuiteta, dok se implicitna formulacija najčešće rješava konačnim elementima $C^0$ kontinuiteta temeljenim na mješovitoj formulaciji. Iako su $C^0$ konačni elementi u osnovi jednostavniji od konačnih elemenata $C^1$ kontinuiteta, upitno je postiže li se uvođenjem mješovite formulacije bolja numerička učinkovitost.

Usprkos tome što se implicitnom gradijentnom formulacijom mogu dobiti rješenja neovisna o gustoći i usmjerenju mreže, u literaturi je prijavljeno nekolika slučajeva u kojima dolazi do nefizikalnog širenja oštećenja po računalnom modelu. Opisana pojava karakteristična je i za integralne i za gradijentne pristupe klasičnog tipa, u kojima područje mikrostrukturnog međudjelovanja ostaje konstantno tijekom cijelog procesa opterećivanja. Kao što je objašnjeno u literaturi, navedena pretpostavka ima za posljedicu prijenos energije iz područja u kojoj se oštećenje odvija u susjedno područje koje elastično popušta. Na taj način dolazi do rasta oštećenja u područjima gdje ga fizikalno ne bi trebalo biti, te je onemogućeno stvaranje uskog pojasa lokalizacije deformacije. Problem je riješen uvođenjem modificiranih nelokalnih formulacija u kojima je veličina područja mikrostrukturnog djelovanja podložna promijeni tijekom procesa opterećivanja. Međutim, većina takvih formulacija opisuje povećanje navedenog područja s porastom oštećenja, što nije u skladu s fizikalnim procesom stvaranja makropukotine, gdje je situacija upravo suprotna, pogotovo u slučaju kvazi-krhkih materijala. Od nedavno sve više se razvija modeliranje putem takozvanog faznog polja, koje dijeli mnogo sličnosti s gradijentnim formulacijama po pitanju matematičke strukture. Iako se navedenim pristupom mogu dobiti u potpunosti regularizirana rješenja, kako bi se dobio točan razvoj faznog polja, odnosno oštećenja, potrebno je značajno povećati broj konačnih elemenata u području gdje se očekuje pojava pukotine, što naposljetku dovodi i do značajnog povećanja računalnog vremena.

Drugi tip gradijentnog pristupa gdje u funkciju energije deformiranja ulaze i gradijenti deformacije zajedno s njihovim konjugiranim veličinama do sada je nešto rjeđe korišten, prvenstveno zato jer je složeniji za numeričku implementaciju. Prednost pune gradijentne teorije je jednostavnije opisivanje proizvoljne materijalne heterogenosti uvodeći u konstitutivne relacije vandijagonalne tangentne krutosti višeg reda, koje se mogu dobiti procesom homogenizacije na odgovarajućem reprezentativnom volumnom elementu (RVE-u). RVE predstavlja statistički reprezentativan uzorak materijala. Razmatranja problema oštećenja putem pune gradijentne teorije na jednodimenzijskim primjerima dovela su do zaključka kako dodatak naprezanja višeg reda doprinosi stabilizaciji pozitivne definitnosti tangentne krutosti prilikom ulaska u fazu popuštanja. Daljnja istraživanja s jednodimenzijskog na dvodimenzijski

problem procesa lokalizacije i popuštanja provedena su primjenom bezmrežne EFG metode, gdje je formulacija ograničena samo na homogene materijale.

## Višerazinsko modeliranje oštećenja

U modeliranju procesa popuštanja heterogenih materijala važnu ulogu zauzimaju višerazinske metode kojima se omogućuje eksplicitno modeliranje mikrostrukture putem RVE-a, što je značajno budući da makrostrukturno ponašanje izravno proizlazi iz deformacijskih procesa na mikrorazini. Glavni izazov u višerazinskim metodama gdje se razmatra oštećenje na razini RVE-a je povezivanje razvoja mikroskopske lokalizacije deformacije ka stvaranju makroskopske pukotine. Taj je problem u literaturi tek djelomično riješen putem takozvanih tehnika lokalnog progušćivanja mreže konačnih elemenata. Primjerice, kod višemrežnih metoda ili metoda temeljenih na superpoziciji koristi se hijerarhijska podjela na makro- i mikostrukturne efekte na način da se makrostrukturna mreža lokalno prekrije diskretizacijom detaljno opisane mikrostrukture. Slično, metode dekompozicije domene temelje se na podijeli makrorazine materijala na nekoliko područja od kojih svako može imati različitu prostornu diskretizaciju s prikladnim unutarnjim duljinskim skalama, što omogućuje rješavanje problema lokalizacije uz smanjivanje računalnog vremena. Bitno je spomenuti kako su navedene tehnike lokalnog progušćivanja mreže efikasne jedino u slučaju blažih i manjih lokalizacijskih zona čiji se položaj mora znati unaprijed.

Najveći napredak u višerazinskom modeliranju mikroskopske lokalizacije deformacije postignut je primjenom metoda računalne homogenizacije. Njihova velika prednost je u tome što na zahtijevaju poznavanje konstitutivnih pretpostavki na makrorazini, već se odaziv homogenog materijala određuje u toku analize rješavanjem problema rubnih uvjeta na RVE-ovima, od kojih je svaki povezan s odgovarajućom točkom integracije na makrorazini. Klasične tehnike homogenizacije temelje se na principu separacije skala, koji nalaže da bi veličina RVE-a trebala biti mnogo manja, nego karakteristična duljina preko koje se makroskopsko opterećenje mijenja u prostoru. Homogenizacijom prvog reda ne može se modelirati lokalizacija i popuštanje bez gubitka eliptičnosti osnovnih jednadžbi, dok je homogenizacija drugog reda pogodna tek za opisivanje umjerene lokalizacije koja nije u proturječju s principom separacije skala, odnosno dopušta lokalizaciju u makroskopskoj zoni koja je veća od veličine RVE-a. Budući da takav pristup nije pogodan za opisivanje snažnih lokalizacija unutar RVE-a, većina radova je posljednjih godina orijentirana pristupu kojim se kontinuum na makrorazini

proširuje diskontinuitetom čime se omogućuje prijenos lokalizacije deformacije s mikrorazine u pukotinu na makrorazini. U sklopu tog pristupa u literaturi se može naći više različitih tehnika kojima se izračunava ekvivalentni diskontinuitet i odgovarajuća konstitutivna relacija odziva mikrostrukture. Sljedeći problem koji se javlja kod homogenizacijskih metoda gdje dolazi do oštre lokalizacije na mikrorazini je ovisnost makrostrukturnog odaziva modela o veličini RVE-a, na način da s povećanjem RVE-a dolazi do sve krućeg ponašanja materijala na makrorazini. U tom slučaju RVE gubi svoju reprezentativnost za odgovarajuću makroskopsku točku, te je stoga u literaturi prozvan mikrostrukturnim volumnim elementom (MVE). Postojanje RVE-a u kojem dolazi do primjetne lokalizacije deformacije potvrđeno je u literaturi putem tehnike temeljene na homogenizaciji konstitutivne relacije samo iz lokalizacijskog pojasa, što je naknadno ugrađeno i u shemu računalne homogenizacije za modeliranje diskretne makroskopske pukotine. Usprkos trenutnom intenzivnom istraživanju u navedenom području, još uvijek je ostalo mnoštvo otvorenih pitanja pri prijenosu varijabli stanja s mikrorazine na makrorazinu. Potrebno je povećati točnost i numeričku učinkovitost predloženih postupaka.

## Ciljevi i hipoteze istraživanja

Cilj istraživanja u prvom dijelu disertacije je razvoj modela oštećenja temeljenog na teoriji gradijentnih deformacija, u kojoj u energiji deformiranja gradijenti deformacije sudjeluju zajedno s njihovim energijski konjugiranim veličinama. Očekuje se da će se primjenom teorije kontinuuma višeg reda uspjeti eliminirati nefizikalan razvoj oštećenja, tipično povezan s klasičnom implicitnom gradijentnom formulacijom koja je još uvijek jedna od najčešće primjenjivanih metoda za modeliranje oštećenja. Također, konstitutivno ponašanje materijala modelirat će se na način koji uključuje smanjivanje unutarnje duljinske skale s porastom oštećenja, čime će se numerički opisati stvaran proces koji prethodi stvaranju makropukotine. Budući da konstitutivne relacije koji proizlaze iz teorije gradijentnih deformacija omogućuju razmatranje mikrostrukturnih heterogenosti, razmotrit će se i mogućnosti modeliranja oštećenja heterogenih materijala. Pritom će se inicijalni, elastični konstitutivni tenzori izračunavati primjenom računalne homogenizacije drugog reda na odgovarajućem RVE-u, a analiza popuštanja će se potom odvijati isključivo na makrorazinskom modelu.

Drugi dio istraživanja usmjeren je na razvoj nove metode za numeričko modeliranje oštećenja u heterogenim materijalima primjenom višerazinskih algoritama temeljenih na teoriji gradijentnih deformacija. Razmotrit će se mogućnosti modeliranja oštećenja putem

višerazinskog algoritma pri kojem su obje materijalne razine opisane kontinuumom višeg reda, koji uključuje primjenu diskretizacije $C^1$ kontinuiteta i podrazumijeva nelokalno ponašanje materijala. Očekuje se da će se na taj način eliminirati problemi u opisivanju lokalizacije povezani s diskretizacijom i na makro- i na mikrorazini. Za homogenizaciju varijabli s mikrorazine koristit će se klasična homogenizacija drugog reda, pri čemu će doprinos biti sadržan u formulaciji pomoćnog algoritma za prepoznavanje gubitka strukturnog integriteta RVE-a.

Hipoteze istraživanja su sljedeće:

1. Moguće je modelirati pojavu oštećenja u materijalu primjenom prostorne diskretizacije temeljene na metodi pomaka. Predložena nova formulacija pokazat će prednosti u odnosu na dosadašnju primjenu diskretizacije temeljene na mješovitoj formulaciji.

2. Primjenom postupka homogenizacije u okviru višerazinskih algoritama moguće je postići veću točnost pri modeliranju oštećenja u heterogenim materijalima od one koja se postiže dosadašnjim formulacijama koje se nalaze u literaturi.

# Zaključak i doprinos rada

Poznato je kako klasična mehanika kontinuuma ne može objektivno opisati problem lokalizacije deformacije zbog matematičke nekonzistentnosti modela koja se počinje javljati s popuštanjem materijala. Razvojem materijalnih nestabilnosti dolazi do pojave gubitka pozitivne definitnosti tangentne krutosti, što za posljedicu ima gubitak eliptičnosti jednadžbi ravnoteže te stvaranje loše uvjetovanog problema rubnih vrijednosti. U takvim okolnostima može doći do nestabilnog razvoja oštećenja što naposljetku dovodi do nefizikalnog ponašanja materijala, što se kod diskretizacije konačnim elementima očituje u ovisnosti numeričkih rezultata o gustoći i usmjerenju mreže. Također, oštećenje u takvom razvoju situacije lokalizira u najmanji mogući konačni element ili najtanji sloj konačnih elemenata. U ovome radu izveden je matematički konzistentan kontinuumski model oštećenja koji može realistično opisati iniciranje i naknadni razvoj oštećenja.

Nefizikalno ponašanje materijala povezano s korištenjem modela oštećenja temeljenih na klasičnoj mehanici kontinuuma, odnosno lokalnom pristupu, u radu je uklonjeno uvođenjem

nelokalnog ponašanja materijala putem kontinuuma višeg reda. U nelokalnim modelima važnu ulogu ima parametar unutarnje duljinske skale, koji opisuje veličinu područja mikrostrukturnih međudjelovanja i koji služi za ograničavanje lokalizacije deformacije, i to na način da sprječava pojavu diskontinuiteta pomaka i osigurava neometan razvoj oštećenja. Kontinuum višeg reda opisan je pomoću teorije gradijentnih deformacija, pri čemu je unutarnja duljinska skala uključena u model preko konstitutivnih tenzora višeg reda, a nelokalno ponašanje uvedeno je gradijentnim članovima što proizlaze iz polja pomaka. Iako su gradijenti s matematičke perspektive lokalne veličine, u mogućnosti su opisati deformiranje okolnog materijala.

Predložen je novi računalni pristup modeliranju oštećenja u kvazi-krhkim materijalima, temeljen na teoriji gradijentnih deformacija. Model je izveden uz primjenu izotropnog zakona oštećenja na način da je desna strana konstitutivnih relacija pomnožena s istim članom koji opisuje degradaciju materijala. Porastom oštećenja navedeni se član smanjuje, a njegovo djelovanje na konstitutivne tenzore očituje se u mogućnošću opisivanja popuštanja materijala. Smanjivanjem vrijednosti konstitutivnih tenzora također je osigurano i smanjenje veličine zone mikrostrukturnog utjecaja, čime je omogućeno točno opisivanje završnog pojasa lokalizacije deformacije koji zapravo predstavlja makropukotinu. U početku formiranja oštećenja, veličina područja mikrostrukturnog međudjelovanja je najveća što se fizikalno očituje u široko raspršenoj mreži mikropukotina, od kojih tek manji dio naposljetku sraste u makropukotinu. Iako se modelom ne razmatra fizikalno otvaranje pukotine, ono je virtualno opisano preko integracijskih točaka u kojima je oštećenje dostiglo kritičnu vrijednost, a krutost shodno tome pala na nulu. Opisani nelinearni model za opisivanje popuštanja materijala ugrađen je u trokutni konačni element $C^1$ kontinuiteta putem komercijalnog softverskog paketa ABAQUS/Standard i korisničke rutine UEL. Mogućnosti predloženog računalnog pristupa u problemima lokalizacije deformacije ispitane su na nekoliko tipičnih testnih primjera, a verifikacija rezultata izvršena je usporedbom s raspoloživim rješenjima iz literature. U usporedbi s rezultatima dobivenih standardnom implicitnom gradijentnom formulacijom, ovdje dobiveni rezultati pokazuju u potpunosti lokaliziran deformacijski pojas uz točno širenje oštećenja. Provedena analiza pokazuje da se predloženim modelom oštećenja temeljenim na teoriji gradijentnih deformacija može uspješno predvidjeti područje iniciranja rasta oštećenja, kao i naknadna lokalizacija deformacije prema makroskopskoj pukotini. Uzimajući u obzir da rezultati ne ovise o gustoći ni o rasporedi konačnih elemenata, može se reći kako je postignuta potpuna regularizacija matematičkog modela koji opisuje proces oštećivanja materijala. Trenutni nedostatak modela očituje se u nemogućnošću opisivanja pada reaktivnih sila na vrijednosti blizu nule u slučaju kada lokalizacijska zona presijeca računalni model, odnosno u slučaju

formiranja makropukotine. Zaključeno je kako je takav strukturni odaziv posljedica ovisnosti varijable oštećenja samo o tenzoru deformacije, a unaprjeđenje modela izvedivo je proširenjem navedene ovisnosti i na tenzor deformacija drugog reda.

Drugi dio disertacije usmjeren je na ispitivanje mogućnosti već postojećeg $C^1$-$C^1$ višerazinskog algoritma u modeliranju lokalizacije deformacije, pri čemu se analiza oštećenja promatra na mikrorazini materijala opisanoj putem RVE-a. Budući da je mikrostruktura u navedenom višerazinskom algoritmu opisana preko Aifantisove teorije linearne elastičnosti, postojeći konačni element proširen je na mogućnost opisivanja oštećenja uvođenjem izotropnog zakona, na sličan način kao što je već urađeno u slučaju teorije gradijentnih deformacija. Izvedeni element testiran je u simulacijama popuštanja mikrostrukture materijala, pri čemu se utvrdilo kako je element pogodan za opisivanje oštećenja unutar RVE-a. Kako bi se ustanovili nedostaci upotrebe klasičnog kontinuuma na makrorazini, razvijena je $C^0$-$C^1$ shema prijenosa varijabli između dviju strukturnih razina. Višerazinski algoritam implementiran je u softverski paket ABAQUS/Standard putem UMAT korisničke rutine za makrorazinu, te UEL korisničke rutine za mikrorazinu. Na primjeru mikrostrukturno homogenog materijala utvrđeno je kako se lokalnim pristupom na makrorazini ne može objektivno opisati problem lokalizacije deformacije, što je omogućeno primjenom nelokalnog kontinuuma u slučaju $C^1$-$C^1$ višerazinskog algoritma. Za slučaj snažne lokalizacije unutar RVE-a, što efektivno označava gubitak mehaničkog integriteta makrorazinske točke integracije, razvijen je algoritam koji u takvom slučaju uklanja konstitutivni utjecaj te točke. Mogućnosti predložene višerazinske strategije najprije su ispitane na jednostavnom numeričkom primjeru koji ne uključuje pojavu makrorazinske lokalizacije deformacije, a rezultati pokazuju ovisnost strukturnog odaziva heterogene mikrostrukture o veličini mikrostrukturnog parametra unutarnje duljinske skale. U slučaju većeg parametra dolazi do puno blaže lokalizacije te su rezultati tada usporedivi s rješenjima dobivenima putem jednorazinskog modela oštećenja kojim se ne razmatra kontinuirani razvoj mikrostrukture. U primjerima koji obuhvaćaju pojavu makrorazinske lokalizacije deformacije, pokazano je kako je putem predloženog $C^1$-$C^1$ višerazinskog algoritma moguće opisati fizikalno iniciranje popuštanja materijala na makrorazini uz razmatranje širenja oštećenja po heterogenoj mikrostrukturi materijala.

# 1 Introduction

## 1.1 Background and motivation

In recent times, an application of novel structural materials, such as advanced high-strength steels or composites, has significantly increased due to the efficiency, reliability and multi-functionality they offer. These materials often have a complex and heterogeneous microstructure, which can be engineered to take advantage of the required properties of each constituent. By doing so, the final system or product that exhibits the desired overall characteristics can be fabricated more efficiently. Since there is always a strong demand for production of cheaper and lighter material solutions, a special attention has to be paid in the designing process on the prevention of formation and growth of the damage, since this phenomenon can very easily lead to the complete failure of the mechanical systems. In the conventional engineering yield limit of the material is usually used as a failure criterion, meaning that the component will always stay in the elastic deformation domain. However, in more delicate production situations where the safety and reliability are of utmost importance, e.g. nuclear and aircraft industry, more precise evaluations of damage initiation and subsequent evolution up to and beyond forming of fracture are necessary. After the fracture has been formed, traditionally the fracture mechanics was employed for the prediction of crack growth, where necessarily a large degree of simplification has to be used. Review of fracture mechanics techniques can be found in [1]. However, with the advancement of the computational technology, possibilities for more accurate prediction of damage and cracking process have extended remarkably. Herein, the most important contribution is made in the field of continuum damage mechanics, where the introduction of the set of field variables, or so-called damage variables, explicitly describes the material degradation [2-4]. This theory can also be used for the description of the growth of the macroscopic cracks, which are then represented by the material domain where damage variable becomes critical [5-7]. Generally, the formation of cracks in most engineering applications is tried to be avoided, and the most important part for the assessment of the working lifespan is done by keeping track of the damage, i.e. material degradation, which precedes the formation of crack.

Physically, formation of damage and macroscopic cracks is a direct result of the cascade of events happening at the microstructural level [3, 4]. Due to this strong interconnection, numerical calculation of the macroscopic damage is in the most efficient damage mechanics models usually based on the employment of the so-called nonlocal parameter [8], which takes into account all of the microstructural heterogeneities and interactions. Assessment of this parameter can be especially difficult for the materials with complex and heterogeneous microstructures, which, e.g., consist of multiple constituents embedded in the matrix material. Therefore, a more accurate evolution of damage at the macrostructural level could be made if the assessment of damage is firstly done at the microstructural level, where the material can be modeled more precisely. This is where multiscale modeling can help significantly, a method which aims to consistently bridge the material behavior at different length scales, usually macro- and microscale [9-11]. Essentially, multiscale techniques are homogenization techniques where the certain properties are averaged over a representative volume element (RVE), which is assumed to be statistically representative for the macroscopic material point [12-14]. The RVE is a bounded segment of the microstructural material, where the all relevant microstructural properties needed for the analysis are modeled explicitly. Within homogenization techniques, the computational homogenization (CH) scheme is shown to be most accurate and versatile, mainly due to the reason that it does not require an explicit a priori constitutive relation at the macrolevel. Constitutive behavior is being determined during the course of simulation and it is dependent on the RVE homogenization results. This allows the modeling of nonlinear behavior of complex and evolving microstructures in a rather straightforward manner. Two boundary value problems (BVPs) have to be solved simultaneously during the calculation, one for the macroscale and the other for the underlying microstructure, where the transfer of the solution variables between two BVPs represents a crucial and most challenging part of the multiscale modeling. This is particularly relevant when damage modeling is included at the RVE level, where the efficient and accurate upscaling of the variables is still a very delicate research topic. For example, a second-order CH technique is demonstrated as superior when it comes to multiscale modeling of majority non-linear problems [15-18], except in case when localization of the deformation occurs at the microscale. Transfer of the variables from micro- to macroscale then becomes questionable due to loss of the representative character of the RVE [19, 20].

## 1.2 Overview of damage modeling in continuum

The damage phenomenon, macroscopically characterized by decrease in the elastic material stiffness or so-called strain softening, is common in all engineering materials and can significantly decrease structural load-carrying capacity and eventually lead to a complete loss of mechanical integrity. When there is no plasticity involved before or after initiation of damage, materials soften immediately after reaching the critical elastic deformation and can be then classified as quasi-brittle. Materials like these include, among others, high-strength steels, polymers, composites and various geo-materials such as concrete and rock.

Concerning the numerical simulations, it is well-known that the strain softening cannot be properly resolved with the application of the classical continuum mechanics. This approach leads to the local loss of positive definiteness of the material tangent stiffness, which may cause the local loss of ellipticity of the governing differential equations. The mathematical description of the model than becomes ill-posed and numerical solutions do not converge to a physically meaningful solution [21]. If the finite elements are applied as a discretization technique, the solutions are then completely dependent on both mesh refinement and mesh alignment. In other words, the energy dissipated in the fracture process tends to zero when the size of the elements involved in the softening process is reduced, and the localization zone exhibits an extreme tendency to propagate along the mesh lines [22].

Various regularization techniques have been developed in the past few decades to overcome this problem. Many of them are based on the improvement of the classical continuum model, precisely on its enrichment with the internal length scale parameter in several different ways. Some of the known methods include the micropolar theory [23], viscoplastic theory [24], fracture energy approach [25] and crack band model [26] but all off them suffer from the lack of generality since the preservation of ellipticity is possible only in some specific cases. On the other hand, the theories related to the nonlocal material behavior have been shown to be the most versatile. In the case of the nonlocal models, the stress at a material point does not depend only on the strain and other state variables at this point, as it is the case with the classical continuum theory, but also on the strains and other state variables of the points in the surrounding area. Physically, the nonlocality represents the heterogeneities and interactions taking place at the microscale, which cannot be neglected in the damage analysis, where the scale of the macrostructural fluctuations of the constitutive variables approaches the scale of the microstructure [27]. The intensity of these interactions is described by the aforementioned

internal length scale parameter, which in this way introduces a microstructural contribution in the model [6].

Basically, there are two different approaches regarding the implementation of the material nonlocality in the model, the integral and the gradient approach. The integral approach, introduced in [28], accounts for the influence of previously mentioned microstructural interactions through the weighted average of a variable driving the damage process, typically strain. This leads to very complicated constitutive relations made of convolution-type integrals, making the numerical implementation very demanding. In the case of the gradient approach, either the classical constitutive relation is enhanced with the strain gradients, or both the strain gradients and their stress conjugates are introduced in the model via the higher-order continuum. In the case when only strain-gradients are used as an enhancement of the constitutive relation, the explicit and especially the implicit gradient formulations are usually used when dealing with softening, either in elasticity context [29], plasticity context [30, 31] or in the analysis of the elastic wave propagation [32]. Although the structural responses are mesh objective, the mentioned formulations suffer from the spurious damage growth reported in [33], where the damage process zone evolves incorrectly after initiation in the mode-I and the shear band problems. The described phenomenon occurs if the conventional integral and gradient enhancements are used, which assume a constant interaction domain throughout the entire load history. Because of this assumption, the energy is transferred from the damage process zone to a neighboring elastically unloading region, resulting in a smeared damage zone instead in a localized deformation band [34]. This problem can be more or less successfully avoided by using the modified nonlocal formulations which assume the evolving internal length scale parameter. Most of these formulations employ the increasing length scale parameter with the rising deformation level [35-37]. By doing so, it is presumed that the intensity of microstructural interactions also increases, which does not have a correct physical background. This is explained in more detail in [34], where a new model based on the decreasing microstructural interactions is presented, recognizing that the width of the fracture process zone localizes towards a macroscopic crack in the quasi-brittle fracture. Recently, a phase-field model is commonly employed in the problems including damage and localization [38-41]. The model shares a lot of similarities with gradient-damage formulation in terms of the mathematical structure, with the main difference in the interpretation of the governing Helmholtz equations. Whereas nonlocal variables in the gradient approach can be interpreted as a spatial averaging operators, in the phase-field model they follow from the regularized energy variation due to fracture evolution [42]. Although phase-field models provide fully regularized solutions, to

accurately capture the evolution of the phase-field, i.e. damage, the mesh has to be substantially refined along the anticipated crack path, which significantly contributes to the increased computational costs.

The strain gradient continuum theory, where both the strain gradients and their stress conjugates contribute to the internal energy [43] is employed less often, mainly because it is numerically more complex. In the recent developments, this higher-order stress-strain theory is employed in the context of a damage modeling of an infinitely long bar [44], where it is concluded that the addition of the higher-order stress terms results in stabilizing the positive definiteness of the tangent stiffness moduli when entering the strain softening regime. In such a way the physically consistent solutions leading to a realistic reproduction of the softening phenomenon can be ensured. Further development from one-dimensional to multi-dimensional simulation of a localized failure process is made in [45]. In both [44] and [45] element-free Galerkin (EFG) meshless method is used for finding the approximate solutions to the corresponding boundary value problems. Another advantage of the higher-order stress-strain theory is that material heterogeneity in the constitutive relations can be easily introduced through the non-diagonal higher order material stiffness tangents [46]. The stiffness tangents can be obtained by applying the second-order homogenization technique on the RVE. The constitutive relations emerging from the second-order homogenization are dependent on the choice of the RVE size, or in other words, the size effect can be studied by changing the RVE sizes rather than changing the model dimensions. On the other hand, as suggested in [47] and [48], the gradient constitutive behavior is a material property, and as such it should not be influenced by the choice of the RVE size, but only by a stochastic aspect of the heterogeneities included in the RVE. For this purpose, a correction that is to be applied on the strain gradient modulus of the sixth order is derived in [47], making the overall constitutive relations more consistent and intrinsic. Although the previously mentioned gradient feature of the constitutive law resulting from the standard homogenization procedure is not as physically as appropriate, when a real engineering material is considered, the necessary RVE size can be determined and the unique and consistent strain gradient constitutive relations can be obtained. Another limitation of the standard second-order homogenization is concerned with the microfluctuation field inside the RVE, as it is recognized in [49]. Here the authors suggest another approach for its resolution by treating the microfluctuation term in the extended Hill-Mandel condition different from zero, which is exactly the opposite from what is generally used in the standard approach, e.g. as described in [17, 50]. Beside the second-order CH, which can be used for an arbitrary RVE geometry and is the most general in that sense, a constitutive model for the

materials with a simple microstructure can be established using an analytical approach, e.g. as described in [51].

Concerning the numerical implementation of the strain gradient continuum theory using the finite element method, both $C^0$ and $C^1$ continuous elements have already been employed. In [52] a superior robustness of the $C^1$ displacement based finite elements over the $C^0$ elements used with a penalty function approach is shown. In [53], the $C^1$ formulation is used for the crack analysis in the context of the linear elastic fracture mechanics. Authors in [54] presented an in-depth analysis of the performance of three different $C^1$ continuous finite elements and additionally made a comparison with the $C^1$ natural element method. In [17] a triangular displacement based $C^1$ finite element and used it in the scope of the multiscale modeling of heterogeneous materials is developed. Regarding the damage mechanics, the $C^0$ finite elements based on the mixed formulation are mostly used due to their lower complexity, either when the implicit gradient enhancement [21] or the micromorphic approach [34] is used as a regularization technique. To the authors' knowledge, the two-dimensional $C^1$ displacement based finite elements have not yet been employed for the analysis of softening materials. Although the $C^1$ formulation is considered more complex owing to a relatively high polynomial used for the displacement field approximation, there is no need for the introduction of the additional variables representing the link to the microstructure, e.g. the non-local equivalent strain or the micromorphic variable, which are specific for the $C^0$ formulations. In that sense, the $C^1$ displacement based finite elements can be considered more intrinsic as all state variables are calculated in terms of the displacements and their derivatives. Besides, due to the mentioned displacement field approximation using a high polynomial, a much coarser discretization is generally sufficient, compared to the $C^0$ finite elements.

## 1.3 Multiscale modeling of damage

The mechanical response of heterogeneous materials, observed from a macrostructural level, is highly dependent on the microstructural characteristics, such as size, shape, spatial distribution, volume fraction and properties of the individual constituents. Modeling of the microstructure of such materials can be used to assess the overall or effective material properties, and also to predict the occurrence of failure which limits the operational use of many engineering structures. One of the possible ways to model such a material where localization at the microscale has arisen is by using direct numerical simulation, where the exact microstructure

is explicitly modeled at the macrostructural level. Although this method provides very accurate results, its applicability is still very limited due to high computational costs.

Another class of methods for the incorporation of the micromechanical localized response in the structural analysis of the macrostructure are multiscale methods. The main challenge here is bridging the evolution of the microscopic localization towards material failure at the large scale, i.e. engineering level. This problem is tackled only with a partial success by development of so-called local mesh refinement techniques. In multigrid or superposition based methods hierarchical decomposition of macro- and microscale effects is employed, such that the coarse macroscopic mesh is locally overlaid with a detailed microscale description where localization is to be expected [55, 56]. Similarly, domain decomposition methods are based on disassembly of the macroscale in several subsets where each of them can have different spatial resolutions with appropriate length scales, which allows to resolve a strain localization in the zone of interest and thereby save the computational costs [57, 58]. Given local mesh refinement techniques are mainly efficient if only a mild and small localization zone is expected, position of which is known a priori.

However, the most progress in the multiscale modeling of the microscopic localization is achieved by utilization of CH methods. As stated before, there is no need to make any constitutive assumptions at the macroscale, as the response of the homogenized material is determined during the analysis by solving a microscale BVP associated with each macroscopic integration point, represented by an RVE. Through the homogenization process, response of the heterogeneous microstructure is averaged over an RVE, whereby a new, effective homogeneous material is formed, as presented in Figure 1.1. Classical homogenization techniques are built upon the principle of separation of scales, which states that the RVE size should be much smaller, than a characteristic length over which the macroscopic loading varies in space. In other words, the uniform distribution of the macro-strain over the entire RVE domain is assumed. This, however, is violated when the first-order CH schemes, which are based on classical continuum formulation at both scales, as described in [59-62], are used with the problems where strain softening occurs at the microlevel. When there is no clear separation of scales, capturing of the propagation of the underlying rapidly fluctuating responses can be remedied to some extent by higher-order enrichment of the macroscopic continuum. Besides, standard continuum formulation at the macroscale cannot regularize the formation of the strain localization, which in addition leads to the ill-posedness of the macrostructural BVP. As an improvement to the first-order CH, second-order CH is proposed [18], which is shown to be successful in treating only the mildly softening materials, specifically the materials not

exhibiting the deformation beyond a quadratic nature in the displacements, as stated in [63]. Classical homogenization in its essence implies the averaging of some physical phenomenon, and it is believed that, in the case of the sharp localization which is characteristic to the certain RVE, it should not be performed. Additionally, with the occurrence of the sharp strain localization, homogenized response stops being objective with the respect to the size of the RVE - by increasing the size of the micro-sample, the macroscopic structural response becomes more brittle [12]. In that case RVE stops being statistically representative for the macroscopic material point and should be called a microstructural volume element (MVE) instead, as stated in [64]. Another class of homogenization methods which deal with the strain softening problems is based upon the enrichment of the macroscale continuum with a discontinuity, where the microscale strain localization band is lumped into a macroscale cohesive crack. Taking into account the techniques used for the extraction of the equivalent discontinuity from the localized MVE and formation of the corresponding macrostructural effective constitutive relation, several different procedures can be found in the literature [65-71]. The existence of an RVE for softening materials undergoing localized damage has been confirmed in [72], where a new averaging technique based on extraction of the deformation of just a localization band is proposed. By using this technique, a CH scheme for discrete macroscopic crack modeling that is objective with respect to the size of the RVE is presented in [66, 68].

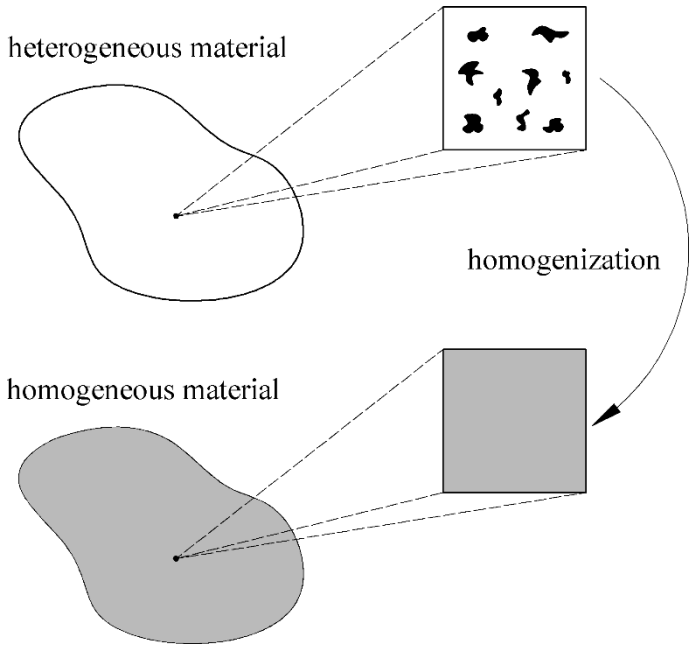


**Figure 1.1** Homogenization of a heterogeneous material. Based on [60].

In [73], a new second-order CH scheme is derived, where the $C^1$ continuous finite elements are employed at both macro- and microlevel. Employment of the nonlocal theory at the microscale has shown better efficiency compared to available homogenization schemes, additionally offering an advanced frame for damage modeling. Regarding the modeling of localization phenomena by using the $C^1$ continuity, a new damage model employing the strain gradient theory embedded into $C^1$ continuous finite element is recently presented in [74], where the exceptional regularization capabilities of such model are demonstrated. Potentially, merging of this damage model with the two-scale scheme presented in [73] could resolve some of the issues related to multiscale modeling of localization phenomena, which is one of the topics of this thesis. It is clear from the given overview that development of the multiscale models which deal with the damage localization problems still needs to be improved in order to enable their employment in practical, engineering considerations.

## 1.4 Scope and objective

The main objective of the research is a development of the damage formulation based on the strain gradient theory, which includes a spatial discretization with the continuity of displacements and first derivatives of displacements ($C^1$ continuity). Besides, a new method for numerical modeling of damage in heterogeneous materials using the multiscale algorithms based on the higher-order continuum theory will be proposed.

The hypotheses of the research are:

1. It is possible to model the damage phenomenon using the displacement based spatial discretization. Proposed novel method will show advantages in comparison with spatial discretization based on mixed formulation.

2. It is possible to achieve the higher accuracy of modeling of damage in the heterogeneous materials using the homogenization procedure within a framework of multi-scale algorithms, then the accuracy that can be reached by the formulations available in literature.

Research in the scope of the thesis is divided in two parts. In the first part, objective is to develop a damage model based on the strain gradient continuum theory which includes both the strain

gradients and their stress conjugates, where the $C^1$ continuity displacement based triangular finite element developed in [17] will be utilized. It is expected that the employment of the higher-order continuum should resolve the existing issues with spurious damage growth that can be observed in problems where conventional gradient implicit formulation is typically used. In addition, constitutive relations will be modeled in a way that will decrease the intensity of the microstructural interactions in the process zone while the softening progresses. In this way a physically correct structural response standing behind a fracturing process can be captured, unlike the results obtained using the conventional implicit gradient damage model, where the spurious damage growth can be observed [33, 75]. The microstructural contribution will be incorporated through the constitutive tensors obtained using the second-order CH, while the softening analysis will be performed exclusively on the macroscale model. Thus, not only the internal length scale, but also the heterogeneous contribution of the RVE will be acquired for the implementation in the macroscale constitutive model. Although simplified, incorporation of heterogeneities by the described means should be a computationally effective way to model the damage in the heterogeneous materials. This procedure could potentially find its application in the preliminary analyses of heterogeneous structures where damage is expected, complementing as such the subsequent employment of the multiscale method.

Second part of the thesis aims to provide a two-scale method for the analysis of the damaged material, where both structural levels will be described as a higher-order continuum, which necessitates the employment of the $C^1$ continuity. Since the nonlocality is intrinsically included in this type of continuum, neither objectivity issues related to discretization nor spurious damage growth are expected, i.e. a full regularization of the localization problems at both scales should be achieved. The topic regarding the preservation of the objectivity with respect to the size of the RVE will not be included in this thesis. Conventional homogenization will be applied during the calculation up until the full formation of the localization zone in the certain RVE, when the appropriate stiffness conditions for the cracked material point will be included in the macrostructural constitutive model. This should allow for a more realistic description of the structural behavior of the large scale model when localization occurs at the microscale.

To summarize, the expected scientific contribution of the thesis is:

1. Development of the damage model based on the strain gradient theory which allows the displacement based discretization. In this way numerical efficiency with respect to the gradient formulations based on the mixed finite elements will be increased.

2. Development of the novel numerical method for the multi-scale modeling of damage in heterogeneous materials which utilizes constitutive relations derived by the homogenization algorithm within the multi-scale algorithm. This will contribute to the higher accuracy of the modeling, and accordingly to the higher safety of the structures.

## 1.5 Outline of the thesis

The thesis is organized in five chapters. After the introduction, general concepts of elasticity-based continuum damage mechanics are given in Chapter 2. Constitutive modeling for description of the damage phenomenon in quasi-brittle materials is provided. The shortcomings of the classical continuum approach are described and the origins of the inaccurate localization are discussed afterwards. Finally, a brief overview of the existing methods that prevent such unwanted behavior is given. In Chapter 3, a $C^1$ continuity triangular finite element derived in [17] is extended to the consideration of the softening phenomena in quasi-brittle materials. A brief description of the basic element together with the fundamental relations of the gradient theory are given at the beginning. A formulation and numerical implementation of the higher-order stress-strain damage theory into the $C^1$ continuity finite element is presented. Verification of the new procedure is then made on several standard benchmark examples, where both the homogeneous and heterogeneous materials are taken into consideration. A special attention is directed to the advanced regularization capability of derived model to prevent the spurious damage growth. Chapter 4 is dedicated to the derivation of the multiscale procedure that enables the softening analysis at the macrostructural level by homogenizing the localized response of the RVE level. Numerical implementation of the previously derived damage model at the microstructural scale is firstly discussed. In order to test the applicability of the classical continuum at macroscale, $C^0$-$C^1$ macro-micro scale transition relations are derived afterwards. Basic relations of the existing two-scale scheme that employs the gradient continuum at both structural levels presented in [73] are then given. RVE cracking conditions, i.e. conditions that

indicate the full formation of the localization band at the RVE level and consequential change of the macrostructural stiffness are derived. Numerical example including both $C^0$ and $C^1$ continuity macrolevel discretization together with the homogeneous microstructure is provided in order to show the deficiencies of using the local approach when damage occurs at the microscale. In addition, few numerical examples where the heterogeneous RVE is employed are presented and compared with the one-scale solutions obtained by the model from Chapter 3, where the same RVE is used for the extraction of the stiffness tensors. At the end of this chapter, a short discussion on perspectives for multiscale modeling of heterogeneous materials undergoing damage is provided. Finally, concluding remarks are given in Chapter 5.

# 2 Damage modeling in linear-elastic materials

Continuum damage mechanics, being a part of the continuum mechanics, is a theory used to analyze the mechanical effects of material damage and fracture process. Damage is defined as a phenomenon where the nucleation, growth and coalescence of the microscopic cavities and cracks lead to the initiation of the macroscopic crack, resulting in the deterioration of the mechanical properties of the observed material [4, 76]. Considering the differences in materials and loading conditions, damage may be classified phenomenologically in several categories [3], such as brittle, ductile, creep and fatigue damage among others. Since the thesis deals with the development of the new damage model, complexity level of the underlying physics is reduced to minimum for the clarity reasons. Accordingly, viscous and dynamic effects together with thermal and other non-mechanical influences are excluded from the consideration, while strains and rotations are assumed to be small. Additionally, material behavior is assumed to be linear-elastic when there is no damage growth, which finally leads to the class of damage models often called elasticity based damage or damage coupled with elasticity [77]. Predominant dissipation mechanism in phenomena which can be described by elasticity based damage is growth of material defects which involves a high degree of microstructural change before complete loss of mechanical integrity. Also, the dissipation caused by the plastic deformations can be neglected in such problems. Ultimately, the only fracture mechanism corresponding to all of the aforementioned criteria is quasi-brittle fracture, which occurs in many realistic materials where cohesive strength is much lower than the slip strength. Materials like these include, among others, high-strength steels, polymers, composites and various geo-materials like concrete and rock.

The basic theory of the classical damage mechanics in general is given in Section 2.1, following by the particular case of elasticity based damage associated with quasi-brittle materials, presented in Section 2.2, where constitutive modeling is described in more detail. In Section 2.3 local approach to damage and problems related to it are presented, while in Section 2.4 overview of the existing regularization techniques is given.

## 2.1 Basic theory of continuum damage mechanics

The fundamental procedure of the continuum damage mechanics begins with a representation of the damage state of the material by a set of continuous damage variables, which are then used for the description of the mechanical behavior of the damaged material and the subsequent development of the damage. Damage variable $D$ represents a measure of the number and size of the defects in a small volume of a material point, usually called representative volume element (RVE) [78]. By taking an RVE of the appropriate size at each material point, mechanical effects of the discontinuous microstructure can be statistically averaged as a continuous field on the macroscale. In order to obtain a unique mechanical state of the continuum, RVE should be large enough to contain a sufficient number of microstructural discontinuities, and also sufficiently small that an increase in its size does not lead to considerable differences in the homogenized properties [12]. When the microvoids are randomly distributed over the RVE, the local damage state is usually taken to be isotropic and can be described by means of the scalar damage variable $D$. On the other hand, when microvoids have oriented geometry multiple anisotropic damage states exist, and in that case a set of damage variables or a tensor have to be used [79]. Due to simple mathematical implementation of the scalar damage variable, isotropic damage theory is assumed throughout the thesis. Damage variable can generally be obtained in few different ways [4], and the most common one is the modeling by effective area reduction proposed in [80]. Considering the two-dimensional case of homogeneous damage pictured in Figure 2.1, the value of damage $D$ attached to the point $M$ can be defined as

$$D(M) = \frac{\mathrm{d}A_D}{\mathrm{d}A}, \tag{2.1}$$

where $\mathrm{d}A_D$ represents an effective area of all microstructural defects inside the RVE of an area $\mathrm{d}A$. Damage variable $D$ ranges from zero to one, where $D = 0$ represents the initial, undamaged state of the material, while $D = 1$ represents the final fractured state or a complete loss of mechanical integrity of a material point. For the values between zero and one, certain development of damage has occurred, but material still has the capacity to carry the loading. Three different material domains involving the damage distribution are depicted in Figure 2.2

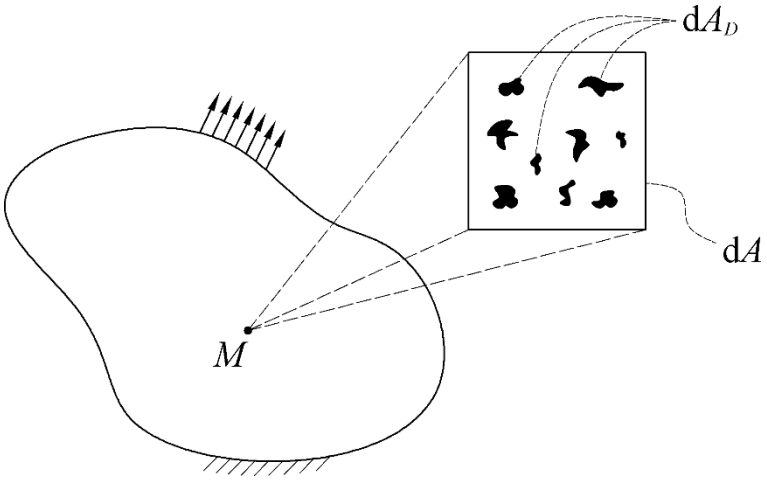


**Figure 2.1** Damaged body and RVE of the point *M*

Regions of material where damage reached the critical value of one are basically the continuum representation of cracks, where the stresses are non-existent and the equilibrium equations therefore meaningless. This implies that cracked region should be excluded from the rest of the material by introducing an internal boundary of zero stress value, position of which changes with the subsequent damage growth [6]. In the numerical calculations throughout the thesis, damage variable is set to never reach the critical value, which means that all cracking integration points will still have a very small stiffness and thus remain the part of continuum. By doing so, there is no need to continuously formulate the new free boundaries, which is in the finite element context described by removal of the cracked finite elements from the initial boundary value problem.

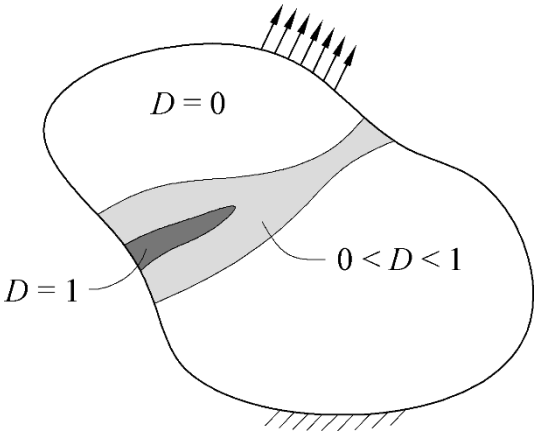


**Figure 2.2** Distribution of damage in a continuum. Based on [21].

## 2.2 Damage in quasi-brittle materials

Quasi-brittle material is type of the material where a certain amount of dissipation occurs before the crack initiation, as opposed to brittle material where no dissipation prior to crack exists [4]. Typically, in quasi-brittle materials, fracture is not the consequence of the growth of one dominant crack, but rather starts in a volume characterized by a diffuse network of microcracks. The evolution of the failure process, as observed in concrete experiments [81] and meso-scale simulations [82], can be described in few separate stages, which are shown in Figure 2.3. After a diffuse network of the microcracks has been established in the initial stage ($t_1$), propagation of the microcracks is continued in much narrower volume ($t_2$). The rest of the microcracks excluded from the propagation process zone unload elastically which eventually leads to their closure, depicted in Figure 2.3 as dotted lines. With the further increase in the deformation, rapid coalescence of the microcracks can be observed in the process zone, which is simultaneously becoming smaller in width. In the final stage ($t_3$), a localized macroscopic crack is formed occupying only a fragment of the initial volume of diffused microcracks. As a consequence of the described process, a gradual decrease in load carrying capacity of material point is usually observed, in contrast to the abrupt loss of strength in perfectly brittle fracture.

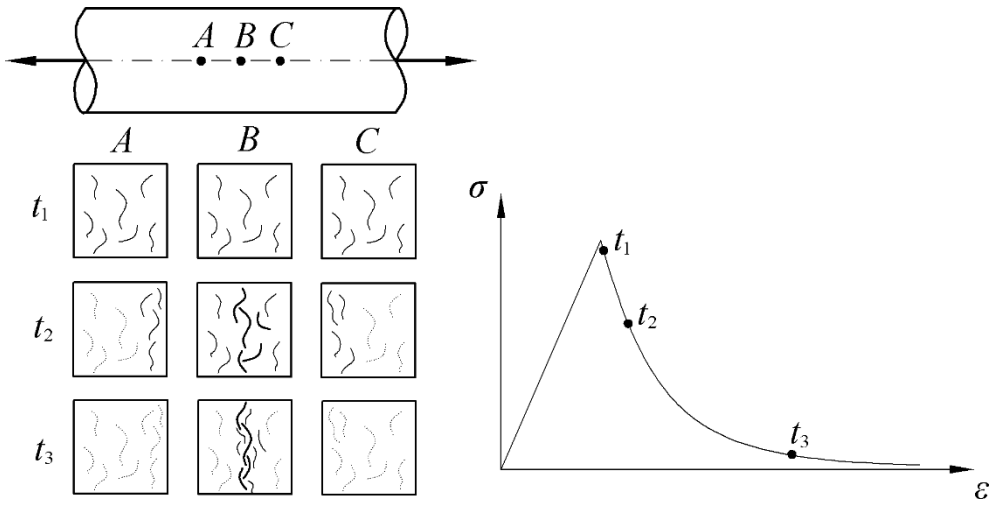


**Figure 2.3** Evolution of the failure process in quasi-brittle materials. Based on [34].

In the elasticity based damage mechanics and under the assumption of the isotropic damage, the gradual decrease in load carrying capacity can be expressed according to [77] as

$$\boldsymbol{\sigma} = \mathbf{C}^{\text{eff}}\boldsymbol{\varepsilon}, \tag{2.2}$$

with

$$\mathbf{C}^{\text{eff}} = (1-D)\mathbf{C}\,. \tag{2.3}$$

In the above relations, $\boldsymbol{\sigma}$ and $\boldsymbol{\varepsilon}$ are Cauchy stress tensor and linear strain tensor, while $\mathbf{C}^{\text{eff}}$ and $\mathbf{C}$ denote the effective and the elastic stiffness tensors, respectively. As can be seen from (2.3), increase in the damage variable $D$ leads to decrease of the effective stiffness $\mathbf{C}^{\text{eff}}$. As mentioned above, when $D$ = 1, stiffness in non-existent and stresses cannot be transferred anymore, a state which is physically represented by a crack. Equations (2.2) and (2.3) define how the damage affects the stress and the strain field, but at the same time, increase of the damage variable is dependent on change of stresses and strains. The damage state is governed by the monotonically increasing scalar history parameter $\kappa$, which can be determined as the largest value of the equivalent strain $\varepsilon_{\text{eq}}$ reached in a material point during the loading history. Since the damaging process is irreversible in a material point, damage variable can only increase when the equivalent strain reaches the history parameter $\kappa$, i.e., when $\varepsilon_{\text{eq}} \geq \kappa$. By using the selected parameters, growth of the damage is usually expressed through the damage loading function

$$f\left(\varepsilon_{\text{eq}}, \kappa\right) = \varepsilon_{\text{eq}} - \kappa\,, \tag{2.4}$$

where $f = 0$ defines a loading surface in strain space. The qualities of the loading surface are dependent on the definition of the equivalent strain $\varepsilon_{\text{eq}}$ and the history parameter $\kappa$, which will be given later. When the strain state lies inside the loading surface, damage cannot increase and material behaves elastically. For the increasing damage, elastic domain defined within the loading surface has to continuously grow such that the strain state remains on the loading surface, i.e. conditions $f = 0$ and $\dot{f} = 0$ have to be satisfied. This can mathematically be expressed through Kuhn-Tucker relations

$$\kappa \geq 0, \quad \varepsilon_{\text{eq}} - \kappa \leq 0, \quad \dot{\kappa}\left(\varepsilon_{\text{eq}} - \kappa\right) = 0\,, \tag{2.5}$$

where the initial elastic domain is determined by $\kappa = \kappa_0$, and denotes the equivalent strain needed to be reached for the start of the damaging process ($D > 0$).

Evolution of damage is usually for the quasi-brittle materials specified directly in the form $D = D(\kappa)$. When it comes to the theoretical considerations of the damage process, the damage evolution governed by the linear softening law [6] is usually used

$$D=\begin{cases}\dfrac{\kappa_{\mathrm{u}}\left(\kappa-\kappa_0\right)}{\kappa\left(\kappa_{\mathrm{u}}-\kappa_0\right)} & \text{if} \quad \kappa_0\le\kappa\le\kappa_{\mathrm{u}} \\ 1 & \text{if} \quad \kappa>\kappa_{\mathrm{u}}\end{cases}, \tag{2.6}$$

where $\kappa_{\mathrm{u}}$ is material parameter representing the strain at which material completely loses its stiffness. Relation (2.6) together with the corresponding uniaxial stress-strain responses is depicted in Figure 2.4a. Real materials usually soften in a nonlinear fashion, where the initial pronounced descent of stress can be noticed followed by a milder decrease. The application of exponential softening law is the most common here, especially for the concrete [83], given as

$$D=1-\frac{\kappa_0}{\kappa}\left\{1-\alpha+\alpha\exp\left[\beta\left(\kappa_0-\kappa\right)\right]\right\} \quad \text{if} \quad \kappa>\kappa_0\ , \tag{2.7}$$

and shown in Figure 2.4b. Here, damage variable asymptotically approaches $D=1$, which means that the material will always have a very small stiffness that prevents the crack formation. Parameters $\alpha$ and $\beta$ determine how low will the stress decrease and the rate at which damage grows, respectively. With higher value of $\alpha$, stress can reach a smaller values when approaching $D=1$, while a higher value of $\beta$ leads to a more rapid growth of damage, resulting in a more brittle structural response.

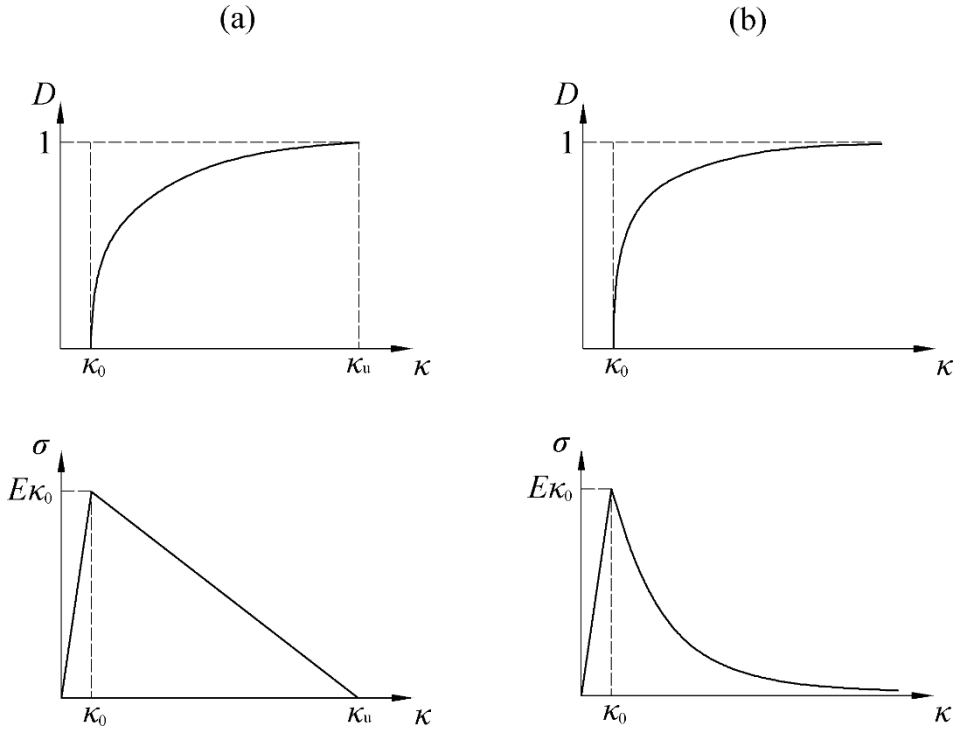


**Figure 2.4** Damage growth and corresponding uniaxial stress-strain response for (a) linear softening and (b) exponential softening. Based on [6].

In order to a have a fully defined quasi-brittle damage model, the equivalent strain $\varepsilon_{\text{eq}}$ has to be known beside the damage evolution law. The equivalent strain $\varepsilon_{\text{eq}}$ is a scalar representation of the strain tensor, which can be defined in various ways depending on the material properties and loading conditions. Due to the different effects of the strain tensor components on the damage growth, they have to be weighted appropriately to obtain the desired equivalent strain. Two different elastic strain measures are generally used within the context of the softening behavior of a quasi-brittle material. The first one is defined in [83] as

$$\varepsilon_{\text{eq}} = \sqrt{\sum_{i=1}^{3} \langle \varepsilon_i \rangle^2}\,, \tag{2.8}$$

with $\varepsilon_i \ (i = 1, 2, 3)$ representing the principal strains, while $\langle \varepsilon_i \rangle = \frac{1}{2}\left(\varepsilon_i + |\varepsilon_i|\right)$. So called Mazars' definition (2.8) is plotted in Figure 2.5a under the assumption of the plane stress state, where a constant $\varepsilon_{\text{eq}} = 1$ curve is shown in the principal strain space and for the Poisson's ratio $\nu = 0.2$. Dashed lines represent the uniaxial stress paths.

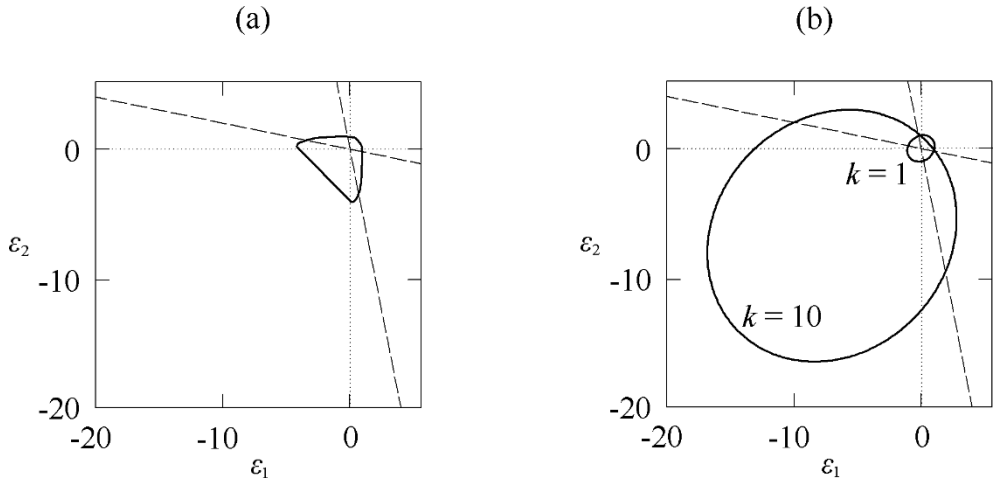


**Figure 2.5** Equivalent strain measurements in principal strain space for (a) Mazars' definition (2.8) and (b) modified von Mises' definition (2.9). Based on [6].

It is clear form (2.8) and Figure 2.5a that the Mazars' equivalent elastic strain measure depends only on the positive principal strains, making it more sensitive to tensile than to compressive strains, which is a behavior very often observed in engineering materials, e.g. concrete. On the other hand, the modified von Mises' equivalent strain measure is according to [84] given by

$$\varepsilon_{\text{eq}} = \frac{k-1}{2k(1-2\nu)} I_1 + \frac{1}{2k}\sqrt{\left(\frac{k-1}{1-2\nu} I_1\right)^2 + \frac{12k}{(1+\nu)^2} J_2}\,, \tag{2.9}$$

and includes a parameter *k* which represents the ratio between uniaxial compressive and tensile strength of the material. Graphical representations of the definition (2.9) for $k=1$ and $k=10$ are given in Figure 2.5b. For the $k=1$, meaning that both compression and tension influence the equivalent strain measure equally, modified von Mises' definition results in

$$\varepsilon_{\text{eq}} = \frac{1}{1+\nu}\sqrt{3J_2}\,. \tag{2.10}$$

In above expressions $I_1$ and $J_2$ are the first invariant of the strain tensor and the second invariant of the deviatoric strain tensor, respectively, defined as

$$\begin{aligned} I_1 &= \text{tr}(\boldsymbol{\varepsilon}), \\ J_2 &= \frac{1}{2}\text{tr}(\boldsymbol{\varepsilon}\cdot\boldsymbol{\varepsilon}) - \frac{1}{6}\text{tr}^2(\boldsymbol{\varepsilon}). \end{aligned} \tag{2.11}$$

Here, only the description of softening laws and equivalent strain definitions are given which are used throughout the thesis. As far as quasi-brittle material damage is concerned, a so-called modified power law usually used to describe the damage evolution in short glass-fibre reinforced polymers is proposed in [85], and equivalent strain measure related to the energy release rate associated to the damage variable is suggested in [77].

## 2.3 Local approach to damage

The method of damage analysis is defined as local when it is based on the damage mechanics parameters defined by the strain and other relevant state variables which exist in the observed material point. On the other hand, when the method of damage analysis is based on the global damage mechanics parameters defined by the stress and strain fields in the neighboring region around the observed material point, then the method of damage analysis is said to be nonlocal. When the local approach is used by means of the continuum damage mechanics and the finite element method, material softening caused by damage can lead to so called mesh sensitivity, an unwanted condition when numerical solution does not converge to a physically reasonable solution of the problem [86]. At the onset of the strain softening, i.e. material instability, loss of positive-definiteness of the tangent stiffness matrix is induced, which leads to the loss of ellipticity of the equilibrium rate equations. As a consequence, loss of the well-posedness of

the rate boundary value problem can be expected eventually [22, 87, 88]. It is important to stress that the mesh sensitivity is a numerical consequence of limitations of the underlying mathematical modeling, and it is not caused by numerical artifacts or inappropriate boundary value problem solving algorithms, as stated in [6].

The most prominent characteristic related to mesh-dependence of the softening materials is the formation of the deformation localization zones of the width similar to the size of the finite elements. Because the energy dissipation caused by the damaging process is strongly connected to the localization zone, it is therefore governed by the mesh size. This implies that with the refinement of the spatial discretization, the predicted dissipation of the fracture energy becomes smaller, physically meaning that the actual crack would propagate faster. In the limit of the infinitely small elements, this phenomenon may lead to unlimitedly small dissipation for the fracture of the material, i.e. an infinite crack growth rate or perfectly brittle fracture. Increase in the brittleness of the structural responses with the mesh refinement, which is also connected with a decrease in the total dissipated energies represented by the areas under the particular responses, is shown qualitatively in Figure 2.6.

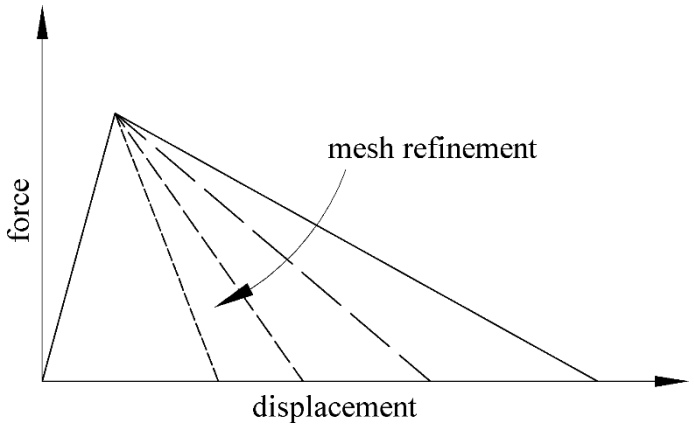


**Figure 2.6** Qualitative softening responses for different finite element discretizations in the framework of classical continuum mechanics

Material instability due to damage can be mathematically briefly explained as follows. Assuming a time-independent material with the rate constitutive equation, that is an incrementally-linear stress-strain relation

$$\dot{\boldsymbol{\sigma}} = \mathbf{C}(D)\dot{\boldsymbol{\varepsilon}}, \tag{2.12}$$

the condition of material stability according to [89] is given by

$$\dot{\boldsymbol{\varepsilon}}^T \dot{\boldsymbol{\sigma}} > 0, \tag{2.13}$$

or after the substitution of (2.12), by

$$\dot{\boldsymbol{\varepsilon}}^T \mathbf{C}(D)\dot{\boldsymbol{\varepsilon}} > 0\,. \tag{2.14}$$

By performing a uniaxial tension or compression test, it is obvious that dot product (2.13) becomes negative if the axial stress is decreasing for the increasing axial deformation, resulting in the negative slope of the stress-strain curve – a phenomenon called strain softening. From (2.14) the condition of the positive-definiteness of the tangent stiffness tensor $\mathbf{C}(D)$ can be obtained as

$$\det\left(\mathbf{C}+\mathbf{C}^T\right) > 0\,, \tag{2.15}$$

which ensures uniqueness of the deformation and therefore no mesh-related problems. The limiting case when the inequality (2.15) is replaced by the equality indicates the onset of the strain softening, which is associated with the loss of positive-definiteness of the tensor $\mathbf{C}(D)$. The condition can be written as

$$\det\left(\mathbf{C}+\mathbf{C}^T\right) = 0\,, \tag{2.16}$$

and indicates the possibility for the loss of ellipticity of the equilibrium rate equation and consequentially the loss of well-posedness of the rate boundary value problem. As long as the ellipticity condition is valid, a finite number of linearly independent solutions with no discontinuities are allowed [90]. Loss of ellipticity occurs if

$$\det\left(n_j C_{ijkl} n_l\right) = 0\,, \tag{2.17}$$

which physically indicates the existence of a discontinuity in the velocity gradient, as explained in more detail in [6]. This situation marks the start of the so-called bifurcation of the deformation [91-93] and formation of the intense localization band, the width and the direction of which are governed by the spatial discretization.

The material instability described by (2.16) can also be a cause of the structural instability, even when there are no destabilizing terms related to geometry of the structure. Hill's criterion of material stability, [89], can be reformulated for a structure that occupies a volume $V$ as

$$\int_V \dot{\boldsymbol{\varepsilon}}^T \dot{\boldsymbol{\sigma}}\,\mathrm{d}V > 0\,, \tag{2.18}$$

and the neutral stability of a discrete mechanical system is according to [94, 95] reached when

$$\det\left(\mathbf{K}+\mathbf{K}^{T}\right)=0\,, \tag{2.19}$$

where **K** represents a structural stiffness matrix. This implies that local loss of positive-definiteness of the material tangent stiffness tensor $\mathbf{C}(D)$ may lead to the loss of positive-definiteness of the structural stiffness matrix **K.**

## 2.4 Regularization techniques

In order to preserve the well-posedness of the boundary value problems and eliminate the instability and mesh-dependence of the numerical solutions, numerous schemes called regularization techniques have been developed throughout the years. In the following text a brief overview of most well-known regularization techniques is given.

So-called fracture energy approach is based on imposing a limit on the damage dissipation through adaptation of the parameters of the damage evolution equation to the mesh size. Thereby, a constant global response can be obtained for different spatial discretizations, as shown in [25, 88]. Although this approach may be practical in some considerations by providing the reasonable global responses, the prediction of local states is still sensitive to the orientation and size of the finite element mesh, which can lead to unrealistic results.

Another similar technique imposes a limit on the size of the localization band, rather than on damage dissipation. This is done by setting a lower threshold on the finite element discretization, and technique is called a crack band model [26] or a cell model [96]. Because of its simple implementation, technique is often used in realistic engineering problems, but can be challenging in selection of the appropriate mesh size for specific materials and also in securing the calculation accuracy.

Majority of regularization techniques are essentially based on the enrichment of the classical continuum theories, which rely on the principle of local action, with so-called internal length scale parameters in various ways. For example, the viscoplastic theory utilizes the addition of the rate-dependent terms, i.e. the viscous effects in the constitutive models to avoid the loss of ellipticity [97, 98]. The problem with this theory is that it can provide reasonable results only for limited range of cases where the width of the localization zone has to be known prior to numerical analysis, or where the transient loading is bounded by specific range of strain rates.

Employment of the Cosserat, or micropolar continuum, characterized by the additional material rotational degree of freedom alongside the conventional displacements [99-101], is proven successful for determination of the size effects and in the analyses where the additional rotational degree of freedom is activated during the calculation, e.g. in the shear, i.e. mode-II localization problems [102]. Otherwise, in analyses where mode-I deformation is predominant, the abnormal localization may still occur [103].

As mentioned earlier, nonlocal approach to damage does not rely on the principle of local action as observed in classical continuum models, but also utilizes the strain state and state of the other state variables in the surrounding material points for the calculation of the strain and other variable states in the observed point. The main idea behind such approach is that the nonlocality provides a smoothing effect on the deformation and damage field, and thus prevents the localization in a smallest possible volume [84]. One of such schemes shown to be successful in eliminating the mesh-related problems is so-called nonlocal damage theory, described in more detail in [8, 28, 87, 104]. The concept of this method is to introduce direct spatial interactions in the continuum model, which is done by utilization of the weighted volume averages of certain state variables, defined as nonlocal variables in form of

$$\bar{\alpha}(\mathbf{x}) = \frac{1}{\int_V \vartheta(\mathbf{y};\mathbf{x})\,\mathrm{d}A} \int_V \vartheta(\mathbf{y};\mathbf{x})\,\tilde{\alpha}(\mathbf{y})\,\mathrm{d}A, \tag{2.20}$$

where $\vartheta(\mathbf{y},\mathbf{x})$ is the weight function that depends only on the distance $|\mathbf{x}-\mathbf{y}|$ between points **x** and **y**. $V$ represents the integration domain of the body where $D<1$, while $\bar{\alpha}(\mathbf{x})$ denotes the nonlocal variable for the local quantity $\tilde{\alpha}(\mathbf{y})$. Several weighting functions $\vartheta(\mathbf{y},\mathbf{x})$ exist in the literature of which the Gaussian function is employed most often, given by

$$\vartheta(\mathbf{y},\mathbf{x}) = \exp\left[-\frac{|\mathbf{x}-\mathbf{y}|^2}{2l^2}\right], \tag{2.21}$$

where the length scale parameter $l$ determines the volume of the material which contributes to the nonlocal variable, thus representing the maximum size of material inhomogeneity. Theoretical nonlocal neighborhood of the point where the weighted averaging is performed is graphically represented in Figure 2.7. Obviously, the intensity of the weighting function, and thus the appropriate nonlocal variable, decreases with the distance from the point considered for the averaging.

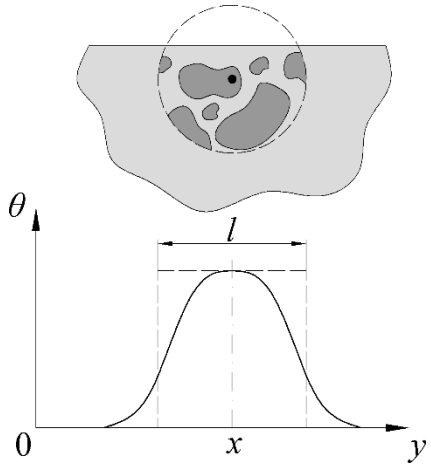


**Figure 2.7** Representation of the nonlocal material behavior (top) and weighted averaging for an irregular microstructure (bottom). Based on [104].

Physically, nonlocality represents the interactions and heterogeneities taking place at the microscale, which cannot be suppressed anymore when the fluctuations of the constitutive variables get closer in size to the fluctuations of the microstructure [105]. The integral nonlocal damage theory represents one of the most effective numerical procedures for the regularization of the strain localization, but still has few drawbacks, like challenging numerical implementation of the convolution-type integrals which appear in constitutive model. In addition, due to the asymmetry of the tangent stiffness matrix computational time is necessarily increased.

For sufficiently smooth fields of $\tilde{\alpha}$, the integral relation (2.20) can be reformulated by using the gradients of $\tilde{\alpha}$ through expansion into a Taylor series , which can be rearranged after some calculus in

$$\bar{\alpha}(\mathbf{x}) = \tilde{\alpha}(\mathbf{x}) + c_1 \nabla \tilde{\alpha}(\mathbf{x}) + c_2 \nabla^2 \tilde{\alpha}(\mathbf{x}) + \dots , \tag{2.22}$$

with $\nabla, \nabla^2, \dots$ denoting the gradient operators of first-, second-, … order. Hence the name gradient formulations for this technique, where the regularization is achieved by replacing the local equivalent strain $\tilde{\varepsilon}(\mathbf{x})$ in the loading function (2.4) and in the appropriate softening law formulation with the gradient-dependent nonlocal strain

$$\bar{\varepsilon}_{\mathrm{eq}}(\mathbf{x}) = \tilde{\varepsilon}_{\mathrm{eq}}(\mathbf{x}) + c\nabla^2 \tilde{\varepsilon}_{\mathrm{eq}}(\mathbf{x}). \tag{2.23}$$

Relation (2.23) is derived from (2.22) by inserting equivalent strain values $\varepsilon_{eq}$ instead of $\alpha$, and by neglecting the terms of order fourth and higher. Internal length scale parameter *l* is

included in the gradient coefficient *c*, and the relation between them depends on the choice of the weighting function $\vartheta(\mathbf{y},\mathbf{x})$. After the insertion of the model given by (2.23), usually called explicit gradient formulation [6], into the constitutive model, complexity of the equilibrium problem is necessarily increased due to additional gradients. In order to avoid this, implicit gradient formulation can be derived from (2.23), as shown in [6], in form of

$$\bar{\varepsilon}_{\mathrm{eq}}(\mathbf{x}) - c\nabla^2\bar{\varepsilon}_{\mathrm{eq}}(\mathbf{x}) = \tilde{\varepsilon}_{\mathrm{eq}}(\mathbf{x}), \tag{2.24}$$

which represents one of the most often used techniques for the regularization of the damage process.

Although both nonlocal integral and gradient formulations yield mesh-independent structural responses, they still suffer from nonphysical, spurious damage growth, as reported in number of articles [33, 34, 75]. The reason for such unwanted behavior, as stated in [34], is the constant interaction domain throughout the entire loading history, represented by the nonlocal damage parameter *l*, which leads to the transfer of the energy from the damage process zone to a neighboring elastically unloading region. In other words, evolution of the nonlocal strain $\bar{\varepsilon}_{eq}(\mathbf{x})$ can be observed outside of the initial localized damage profile, which consequentially provokes further damage growth beyond the initial localized zone. There are several suggestions in the literature to remedy this problem, and majority of them are based on introducing an evolving nonlocality. Initially, this was accomplished by allowing the weight of the nonlocal variable to be greater than unity [106, 107], which was afterwards extended to utilization of an evolving weight dependent on the damage or deformation [36]. Evolving length scale parameter given as a function of the local equivalent strain, and thus damage, is proposed in [75]. In [37], it is shown that in order to satisfy the thermodynamic aspect, the evolving length scale has to increase when made dependent on the damage and that by decreasing it, effective regularization cannot be achieved [108]. Departure from such models is made in [34], where the authors successfully incorporated the decreasing interaction domain, which is acceptable from physical point of view. As described in Section 2.2, width of the process zone in quasi-brittle materials localizes towards a microscopic crack, which indicates a decrease of the microstructural interactions domain with the deformation.

Similarly to gradient theories, the phase field approach provides a regularization by employing the nonlocal material behavior, introduced in the model through the phase-field parameter $\bar{d}$ which basically describes the spatially averaged damage. Therein, the assumption is made that the evolution of the phase-field is directly related to the crack growth by

introducing the fracture energy $G_c$, i.e. the amount of the energy dissipation per unit of created fracture surface. The diffusion equation that governs the phase-field evolution is according to [42] given by

$$\bar{d} - 4l^2\nabla^2\bar{d} = -\frac{2lh'\left(\bar{d}\right)\kappa}{G_c}, \tag{2.25}$$

where $h\left(\bar{d}\right)$ is a degradation function. It is obvious that partial differential equation (2.25) closely resembles to (2.24), and can be in fact brought down to implicit gradient-damage formulation through some minor changes [42]. The main advantage of the phase-field model over the implicit gradient formulation is that the derivative of the degradation function $h\left(\bar{d}\right)$ vanishes at a complete loss of material integrity, which ensures the stable localization zone with no spurious damage growth. Downside of phase-field modeling is the necessity for very fine discretization in the damage process zone, due to direct correlation of the internal length scale and the characteristic element size.

Gradient theories given above are based on the enhancement of the constitutive law by the introduction of only strain-related gradients. On the other hand, employment of the strain gradient continuum theory, where both the strain gradients and their stress conjugates contribute to internal energy, is shown to be unconditionally stable, thus offering a more robust approach. Authors in [44] concluded that the addition of the higher-order stress terms results in stabilizing the positive definiteness of the tangent stiffness moduli when entering the strain softening regime. This eliminates some numerical difficulties with regard to strain softening associated with gradient theories where only strain gradients are employed. Although numerically more complex, mainly due to the need for continuity requirements of the higher order, strain gradient continuum theory is successfully applied in various localization problems, either by the usage of the element-free Galerkin (EFG) meshless method [45, 109, 110] or the finite element method [74].

# 3 Higher-order finite element for softening analysis

Introduction of the second-order gradients of displacements in the virtual work statement necessarily leads to the higher-order differential equations. Solution to these equations by using the analytical methods would be strenuous even for the very simple problems, so the employment of some numerical method, e.g. finite element method is practically unavoidable. Since a numerical solution of the governing partial differential equation requires in this case a higher interpolation scheme, $C^1$ continuity has to be ensured. Consequentially, finite elements have to be enhanced with additional degrees of freedom, which inevitably increases a structural complexity of the problem. In order to reduce the $C^1$ interpolation requirements, various $C^0$ continuity finite elements based on mixed formulation are developed [52, 111-113]. Although more demanding when it comes to numerical implementation, $C^1$ continuity finite elements, described in [52, 114], are shown to be superior when compared to mixed $C^0$ continuity finite elements, which suffer from several shortcomings that can often lead to unacceptable results. When it comes to the analysis of damage and localization, $C^0$ continuity finite elements based on the mixed formulation are predominantly used, most often in the framework of the implicit gradient formulation [21, 115], micromorphic continuum formulation [34, 116, 117] and phase-field formulation [38-40, 42]. Neither the conventional implicit gradient nor conventional micromorphic formulation cannot completely regularize the localization process, where the spurious damage growth can be observed as a consequence [33, 75]. When it comes to the phase-field formulation, a very fine discretization of the model is usually needed, which can lead to the significant increase in the computational time. $C^1$ continuity is much easier to satisfy by using the meshless methods, where the approximation function with high-order of continuity can be straightforwardly incorporated into the formulation without increasing the problem size [118, 119]. However, high computational costs associated with the calculation of the approximation functions still represent a major shortcoming [120]. To author's knowledge, no existing $C^1$ continuity finite elements are used so far in the problems that include the localization of the damage. Herein, the $C^1$ continuity finite element formulation developed in [17] is used as a basis for the further extension of the element capabilities towards consideration of the material softening behavior.

In Section 3.1 higher-order theory is briefly described and basic $C^1$ continuity finite element is presented, while the implementation of the material softening and all belonging algorithms needed for the performing of the damage analysis are given in Section 3.2. In Section 3.3, the newly derived element is tested on few benchmark examples and compared with the solutions from the literature.

# 3.1 $C^1$ continuity finite element based on the second-gradient continuum theory

## 3.1.1 Higher-order continuum theory

When it comes to objective modeling of damage, introduction of nonlocal material behavior is shown to have a major contribution to the regularization capabilities of the localization phenomena. As described in Chapter 2, the term nonlocality refers to all heterogeneities and interactions taking place at the microscale, which cannot be neglected in the damage analysis where the sharp fluctuations of the variables at the macroscale are of the similar size as the microstructure [27]. Since the classical continuum theory does not contain internal length scale, effects originating from the microstructure cannot be captured, which leads to the unacceptable results in numerical observations. Extension of the classical continuum theory towards higher-order continuum is stimulated when so-called size effect was discovered in engineering, which is basically a problem of obtaining different structural responses with scaling of the structure, as described in [121]. Work of Cosserat brothers [122], based on the introduction of the additional rotational degrees of freedom at the microlevel, together with non-symmetric stress tensor and higher-order couple stress tensor, is further extended during that time in [123-126]. By the addition of the stretch gradients in the Cosserat theory, development of the full second-gradient theory began in [127], where so-called double stress tensor is introduced as an energetically conjugated term to the second derivative of the displacement field. In addition, material with the microstructure where each material point has its own degrees of freedom is described in [128, 129]. Besides modeling of size effects and damage phenomena [8, 32, 85], higher-order theories are also recognized as a valuable tool for modeling of material elastoplasticity derived within a gradient dependent plasticity [30, 130, 131]. Here, only the basic relations of the strain gradient continuum will be presented, while the detailed derivation

of all relations is given in [11, 53]. A comprehensive review of generalized continua can be found in [132].

According to the classical small strain theory, equilibrium is always considered by using the reference body configuration, i.e. an undeformed body, where the kinematical behavior at time $t$ is described by the displacement field $\mathbf{u}$. The fundamental strain gradient continuum relations are given in Table 3.1. In the small strain continuum theory the strain tensor $\boldsymbol{\varepsilon}$ is defined as a symmetric part of the displacement gradient field $\nabla \otimes \mathbf{u}$ , as shown in (3.1). In (3.4) $\boldsymbol{\sigma}$ is the Cauchy stress tensor and ${}^{3}\boldsymbol{\mu}$ stands for the third-order double-stress tensor, representing an energetically conjugate measure to the strain gradient tensor ${}^{3}\boldsymbol{\eta}$, defined in (3.2). As obvious from (3.3), strain density function is in the higher-order theory dependent on both the strain and the strain gradient tensors. Variation of the work done by internal forces is defined by (3.5) with $\nabla^{A}$ and $D$ as the surface gradient and normal gradient operators, respectively, while $\mathbf{n}$ represents the unit outward normal to surface $A$ of a body of volume $V$. In the variation of the external work given by (3.6), $\mathbf{t}$ and $\boldsymbol{\tau}$ stand for the traction and double surface traction vectors, respectively, with their definitions given in (3.7) and (3.8). Equilibrium equation (3.10) is derived from the principle of virtual work ($\delta W^{\text{int}} = \delta W^{\text{ext}}$), where $\tilde{\boldsymbol{\sigma}}$ represents the effective stress defined by (3.9).

**Table 3.1** Basic relations of the strain gradient continuum [17]

The strain tensor:

$$\boldsymbol{\varepsilon} = \frac{1}{2}\left(\nabla \otimes \mathbf{u} + (\nabla \otimes \mathbf{u})^T\right). \tag{3.1}$$

The strain gradient tensor:

$$^3\boldsymbol{\eta} = \nabla \otimes \boldsymbol{\varepsilon}. \tag{3.2}$$

The strain energy density function:

$$W = W\left(\boldsymbol{\varepsilon}, {}^3\boldsymbol{\eta}\right). \tag{3.3}$$

Variation of the strain energy function:

$$\delta W = \boldsymbol{\sigma} : \delta\boldsymbol{\varepsilon} + {}^3\boldsymbol{\mu} \vdots \delta {}^3\boldsymbol{\eta}. \tag{3.4}$$

Variation of the internal work:

$$\begin{aligned} \delta W^{\text{int}} = & \int_A \left\{ \left[ \mathbf{n} \cdot \left( \boldsymbol{\sigma} - \left( \nabla \cdot {}^3\boldsymbol{\mu} \right) \right) + \left( \nabla^A \cdot \mathbf{n} \right) \otimes \mathbf{n} \cdot \left( \mathbf{n} \cdot {}^3\boldsymbol{\mu} \right) - \nabla^A \cdot \left( \mathbf{n} \cdot {}^3\boldsymbol{\mu} \right) \right] \cdot \delta\mathbf{u} \right\} \mathrm{d}A - \\ & - \int_V \left\{ \left[ \nabla \cdot \left( \boldsymbol{\sigma} - \left( \nabla \cdot {}^3\boldsymbol{\mu} \right) \right) \right] \cdot \delta\mathbf{u} \right\} \mathrm{d}V + \\ & + \int_A \left[ \left( \mathbf{n} \cdot {}^3\boldsymbol{\mu} \cdot \mathbf{n} \right) \cdot \left( D \otimes \left( \delta\mathbf{u} \right) \right) \right] \mathrm{dA} \end{aligned}, \tag{3.5}$$

with $\nabla^A = \nabla \cdot \left( \mathbf{I} - \mathbf{n} \otimes \mathbf{n} \right)$ and $D = \mathbf{n} \cdot \nabla$.

Variation of the external work:

$$\delta W^{\text{ext}} = \int_A \left( \mathbf{t} \cdot \delta\mathbf{u} \right) \mathrm{d}A + \int_A \left[ \boldsymbol{\tau} \cdot \left( D \otimes \left( \delta\mathbf{u} \right) \right) \right] \mathrm{d}A, \tag{3.6}$$

where

$$\mathbf{t} = \mathbf{n} \cdot \left( \boldsymbol{\sigma} - \left( \nabla \cdot {}^3\boldsymbol{\mu} \right) \right) + \left( \nabla^A \cdot \mathbf{n} \right) \otimes \mathbf{n} \cdot \left( \mathbf{n} \cdot {}^3\boldsymbol{\mu} \right) - \nabla^A \cdot \left( \mathbf{n} \cdot {}^3\boldsymbol{\mu} \right) \tag{3.7}$$

$$\boldsymbol{\tau} = \mathbf{n} \cdot {}^3\boldsymbol{\mu} \cdot \mathbf{n}. \tag{3.8}$$

The effective stress:

$$\tilde{\boldsymbol{\sigma}} = \boldsymbol{\sigma} - \left( \nabla \cdot {}^3\boldsymbol{\mu} \right). \tag{3.9}$$

The equilibrium equation:

$$\nabla \cdot \tilde{\boldsymbol{\sigma}} = \mathbf{0}. \tag{3.10}$$

A special case of the general strain gradient continuum theory is described in [133-135], where a modified case of Mindlin's form II strain energy density [43] is proposed as

$$W = \frac{1}{2}\lambda\varepsilon_{ii}\varepsilon_{jj} + \mu\varepsilon_{ij}\varepsilon_{ij} + l^2\left(\frac{1}{2}\lambda\varepsilon_{ii,k}\varepsilon_{jj,k} + \mu\varepsilon_{ij,k}\varepsilon_{ij,k}\right), \tag{3.11}$$

with $l^2$ as the microstructural parameter or the internal length scale, and $\lambda$ and $\mu$ as elastic Lamé's constants, given by

$$\lambda = \frac{E\nu}{(1+\nu)(1-2\nu)}, \tag{3.12}$$

$$\mu = \frac{E}{2(1+\nu)}. \tag{3.13}$$

Employment of (3.4) and (3.11) then leads to following identities

$$\boldsymbol{\sigma} = \frac{\partial W}{\partial \boldsymbol{\varepsilon}} = (\lambda \operatorname{tr}\boldsymbol{\varepsilon})\otimes\mathbf{I} + 2\mu\boldsymbol{\varepsilon}, \tag{3.14}$$

$$\boldsymbol{\mu} = \frac{\partial W}{\partial^3 \boldsymbol{\eta}} = l^2\left[(\lambda \operatorname{tr}(\nabla\otimes\boldsymbol{\varepsilon}))\otimes\mathbf{I} + 2\mu(\nabla\otimes\boldsymbol{\varepsilon})\right], \tag{3.15}$$

$$\tilde{\boldsymbol{\sigma}} = (\lambda \operatorname{tr}\boldsymbol{\varepsilon})\otimes\mathbf{I} + 2\mu\boldsymbol{\varepsilon} - l^2\left[\nabla^2\left((\lambda \operatorname{tr}\boldsymbol{\varepsilon})\otimes\mathbf{I} + 2\mu\boldsymbol{\varepsilon}\right)\right]. \tag{3.16}$$

This simplified version of the higher-order continuum theory is especially convenient for modeling of the microstructure in the multiscale models, which will be explained in Chapter 4.

### 3.1.2 Formulation of the basic $C^1$ continuity finite element

Here, the $C^1$ continuity plane strain triangular finite element derived in [11] is presented, which will be extended in the thesis to the capability of describing the material softening behavior. As obvious from Figure 3.1, the element consists of three nodes and 36 degrees of freedom with the displacement field approximated by the complete fifth order polynomial, defined as

$$\begin{aligned} u = {} & a_1 + a_2x_1 + a_3x_2 + a_4x_1^2 + a_5x_1x_2 + a_6x_2^2 + a_7x_1^3 + a_8x_1^2x_2 + \\ & a_9x_1x_2^2 + a_{10}x_2^3 + a_{11}x_1^4 + a_{12}x_1^3x_2 + a_{13}x_1^2x_2^2 + a_{14}x_1x_2^3 + a_{15}x_2^4 + \\ & a_{16}x_1^5 + a_{17}x_1^4x_2 + a_{18}x_1^3x_2^2 + a_{19}x_1^2x_2^3 + a_{20}x_1x_2^4 + a_{21}x_2^5. \end{aligned} \tag{3.17}$$

The nodal degrees of freedom are the two displacements and their first- and second-order derivatives with respect to the Cartesian coordinates. The physical interpretation of the mentioned nodal degrees of freedom is comprehensively described in [73].

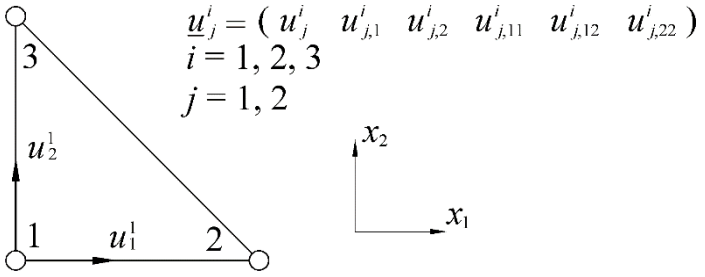


**Figure 3.1** $C^1$ continuity triangular finite element. Based on [11].

The derivation of the element equations is obtained by employing the principle of virtual work, which can be expressed for the strain gradient continuum as

$$\int_A \left(\boldsymbol{\sigma} : \delta\boldsymbol{\varepsilon}\right) \mathrm{d}A + \int_A \left({}^3\boldsymbol{\mu} \vdots \delta\,{}^3\boldsymbol{\eta}\right) \mathrm{d}A = \int_s \left(\mathbf{t} \cdot \delta\mathbf{u}\right) \mathrm{d}s + \int_s \left[\mathbf{T} : \left(\nabla \otimes \delta\mathbf{u}\right)\right] \mathrm{d}s\,, \tag{3.18}$$

with $s$ representing the perimeter of the element and $\mathbf{T}$ the double traction tensor, $\mathbf{T} = \boldsymbol{\tau} \otimes \mathbf{n}$. All other quantities are already mentioned and described above. In addition to (3.18), the boundary conditions expressed by the displacement and the normal derivative of displacement $\left(\nabla \otimes \mathbf{u}\right) \cdot \mathbf{n}$ should be prescribed to solve the boundary value problem. After the discretization of the field variables in weak form given by (3.18), the strain and strain gradient tensors can be written as

$$\boldsymbol{\varepsilon} = \begin{bmatrix} \varepsilon_{11} \\ \varepsilon_{22} \\ 2\varepsilon_{12} \end{bmatrix} = \mathbf{B}_\varepsilon \mathbf{v}\,, \tag{3.19}$$

$$\boldsymbol{\eta} = \begin{bmatrix} \eta_{111} \\ \eta_{222} \\ \eta_{221} \\ \eta_{112} \\ 2\eta_{121} \\ 2\eta_{212} \end{bmatrix} = \mathbf{B}_\eta \mathbf{v}\,. \tag{3.20}$$

In (3.19) and (3.20), $\mathbf{B}_\varepsilon$ and $\mathbf{B}_\eta$ represent the matrices containing adequate first and second derivatives of the element shape functions $\mathbf{N}$, while $\mathbf{v}$ is the vector of the nodal degrees of

freedom. Considering a nonlinear problem described by (3.18), the displacement vector **u**, the stress tensor $\boldsymbol{\sigma}$ and the double stress $\boldsymbol{\mu}$ are updated according to

$$\mathbf{u} = \mathbf{u}^{i-1} + \Delta\mathbf{u}, \tag{3.21}$$

$$\boldsymbol{\sigma} = \boldsymbol{\sigma}^{i-1} + \Delta\boldsymbol{\sigma}, \tag{3.22}$$

$${}^{3}\boldsymbol{\mu} = {}^{3}\boldsymbol{\mu}^{i-1} + \Delta\,{}^{3}\boldsymbol{\mu}\ , \tag{3.23}$$

where the exponent $(i-1)$ refers to the last converged equilibrium state, and the symbol $\Delta$ indicates an incremental change and mathematically acts as a differential operator. The linearized incremental constitutive relations are defined as

$$\Delta\boldsymbol{\sigma} = {}^{4}\mathbf{C}_{\sigma\varepsilon} : \Delta\boldsymbol{\varepsilon} + {}^{5}\mathbf{C}_{\sigma\eta} \vdots \Delta\,{}^{3}\boldsymbol{\eta}, \tag{3.24}$$

$$\Delta\,{}^{3}\boldsymbol{\mu} = {}^{5}\mathbf{C}_{\mu\varepsilon} : \Delta\boldsymbol{\varepsilon} + {}^{6}\mathbf{C}_{\mu\eta} \vdots \Delta\,{}^{3}\boldsymbol{\eta}, \tag{3.25}$$

with ${}^{4}\mathbf{C}_{\sigma\varepsilon}$, ${}^{5}\mathbf{C}_{\sigma\eta}$, ${}^{5}\mathbf{C}_{\mu\varepsilon}$ and ${}^{6}\mathbf{C}_{\mu\eta}$ as the constitutive stiffness matrices. As evident from (3.24) and (3.25), in generalized constitutive relations both first- and second-gradients of displacements contribute in a calculation of the stress fields. Herein, non-diagonal matrices ${}^{5}\mathbf{C}_{\sigma\eta}$ and ${}^{5}\mathbf{C}_{\mu\varepsilon}$ are different from zero when the material with the heterogeneous microstructure is observed. The strain and the second-order strain increments, employing (3.19) and (3.20), in terms of the displacement vector increment $\Delta\mathbf{v}$, read

$$\Delta\boldsymbol{\varepsilon} = \mathbf{B}_{\varepsilon}\Delta\mathbf{v}, \tag{3.26}$$

$$\Delta\boldsymbol{\mu} = \mathbf{B}_{\eta}\Delta\mathbf{v}\ . \tag{3.27}$$

Since the $C^1$ continuity finite element for softening analysis is based on the enhancement of the generalized constitutive relations (3.24) and (3.25), further derivation of the basic $C^1$ continuity finite element will not be included here, but can be found in [11].

## 3.2 $C^1$ continuity finite element for softening analysis

### 3.2.1 Weak formulation

Implementation of the softening behavior into the finite element starts with the application of the isotropic damage model (2.3) to the generalized strain gradient constitutive model where the linearization is omitted, as follows

$$\boldsymbol{\sigma} = (1-D)\,{}^{4}\mathbf{C}_{\sigma\varepsilon} : \boldsymbol{\varepsilon} + (1-D)\,{}^{5}\mathbf{C}_{\sigma\eta} \vdots {}^{3}\boldsymbol{\eta}, \tag{3.28}$$

$${}^{3}\boldsymbol{\mu} = (1-D)\,{}^{5}\mathbf{C}_{\mu\varepsilon} : \boldsymbol{\varepsilon} + (1-D)\,{}^{6}\mathbf{C}_{\mu\eta} \vdots {}^{3}\boldsymbol{\eta}. \tag{3.29}$$

Introduction of the damage enhanced constitutive relations represented by (3.28) and (3.29) into the principle of the virtual work for the strain gradient continuum, given by (3.18), leads to the following variational expression in terms of the damage variable

$$\begin{aligned}
&\int_A \left\{ \left[ (1-D)\,{}^{4}\mathbf{C}_{\sigma\varepsilon} : \boldsymbol{\varepsilon} + (1-D)\,{}^{5}\mathbf{C}_{\sigma\eta} \vdots {}^{3}\boldsymbol{\eta} \right] : \delta\boldsymbol{\varepsilon} \right\} \mathrm{d}A + \\
&\int_A \left\{ \left[ (1-D)\,{}^{5}\mathbf{C}_{\mu\varepsilon} : \boldsymbol{\varepsilon} + (1-D)\,{}^{6}\mathbf{C}_{\mu\eta} \vdots {}^{3}\boldsymbol{\eta} \right] \vdots \delta\,{}^{3}\boldsymbol{\eta} \right\} \mathrm{d}A = \\
&\int_s (\mathbf{t} \cdot \delta\mathbf{u})\,\mathrm{d}s + \int_s \left[ \mathbf{T} : (\nabla \otimes \delta\mathbf{u}) \right] \mathrm{d}s.
\end{aligned} \tag{3.30}$$

The linearized finite element equation is derived from the principle of the virtual work expressed by (3.18), using the standard incremental approach. By substitution of the discrete form of the field variables given by (3.19) and (3.20) into (3.18) following relation is obtained

$$\int_A \left[ \boldsymbol{\sigma} : (\mathbf{B}_{\varepsilon}\delta\mathbf{v}) \right] \mathrm{d}A + \int_A \left[ {}^{3}\boldsymbol{\mu} \vdots (\mathbf{B}_{\eta}\delta\mathbf{v}) \right] \mathrm{d}A = \int_s \left[ \mathbf{t} \cdot (\mathbf{N}\delta\mathbf{v}) \right] \mathrm{d}s + \int_s \left[ \mathbf{T} : ((\nabla \otimes \mathbf{N})\delta\mathbf{v}) \right] \mathrm{d}s\,, \tag{3.31}$$

where the relations listed below are employed

$$\delta\mathbf{u} = \mathbf{N}\delta\mathbf{v}\,, \tag{3.32}$$

$$\delta\boldsymbol{\varepsilon} = \mathbf{B}_{\varepsilon}\delta\mathbf{v}\,, \tag{3.33}$$

$$\delta\boldsymbol{\eta} = \mathbf{B}_{\eta}\delta\mathbf{v}\,. \tag{3.34}$$

Next, by inserting (3.22) and (3.23) into (3.31), and after some straightforward mathematical manipulation, the following incremental relation in matrix notation can be acquired

$$\int_A \mathbf{B}_{\varepsilon}^{T}\Delta\boldsymbol{\sigma}\,\mathrm{d}A + \int_A \mathbf{B}_{\eta}^{T}\Delta\boldsymbol{\mu}\,\mathrm{d}A = \int_s \left( \mathbf{N}^{T}\mathbf{t} + \mathrm{grad}\,\mathbf{N}^{T}\mathbf{T} \right) \mathrm{d}s - \int_A \left( \mathbf{B}_{\varepsilon}^{T}\boldsymbol{\sigma}^{i-1} + \mathbf{B}_{\eta}^{T}\,\boldsymbol{\mu}^{i-1} \right) \mathrm{d}A\,. \tag{3.35}$$

The right-hand side terms in the above expression represent the external and internal nodal force vectors $\mathbf{F}_{\mathrm{e}}$ and $\mathbf{F}_{\mathrm{i}}$, respectively. Considering the constant values of the constitutive stiffness matrices and the updates of the strain tensor, the strain gradient tensor and the damage variable in the form of

$$\boldsymbol{\varepsilon} = \boldsymbol{\varepsilon}^{i-1} + \Delta\boldsymbol{\varepsilon}\,, \tag{3.36}$$

$$\boldsymbol{\eta} = \boldsymbol{\eta}^{i-1} + \Delta\boldsymbol{\eta}\,, \tag{3.37}$$

$$D = D^{i-1} + \Delta D\,, \tag{3.38}$$

generalized strain gradient damage constitutive model given by (3.28) and (3.29) reads

$$\Delta\boldsymbol{\sigma} = \left(1-D^{i-1}\right)\left(\mathbf{C}_{\sigma\varepsilon}\Delta\boldsymbol{\varepsilon}+\mathbf{C}_{\sigma\eta}\Delta\boldsymbol{\eta}\right)-\Delta D\left(\mathbf{C}_{\sigma\varepsilon}\boldsymbol{\varepsilon}^{i-1}+\mathbf{C}_{\sigma\eta}\boldsymbol{\eta}^{i-1}\right), \tag{3.39}$$

$$\Delta\boldsymbol{\mu} = \left(1-D^{i-1}\right)\left(\mathbf{C}_{\mu\varepsilon}\Delta\boldsymbol{\varepsilon}+\mathbf{C}_{\mu\eta}\Delta\boldsymbol{\eta}\right)-\Delta D\left(\mathbf{C}_{\mu\varepsilon}\boldsymbol{\varepsilon}^{i-1}+\mathbf{C}_{\mu\eta}\boldsymbol{\eta}^{i-1}\right). \tag{3.40}$$

Here, the incremental change of the damage variable may be expressed by

$$\Delta D = \left(\frac{\mathrm{d}D}{\mathrm{d}\boldsymbol{\varepsilon}}\right)^{i-1}\Delta\boldsymbol{\varepsilon}, \tag{3.41}$$

since the damage variable is assumed to be a function only of the strain tensor $D = D(\boldsymbol{\varepsilon})$. Calculation of the derivative given in (3.41) is made by using the chain rule in the following way

$$\frac{\mathrm{d}D}{\mathrm{d}\boldsymbol{\varepsilon}} = \frac{\mathrm{d}D}{\mathrm{d}\kappa}\frac{\mathrm{d}\kappa}{\mathrm{d}\varepsilon_{\mathrm{eq}}}\frac{\mathrm{d}\varepsilon_{\mathrm{eq}}}{\mathrm{d}\boldsymbol{\varepsilon}}, \tag{3.42}$$

where the term $\dfrac{\mathrm{d}\kappa}{\mathrm{d}\varepsilon_{\mathrm{eq}}}$ is equal to one when damage rises and zero when there is no damage growth. According to (2.6) and (2.7) damage $D = D(\kappa)$ has to be differentiated with respect to history parameter $\kappa$, while equivalent elastic deformation $\varepsilon_{\mathrm{eq}} = \varepsilon_{\mathrm{eq}}(\boldsymbol{\varepsilon})$ as a function of the strain tensor $\boldsymbol{\varepsilon}$ is differentiated with respect to strain tensor components, as evident from (2.8) and (2.9). When the incremental higher-order damage constitutive model represented by (3.39) and (3.40) is embedded into the incremental relation (3.35), and by using (3.41), the following expression is obtained

$$\begin{aligned}
&\int_A \mathbf{B}_\varepsilon^T\left[\left(1-D^{i-1}\right)\mathbf{C}_{\sigma\varepsilon}\mathbf{B}_\varepsilon\Delta\mathbf{v}-\mathbf{C}_{\sigma\varepsilon}\boldsymbol{\varepsilon}^{i-1}\left(\frac{\mathrm{d}D}{\mathrm{d}\boldsymbol{\varepsilon}}\right)^{i-1}\mathbf{B}_\varepsilon\Delta\mathbf{v}\right]\mathrm{d}A+\\
&\int_A \mathbf{B}_\varepsilon^T\left[\left(1-D^{i-1}\right)\mathbf{C}_{\sigma\eta}\mathbf{B}_\eta\Delta\mathbf{v}-\mathbf{C}_{\sigma\eta}\boldsymbol{\eta}^{i-1}\left(\frac{\mathrm{d}D}{\mathrm{d}\boldsymbol{\varepsilon}}\right)^{i-1}\mathbf{B}_\varepsilon\Delta\mathbf{v}\right]\mathrm{d}A+\\
&\int_A \mathbf{B}_\eta^T\left[\left(1-D^{i-1}\right)\mathbf{C}_{\mu\varepsilon}\mathbf{B}_\varepsilon\Delta\mathbf{v}-\mathbf{C}_{\mu\varepsilon}\boldsymbol{\varepsilon}^{i-1}\left(\frac{\mathrm{d}D}{\mathrm{d}\boldsymbol{\varepsilon}}\right)^{i-1}\mathbf{B}_\varepsilon\Delta\mathbf{v}\right]\mathrm{d}A+\\
&\int_A \mathbf{B}_\eta^T\left[\left(1-D^{i-1}\right)\mathbf{C}_{\mu\eta}\mathbf{B}_\eta\Delta\mathbf{v}-\mathbf{C}_{\mu\eta}\boldsymbol{\eta}^{i-1}\left(\frac{\mathrm{d}D}{\mathrm{d}\boldsymbol{\varepsilon}}\right)^{i-1}\mathbf{B}_\varepsilon\Delta\mathbf{v}\right]\mathrm{d}A\\
&=\int_s\left(\mathbf{N}^T\mathbf{t}+\operatorname{grad}\mathbf{N}^T\mathbf{T}\right)\mathrm{d}s-\int_A\left(\mathbf{B}_\varepsilon^T\boldsymbol{\sigma}^{i-1}+\mathbf{B}_\eta^T\boldsymbol{\mu}^{i-1}\right)\mathrm{d}A.
\end{aligned} \tag{3.43}$$

After some regrouping of the terms in the above relation, the finite element equation can be written as

$$\left(\mathbf{K}_{\varepsilon\varepsilon}+\mathbf{K}_{\varepsilon\eta}+\mathbf{K}_{\eta\varepsilon}+\mathbf{K}_{\eta\eta}\right)\Delta\mathbf{v}=\mathbf{F}_{\mathrm{e}}-\mathbf{F}_{\mathrm{i}}\,, \tag{3.44}$$

where the particular element stiffness matrices are defined as

$$\mathbf{K}_{\varepsilon\varepsilon}=\int_{A}\mathbf{B}_{\varepsilon}^{T}\left[\left(1-D^{i-1}\right)\mathbf{C}_{\sigma\varepsilon}-\mathbf{C}_{\sigma\varepsilon}\boldsymbol{\varepsilon}^{i-1}\left(\frac{\mathrm{d}D}{\mathrm{d}\boldsymbol{\varepsilon}}\right)^{i-1}-\mathbf{C}_{\sigma\eta}\boldsymbol{\eta}^{i-1}\left(\frac{\mathrm{d}D}{\mathrm{d}\boldsymbol{\varepsilon}}\right)^{i-1}\right]\mathbf{B}_{\varepsilon}\mathrm{d}A\,, \tag{3.45}$$

$$\mathbf{K}_{\varepsilon\eta}=\int_{A}\mathbf{B}_{\varepsilon}^{T}\left(1-D^{i-1}\right)\mathbf{C}_{\sigma\eta}\mathbf{B}_{\eta}\,\mathrm{d}A\,, \tag{3.46}$$

$$\mathbf{K}_{\eta\varepsilon}=\int_{A}\mathbf{B}_{\eta}^{T}\left[\left(1-D^{i-1}\right)\mathbf{C}_{\mu\varepsilon}-\mathbf{C}_{\mu\varepsilon}\boldsymbol{\varepsilon}^{i-1}\left(\frac{\mathrm{d}D}{\mathrm{d}\boldsymbol{\varepsilon}}\right)^{i-1}-\mathbf{C}_{\mu\eta}\boldsymbol{\eta}^{i-1}\left(\frac{\mathrm{d}D}{\mathrm{d}\boldsymbol{\varepsilon}}\right)^{i-1}\right]\mathbf{B}_{\varepsilon}\mathrm{d}A\,, \tag{3.47}$$

$$\mathbf{K}_{\eta\eta}=\int_{A}\mathbf{B}_{\eta}^{T}\left(1-D^{i-1}\right)\mathbf{C}_{\mu\eta}\mathbf{B}_{\eta}\,\mathrm{d}A\,. \tag{3.48}$$

### 3.2.2 Calculation of constitutive stiffness matrices

For the analysis of the softening behavior of an arbitrary heterogeneous material all constitutive stiffness matrices appearing in (3.45)-(3.48) have to be known. To compute these matrices, the second-order computational homogenization procedure is utilized, for which the basic relations are listed in Table 3.2. Generally, the procedure is performed in the multiscale analyses, where the quantities from lower scales have to be homogenized to put them in use at higher scales. The sequential macro-micro algorithm, which consists of the solutions of the boundary value problems at two different levels, is employed. The macrolevel refers to the model discretized by the aforementioned $C^1$ triangular finite elements, where in each integration point the microstructural contribution is included through the analysis of the RVE, in this thesis discretized by the $C^0$ quadrilateral finite elements. In the Table 3.2, the presented quantities denoted by the subscript "M" correspond to the macrolevel, while the subscript "m" indicates a microlevel quantity. In (3.49), $\mathbf{x}$ is the spatial coordinate on the RVE boundary, while $\mathbf{r}$ represents the microstructural fluctuation field. By means of the Hill-Mandel condition given by (3.50), the first- and second-order stress tensors can be derived in the form of (3.51) and (3.52), where $\mathbf{D}$ and $\mathbf{H}$ are the coordinate matrices which include all boundary nodes $i=1, 2, ..., n$ of the RVE, while $\mathbf{f}_{\mathrm{b}}$ represents the RVE boundary nodal force vector. Taking

into account the internal (subscript "a") and the boundary (subscript "b") contributions of the RVE, the finite element equation for the nonlinear problems can be written in the incremental form as presented in (3.57). By employing (3.24) and (3.25) and the condensed stiffness matrix given by (3.60), the incremental form of the first- and second-order stress tensors represented by (3.62) and (3.63) can then easily be obtained, which yields the tangent stiffness matrices (3.64)-(3.67). Detailed information about the second-order homogenization procedure can be found for example in [17, 46].

**Table 3.2** Basic relations of the second-order homogenization [17]

The RVE displacement field:

$$\mathbf{u}_{\mathrm{m}} = \mathbf{x}^T \boldsymbol{\varepsilon}_{\mathrm{M}} + \frac{1}{2}\mathbf{x}^T \boldsymbol{\eta}_{\mathrm{M}} \mathbf{x} + \mathbf{r}\,. \tag{3.49}$$

The Hill-Mandel condition:

$$\frac{1}{V}\int_V \left(\delta\boldsymbol{\varepsilon}_{\mathrm{m}}^T \boldsymbol{\sigma}_{\mathrm{m}}\right) \mathrm{d}V = \delta\boldsymbol{\varepsilon}_{\mathrm{M}}^T \boldsymbol{\sigma}_{\mathrm{M}} + \delta\boldsymbol{\eta}_{\mathrm{M}}^T \boldsymbol{\mu}_{\mathrm{M}}\,. \tag{3.50}$$

The first- and second-order stress tensors:

$$\boldsymbol{\sigma}_{\mathrm{M}} = \frac{1}{V}\mathbf{D}\mathbf{f}_{\mathrm{b}}\,, \tag{3.51}$$

$$\boldsymbol{\mu}_{\mathrm{M}} = \frac{1}{V}\mathbf{H}\mathbf{f}_{\mathrm{b}}\,, \tag{3.52}$$

where

$$\mathbf{D} = \frac{1}{2}\begin{bmatrix}\mathbf{D}_1^T & \mathbf{D}_2^T & \ldots & \mathbf{D}_n^T\end{bmatrix}, \tag{3.53}$$

$$\mathbf{H} = \frac{1}{2}\begin{bmatrix}\mathbf{H}_1^T & \mathbf{H}_2^T & \ldots & \mathbf{H}_n^T\end{bmatrix}, \tag{3.54}$$

and

$$\mathbf{D}_i = \frac{1}{2}\begin{bmatrix}2x & 0 & y \\ 0 & 2y & x\end{bmatrix}, \tag{3.55}$$

$$\mathbf{H}_i = \frac{1}{2}\begin{bmatrix}2x^2 & 0 & 2y^2 & 0 & xy & 0 \\ 0 & 2y^2 & 0 & 2x^2 & 0 & xy\end{bmatrix}. \tag{3.56}$$

The partitioned finite element equation in incremental form:

$$\begin{bmatrix}\mathbf{K}_{\mathrm{aa}} & \mathbf{K}_{\mathrm{ab}} \\ \mathbf{K}_{\mathrm{ba}} & \mathbf{K}_{\mathrm{bb}}\end{bmatrix}\begin{bmatrix}\Delta\mathbf{u}_{\mathrm{a}} \\ \Delta\mathbf{u}_{\mathrm{b}}\end{bmatrix} = \begin{bmatrix}\Delta\mathbf{f}_{\mathrm{a}} \\ \Delta\mathbf{f}_{\mathrm{b}}\end{bmatrix}. \tag{3.57}$$

In the convergence state

$$\Delta \mathbf{f}_{\mathrm{a}} = \mathbf{0}\,, \tag{3.58}$$

$$\Delta \mathbf{f}_{\mathrm{b}} = \tilde{\mathbf{K}}_{\mathrm{bb}} \Delta \mathbf{u}_{\mathrm{b}}\,, \tag{3.59}$$

with

$$\tilde{\mathbf{K}}_{\mathrm{bb}} = \mathbf{K}_{\mathrm{bb}} - \mathbf{K}_{\mathrm{ba}} \mathbf{K}_{\mathrm{aa}}^{-1} \mathbf{K}_{\mathrm{ab}}\,. \tag{3.60}$$

The RVE boundary nodes displacement increment:

$$\Delta \mathbf{u}_{\mathrm{b}} = \mathbf{D}^{T} \Delta \boldsymbol{\varepsilon}_{\mathrm{M}} + \mathbf{H}^{T} \Delta \boldsymbol{\eta}_{\mathrm{M}}\,. \tag{3.61}$$

The incremental values of the first- and second-order stress tensors:

$$\Delta \boldsymbol{\sigma}_{\mathrm{M}} = \frac{1}{V}\left( \mathbf{D}\tilde{\mathbf{K}}_{\mathrm{bb}} \mathbf{D}^{T} \Delta \boldsymbol{\varepsilon}_{\mathrm{M}} + \mathbf{D}\tilde{\mathbf{K}}_{\mathrm{bb}} \mathbf{H}^{T} \Delta \boldsymbol{\eta}_{\mathrm{M}} \right), \tag{3.62}$$

$$\Delta \boldsymbol{\mu}_{\mathrm{M}} = \frac{1}{V}\left( \mathbf{H}\tilde{\mathbf{K}}_{\mathrm{bb}} \mathbf{D}^{T} \Delta \boldsymbol{\varepsilon}_{\mathrm{M}} + \mathbf{H}\tilde{\mathbf{K}}_{\mathrm{bb}} \mathbf{H}^{T} \Delta \boldsymbol{\eta}_{\mathrm{M}} \right). \tag{3.63}$$

The tangent stiffness matrices:

$$\mathbf{C}_{\sigma\varepsilon} = \frac{1}{V} \mathbf{D}\tilde{\mathbf{K}}_{\mathrm{bb}} \mathbf{D}^{T}\,, \tag{3.64}$$

$$\mathbf{C}_{\sigma\eta} = \frac{1}{V} \mathbf{D}\tilde{\mathbf{K}}_{\mathrm{bb}} \mathbf{H}^{T}\,, \tag{3.65}$$

$$\mathbf{C}_{\mu\varepsilon} = \frac{1}{V} \mathbf{H}\tilde{\mathbf{K}}_{\mathrm{bb}} \mathbf{D}^{T}\,, \tag{3.66}$$

$$\mathbf{C}_{\mu\eta} = \frac{1}{V} \mathbf{H}\tilde{\mathbf{K}}_{\mathrm{bb}} \mathbf{H}^{T}\,. \tag{3.67}$$

As described previously, in the case of material homogeneity, material isotropy, and symmetry of the RVE considered the tangent stiffness matrices $\mathbf{C}_{\sigma\eta}$ and $\mathbf{C}_{\mu\varepsilon}$ are equal to zero [46]. The remaining two tangent stiffness matrices can be computed analytically [13, 46], which may be written symbolically in the form

$$\mathbf{C}_{\sigma\varepsilon} = \mathbf{C}_{\sigma\varepsilon}\left(E, \nu\right)\,, \tag{3.68}$$

$$\mathbf{C}_{\mu\eta} = \mathbf{C}_{\mu\eta}\left(E, \nu, l\right), \tag{3.69}$$

where $l$ denotes the microstructural length scale. On the other hand, the stiffness matrices can be also computed numerically using the homogenization procedure as already done in [17]. Therein the microstructural parameter is expressed by the relation

$$l^2 = \frac{L^2}{12}, \tag{3.70}$$

where $L$ is the RVE side length. As displayed above, the material nonlocality is included into the second-gradient continuum theory through the higher-order constitutive matrices $\mathbf{C}_{\sigma\eta}$, $\mathbf{C}_{\mu\varepsilon}$ and $\mathbf{C}_{\mu\eta}$ in terms of the microstructural parameter $l$. When these matrices are multiplied by the term $(1-D)$ according to (3.28) and (3.29), the nonlocality decreases if the damage rises. Such behavior is physically acceptable when the formation of the crack in quasi-brittle materials is observed, as discussed earlier. Differences in the calculation of the stiffness behavior for materials with homogeneous and heterogeneous microstructures are briefly summarized in Table 3.3.

**Table 3.3** Stiffness calculation for microstructurally homogeneous and heterogeneous materials

| **Homogeneous material** | **Heterogeneous material** |
|---|---|
| $\mathbf{C}_{\sigma\eta}, \mathbf{C}_{\mu\varepsilon} = \mathbf{0}$ | $\mathbf{C}_{\sigma\eta}, \mathbf{C}_{\mu\varepsilon} \neq \mathbf{0}$ |
| $\mathbf{C}_{\sigma\varepsilon}$<br>$\mathbf{C}_{\mu\eta} = \mathbf{C}_{\mu\eta}(l)$ } analytical relations | $\mathbf{C}_{\sigma\varepsilon}$<br>$\mathbf{C}_{\sigma\eta} = \mathbf{C}_{\sigma\eta}(L)$<br>$\mathbf{C}_{\mu\varepsilon} = \mathbf{C}_{\mu\varepsilon}(L)$<br>$\mathbf{C}_{\mu\eta} = \mathbf{C}_{\mu\eta}(L)$ } second-order computational homogenization |
| $l^2 = \frac{L^2}{12}$ | |
| $\boldsymbol{\sigma} = \left[1-D(\boldsymbol{\varepsilon})\right]^4\mathbf{C}_{\sigma\varepsilon} : \boldsymbol{\varepsilon}$<br>$^3\boldsymbol{\mu} = \left[1-D(\boldsymbol{\varepsilon})\right]^6\mathbf{C}_{\mu\eta} \vdots {}^3\boldsymbol{\eta}$ | $\boldsymbol{\sigma} = \left[1-D(\boldsymbol{\varepsilon})\right]^4\mathbf{C}_{\sigma\varepsilon} : \boldsymbol{\varepsilon} + \left[1-D(\boldsymbol{\varepsilon})\right]^5\mathbf{C}_{\sigma\eta} \vdots {}^3\boldsymbol{\eta}$<br>$^3\boldsymbol{\mu} = \left[1-D(\boldsymbol{\varepsilon})\right]^5\mathbf{C}_{\mu\varepsilon} : \boldsymbol{\varepsilon} + \left[1-D(\boldsymbol{\varepsilon})\right]^6\mathbf{C}_{\mu\eta} \vdots {}^3\boldsymbol{\eta}$ |

### 3.2.3 Analysis procedure

The analysis procedure is concisely shown as a flowchart in Figure 3.2. It should be noted that this is not a true multiscale algorithm which includes subsequent solving of the two boundary

value problems, the one at the macrolevel and the other at the microlevel. Instead, the boundary value problem has to be solved here only for the macromodel, while the microstructural RVE analysis, comprised only of the stiffness homogenization, is performed in a preprocessing step to obtain the values of the constitutive stiffness tensors. Since the linear elastic material behavior is considered in the presented damage analysis, the homogenized solutions do not depend on the macroscale deformation. Therefore, the homogenization procedure has to be performed only once in each analysis. The homogenized stiffness values then enter the constitutive relations, and remain constant until the end of the nonlinear damage analysis. When the damage is initiated in the model, the elastic stiffness is being reduced according to (2.3) and to the damage enhanced constitutive relations (3.28) and (3.29) as well. In each finite element integration point, the incremental-iterative procedure is carried out, where the stress and double stress tensors are calculated from the updated values of the strain tensor, the second-order strain tensor and the damage variable, as well as the constant elastic stiffness tensors obtained in the preprocessing step. The presented damage algorithm together with the formulation of the triangular finite element is implemented into the commercial finite element software ABAQUS/Standard employing its nonlinear solver and the user-defined subroutine UEL [136, 137], which is written in FORTRAN programming language. More details on the numerical implementation of the presented finite element formulations into ABAQUS/Standard can be found in [11].

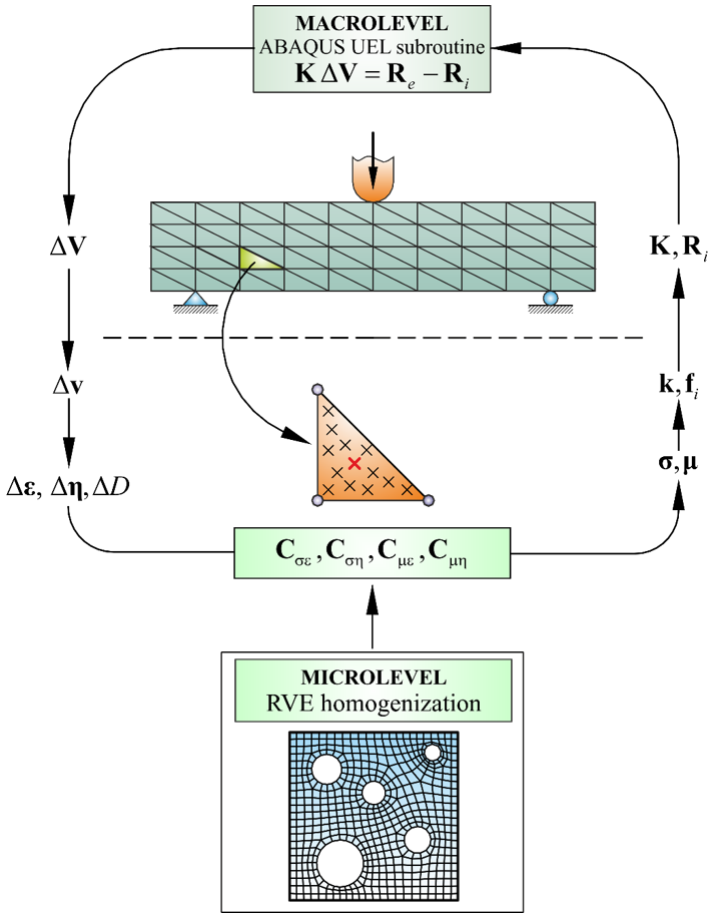


**Figure 3.2** Scheme of the damage algorithm

# 3.3 Numerical examples

## 3.3.1 Plate with an imperfect zone subjected to tensile load, homogeneous microstructure

The presented algorithm is verified in a benchmark problem already studied in [45], where only a homogeneous material is considered. In this contribution the analysis is extended to the consideration of heterogeneous materials, too. The geometry and boundary conditions of the rectangular plate with an imperfect zone under tension are shown in Figure 3.3. The Mazars' equivalent strain measure (2.8) is used together with the damage evolution governed by the linear softening (2.6). The material data are: the Young's modulus $E = 20000$ N/mm$^2$, the Poisson's ratio $\nu = 0.25$, the limit elastic strain $\kappa_0 = 0.0001$, the equivalent strain corresponding to the fully damaged state $\kappa_u = 0.0125$. The horizontal displacement of

$u = 0.0325$ mm is prescribed at the right edge. In order to trigger localization, the Young's modulus is reduced by 10% in the 10 mm wide zone in the middle hatched area of the plate. Along the vertical edges the second-order derivatives of the displacement component in the normal direction, $u_{1,11}$ and $u_{1,22}$, together with the mixed derivatives, $u_{1,12}$ and $u_{2,12}$, are suppressed. The first-order derivatives associated with the shear deformation, $u_{1,2}$ and $u_{2,1}$, are also set to zero. These boundary conditions yield the straight vertical edges. Here, the indices 1 and 2 refer to the Cartesian coordinates *x* and *y*, respectively.

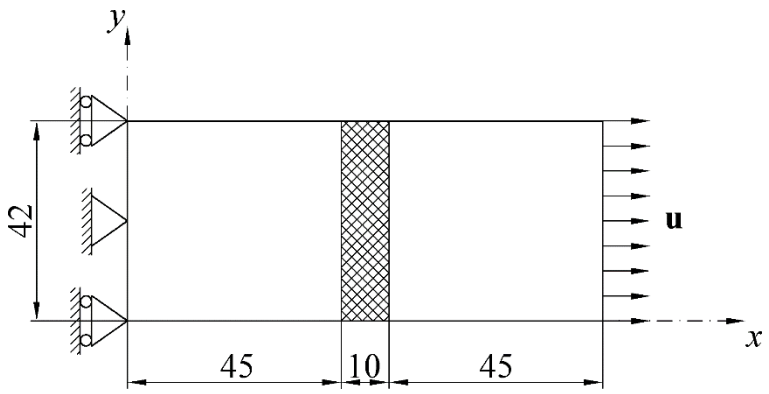


**Figure 3.3** Geometry and boundary conditions of the plate subjected to tensile load. Based on [45].

The solutions of the same numerical example are obtained by means of the EFG meshless method in [45]. Therein, the constitutive tensors are derived for the materials with granular microstructure, so the underlying microstructural theory differs when compared with the second-order homogenization approach. The constitutive model is restricted only to homogeneous materials, where the corresponding stiffness tensors can be written in the form of (3.68) and (3.69) with the particle radius *r* instead of the microstructural parameter *l*. The same constitutive model is used for the computation of the softening response of the plate by means of the proposed FEM algorithm. The damage responses obtained for the same microstructural values and using different approaches are presented in Figure 3.4. In this numerical example, the distributions of the damage and equivalent strain are considered along the horizontal central axis of the plate, crossing the hinged joint at $y = 21$ mm.

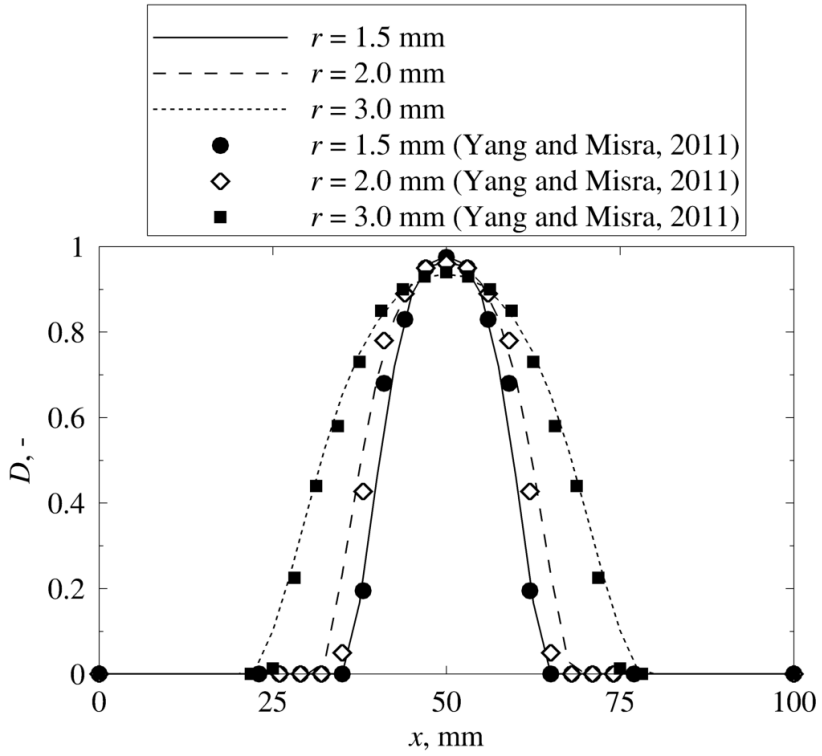


**Figure 3.4** Comparison of damage profiles along the horizontal central axis of the plate obtained using the presented FEM damage model to the EFG results from the literature

As can be seen from Figure 3.4, the calculated damage profiles show very good agreement with the solutions from the literature. The figure also illustrates the effect of the microstructural size on the macrostructural behavior. The increase in the microstructural values leads to the expansion of the localization zone and a slight decrease in the peak damage values, as expected. Furthermore, the mesh sensitivity of the proposed algorithm is examined by using the three different finite element discretizations. Figure 3.5 presents the coarsest mesh of 72 elements with the reduced material properties in the marked area covered by only few elements. A homogeneous material with the internal length scale of $l = 1.5$ mm is considered.

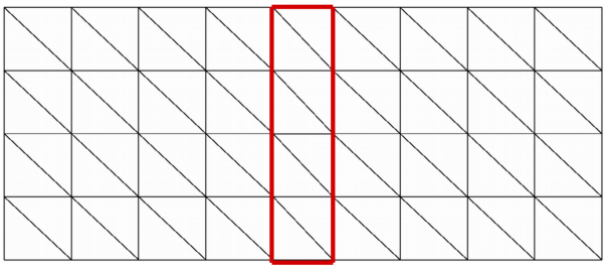

**Figure 3.5** The coarsest finite element mesh of the plate under tension

As evident from Figure 3.6, the reduction of the element size in the last two discretizations does not lead to the further localization of the damage profile in the softening zone, which proves that the presented damage model is independent on the mesh refinement. It is also interesting to note that values of the nodal variables computed by the coarsest and the finest discretization are quite similar, leading to the conclusion that convergence can be achieved with a relatively coarse mesh and accordingly with a significant reduction of the computational time. In order to achieve a more detailed visualization of variables, discretization consisting of 1280 finite elements is used for the depiction of following diagrams and contour plots.

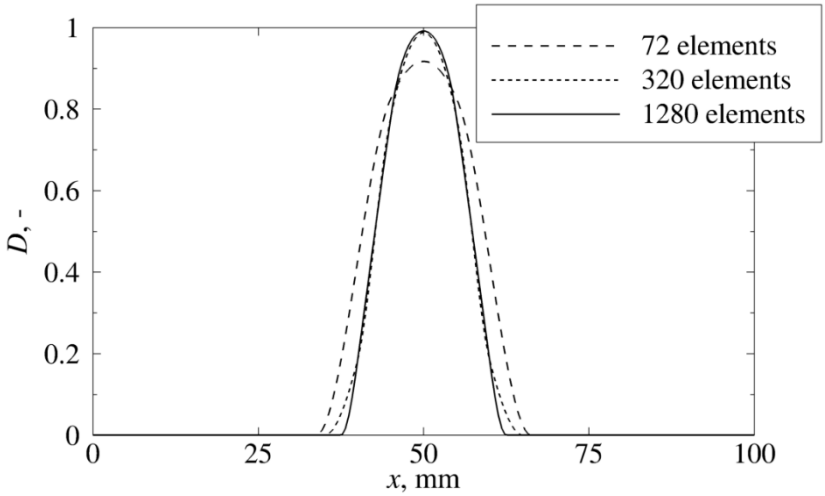


**Figure 3.6** Comparison of damage profiles along horizontal central axis of the plate under tension for three different mesh densities

Next, the evolution of the equivalent elastic strain measure as well as the damage variable are depicted in Figure 3.7 and Figure 3.8, respectively. It can be noted that the growth of the equivalent elastic strain emerges within the imperfection and rather early in the softening process reaches its final width, which does not change in the subsequent loading stages. Instead, the localization drastically intensifies during final loading stages in the narrow region in the middle of the plate, which is basically a continuum representation of the macroscopic crack. In [75] the similar problem is studied in only one dimension employing the conventional implicit gradient enhancement, resulting in an unacceptable growth of the damage zone. Instead of the localization into a macroscopic crack, the expansion of the damaged zone with the loading progression is reported for the analyzed bar in tension. The solutions obtained by the strain gradient formulation proposed in this contribution show no such spurious damage growth, which is obviously an advantage when compared with the conventional implicit gradient formulation. The described physically meaningless phenomenon is eliminated in [75] in the

form of the somewhat complicated strain-based transient-gradient damage method which couples the nonlocal effect to the local deformation state of the material. It can be noted that a similar thing is basically done in the present contribution, where the local and nonlocal effects are coupled through the damage constitutive relations of the second-gradient continuum theory, knowing that the damage variable is a function of the local equivalent strain measure.

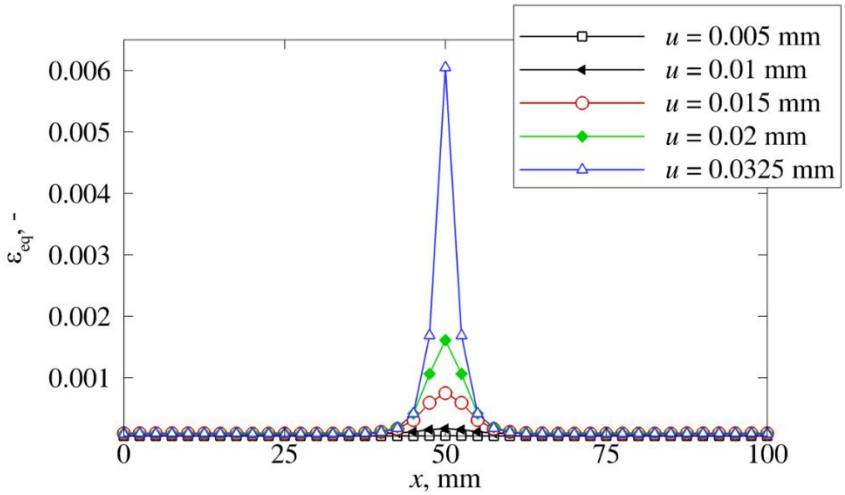


**Figure 3.7** Evolution of the equivalent elastic strain $\varepsilon_{eq}$ along horizontal central axis of the plate for different loading levels

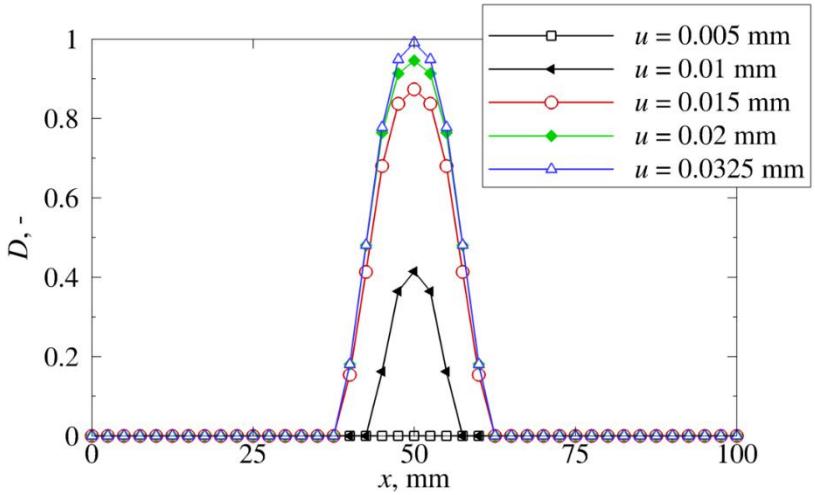


**Figure 3.8** Evolution of the damage variable *D* along horizontal central axis of the plate for different loading levels

For a better perception of the softening process in the failure deformation stage, the distributions of equivalent elastic strain measure and damage variable are displayed in Figure 3.9 and Figure 3.10, respectively. In Figure 3.9 the localized deformation band can be clearly seen, with the

highest values of equivalent elastic strain in the central part of the plate, being a consequence of the lateral contraction. Namely, since the edges defined by the normal vectors in vertical direction are free boundaries, the material is more pliable in their vicinity and it stretches in the loading direction more than the material in the central part of the plate. Besides, due to the Poisson's effect, it contracts more laterally and therefore does not contribute to the Mazars' equivalent elastic strain measure defined in (2.8). As evident, the damage distribution in Figure 3.10 appears overly spread in contrast to the equivalent elastic strain distribution in Figure 3.9. This phenomenon can be explained by considering the damage irreversibility and knowing that the fracture usually starts as a zone of high material nonlocal behavior, and ends as a narrow localized deformation band where nonlocality is significantly reduced. Additionally, it is worth to mention that softening laws for the quasi-brittle materials usually give rather high damage values for the equivalent elastic strain values just slightly above the limit strain $\kappa_0$.

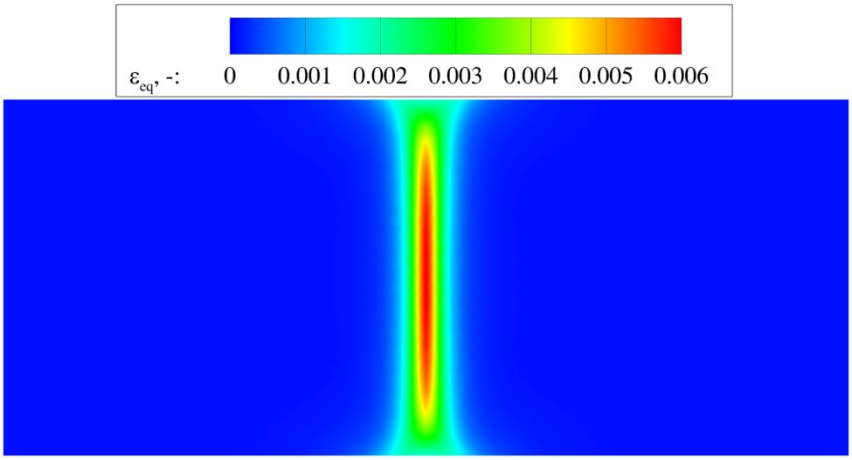


**Figure 3.9** Distribution of the equivalent elastic strain $\varepsilon_{eq}$ for homogeneous material at failure stage

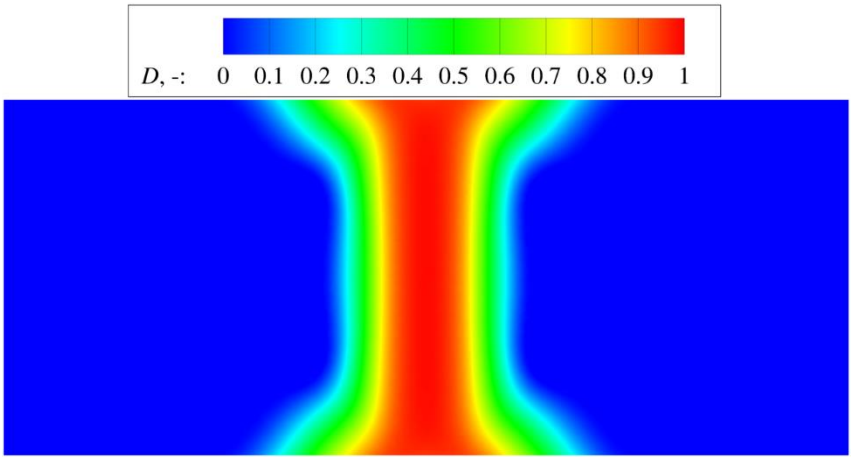


**Figure 3.10** Distribution of the damage *D* for homogeneous material at failure stage

The equivalent stress field defined by

$$\sigma_{\mathrm{eq}} = (1-D)\, E\varepsilon_{\mathrm{eq}} \tag{3.71}$$

is depicted in Figure 3.11, where its reduction can clearly be seen in the area which coincides with the localization zone shown in Figure 3.9. As it is obvious from Figure 3.9, the softening of the material is at its highest in the middle of the plate, whereas its intensity decreases towards the free boundaries. Therefore, it is to expect that the material at the free horizontal boundaries carries more load than that which is closer to the central part of the plate. The direct consequence of such a behavior are the higher equivalent stress values of the material closer to the boundaries, taking into account the (3.71). Of course, with the increasing distance from the highly damaged area, where the high gradients are present, the stress field becomes more uniform towards the left and the right vertical boundaries, where the straight edges are enforced.

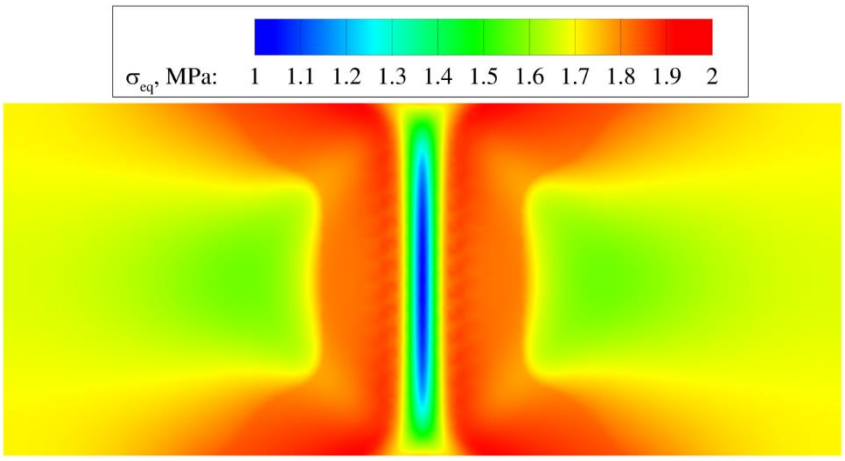


**Figure 3.11** Distribution of the equivalent stress $\sigma_{\mathrm{eq}}$ for homogeneous material at failure stage

The contour plots of the strain gradient component $\eta_{111}$ and the corresponding double stress component $\mu_{111}$ are shown in Figure 3.12 and Figure 3.13, respectively. As evident from Figure 3.12, the two symmetrically mirrored strain gradient bands are formed on the edges of the localization band displayed in Figure 3.9. In the narrow area in the middle of the localization band, where the strain $\varepsilon_{11}$ reaches its peak value, the strain gradient component $\eta_{111}$ changes the sign and it is equal or very close to zero. The double stress component $\mu_{111}$ in Figure 3.13 closely resembles the strain gradient component $\eta_{111}$, which is logical due to their direct connection through the second constitutive relation of the strain gradient continuum theory shown in (3.29).

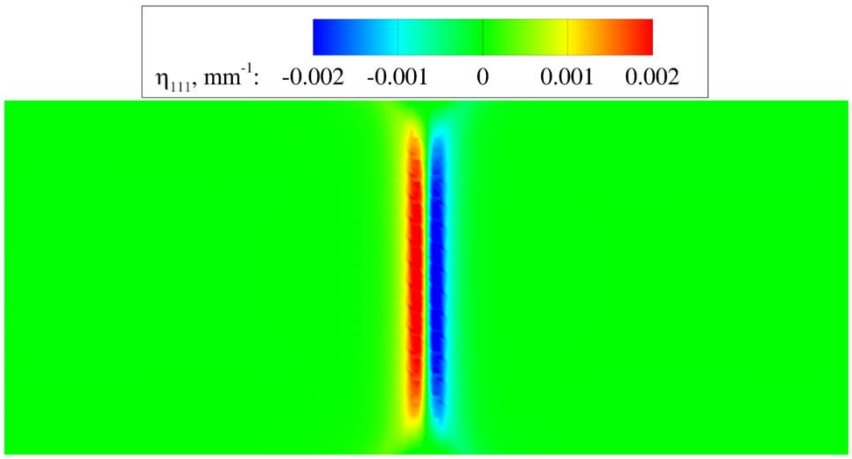


**Figure 3.12** Distribution of the strain gradient component $\eta_{111}$ for homogeneous material at failure stage

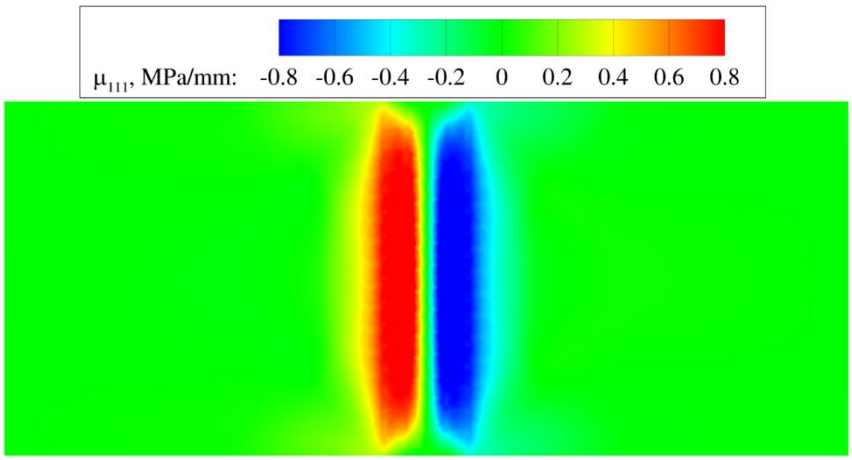


**Figure 3.13** Distribution of the double stress component $\mu_{111}$ for homogeneous material at failure stage

Deformed shape of the plate under tension with the distribution of the strain tensor component $\varepsilon_{11}$ is provided in Figure 3.14, which basically corresponds to the equivalent elastic strain $\varepsilon_{eq}$ due to the nature of the Mazars' definition (2.8) which takes into account only positive principal strains. As evident, a necking effect can be observed in the middle of the plate which is a consequence of the softening of the material in the localization area.

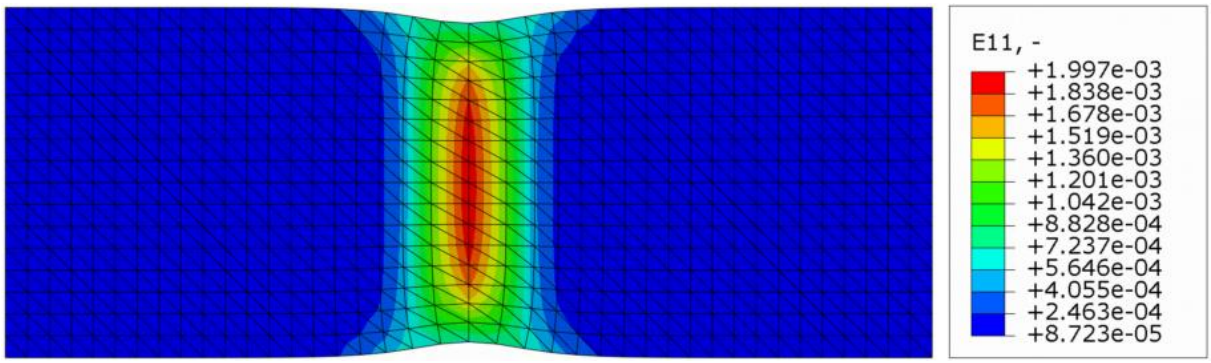


**Figure 3.14** Deformed shape with the distribution of strain component $\varepsilon_{11}$ for homogeneous material with the internal length scale $l$ = 1.5 mm

### 3.3.2 Plate with an imperfect zone subjected to tensile load, heterogeneous microstructure

The next step is the consideration of damage responses of the plate with heterogeneous microstructure. The materials used in the following calculations are described by the porous RVEs at microstructural level. Here all homogenized stiffness tensors according to the damage enhanced constitutive relations (3.28) and (3.29) are included in the computation. As stated earlier in the paper, the influence of the heterogeneous microstructure described by the RVE on the macrostructural anisotropic response is carried by the non-diagonal constitutive tensors of the fifth order, $\mathbf{C}_{\sigma\eta}$ and $\mathbf{C}_{\mu\varepsilon}$. The calculation of the constitutive tensors by employment of the homogenization process has been described in the previous section. The RVEs differ in the size, porosity and in the number, size and distribution of the holes. The material properties are the same as for the homogeneous plate. Firstly, a simple, academic example of an RVE, presented in Figure 3.15, is used to analyze the plate softening behavior. This RVE geometry is labelled as RVE_0 in the following consideration.

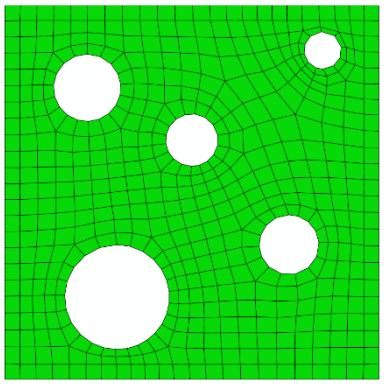

**Figure 3.15** RVE_0 described by the size $L$ = 5.2 mm ($l$ = 1.5 mm), average hole radius $r_{ave} = 1.118$ mm and porosity $e$ = 0.13

As it is the case with the plate where homogenous microstructure is observed, 1280 finite elements are used for the discretization in the following considerations of heterogeneous microstructures. The evolution of the equivalent elastic strain measure and the damage variable is depicted in Figure 3.16 and Figure 3.17 for different loading levels. The distributions of the same variables over the whole plate at the failure stage are depicted as contour plots in Figure 3.18 and Figure 3.19, respectively. A slight shift of the presented variables to the right can be seen from the given diagrams and contour plots when compared with the diagrams and contour plots concerning the homogeneous material, given in Figure 3.7 - Figure 3.10. Such behavior can be ascribed to the microscopic heterogeneity which is mathematically expressed by the relatively high values of the non-diagonal $\mathbf{C}_{\sigma\eta}$ and $\mathbf{C}_{\mu\varepsilon}$ matrices in the damage enhanced constitutive equations (3.28) and (3.29). As obvious, the differences between the damage distributions in Figure 3.10 and Figure 3.19 are just barely visible, but in order to retain the consistence of the whole work presented, the latter figure is shown too.

Additionally, if the softening analysis is performed by the constitutive tensors acquired for the RVE_0 rotated for 180°, the obtained results are symmetrically mirrored to the ones depicted in Figure 3.16 - Figure 3.19, as expected. Taking this into account, and knowing that microscopic samples in the form of RVE_0 are randomly distributed in various directions in the real material, an average contribution of all RVEs could lead to the isotropic macrostructural response. Thus, it is clear that the given academic RVE lacks the statistical representativeness, i.e. it is not representative in a global sense, for the whole material. From comparison of Figure 3.7 and Figure 3.16, it can be noted that the maximum equivalent strain value for the homogenous material is slightly higher than that for the heterogeneous material. Because the heterogeneous plate is more pliable in the whole domain due to the holes in the microstructure,

the bulk material outside of the localization zone permits higher equivalent strain in this particular area, leading to the slightly smaller equivalent strain in the middle of the plate when compared with the equivalent strain in the homogeneous plate.

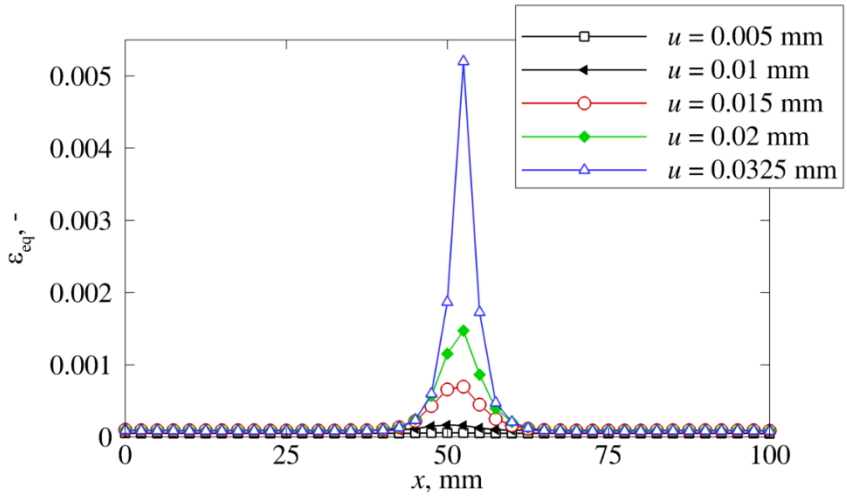


**Figure 3.16** Evolution of the equivalent elastic strain $\varepsilon_{eq}$ along horizontal central axis of the heterogeneous plate for different loading levels

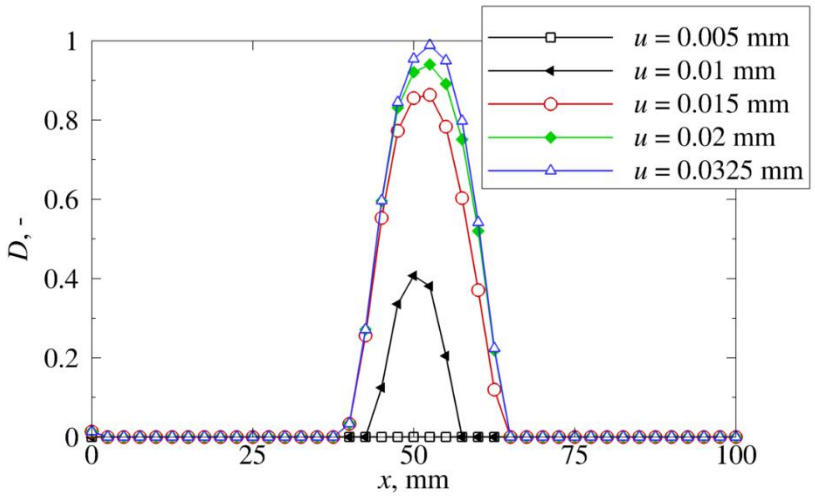


**Figure 3.17** Evolution of the damage variable *D* along horizontal central axis of the heterogeneous plate for different loading levels

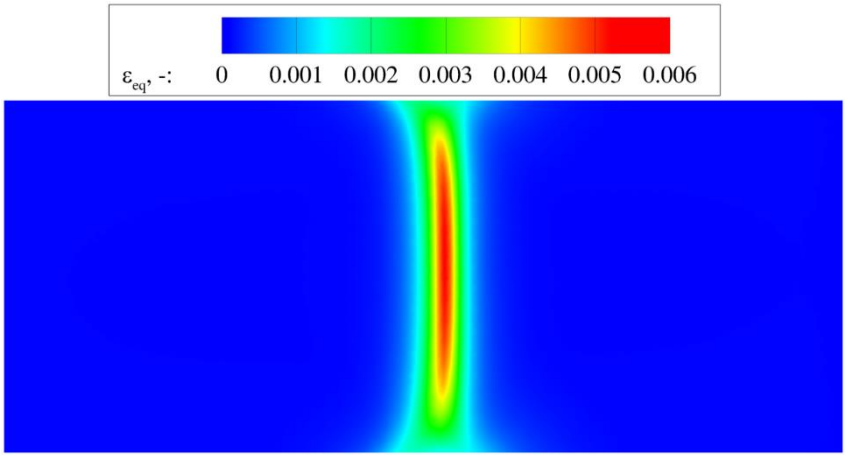


**Figure 3.18** Distribution of the equivalent elastic strain $\varepsilon_{eq}$ for heterogeneous material represented by RVE_0 at failure stage

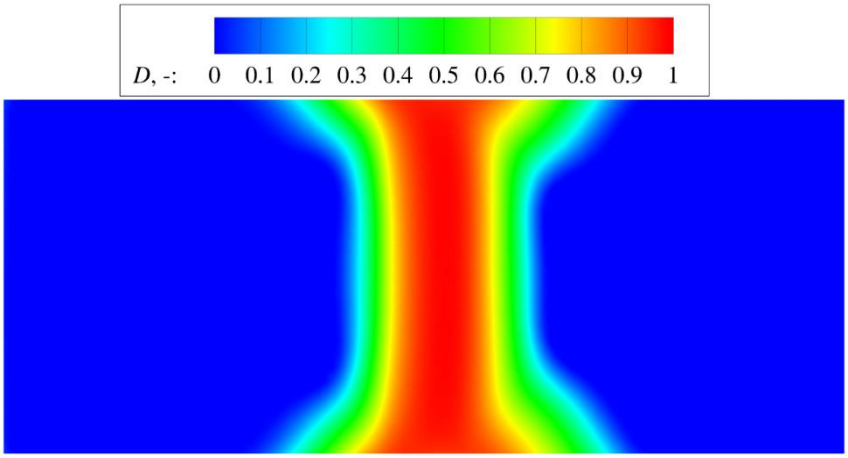


**Figure 3.19** Distribution of the damage *D* for heterogeneous material represented by RVE_0 at failure stage

As for the homogeneous material, the increase in the RVE size, which expresses the change in the size of microstructural interactions, leads to the expansion of the localization zone. Here the three different-sized RVEs of the same heterogeneity are considered, which is defined by the porosity of $e = 0.13$ and the average hole radius of $r_{ave} = 0.744$ mm, as shown in Figure 3.20. In Figure 3.21, the damage profiles for the three described heterogeneous RVEs are compared to the damage responses of the homogeneous material with the same nonlocal parameter *l*.

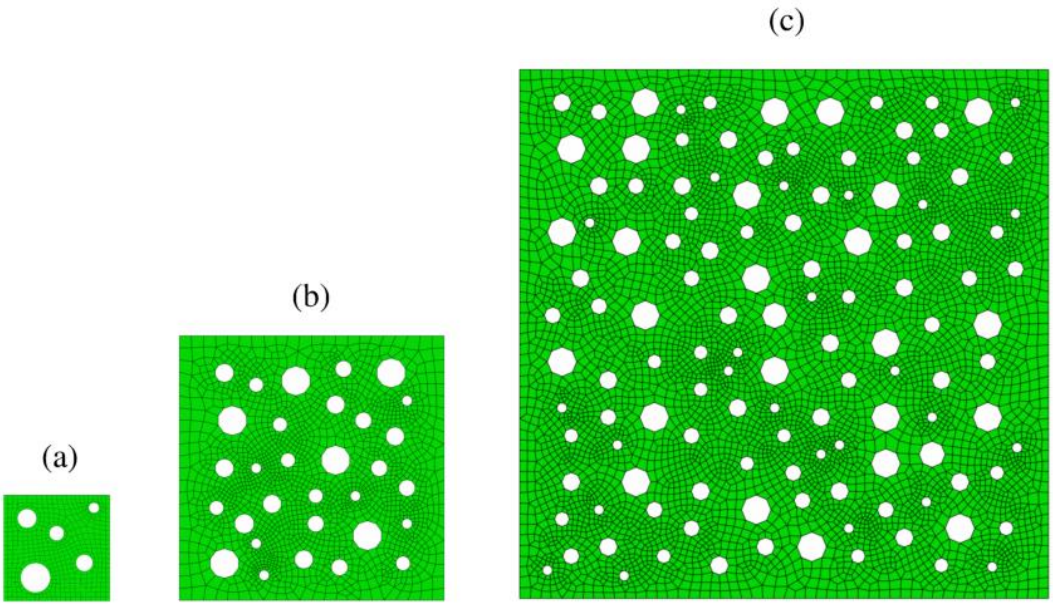


**Figure 3.20** Three different-sized samples of the same heterogeneous material: (a) RVE_1 with the size $L$ = 3 mm ($l$ = 0.87 mm), (b) RVE_2 with the size $L$ = 7.5 mm ($l$ = 2.16 mm) and (c) RVE_3 with the size $L$ = 15 mm ($l$ = 4.33 mm)

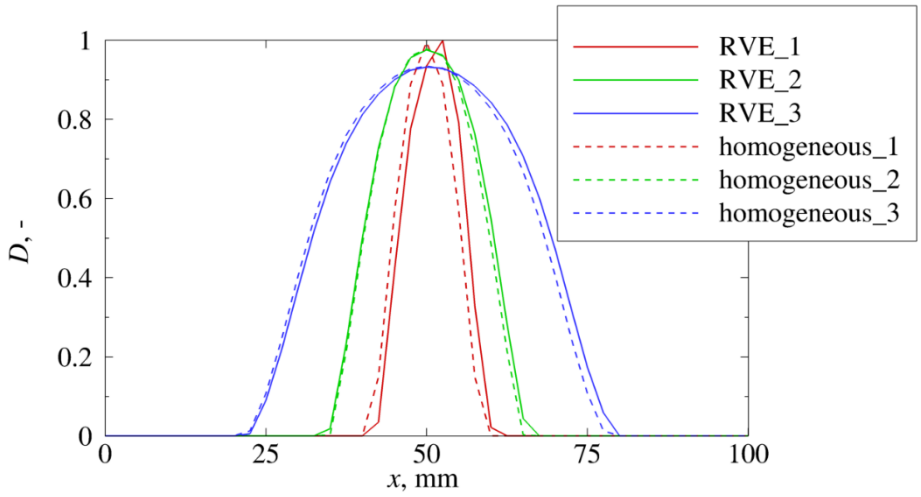


**Figure 3.21** Comparison of damage profiles along horizontal central axis of the plate for heterogeneous material represented by three different-sized RVEs and homogenous material of the corresponding internal length scales

As can be seen from Figure 3.21, a slight deviation from the damage profile of the corresponding homogenous material is shown for the damage profile obtained using the smallest RVE, while this difference is much less pronounced for the other two heterogeneous samples. This confirms that for statistically well-defined RVE, the damage distribution in qualitative sense should not deviate significantly from the damage distribution for the

homogeneous material of the same internal length scale. Next, an analysis employing the two different heterogeneous materials, defined by the RVEs of the same side length of $L = 6.9$ mm and porosity of $e = 0.13$, but different average hole radii, $r_{ave} = 1.5$ and 0.6 mm, is performed. Their damage responses are compared to the damage response of the homogeneous material defined by the same RVE size, as shown in Figure 3.22. As expected, the damage response of the heterogeneous material with larger average hole radius shows a notable shift when compared to the damage response of the corresponding homogeneous material. Obviously, this difference is much smaller for the heterogeneous material with smaller average hole radius. The aforementioned shift in the case of the heterogeneous material defined by the $r_{ave} = 1.5$ mm occurs as a consequence of the larger macrostructural anisotropic response.

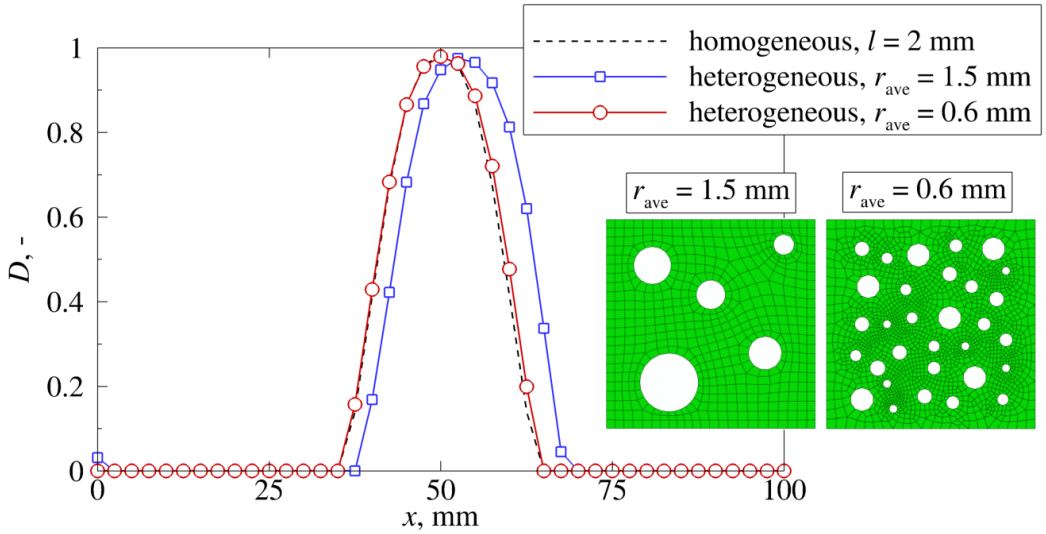


**Figure 3.22** Comparison of damage profiles along horizontal central axis of the plate for two heterogeneous materials of the same porosity and corresponding homogenous material

Finally, the RVE with the higher porosity *e*, labelled RVE_4 and depicted in Figure 3.23, is employed for the calculation of the stiffness matrices required for the softening analysis.

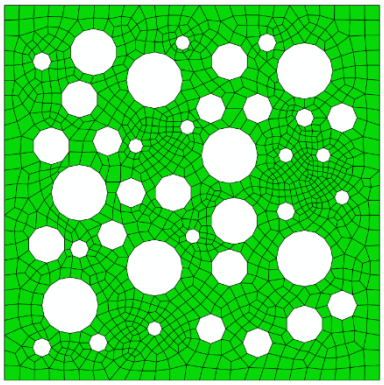

**Figure 3.23** RVE_4 described by the size $L$ = 1.73 mm ($l$ = 0.5 mm), average hole radius $r_{ave}$ = 0.075 mm and porosity $e$ = 0.27

Because of the higher RVE porosity, a significant decrease in the loading associated with the start of the softening process is expected, which is shown in the load-displacement diagram displayed in Figure 3.24. In the diagram, the reaction forces at the right end of the plate are plotted versus the imposed displacement for both the heterogeneous material defined by the RVE_4 and the corresponding homogeneous material. It can clearly be seen that reduced stiffness of the heterogeneous material causes the softening initiation at much lower load level than in the case of the homogeneous material.

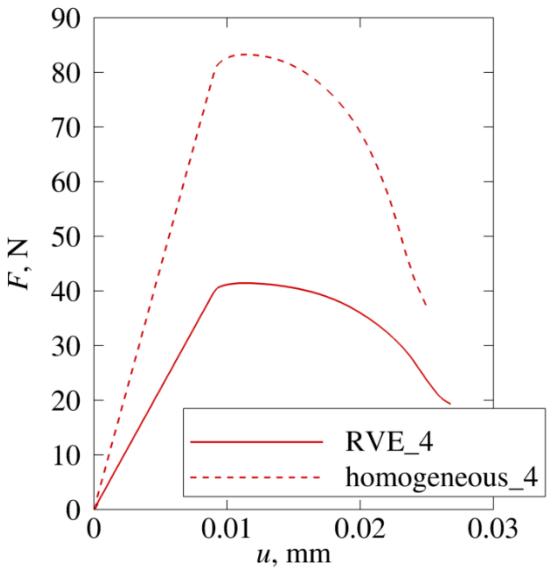


**Figure 3.24** Comparison of structural responses of the plate under tension for heterogeneous material represented by RVE_4 and homogeneous material of the same internal length scale

It is to note that the presented damage analysis of the heterogeneous structure is based on the microlevel homogenization procedure in order to compute the stiffness matrices, while the

softening response is modeled by the damage enhanced constitutive relations (3.28) and (3.29) at the macrolevel. Although the proposed analysis has its advantages due to the simplicity and low computational costs, it should be stressed that a true multiscale analysis should be performed to obtain more accurate results. Namely, a more accurate computation of the damage response of heterogeneous materials requires the application of the constitutive relations directly at the microlevel considering all material constituents in the RVE and, after a homogenization procedure, transfer of the state variables to the macrostructural level.

### 3.3.3 Shear band problem

The second example, where further capacities of the presented algorithm are shown, is a plate with an imperfect zone subjected to compressive load, presented in Figure 3.25a. Due to symmetry, only the upper half of the plate is discretized by the $C^1$ continuity triangular finite element employing appropriate boundary conditions, as depicted in Figure 3.25b. The compressive loading is applied using a direct displacement control, where the analysis stops at the vertical displacement of $v = 0.08$ mm. Firstly the homogeneous material is considered which is characterized by the Young's modulus $E = 20000$ N/mm$^2$ and the Poisson's ratio $\nu = 0.2$. For modeling of damage responses, the modified von Mises' equivalent elastic strain measure (2.10) together with the exponential softening law (2.7) is used, for which the parameters are set to: $\kappa_0 = 0.0001$, $\alpha = 0.99$ and $\beta = 300$. To induce localization, the reduced value of $\kappa_0 = 0.00005$ as a material imperfection is imposed on the small region of $h/10 \times h/10$ as shown in Fig. 24a. The material microstructural parameter is taken as $l = 2$ mm. Since both the symmetry plane and the loaded edge have to remain straight during the analysis, the boundary conditions for the straight edge are enforced there. Herein, the second-order derivatives of the displacement component in the normal direction, $u_{2,11}$ and $u_{2,22}$, together with the mixed derivatives, $u_{1,12}$ and $u_{2,12}$, are suppressed. The first-order derivatives associated with the shear deformation, $u_{1,2}$ and $u_{2,1}$, are also set to zero. As mentioned before, the indices 1 and 2 refer to the Cartesian coordinates *x* and *y*, respectively.

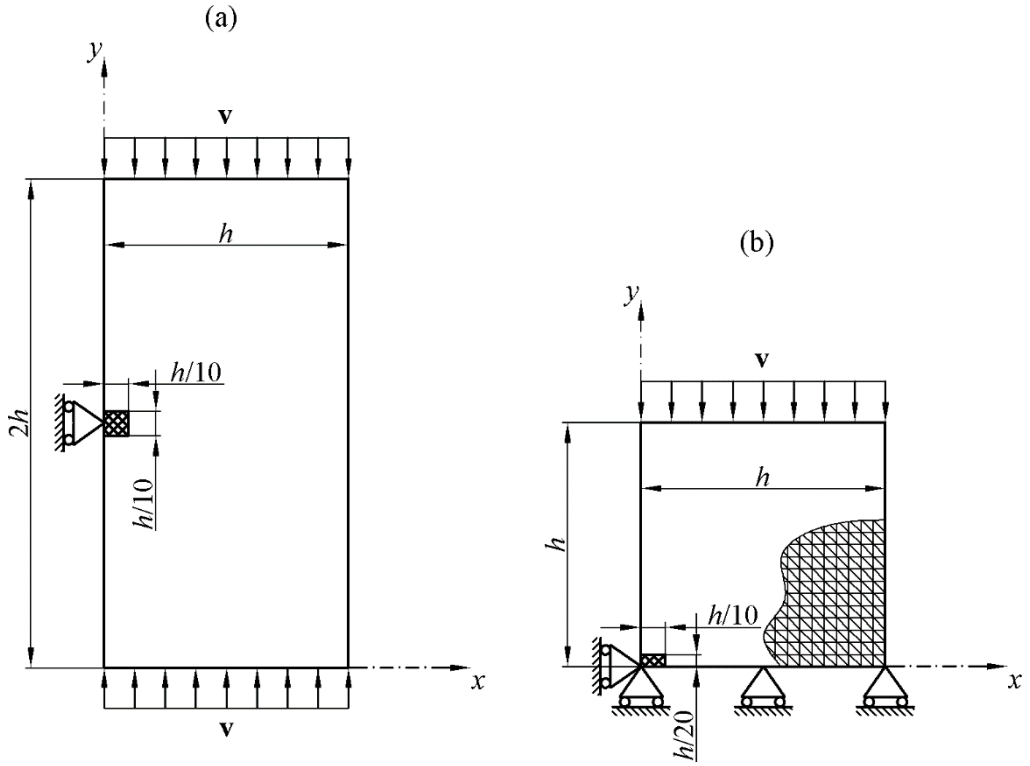


**Figure 3.25** (a) Geometry and boundary conditions of the plate with an imperfect zone subjected to compressive load ($h$ = 60 mm) and (b) computational model consisting of upper half of the plate and appropriate boundary conditions, with a depicted mesh detail

The same specimen has already been studied in [33] with the adoption of the damage model based on the conventional implicit gradient enhancement, resulting in the spurious damage growth along the bottom horizontal boundary with the rise of the deformation level, which is, according to [33, 34], a non-physical behavior. As discussed in [34], the conventional nonlocal models, being either integral or gradient, deal with a material softening employing a constant interaction domain throughout the entire loading history. This leads to the transfer of the energy from the damage process zone to a neighboring elastically unloading region, resulting in the smeared damage distribution within and beyond the shear band. The consequence of such unwanted behavior is the inability of a macrocrack formation.

The regularizing capabilities of the proposed formulation in terms of the elimination of the spurious damage growth are shown by plotting the distribution of the equivalent elastic strain in Figure 3.26 and the distribution of the damage in Figure 3.28, through several loading stages. The results are compared with the solutions obtained in [33], given in Figure 3.27 and Figure 3.29. For a better comparison of the given variables, the loading levels chosen for the contour plots are the same as shown in [33], where the aforementioned spurious damage growth is observed. It can clearly be seen, especially from Figure 3.28, that in the present contribution

the shear band starts to develop from the defect region and propagates towards the right edge of the plate model, as expected. In the formulation in [33] the shear band is developing along the horizontal boundary, which is stated as unrealistic. Furthermore, the contour plots obtained in the present formulation display that once the shear band reaches its final width, which is very early in the softening process, the localization of the deformation continues in its center until the shear fracture occurs. This is particularly visible in Figure 3.26 starting from the loading level at $v = 0.021$ mm. At lower displacements, a development of the localized deformation cannot be seen because the equivalent elastic strain is just slightly beyond the critical value of $\kappa_0$. This can be confirmed by the damage distribution images in Figure 3.28 and knowing that even for a very small equivalent elastic deformation the damage field rises to very high values in the case of exponential softening law. A similar shear band evolution accompanied with the strong localization and no spurious damage growth is also obtained in [34], where the localizing gradient damage model derived in the micromorphic framework is used. The similar realistic results are observed in the experimental investigations in [138] as well.

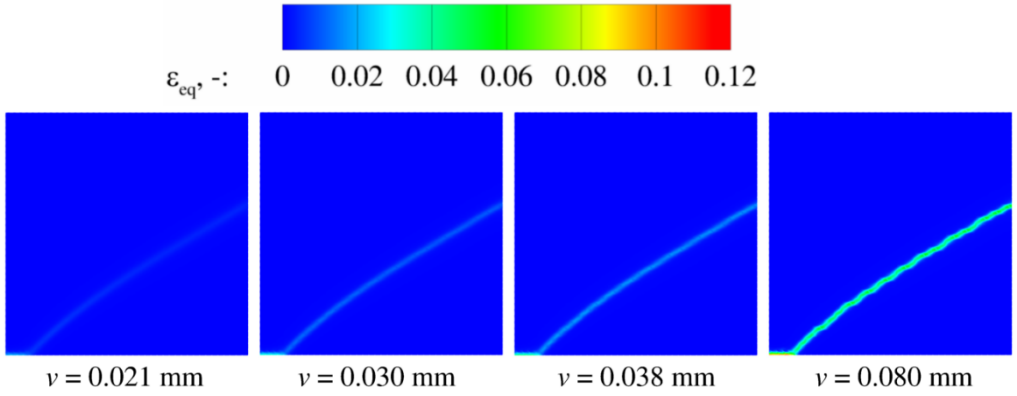


**Figure 3.26** Distribution of the equivalent elastic strain $\varepsilon_{eq}$ through several loading stages for homogeneous material

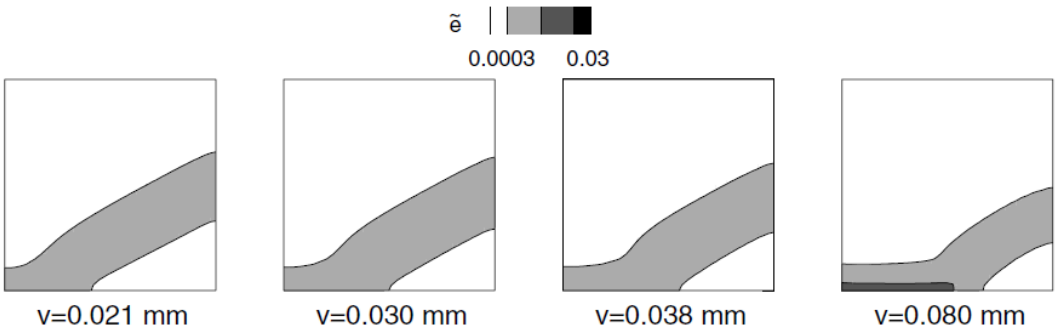


**Figure 3.27** Distribution of the equivalent elastic strain $\tilde{e}$ through several loading stages obtained by conventional implicit gradient formulation [33]

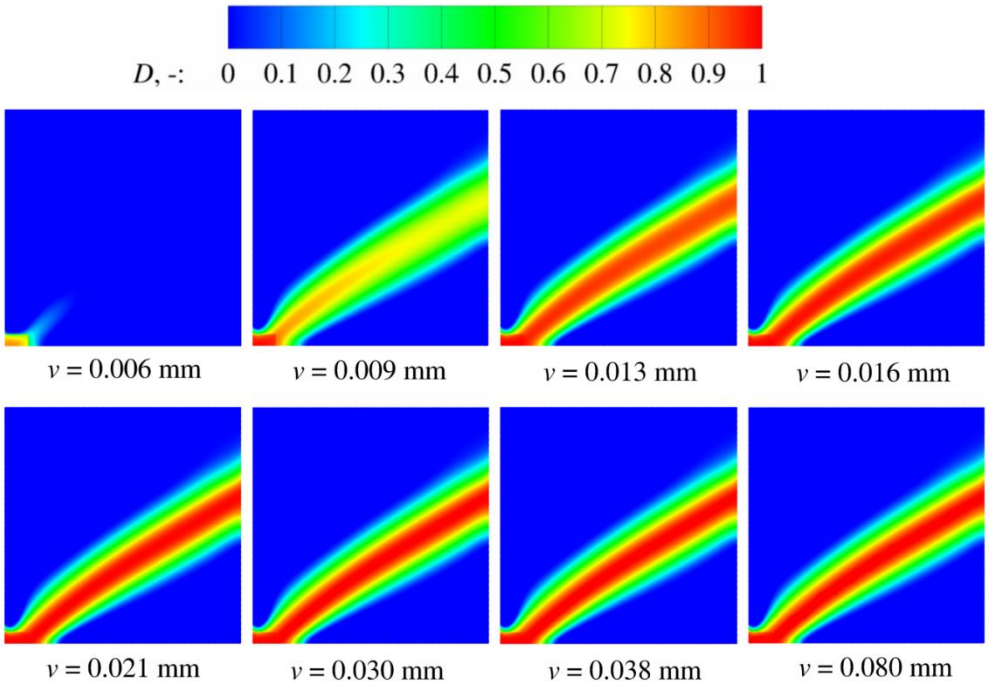


**Figure 3.28** Distribution of the damage *D* through several loading stages for homogeneous material

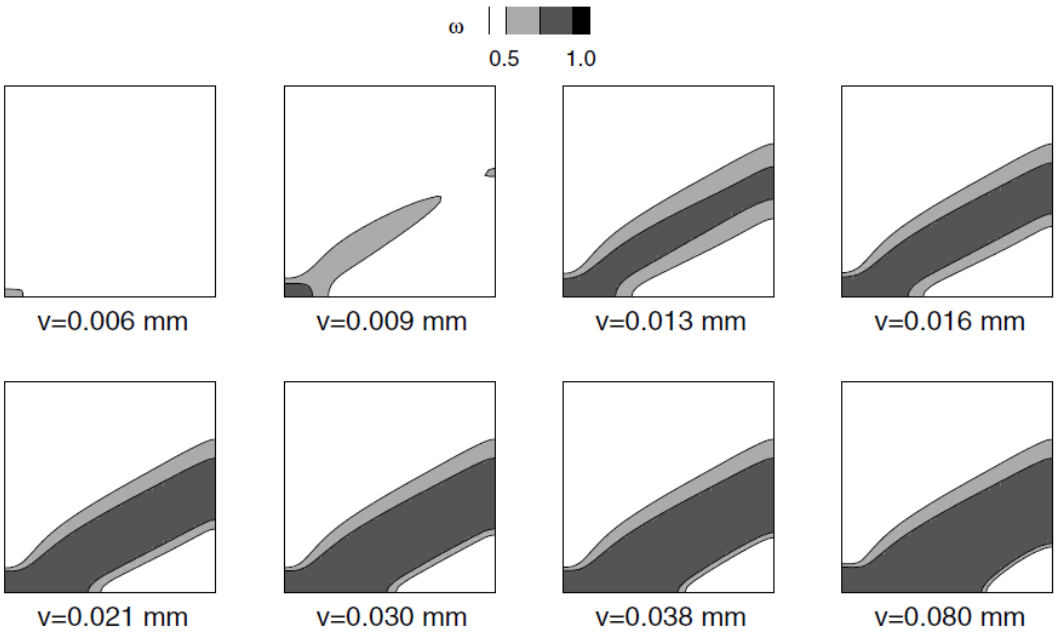


**Figure 3.29** Distribution of the damage $\omega$ through several loading stages obtained by conventional implicit gradient formulation [33]

To examine the mesh sensitivity, an additional finite element discretization of 800 triangular finite elements is considered, opposed to the 3200 elements used so far. Generally, the accurate results could also be obtained by using a non-uniform mesh and much smaller number of finite elements, as proven earlier in the paper. In this case, in order to maintain the mesh uniformity

for simplicity, such fine discretization is conditioned by a very small imperfect region. As portrayed in Figure 3.30, there are no differences in the damage responses. The damage profile is correctly captured for the two different discretization sizes.

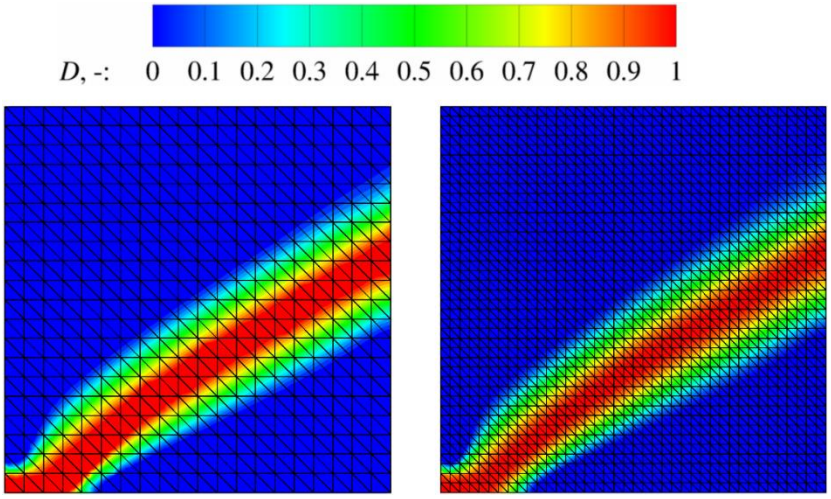


**Figure 3.30** Comparison of damage distribution *D* for homogeneous material for two different disretizations consisting of 800 (left) and 3200 (right) triangular finite elements

If a smaller internal length scale is used, the shear band decreases in the width, as expected, which is shown in Figure 3.31. In Figure 3.32 a deformed shape of the whole plate before complete failure is presented, where obvious shearing typical for mode-II loading case can be noted in the damage localization bands.

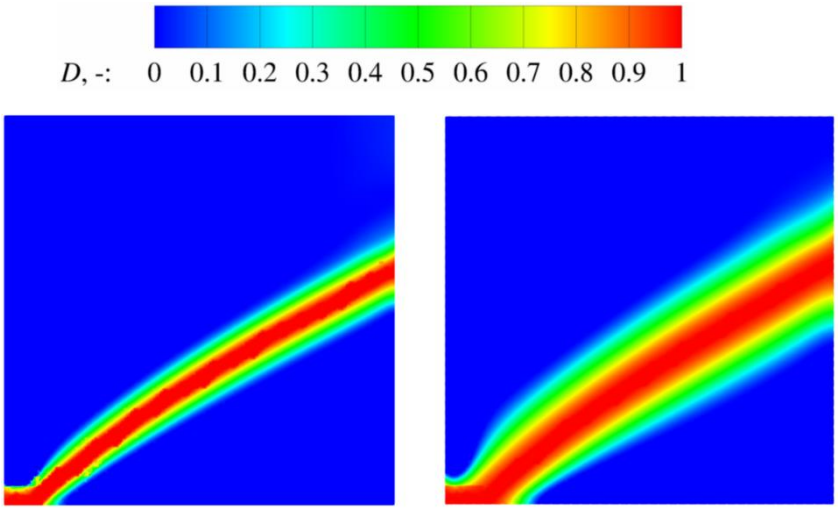


**Figure 3.31** Comparison of damage distribution *D* for homogeneous material defined with the internal length scales $l$ = 1 mm (left) and $l$ = 2 mm (right)

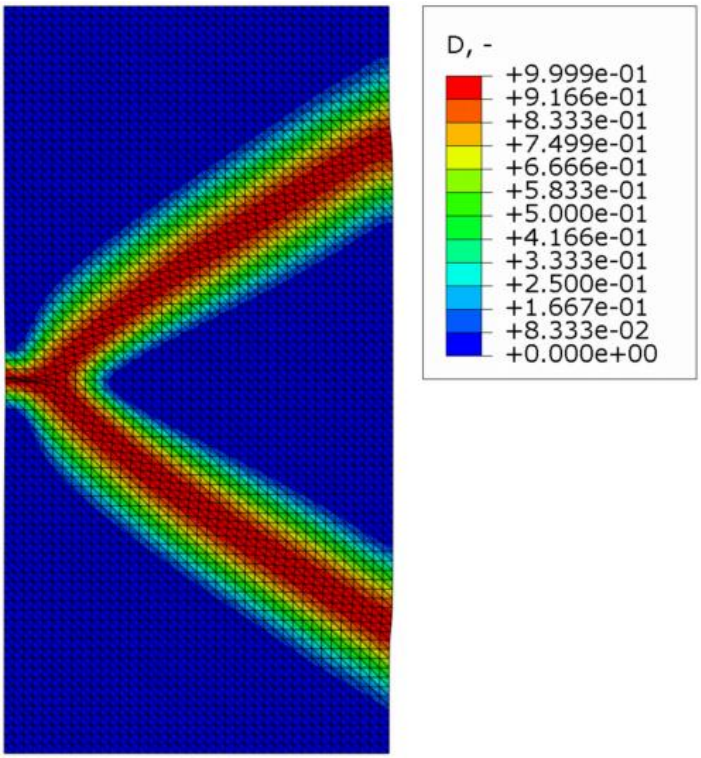


**Figure 3.32** Deformed shape with damage distribution *D* for homogeneous material with the internal length scale $l$ = 2 mm

Calculation of the damage response of the heterogeneous material in the context of the shear band problem is performed with an RVE qualitatively similar to the RVE_4 shown in Figure 3.23, but defined with the side length of $L = 6.9$ mm and the average hole radius $r_{\text{ave}} = 0.297$ mm. Here, the whole plate model depicted in Figure 3.25a has to be used due to the material anisotropy which is a consequence of the microstructural heterogeneity. The contour plots displaying the damage responses of the considered heterogeneous and homogeneous material show barely notable differences and are therefore not shown. This is a consequence of the employed damage growth law (2.7) which shows a very steep initial damage rise for a very narrow range of the history parameter, i.e. equivalent elastic strain, followed by a very slow asymptotic convergence to the value of one. On the other hand, difference in the contour plots can clearly be seen for the equivalent elastic strain on Figure 3.33, where a noticeable influence of the material heterogeneity can be observed. Obviously, the equivalent elastic strain does not evolve symmetrically, which eventually leads to one dominant shear band, indicating the formation of the macrocrack.

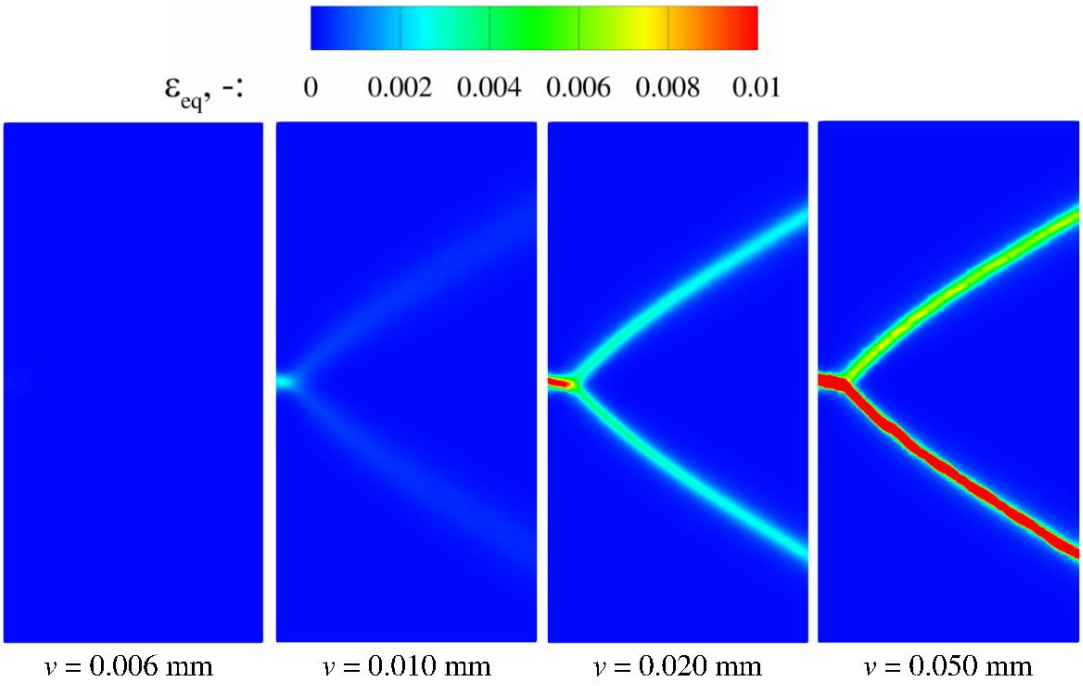


**Figure 3.33** Distribution of the equivalent elastic strain $\varepsilon_{eq}$ through several loading stages for heterogeneous material

From the load-displacement diagram depicted in Figure 3.34, a very pronounced decrease in the reaction force at the initial softening can be seen for the heterogeneous material when compared to the reaction force of the corresponding homogeneous material, similarly as in the previous numerical example.

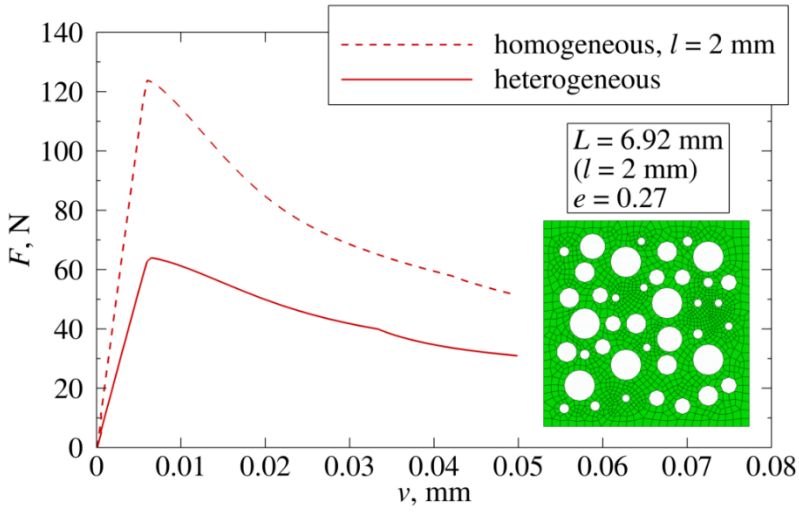


**Figure 3.34** Comparison of structural responses of the plate under compression for heterogeneous material and homogeneous material of the same internal length scale

### 3.3.4 Compact tension specimen

The next example deals with failure of the compact tension specimen with pre-existing crack which can be seen in Figure 3.35a, while the computational model due to the symmetry of the problem consists only of the upper half, as depicted in Figure 3.35b. The tensile loading is applied using a direct displacement control again, with the end of the analysis at the vertical displacement of $v = 0.35$ mm. Homogeneous material considered in this example is characterized by the Young's modulus $E = 1000$ N/mm$^2$ and the Poisson's ratio $\nu = 0.2$. Softening behavior is modeled by von Mises' equivalent elastic strain measure (2.9) with parameter $k = 10$, and by the exponential softening law (2.7), which utilizes following parameters: $\kappa_0 = 0.002$, $\alpha = 0.99$ and $\beta = 200$. Localization is here induced easily due to strong geometrical discontinuity represented by the tip of the pre-existing crack, which automatically induces high strain gradients in this area. In order to prevent confusion with the crack initiation, pre-existing crack will be referred to as notch in the continuation of the text. For the initial analysis the material microstructural parameter is taken as $l = 0.2h = 20$ mm. Conveniently for comparison, all values are set to be equal as in [34] where the same numerical example is analyzed by using the localizing gradient damage model. As in the previous example, both the symmetry plane and the loaded edge have to remain straight during the analysis, hence the same boundary conditions for the straight edge are enforced in those regions.

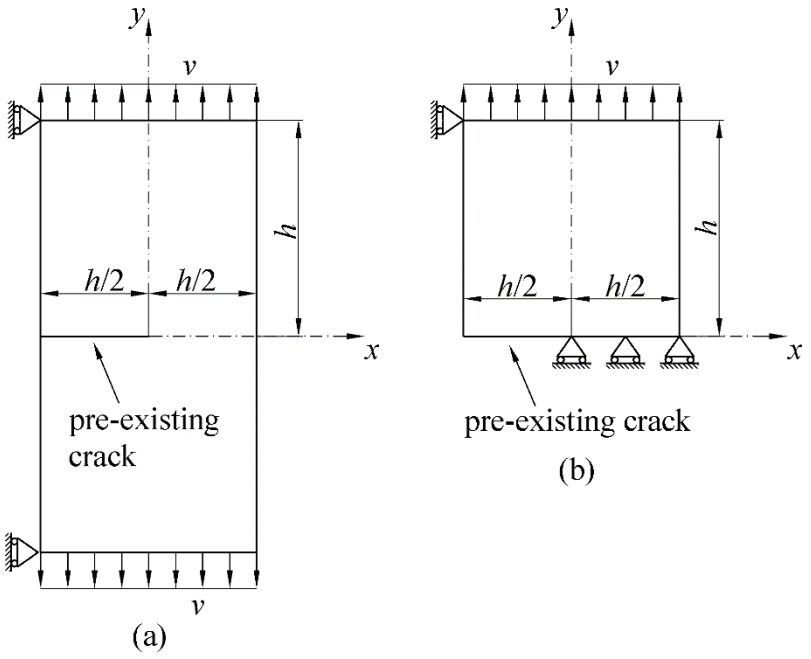


**Figure 3.35** (a) Geometry and boundary conditions of the compact tension specimen ($h$ = 100 mm) and (b) computational model consisting of upper half of the plate and appropriate boundary conditions

Considering the quasi-brittle failure analysis of notched specimens, it is concluded in [139] on the basis of the experimental evidence that cracks should propagate from the notch tip. Numerical analysis conducted in [33] on the same example presented here by employment of the conventional implicit gradient formulation indicates the incorrect initiation and subsequent propagation of the damage. It is observed that the nonlocal damage-driving variable is maximum at some distance away from the notch tip during the whole analysis, i.e. crack initiation is predicted inside the specimen, rather than at the notch tip, which can clearly be seen in Figure 3.36a. (i) and (ii) in Figure 3.36 represent two loading steps which refer to the onset of the softening and a stage where localization zone is fully formed, respectively. As explained in [34], due to constant interaction domain which extends to the region behind the notch tip, a smoothened damage field with a maximum value at a distance away from the notch tip is induced, followed by a further propagation inside the specimen. For the damage values near critical, this anomaly leads to the crack initiation away from the notch tip, which is not physically acceptable for quasi-brittle materials. Along with the wrong damage initiation and propagation along the notch line, spurious damage growth is also observed in [33, 34] leading to the final damage zones much larger than they should be in the reality, as it is shown in Figure 3.37. This nonphysical behavior is improved in [34] by introduction of the interaction function that decreases the nonlocal material response with progression of the damage. Although the spurious damage growth is in that way completely resolved and the propagation of the macroscopic crack correctly captured at the notch tip for the critical value of damage, shift of the maximum damage value at the initiation of the localization is still observed inside the specimen, as evident from Figure 3.36b.

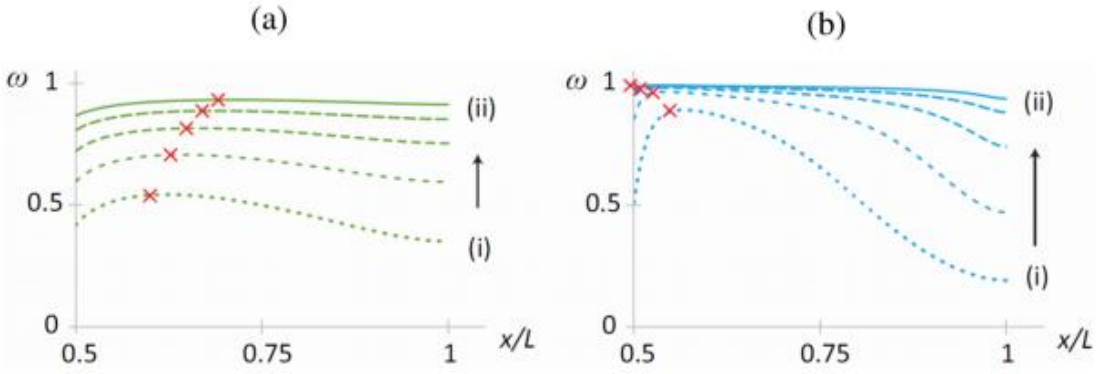


**Figure 3.36** Damage evolution ahead of the notch tip through several loading stages obtained by (a) conventional implicit gradient damage formulation and (b) localizing gradient damage model with decreasing interactions [34]

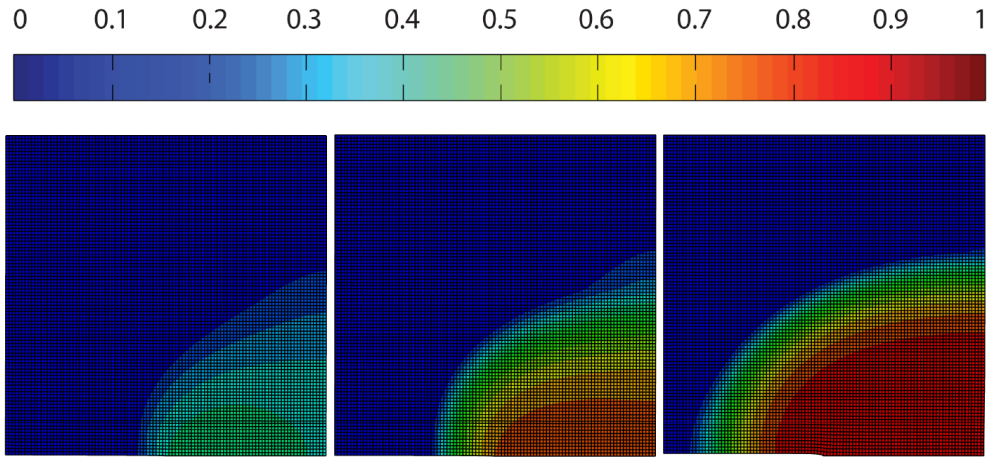


**Figure 3.37** Damage profiles at different loading stages obtained by conventional implicit gradient damage formulation [34]

However, when the strain gradient damage model described in the thesis here is applied, a complete regularization is achieved, i.e. spurious damage growth is eliminated along with the mesh sensitivity of the solutions, while the maximum values of the damage variable are located right at the notch tip from the start of the localization until the initiation of the macroscopic crack. Evolution of the damage ahead of the notch tip can be observed in Figure 3.38, damage distributions for two different discretizations are given in Figure 3.39, and damage profiles for two different internal length scales are shown in Figure 3.40. Finally, deformed shape of the whole compact tension specimen with the damage contour plot is provided in Figure 3.41, where a clear mode-I opening can be observed.

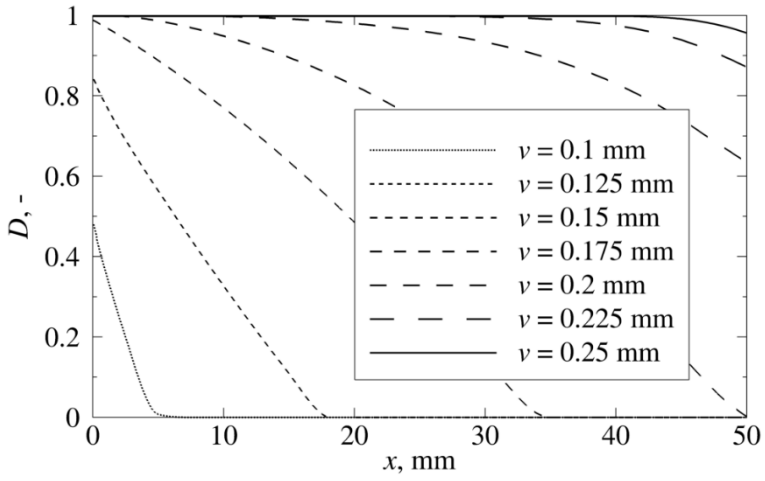


**Figure 3.38** Damage evolution ahead of the notch tip through several loading stages for homogeneous material

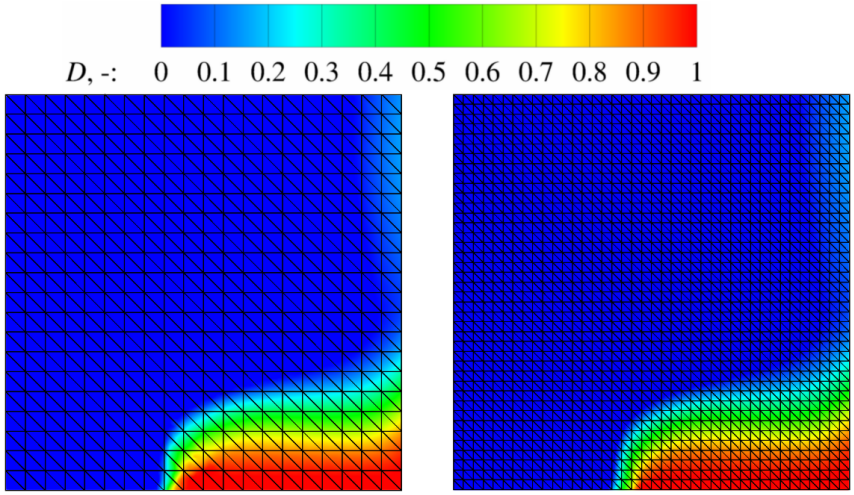


**Figure 3.39** Comparison of damage distribution *D* for homogeneous material for two different disretizations consisting of 800 (left) and 3200 (right) triangular finite elements

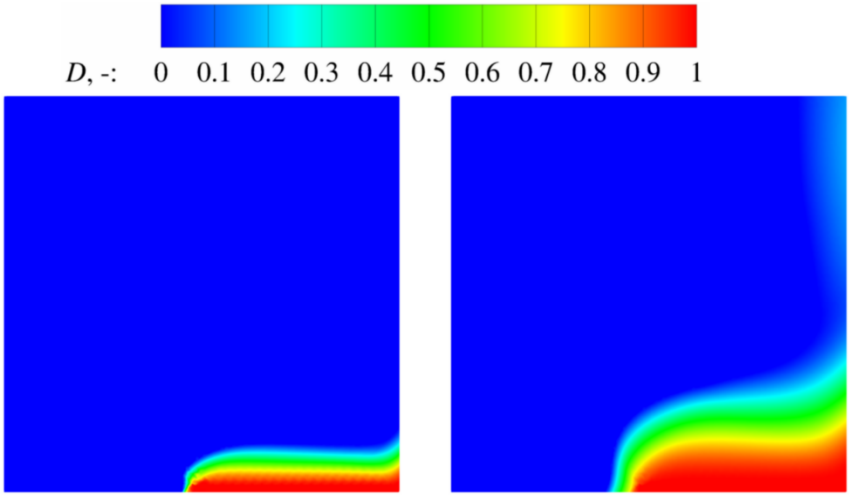


**Figure 3.40** Comparison of damage distribution *D* for homogeneous material defined with the internal length scales $l$ = 8 mm (left) and $l$ = 20 mm (right)

When it comes to the analysis of the material with the heterogeneous microstructure, distributions of the damage and equivalent elastic strain are qualitatively very similar to the distributions of the homogeneous material, presumably due to sharp geometrical discontinuity in form of the notch which strongly determines the course of the damage evolution. Difference can be seen in Figure 3.42, where the load-displacement curves of both homogeneous and heterogeneous material are plotted. In all the figures so far where structural responses are showed, namely Figure 3.24, Figure 3.34 and Figure 3.42, reactive forces do not drop to zero or values close to zero, but have a tendency to stabilize around some value and continue in a straight line, even when physically failure should occur. Stabilization of reaction forces

numerically occurs when the incremental change of damage (3.41) is close to zero or zero in all integration points of the model, i.e. when the formation of the localization zone is complete. A plausible explanation for the phenomenon that reaction forces are not even close to zero in the moment of stabilization might lie in the formulation of the constitutive relations shown in Table 3.3. It can be noticed there that damage variable is a function only of the strain tensor, i.e. of the first-order derivatives of displacement field, and as such evolves in the continuum governed by the constitutive model where also the second-order derivatives of displacements are relevant degrees of freedom. Unfortunately, since the model is relatively novel, there are no definitions of the damage variable dependent both on strain and strain gradient tensor available in the literature. Calibration of the damage growth laws and equivalent measures that account for both strain and strain gradients would certainly be an interesting topic for further research.

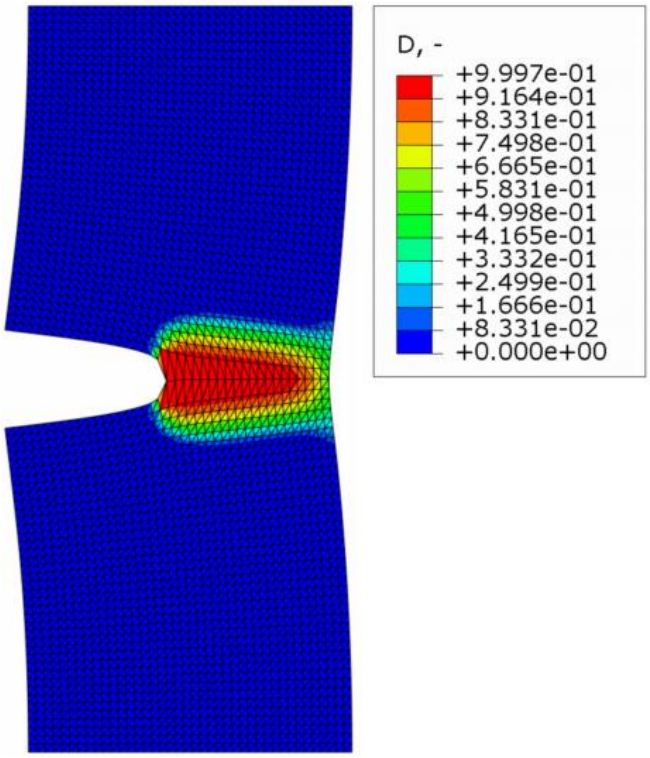


**Figure 3.41** Deformed shape with damage distribution $D$ for homogeneous material with the internal length scale $l$ = 8 mm

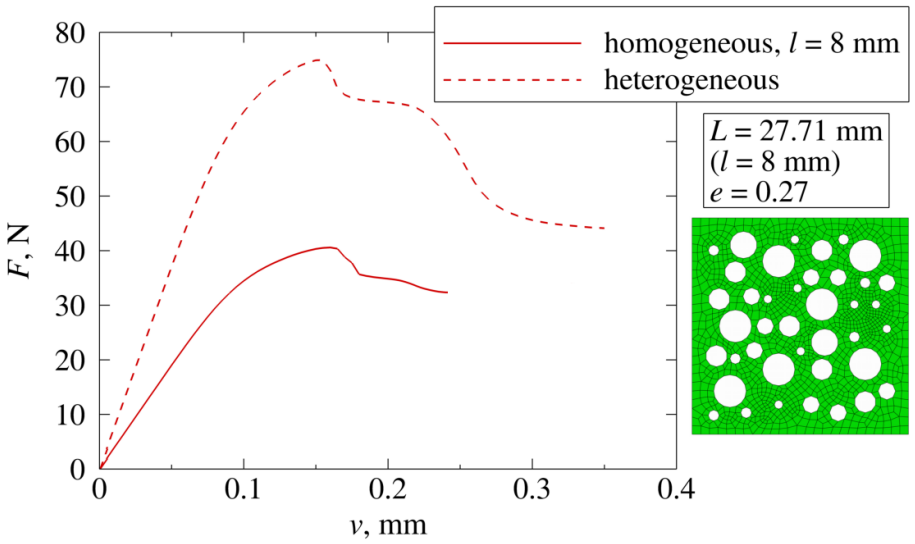


**Figure 3.42** Comparison of structural responses of the compact tension specimen for heterogeneous material and homogeneous material of the same internal length scale

### 3.3.5 Gear tooth damage

So far damage behavior of typical benchmark examples is presented in the thesis, for which the evolution of the localization zone is known apriori from the experimental observations. Here a practical engineering problem is analyzed in form of the spur gear with two different imperfections in the root of a tooth, a notch and a pre-existing crack, as can be seen in Figure 3.43a and Figure 3.43b. Such imperfections usually arise during the working regime due to wear or fatigue of the material, and represent the main stress concentrators from where the macrocrack would eventually start to propagate. Gear geometry and computational model are chosen according to [140], by employing the following geometrical characteristics of the gear: teeth number $z = 25$, module $m = 2$ mm, pressure angle $\alpha = 20°$, while tooth profile is taken as ISO53-A norm. Damage growth is observed for the loading case of highest point of single tooth contact (HPSTC), where loading is prescribed as a displacement normal to surface of the tooth of the involute gear. As explained in [141], HPSTC is one of the characteristic points in the analysis of gear kinematics, which represents a moment when two working gears are in contact only in this particular point and when all loading is taken over by a single tooth, causing the stresses in its the root to grow to maximum.

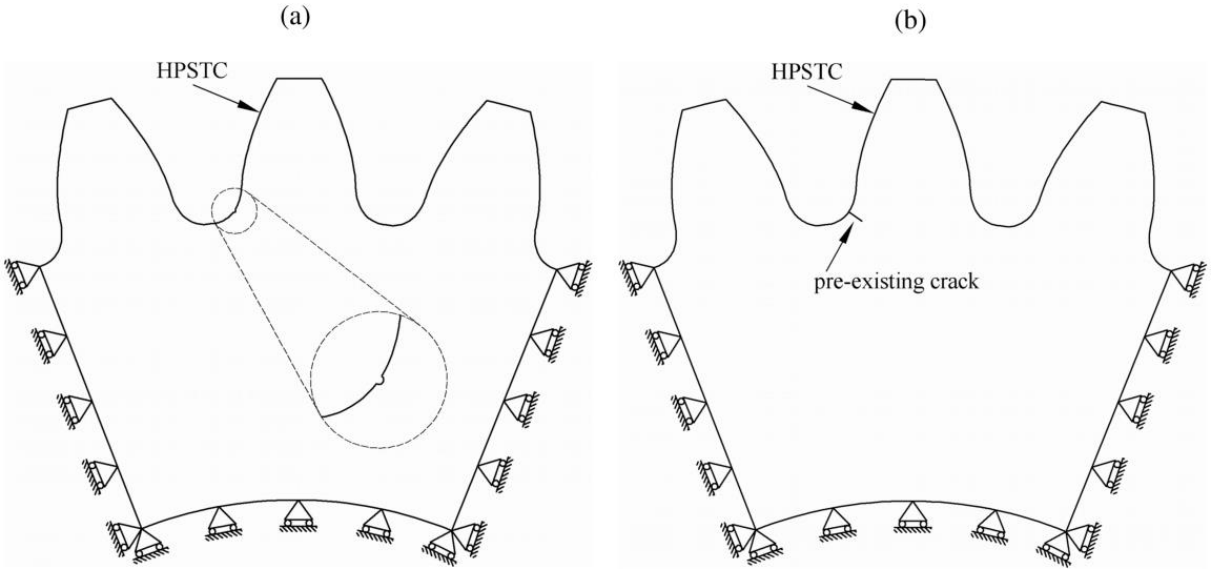


**Figure 3.43** Computational model of the spur gear with: (a) notch and (b) pre-existing crack

Problem observed here is slightly simplified compared to reality, primarily due to prescribed loading which should be taken as force-controlled. Unfortunately, the arc-length iterative method needed for the convergence of the numerical solutions in softening problems cannot be used in ABAQUS/Standard with presented $C^1$ continuity user-defined finite elements. Hence, displacement control which relies on Newton-Raphson iterative scheme is used instead, with the applied normal displacement of $\bar{u}_{\text{HPSTC}} = 0.065$ mm. When it comes to material behavior, usually in reality only the cemented and hardened teeth surface shows a quasi-brittle behavior, while the bulk of the gear is tougher and more ductile in order to endure eventual impacts. However, the main focus here is to show the applicability of the strain gradient damage algorithm to practical examples, so the material used in the numerical analysis here can be qualitatively classified as a quasi-brittle high-strength steel for the whole computational model. Homogeneous microstructure described by the internal length scale of $l = 0.15$ mm is employed, while the Young's modulus and Poisson's ratio are taken as $E = 2.1\times10^5$ N/mm$^2$ and $\nu = 0.3$, respectively. For the description of the damage growth, von Mises' equivalent strain (2.9) and parameter $k = 10$ together with the softening law (2.7) and parameters $\kappa_0 = 0.002$, $\alpha = 0.99$, $\beta = 200$ are utilized. In Figure 3.44 distribution of the equivalent elastic strain over the computational model of gear with the notch is presented, which is basically a contour plot of the macrocrack that would appear in such material and loading conditions. Deformed shape of the gear model with pre-existing crack showing the damage distribution is depicted in Figure 3.45. Due to geometrical discontinuity, discretization size in the middle tooth

has to be drastically decreased in order to preserve a proper finite element size and shape metrics. Similar results as depicted here are obtained in numerous experimental and numerical observations throughout the literature, e.g. in [142, 143].

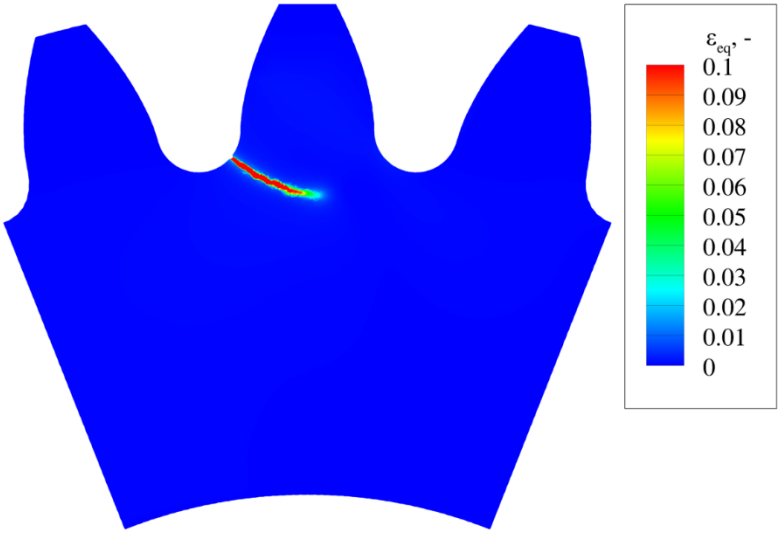


**Figure 3.44** Distribution of the equivalent elastic strain $\varepsilon_{eq}$ over the gear model with notch

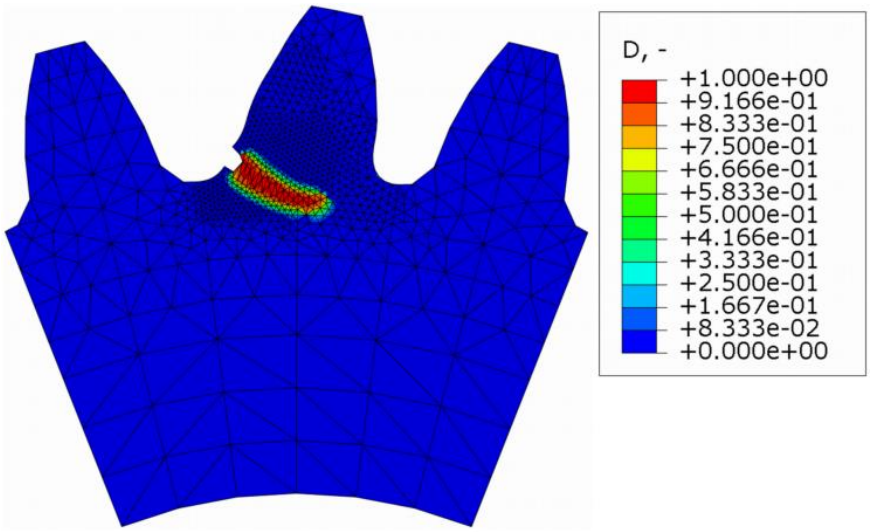


**Figure 3.45** Deformed shape with the distribution of the damage variable *D* over the gear model with pre-existing crack

### 3.3.6 Discussion

At the end of this chapter, it should be stressed that the presented damage model, as evident from all presented numerical examples, can successfully predict the strain localization. In addition, the damage growth without any spurious phenomena can be obtained, in contrast to

the formulation using the conventional implicit gradient-enhanced damage model which yields the non-physical damage response. It is believed that the main reason for this ability lies in the constitutive damage model based on the strain gradient theory, represented by (3.28) and (3.29), where the right-hand side of both equations are influenced by the same factor $(1-D)$ as a result of the damage growth. If this factor is observed as a reduction mechanism of the higher-order stiffness tensors $\mathbf{C}_{\sigma\eta}$, $\mathbf{C}_{\mu\varepsilon}$ and especially $\mathbf{C}_{\mu\eta}$, which are directly connected to the size of the microstructural interaction area, i.e. a nonlocal material behavior, it can be said that the intensity of the microstructural interactions decreases with the damage progression and that the material gradually loses the ability to behave nonlocally at a particular damaged point. Such material behavior is physically completely valid and motivated by the fact that a fracturing of quasi-brittle materials usually starts as a diffuse network of microcracks, represented by a large microstructural interaction domain, and ends with their localization into a macrocrack, characterized by almost non-existent intensity of microstructural interactions, as discussed in more detail in [34].

# 4 Multiscale analysis of quasi-brittle heterogeneous materials undergoing damage

In the previous chapter the one-scale algorithm for damage analysis of both microstructurally homogeneous and heterogeneous materials is derived. Constitutive behavior of the microstructure is thereat basically kept constant during the analysis, while the softening effect is added in the macrostructural analysis, emulating in this way a material degradation of the microstructure. Thus, a simplified damage analysis algorithm is presented which generally provides acceptable results in terms of prediction of the localization initiation and subsequent propagation. However, the impact of the actual evolution of the microstructure might change the outcome of the simulations or generally provide a more accurate solutions and therefore, it should be included in the analysis. As described earlier in the thesis, localization in quasi-brittle materials usually starts as a diffuse network of the microcracks, and in order to take into consideration their influence on the macrostructure, a damage analysis of the microstructure is necessary. Multiscale modeling in form of the computational homogenization is proven reliable when it comes to simulation of various problems where the materials with evolving microstructures are considered, e.g. in the large strain analysis of elasto-plastic materials [144], problems that include moderate strain localization [18], multi-physics or coupled problems [145], cohesive layers [146] and shell problems [147]. It is believed that these schemes are physically justified as long as the scale separation principle remains valid, i.e. if the RVEs are locally representative for the microstructure [63, 64]. Thereat, classical or conventional homogenization can be applied, which relies under the assumption that neighboring material behaves the same as the observed RVE. Specifically, second-order computational homogenization can be successfully applied in the problems where the localization of the deformation over the RVE can be described by the second-order distribution of displacements, but everything beyond cannot be consistently transferred to the macrolevel [63]. In the problems including intense localization in RVEs, where the distribution of displacements is usually higher than that of second-order, the scale separation is respected in the initial stage when strain localization is still mild, but eventually with the formation of sharp localization bands, the principle becomes violated. This means that microstructural material sample gradually evolves

from being representative (RVE) towards unique (MVE), and homogenization based on the classical principles should not be applied there, as stated in the literature [64, 69]. Several schemes are proposed so far for dealing with this problem, whereby the more successful ones are typically based on enriching the macroscale with a discontinuity when localization band is formed at the microscale [65-71]. Such way of thinking emanates from the standpoint that the failure of the MVE cannot be extrapolated to the neighboring material, resulting in the introduction of the equivalent discontinuity at the macroscale integration point, rather than continuous display of localized deformation.

In this thesis, a different approach is employed for the consideration of the microstructural damage. Due to nature of the macrocrack formation in the quasi-brittle materials which is preceded by a diffuse network of microcracks, an assumption can be made that the material locally has a similar structural response. In that sense, the formation of the sharp localization at the RVE level does not necessarily mean the initiation of the macrocrack, but a situation where the macrostructural material point loses its stiffness while still remaining a part of the continuum. By doing so, conventional homogenization can be applied to obtain the averaged stiffness behavior and stresses from the observed damaged RVE until the full formation of the localization zone, when the material conditions that account for the loss of material integrity have to be applied at the appropriate macrolevel integration point. During the evolution stage of the microstructural localization, homogenization process can be interpreted as the means for transformation of the localized deformation band and the rest of elastically unloading area of an RVE, into the equivalent RVE where damage is homogeneously dispersed, as represented graphically in Figure 4.1.

In the proposed approach, a multiscale algorithm based on the second-order computational homogenization developed in [73] is used for the transition of the variables between scales. Damage at the microstructural level is computed by the strain gradient damage algorithm derived in the previous chapter, which is here slightly altered to coincide with the modified case of Mindlin's form II strain energy density used at microlevel in [73]. In order to obtain regularized solutions, $C^1$ continuity is employed at the macrostructural level as well, where localization is induced by degraded stiffness resulting from the RVE homogenization. Although not verified in the thesis, it should be stressed here that the algorithm presented in this chapter presumably still suffers from the objectivity issues related to the size of the RVE [68, 72], and elimination of such behavior is certainly an interesting topic for the further research. In addition, the main idea here is to present the computational possibilities of the proposed algorithm, which, although not ideal, can provide a reasonable results by including

the analysis of evolving microstructure. In comparison with the algorithm derived in the previous chapter where virgin microstructural response is virtually degraded within the macrostructural constitutive model, the ability to analyze the evolving microstructure is by all means a step forward in the damage analysis of heterogeneous materials.

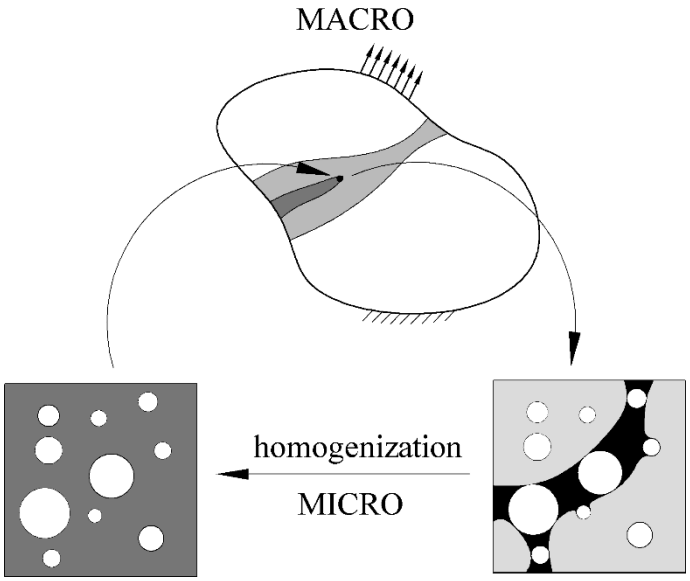


**Figure 4.1** Homogenization of the localized deformation

Formulation of the $C^1$ continuity finite element modified for the damage analysis at the microstructural level is given Section 4.1, where also its applicability is tested on an RVE for few different loading cases. In Section 4.2 basic relations of the scale transitions are derived for the $C^0$-$C^1$ macro-micro discretization, which is then utilized in a numerical example where the shortcomings of using the local approach at the macroscale are demonstrated. The same numerical example is then analyzed by using the $C^1$-$C^1$ macro-micro discretization in Section 4.3. Additionally, conditions indicating the full formation of the localization zone when macrostructural stiffness is lost in the appropriate integration point are given here. Numerical examples that include the damage analysis of both homogeneous and heterogeneous microstructures are given in Section 4.4.

# 4.1 $C^1$ continuity finite element for softening analysis of microstructure

## 4.1.1 Weak formulation

In the work presented in [73] both macro- and microlevel are discretized by $C^1$ continuity finite elements based on the modified case of Mindlin's form II strain energy density as described in [133-135]. In order to make use of this setting, a modification of the previously derived finite element based on strain gradient theory has to be made. A main distinction of the so called Aifantis theory of gradient elasticity is the employment of only the classical constitutive tensor $\mathbf{C}_{\sigma\varepsilon}$ and in the grouping of higher-order variables, which are expressed as the gradients of strain field in form of

$$\boldsymbol{\varepsilon}_{x_1} = \begin{bmatrix} \varepsilon_{11,1} \\ \varepsilon_{22,1} \\ 2\varepsilon_{12,1} \end{bmatrix} = \mathbf{B}_{\eta_1}\mathbf{v}, \tag{4.1}$$

$$\boldsymbol{\varepsilon}_{x_2} = \begin{bmatrix} \varepsilon_{11,2} \\ \varepsilon_{22,2} \\ 2\varepsilon_{12,2} \end{bmatrix} = \mathbf{B}_{\eta_2}\mathbf{v}. \tag{4.2}$$

$\mathbf{B}_{\eta_1}$ and $\mathbf{B}_{\eta_2}$ in the upper relations contain gradients of the interpolation matrix $\mathbf{B}$ with respect to Cartesian coordinates $x_1$ and $x_2$, respectively. Work conjugate of strain tensor is well-known Cauchy stress, given as

$$\boldsymbol{\sigma} = \mathbf{C}_{\sigma\varepsilon}\mathbf{B}_{\varepsilon}\mathbf{v}, \tag{4.3}$$

whereas the work conjugates of strain gradients are defined as

$$\boldsymbol{\mu}_{x_1} = \begin{bmatrix} \mu_{111} \\ \mu_{122} \\ \mu_{112} \end{bmatrix} = l^2\mathbf{C}_{\sigma\varepsilon}\mathbf{B}_{\eta_1}\mathbf{v}, \tag{4.4}$$

$$\boldsymbol{\mu}_{x_2} = \begin{bmatrix} \mu_{211} \\ \mu_{222} \\ \mu_{212} \end{bmatrix} = l^2\mathbf{C}_{\sigma\varepsilon}\mathbf{B}_{\eta_2}\mathbf{v}. \tag{4.5}$$

Obviously, constitutive model of the Aifantis theory is significantly simplified in comparison with the full strain gradient theory, since four constitutive tensors are now reduced to the internal length scale parameter and classical elasticity matrix, which can be easily determined experimentally. Principal of virtual work is now written in terms of strain gradient tensors $\boldsymbol{\varepsilon}_{x_1}$ and $\boldsymbol{\varepsilon}_{x_2}$ as

$$\int_A \left(\boldsymbol{\sigma} : \delta\boldsymbol{\varepsilon}\right) \mathrm{d}A + \int_A \left({}^3\boldsymbol{\mu}_{x_1} \vdots \delta\boldsymbol{\varepsilon}_{x_1}\right) \mathrm{d}A + \int_A \left({}^3\boldsymbol{\mu}_{x_2} \vdots \delta\boldsymbol{\varepsilon}_{x_2}\right) \mathrm{d}A = \int_s \left(\mathbf{t} \cdot \delta\mathbf{u}\right) \mathrm{d}s + \int_s \left[\mathbf{T} : \left(\nabla \otimes \delta\mathbf{u}\right)\right] \mathrm{d}s, \quad (4.6)$$

which after the application of discretization by (3.19), (4.1), (4.2) and $\mathbf{u} = \mathbf{N}\mathbf{v}$ adopts the following form

$$\begin{aligned} &\int_A \left[\boldsymbol{\sigma} : \left(\mathbf{B}_\varepsilon \delta\mathbf{v}\right)\right] \mathrm{d}A + \int_A \left[{}^3\boldsymbol{\mu}_{x_1} \vdots \left(\mathbf{B}_{\eta_1} \delta\mathbf{v}\right)\right] \mathrm{d}A + \int_A \left[{}^3\boldsymbol{\mu}_{x_2} \vdots \left(\mathbf{B}_{\eta_2} \delta\mathbf{v}\right)\right] \mathrm{d}A = \\ &\int_s \left[\mathbf{t} \cdot \left(\mathbf{N}\delta\mathbf{v}\right)\right] \mathrm{d}s + \int_s \left[\mathbf{T} : \left(\left(\nabla \otimes \mathbf{N}\right)\delta\mathbf{v}\right)\right] \mathrm{d}s. \end{aligned} \quad (4.7)$$

In order to linearize the problem (4.7), relations (3.21) and (3.22) along with the following updates for double stress tensors have to be utilized

$${}^3\boldsymbol{\mu}_{x_1} = {}^3\boldsymbol{\mu}_{x_1}^{i-1} + \Delta\,{}^3\boldsymbol{\mu}_{x_1}, \quad (4.8)$$

$${}^3\boldsymbol{\mu}_{x_2} = {}^3\boldsymbol{\mu}_{x_2}^{i-1} + \Delta\,{}^3\boldsymbol{\mu}_{x_2}, \quad (4.9)$$

resulting in the incremental principle of virtual work given in matrix notation as

$$\begin{aligned} &\int_A \mathbf{B}_\varepsilon^T \Delta\boldsymbol{\sigma}\, \mathrm{d}A + \int_A \mathbf{B}_{\eta_1}^T \Delta\boldsymbol{\mu}_{x_1}\, \mathrm{d}A + \int_A \mathbf{B}_{\eta_2}^T \Delta\boldsymbol{\mu}_{x_2}\, \mathrm{d}A = \\ &\int_s \left(\mathbf{N}^T\mathbf{t} + \operatorname{grad}\mathbf{N}^T\mathbf{T}\right) \mathrm{d}s - \int_A \left(\mathbf{B}_\varepsilon^T \boldsymbol{\sigma}^{i-1} + \mathbf{B}_\eta^T \boldsymbol{\mu}^{i-1}\right) \mathrm{d}A. \end{aligned} \quad (4.10)$$

Finally, linearized incremental constitutive relations are expressed by

$$\Delta\boldsymbol{\sigma} = {}^4\mathbf{C}_{\sigma\varepsilon} : \Delta\boldsymbol{\varepsilon}, \quad (4.11)$$

$$\Delta\,{}^3\boldsymbol{\mu}_{x_1} = l^2 \left({}^4\mathbf{C}_{\sigma\varepsilon} : \Delta\boldsymbol{\varepsilon}_{x_1}\right), \quad (4.12)$$

$$\Delta\,{}^3\boldsymbol{\mu}_{x_2} = l^2 \left({}^4\mathbf{C}_{\sigma\varepsilon} : \Delta\boldsymbol{\varepsilon}_{x_2}\right). \quad (4.13)$$

In the same manner as shown in Chapter 3, softening behavior is implemented by inserting the isotropic damage model (2.3) into the non-linearized constitutive model of Aifantis theory of gradient elasticity in the following way

$$\boldsymbol{\sigma} = \left(1 - D\right) {}^4\mathbf{C}_{\sigma\varepsilon} : \boldsymbol{\varepsilon}, \quad (4.14)$$

$$ {}^{3}\boldsymbol{\mu}_{x_1} = l^2\left[\left(1-D\right){}^{4}\mathbf{C}_{\sigma\varepsilon} : \boldsymbol{\varepsilon}_{x_1}\right], \tag{4.15} $$

$$ {}^{3}\boldsymbol{\mu}_{x_2} = l^2\left[\left(1-D\right){}^{4}\mathbf{C}_{\sigma\varepsilon} : \boldsymbol{\varepsilon}_{x_2}\right]. \tag{4.16} $$

Next, by employing (3.36), (3.38) and the updates of the strain gradient tensors

$$ \boldsymbol{\varepsilon}_{x_1} = \boldsymbol{\varepsilon}_{x_1}^{i-1} + \Delta\boldsymbol{\varepsilon}_{x_1}, \tag{4.17} $$

$$ \boldsymbol{\varepsilon}_{x_2} = \boldsymbol{\varepsilon}_{x_2}^{i-1} + \Delta\boldsymbol{\varepsilon}_{x_2}, \tag{4.18} $$

constitutive damage model based on Aifantis theory of gradient elasticity is obtained as

$$ \Delta\boldsymbol{\sigma} = \left(1-D^{i-1}\right)\mathbf{C}_{\sigma\varepsilon}\Delta\boldsymbol{\varepsilon} - \mathbf{C}_{\sigma\varepsilon}\boldsymbol{\varepsilon}^{i-1}\Delta D, \tag{4.19} $$

$$ \Delta\boldsymbol{\mu}_{x_1} = l^2\left(1-D^{i-1}\right)\mathbf{C}_{\sigma\varepsilon}\Delta\boldsymbol{\varepsilon}_{x_1} - l^2\mathbf{C}_{\sigma\varepsilon}\boldsymbol{\varepsilon}_{x_1}^{i-1}\Delta D, \tag{4.20} $$

$$ \Delta\boldsymbol{\mu}_{x_2} = l^2\left(1-D^{i-1}\right)\mathbf{C}_{\sigma\varepsilon}\Delta\boldsymbol{\varepsilon}_{x_2} - l^2\mathbf{C}_{\sigma\varepsilon}\boldsymbol{\varepsilon}_{x_2}^{i-1}\Delta D, \tag{4.21} $$

where the term $\Delta D$ is approximated by (3.41). Implementation of constitutive relations (4.19) - (4.21) into the linearized and discretized principle of virtual work (4.10) leads to the finite element equation

$$ \left(\mathbf{K}_{\sigma} + \mathbf{K}_{\mu_{x_1}} + \mathbf{K}_{\mu_{x_2}}\right)\Delta\mathbf{v} = \mathbf{F}_{\mathrm{e}} - \mathbf{F}_{\mathrm{i}}, \tag{4.22} $$

with the particular element stiffness matrices defined as

$$ \mathbf{K}_{\sigma} = \int_{A}\left(\mathbf{B}_{\varepsilon}\right)^{T}\left[\left(1-D\right)^{i-1}\mathbf{C}_{\sigma\varepsilon}\mathbf{B}_{\varepsilon} - \mathbf{C}_{\sigma\varepsilon}\boldsymbol{\varepsilon}^{i-1}\left(\frac{\mathrm{d}D}{\mathrm{d}\boldsymbol{\varepsilon}}\right)^{i-1}\mathbf{B}_{\varepsilon}\right]\mathrm{d}A, \tag{4.23} $$

$$ \mathbf{K}_{\mu_{x_1}} = l^2\int_{A}\left(\mathbf{B}_{x_1}\right)^{T}\left[\left(1-D\right)^{i-1}\mathbf{C}_{\sigma\varepsilon}\mathbf{B}_{\eta_1} - \mathbf{C}_{\sigma\varepsilon}\boldsymbol{\varepsilon}_{x_1}{}^{i-1}\left(\frac{\mathrm{d}D}{\mathrm{d}\boldsymbol{\varepsilon}}\right)^{i-1}\mathbf{B}_{\varepsilon}\right]\mathrm{d}A, \tag{4.24} $$

$$ \mathbf{K}_{\mu_{x_2}} = l^2\int_{A}\left(\mathbf{B}_{x_2}\right)^{T}\left[\left(1-D\right)^{i-1}\mathbf{C}_{\sigma\varepsilon}\mathbf{B}_{\eta_2} - \mathbf{C}_{\sigma\varepsilon}\boldsymbol{\varepsilon}_{x_2}{}^{i-1}\left(\frac{\mathrm{d}D}{\mathrm{d}\boldsymbol{\varepsilon}}\right)^{i-1}\mathbf{B}_{\varepsilon}\right]\mathrm{d}A, \tag{4.25} $$

and the external and internal forces $\mathbf{F}_{\mathrm{e}}$ and $\mathbf{F}_{\mathrm{i}}$ described by the first and second term on the right-hand side of (4.10), respectively.

### 4.1.2 Numerical test

Applicability of the finite element for softening analysis derived in previous section is tested on an RVE representing a high-strength porous steel of the side length of 0.5 mm, depicted in

Figure 4.2. In order to examine the damage response, three elementary loading cases are applied on the RVE, namely tensile, compressive and shear. Straight edges are enforced both at left and right RVE side by suppressing the following degrees of freedom: the second-order derivatives of the displacement component in the normal direction $u_{1,11}$ and $u_{1,22}$, mixed derivatives $u_{1,12}$ and $u_{2,12}$, and the first-order derivatives associated with the shear deformation $u_{1,2}$ and $u_{2,1}$. The matrix material is considered homogeneous with the elastic behavior described by Young's modulus $E = 2.1\times10^5$ N/mm$^2$ and Poisson ratio $\nu = 0.3$, while the microstructural nonlocal behavior is described by the internal length scale parameter $l = 0.01$ mm. For the description of the damage evolution von Mises' equivalent strain (2.9) in combination with parameter $k = 10$ is employed, along with the softening law (2.7) and parameters $\kappa_0 = 0.0002$, $\alpha = 0.99$, $\beta = 200$. The same absolute displacement $|u| = |v| = 0.002$ mm is applied on the appropriate loading edges. Due to parameter *k* material is ten times more sensitive to tensile than to compressive strain, which causes the tensile loaded RVE to fail in much earlier stage. Computational models and deformed shapes of the RVEs with damage contour plots observed in the failure stages for tensile, compressive and shear loading case are given in Figure 4.3, Figure 4.4 and Figure 4.5, respectively.

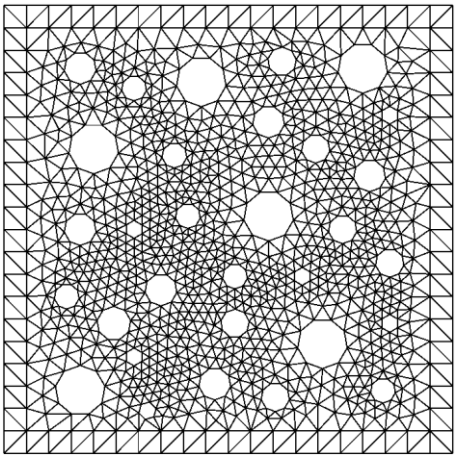

**Figure 4.2** RVE of the side length of 0.5 mm discretized by 2205 $C^1$ triangular finite elements

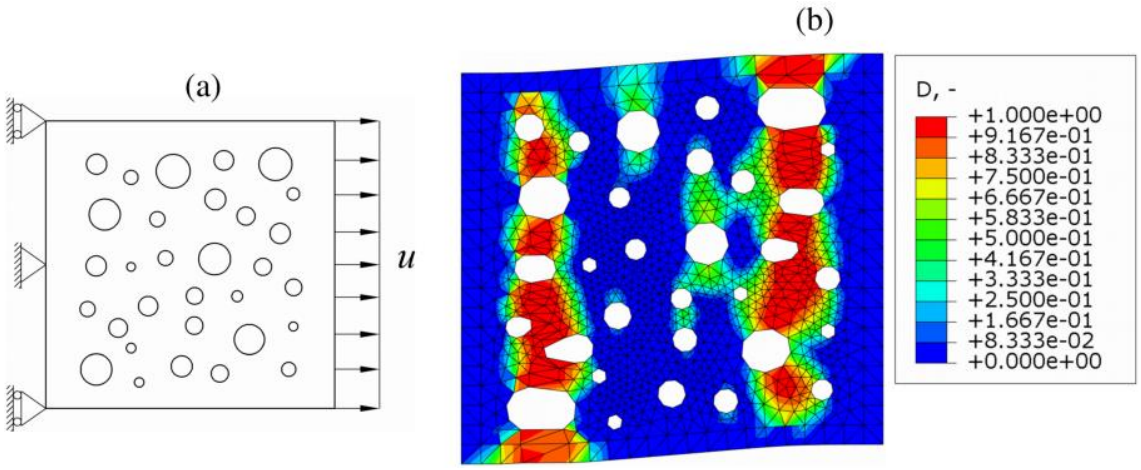


**Figure 4.3** Tensile loading case: (a) computational model and (b) deformed shape with distribution of damage $D$ in failure stage

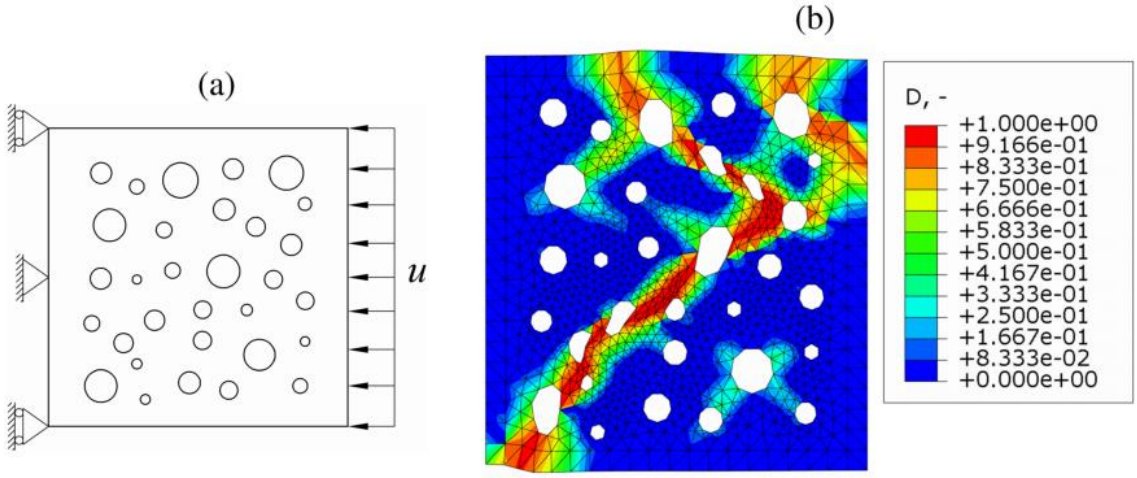


**Figure 4.4** Compressive loading case: (a) computational model and (b) deformed shape with distribution of damage $D$ in failure stage

Load-displacement diagrams for all three loading cases are depicted in Figure 4.6. Right vertical axis is introduced for the compressive structural response, where much higher values of reaction forces are reached due to postponed initiation of damage. This is a consequence of the utilization of parameter $k = 10$ in modified von Mises' equivalent strain definition (2.9), causing the elastic equivalent strain in compressive loading case to increase with the ten times slower rate compared to tensile loading case.

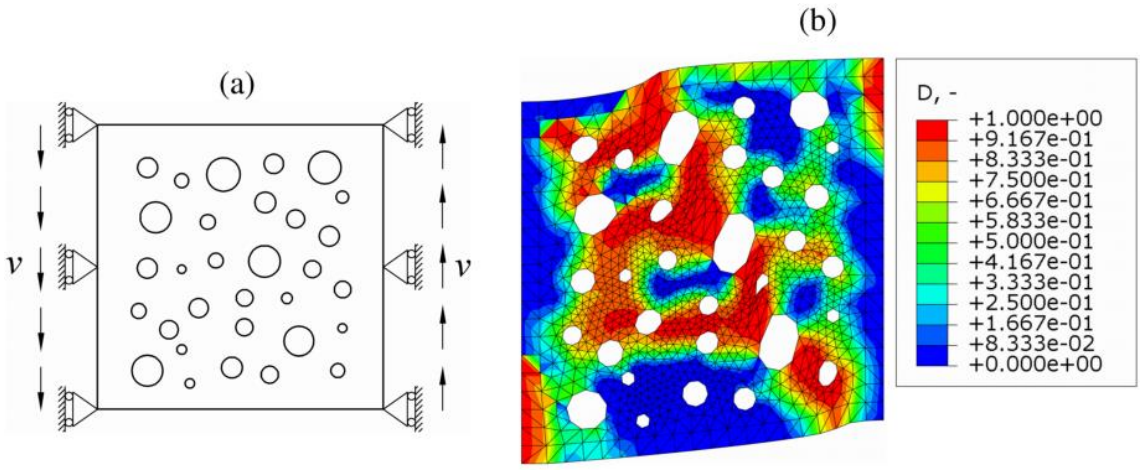


**Figure 4.5** Shear loading case: (a) computational model and (b) deformed shape with distribution of damage $D$ in failure stage

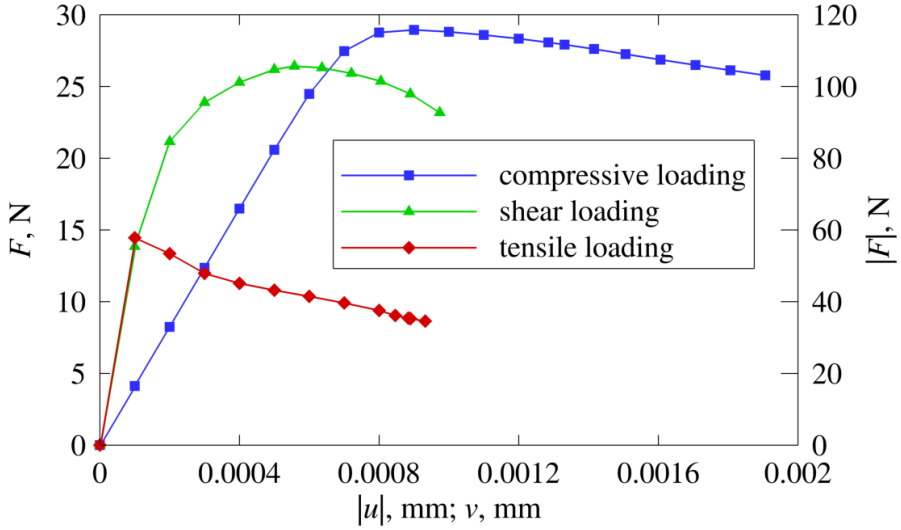


**Figure 4.6** Structural responses for three different RVE loading cases

As evident from the presented figures, derived finite element is capable of capturing the localization of the deformation over the RVE for different loading situations. In order to assess the influence of different internal length scales, an additional analysis is made with a tensile loading case on the RVE with $l = 0.02$ mm. The structural responses for both internal length scales are shown in Figure 4.7. It can be concluded that smaller nonlocal parameter results in more brittle softening, which is in accordance with the nonlocal theory and numerical results obtained in Chapter 3. Evolution of the damage localization zone for several different loading steps for internal length scale $l = 0.01$ mm is given in Figure 4.8, and for $l = 0.02$ mm in Figure 4.9.

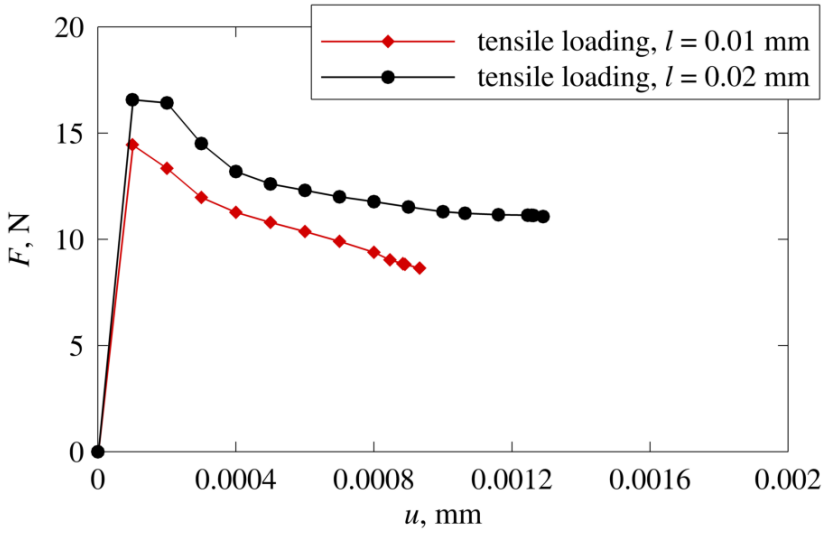


**Figure 4.7** Structural responses for two tensile RVE loading cases with different internal length scale parameters

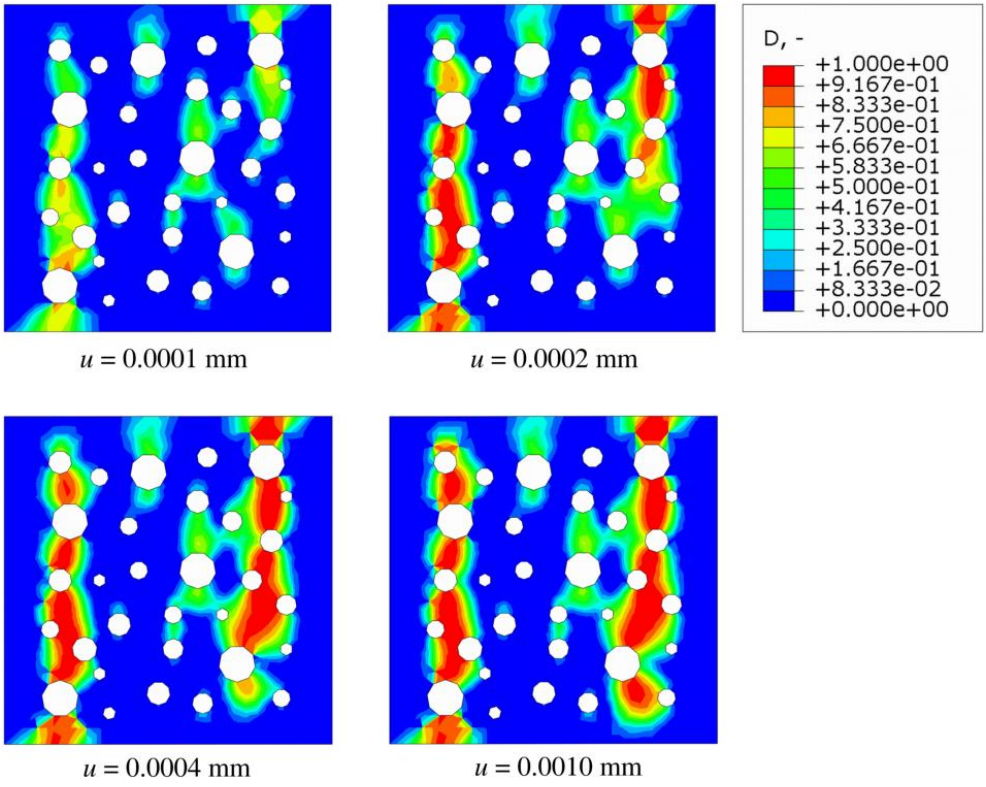


**Figure 4.8** Distribution of the damage $D$ through several loading stages for internal length scale parameter $l$ = 0.01 mm

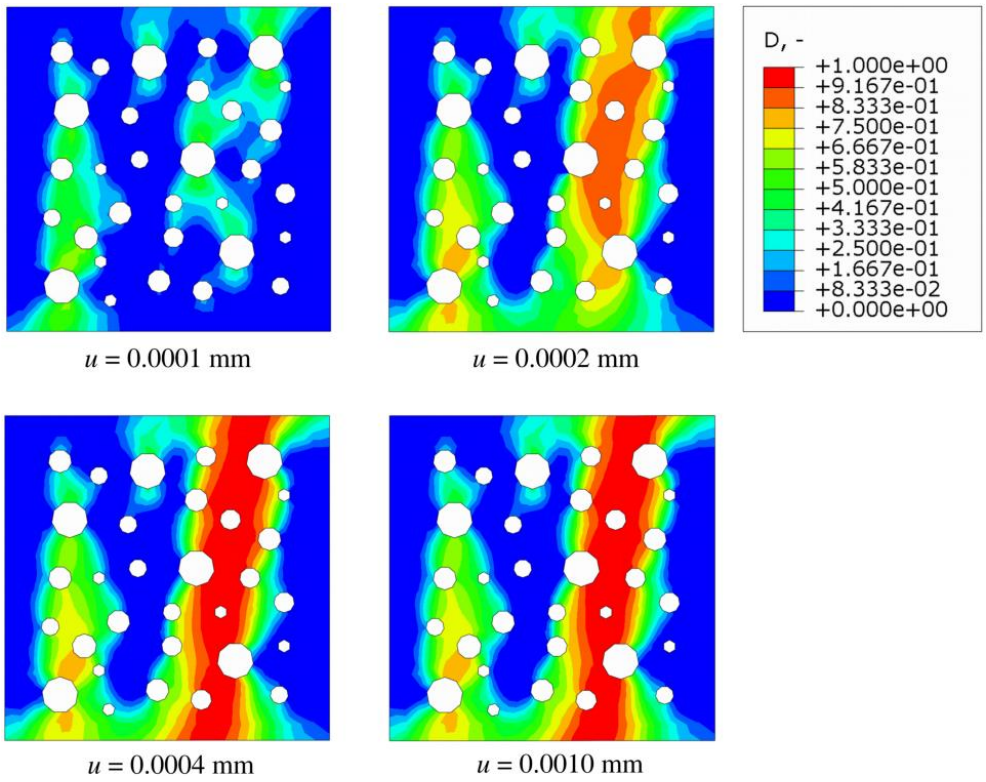


**Figure 4.9** Distribution of the damage $D$ through several loading stages for internal length scale parameter $l$ = 0.02 mm

A different formation of the localization zones can be noted in above figures, which is obviously a consequence of utilization of different internal length scales that define different nonlocal behaviors. When the nonlocal effect is wider, i.e. when a bigger area of neighboring material is in the interaction, one predominant and wider localization zone is formed, as evident from Figure 4.9. In contrast, for the weaker nonlocal effect, two narrower localization bands are formed, as shown in Figure 4.8. This phenomenon would probably not exist in reality, since a crack would be initiated in a dominant localization zone, across which the fracture would eventually happen. Presented constitutive model (4.14) - (4.16) does not consider the crack formation, allowing in this way for the loading to still be carried over the localization zone. As discussed in the previous chapter, definition of the damage variable should probably be written in terms of both strain and strain-gradient tensor in order to reduce the internal forces in the localization zone and overall reaction force response. However, in both examples localization zone is fully formed, where no additional damage growth outside of it can be noticed. In other words, RVEs still have the load-carrying capacity, with the change of strain level allowed only in the middle of the localization band. This trait is important because it allows the simple assessment of the RVE failure, which will be incorporated into the multiscale scheme in the

next section. From the presented numerical tests it can be concluded that $C^1$ continuity finite element for softening analysis based on Aifantis theory of gradient elasticity can successfully predict the growth of the damage and is suitable for the implementation in the multiscale algorithm.

## 4.2 $C^0$-$C^1$ multiscale scheme

### 4.2.1 $C^0$-$C^1$ macro-micro scale transition relations

In order to test the capability of the multiscale algorithm employing the local approach in the problems involving localization of the deformation, classical $C^0$ continuity quadrilateral finite elements are employed at the macroscale, while previously derived $C^1$ elements for softening analysis are considered at the microscale. Since there are no such multiscale schemes in the literature, relations describing transitions of the variables between scales have to be derived first. $C^0$-$C^1$ multiscale scheme is given in Figure 4.10, and can be briefly described in the following way. Starting from the converged global macrolevel nonlinear BVP described by $\mathbf{K}\Delta\mathbf{V} = \mathbf{F}_\mathrm{e} - \mathbf{F}_\mathrm{i}$, obtained global vector of incremental nodal degrees of freedom $\Delta\mathbf{V}$ is used for the formulation of the local vector $\Delta\mathbf{v}$ related to the observed finite element. By computing the increment of macrostrain tensor $\Delta\boldsymbol{\varepsilon}_\mathrm{M}$ in one of the element's integration points, increment of the RVE boundary displacement vector $\Delta\mathbf{u}_\mathrm{b}$ can be then formulated by the appropriate micro-to-macro scale transition relations. The microlevel BVP is formed and solved afterwards, followed by the homogenization of resulting microlevel variables needed for the formation of the macrolevel constitutive behavior. Here, only Cauchy stress tensor $\boldsymbol{\sigma}_\mathrm{M}$ and classical elasticity tensor $\mathbf{C}_{\sigma\varepsilon}$ have to be homogenized since the macrolevel does not account for the higher-order variables that constitute the microlevel. Once computed, homogenized stress and stiffness are transferred back to macrolevel finite element integration point, where they contribute in the calculation of the finite element stiffness matrix $\mathbf{k}$ and internal forces vector $\mathbf{f}_\mathrm{i}$. When the homogenized response is obtained in all integration points for all macrolevel finite elements, global stiffness matrix $\mathbf{K}$ and internal force vector $\mathbf{F}_\mathrm{i}$ are formulated, and the updated macroscale BVP can then be established. From this point the process repeats in the loop until the convergence for the given loading conditions at the macrolevel is reached.

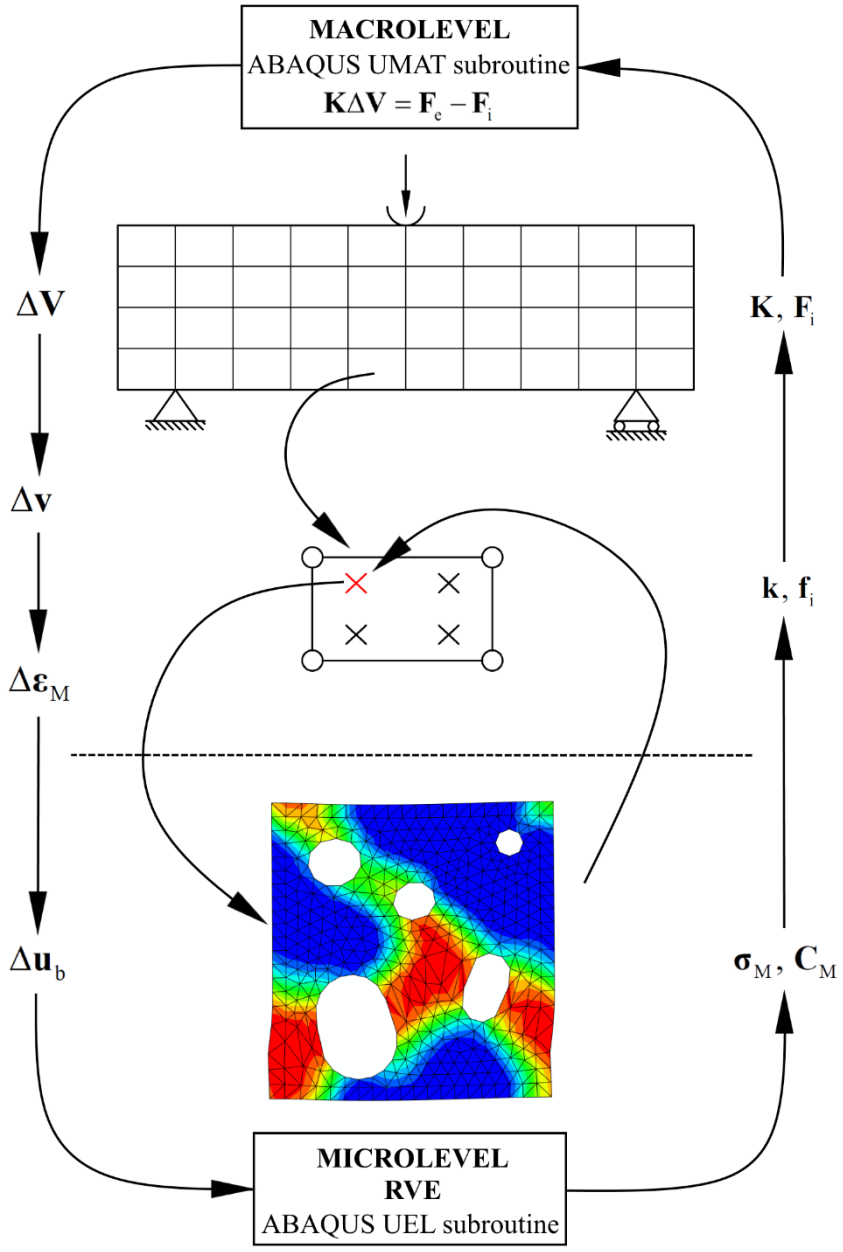


**Figure 4.10** Scheme of $C^0$-$C^1$ multiscale algorithm

In the following, relations describing the macro-to-micro and micro-to-macro scale transitions are described in more detail. A square-shaped RVE is considered with the origin of the coordinate system placed in its centroid, as depicted in Figure 4.11.

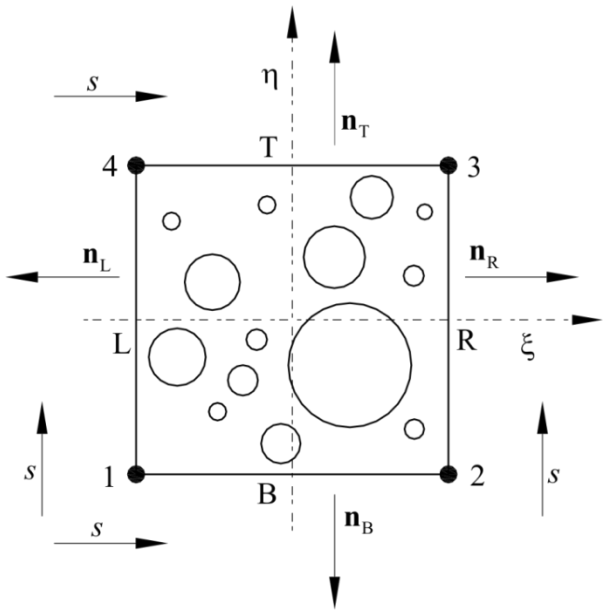


**Figure 4.11** Representative volume element [17]

Formation of the RVE displacement field is made by a Taylor series expansion depending only on the macrolevel strain $\boldsymbol{\varepsilon}_M$ as follows

$$\mathbf{u}_m = \boldsymbol{\varepsilon}_M \cdot \mathbf{x} + \mathbf{r} \,. \tag{4.26}$$

Here, $\mathbf{x}$ is the microlevel spatial coordinate vector while $\mathbf{r}$ represents the microfluctuation field, i.e. the microlevel contribution to the RVE displacement field, as stated in [17]. In accordance with the relation (4.26), microlevel strain tensor can be defined as

$$\boldsymbol{\varepsilon}_m = \nabla_{\mathbf{m}} \otimes \mathbf{u}_m = \boldsymbol{\varepsilon}_M + \nabla_{\mathbf{m}} \otimes \mathbf{r} \,. \tag{4.27}$$

In order to find the necessary transition relations for the microscale strain gradients, following relation holds

$$\nabla_{\mathbf{m}} \otimes \boldsymbol{\varepsilon}_m = \nabla \otimes \boldsymbol{\varepsilon}_M + \nabla_{\mathbf{m}} \otimes \left( \nabla_{\mathbf{m}} \otimes \mathbf{r} \right). \tag{4.28}$$

Considering the principle that in the homogenization volume averages of the microstructural variables have to be equal to the conjugate variables at the macrolevel, relations (4.27) and (4.28) can be written as

$$\frac{1}{V} \int_V \boldsymbol{\varepsilon}_m \mathrm{d}V = \boldsymbol{\varepsilon}_M + \frac{1}{V} \int_V \left( \nabla_{\mathbf{m}} \otimes \mathbf{r} \right) \mathrm{d}V \,, \tag{4.29}$$

$$\frac{1}{V} \int_V \left( \nabla_{\mathbf{m}} \otimes \boldsymbol{\varepsilon}_m \right) \mathrm{d}V = \nabla \otimes \boldsymbol{\varepsilon}_M + \frac{1}{V} \int_V \left[ \nabla_{\mathbf{m}} \otimes \left( \nabla_{\mathbf{m}} \otimes \mathbf{r} \right) \right] \mathrm{d}V \,. \tag{4.30}$$

To satisfy the condition that the macrostrain is equal to the volume average of the microstrain, the second term on the right-hand side of (4.29) should vanish

$$\frac{1}{V}\int_V \left(\nabla_{\mathbf{m}} \otimes \mathbf{r}\right) \mathrm{d}V = \frac{1}{V}\int_A \left(\mathbf{n} \otimes \mathbf{r}\right) \mathrm{d}A = \mathbf{0}\,. \tag{4.31}$$

In above relation, volume integral is transformed into the surface integral by means of the Gauss theorem. Considering that there are no strain gradients at the macrolevel due to $C^0$ continuity discretization, relation (4.30) can be transformed to

$$\frac{1}{V}\int_V \left(\nabla_{\mathbf{m}} \otimes \boldsymbol{\varepsilon}_{\mathrm{m}}\right) \mathrm{d}V = \frac{1}{V}\int_V \left[\nabla_{\mathbf{m}} \otimes \left(\nabla_{\mathbf{m}} \otimes \mathbf{r}\right)\right] \mathrm{d}V\,, \tag{4.32}$$

which basically says that realization of the RVE strain gradient field is interconnected solely with the realization of the microfluctuation field. When it comes to modeling of microfluctuations on the RVE boundaries, usually displacement and periodic boundary conditions are employed, where the former yield a stiffer RVE response [46, 61, 148]. In order to satisfy constraint (4.31), an appropriate choice of boundary conditions has to be made. Displacement boundary conditions prescribe the zero value of microfluctuation on the RVE boundaries, i.e. boundary movements are completely predefined. By the insertion of the $\mathbf{r} = \mathbf{0},\ \forall \mathbf{x} \in \Gamma$, constraint (4.31) is automatically satisfied. Periodic boundary conditions prescribe the equality of the microfluctuation fields on the opposite sides of the RVE, which considering Figure 4.11 leads to

$$\mathbf{r}_{\mathrm{R}}\left(s\right) = \mathbf{r}_{\mathrm{L}}\left(s\right), \tag{4.33}$$

$$\mathbf{r}_{\mathrm{T}}\left(s\right) = \mathbf{r}_{\mathrm{B}}\left(s\right). \tag{4.34}$$

Since the normal vectors on the opposite RVE sides have different signs, i.e. $\mathbf{n}_{\mathrm{R}}\left(s\right) = -\mathbf{n}_{\mathrm{L}}\left(s\right)$ and $\mathbf{n}_{\mathrm{T}}\left(s\right) = -\mathbf{n}_{\mathrm{B}}\left(s\right)$, constraint (4.31) with the application of (4.33) and (4.34) remains valid. Due to periodicity of microfluctuations (4.33) and (4.34), it is sufficient to consider only one of the opposite RVE edges for implementation of the boundary integrals derived in [11], and given as

$$\int_{A_{\mathrm{L}}} \mathbf{r}_{\mathrm{L}} \mathrm{d}A = \mathbf{0}\,, \tag{4.35}$$

$$\int_{A_{\mathrm{B}}} \mathbf{r}_{\mathrm{B}} \mathrm{d}A = \mathbf{0}\,. \tag{4.36}$$

After the microfluctuation field from (4.26) is inserted in (4.35) and (4.36), following expressions are obtained

$$\int_{A_\mathrm{L}} \mathbf{u}_\mathrm{L} \mathrm{d}A = \boldsymbol{\varepsilon}_\mathrm{M} \cdot \int_{A_\mathrm{L}} \mathbf{x}_\mathrm{L} \mathrm{d}A\,, \tag{4.37}$$

$$\int_{A_\mathrm{B}} \mathbf{u}_\mathrm{B} \mathrm{d}A = \boldsymbol{\varepsilon}_\mathrm{M} \cdot \int_{A_\mathrm{B}} \mathbf{x}_\mathrm{B} \mathrm{d}A\,. \tag{4.38}$$

As explained in [11], prescription of the nodal values of displacements to the RVE boundaries is dependent on the nodal position. Numerical implementation of this dependency is, as done by the coordinate matrix $\mathbf{D}_i$ in form of

$$\mathbf{D}_i = \begin{bmatrix} x_1 & 1 & 0 & 0 & 0 & 0 & 0 & 0 & 0 & 0 & 0 & 0 \\ 0 & 0 & 0 & 0 & 0 & 0 & x_2 & 0 & 1 & 0 & 0 & 0 \\ \frac{1}{2}x_2 & 0 & \frac{1}{2} & 0 & 0 & 0 & \frac{1}{2}x_1 & \frac{1}{2} & 0 & 0 & 0 & 0 \end{bmatrix}, \tag{4.39}$$

where the subscript *i* refers to an appropriate node on the RVE boundary. Displacement of a single node can then be expressed by

$$\mathbf{u}_i = \mathbf{D}_i^T \, \boldsymbol{\varepsilon}_\mathrm{M}\,, \tag{4.40}$$

or, in order to avoid the rigid body motions of RVE, by

$$\mathbf{u}_i = \left(\mathbf{D}_i^T - \mathbf{D}_1\right)\boldsymbol{\varepsilon}_\mathrm{M}\,, \tag{4.41}$$

where all prescribed displacements are defined relatively to node 1 of the RVE depicted in Figure 4.11, as defined in [11]. When it comes to displacement boundary conditions, relation (4.41) is applied to every node on the RVE boundary, since all the microfluctuations are suppressed there. On the other hand, generalized periodic boundary conditions require prescription of displacements in the form of (4.40) only in the corner nodes, with the exception of usually corner node 1 in Figure 4.11, where the displacements are set to zero in order to eliminate the rigid body motions. Rest of the nodes on the boundaries are related in accordance with the microfluctuation periodicity assumptions expressed by (4.33) and (4.34), which comes down to linking of the nodal degrees of freedom on opposite edges of the RVE. This is done by expressing the microfluctuation field from (4.26) for every RVE edge by means of (4.40), and by subsequent substitution of the obtained relations in (4.33) and (4.34), where following periodicity equations are obtained after some straightforward calculus

$$\mathbf{u}_{\mathrm{R}} - \mathbf{u}_{\mathrm{L}} = \left(\mathbf{D}_{\mathrm{R}}^{T} - \mathbf{D}_{\mathrm{L}}^{T}\right)\boldsymbol{\varepsilon}_{\mathrm{M}}, \tag{4.42}$$

$$\mathbf{u}_{\mathrm{T}} - \mathbf{u}_{\mathrm{B}} = \left(\mathbf{D}_{\mathrm{T}}^{T} - \mathbf{D}_{\mathrm{B}}^{T}\right)\boldsymbol{\varepsilon}_{\mathrm{M}}. \tag{4.43}$$

In above relations, only a relative ratio between displacements on opposite edges is prescribed rather than the pure values, which, on the other hand, is the case with the displacement boundary conditions. Due to this difference, generalized periodic boundary conditions provide more compliant and realistic RVE response, which consequentially leads to a more compliant material behavior observed at the macrostructural level, as stated in [11]. In addition to periodicity equations (4.42) and (4.43), microfluctuation integrals (4.37) and (4.38) are needed for the full definition of the generalized periodic boundary conditions, which, after the introduction of coordinate matrix $\mathbf{D}$, read

$$\int_{A_{\mathrm{L}}} \mathbf{u}_{\mathrm{L}} \mathrm{d}A = \left( \int_{A_{\mathrm{L}}} \mathbf{D}_{\mathrm{L}}^{T} \mathrm{d}A \right) \boldsymbol{\varepsilon}_{\mathrm{M}}, \tag{4.44}$$

$$\int_{A_{\mathrm{B}}} \mathbf{u}_{\mathrm{B}} \mathrm{d}A = \left( \int_{A_{\mathrm{B}}} \mathbf{D}_{\mathrm{B}}^{T} \mathrm{d}A \right) \boldsymbol{\varepsilon}_{\mathrm{M}}. \tag{4.45}$$

Derivation of the consistent micro-to-macro transition relations for the $C^0$-$C^1$ multiscale scheme starts with the Hill-Mandel energy condition, which equalizes the work variation done at the RVE level with the work variation at the macrostructural material point, in form of

$$\frac{1}{V}\int_{V}\left[\boldsymbol{\sigma}_{\mathrm{m}} : \delta\boldsymbol{\varepsilon}_{\mathrm{m}} + {}^{3}\boldsymbol{\mu}_{\mathrm{m}} \vdots \left(\nabla_{\mathrm{m}} \otimes \delta\boldsymbol{\varepsilon}_{\mathrm{m}}\right)\right]\mathrm{d}V = \boldsymbol{\sigma}_{\mathrm{M}} : \delta\boldsymbol{\varepsilon}_{\mathrm{M}}. \tag{4.46}$$

Microstrain and microstrain gradient can be obtained from (4.27) and (4.28), which, after insertion in (4.46) and considering that macrostrain gradient does not exist, yields the following expression for the Hill-Mandel energy condition

$$\frac{1}{V}\int_{V}\left[\boldsymbol{\sigma}_{\mathrm{m}} : \left(\delta\boldsymbol{\varepsilon}_{\mathrm{M}} + \nabla_{\mathbf{m}} \otimes \delta\mathbf{r}\right) + {}^{3}\boldsymbol{\mu}_{\mathrm{m}} \vdots \left(\nabla_{\mathrm{m}} \otimes \nabla_{\mathbf{m}} \otimes \delta\mathbf{r}\right)\right]\mathrm{d}V = \boldsymbol{\sigma}_{\mathrm{M}} : \delta\boldsymbol{\varepsilon}_{\mathrm{M}}. \tag{4.47}$$

According to [11], integral terms containing microfluctuations (4.47) should vanish, which can be proven by converting them into surface integrals using the Gauss theorem as follows

$$\frac{1}{V}\int_{V}\boldsymbol{\sigma}_{\mathrm{m}} : \left(\nabla_{\mathbf{m}} \otimes \delta\mathbf{r}\right)\mathrm{d}V = \frac{1}{V}\int_{A}\left(\mathbf{n}\cdot\boldsymbol{\sigma}_{\mathrm{m}}\cdot\delta\mathbf{r}\right)\mathrm{d}A = 0, \tag{4.48}$$

$$\frac{1}{V}\int_{V}\left[{}^{3}\boldsymbol{\mu}_{\mathrm{m}} \vdots \left(\nabla_{\mathrm{m}} \otimes \nabla_{\mathbf{m}} \otimes \delta\mathbf{r}\right)\right]\mathrm{d}V = \frac{1}{V}\int_{A}\left[\mathbf{n}\cdot{}^{3}\boldsymbol{\mu}_{\mathrm{m}} : \left(\nabla_{\mathbf{m}} \otimes \delta\mathbf{r}\right)\right]\mathrm{d}A = 0. \tag{4.49}$$

Justification of the above equalities can be provided by the fact that, due to periodicity assumptions on the RVE boundaries, there is no contribution of the microfluctuations to the internal work of the RVE. In addition, corner microfluctuations are not allowed which completely confirms that RVE boundary integrals can be removed from the Hill-Mandel energy condition. By employing the relations (4.48) and (4.49), and considering that $\delta\boldsymbol{\varepsilon}_{\mathrm{M}}$ is a constant value expression (4.47) becomes

$$\left(\frac{1}{V}\int_{V}\boldsymbol{\sigma}_{\mathrm{m}}\mathrm{d}V\right):\delta\boldsymbol{\varepsilon}_{\mathrm{M}}=\boldsymbol{\sigma}_{\mathrm{M}}:\delta\boldsymbol{\varepsilon}_{\mathrm{M}}, \tag{4.50}$$

from where the following relation for the homogenized Cauchy stress tensor can be extracted

$$\boldsymbol{\sigma}_{\mathrm{M}}=\frac{1}{V}\int_{V}\boldsymbol{\sigma}_{\mathrm{m}}\mathrm{d}V\,. \tag{4.51}$$

Only constitutive tangent needed for the macrolevel constitutive model is the classical one, which can be obtained by

$$\mathbf{C}_{\sigma\varepsilon}\left(D\right)=\frac{1}{V}\mathbf{D}\tilde{\mathbf{K}}_{\mathrm{bb}}\left(D\right)\mathbf{D}^{T}\,. \tag{4.52}$$

In (4.52) $\tilde{\mathbf{K}}_{\mathrm{bb}}$ represents a condensed RVE stiffness matrix where only external boundary nodes are taken into account for the calculation of the stiffness behavior, which is derived and clarified in more detail in [11]. According to Table 3.2, condensed RVE stiffness matrix is constructed from the stiffness response of the whole RVE, which is, on the other hand, composed of the finite element stiffness matrices, obtained for the case of Aifantis theory by the relations (4.23) - (4.25). As obvious from the given relations, finite element stiffness matrices are dependent on the damage variable *D*, which implies that the condensed RVE stiffness matrix is implicitly dependent on the damage variable, i.e.

$$\tilde{\mathbf{K}}_{\mathrm{bb}}=\tilde{\mathbf{K}}_{\mathrm{bb}}\left(D\right). \tag{4.53}$$

Generally in the second-order computational homogenization procedure, the macrostructural stiffness is obtained as a function of the condensed stiffness matrix, which can be written in the form of

$$\mathbf{C}_{\mathrm{M}}=\mathbf{C}_{\mathrm{M}}\left(\tilde{\mathbf{K}}_{\mathrm{bb}}\right). \tag{4.54}$$

By insertion of (4.54) in (4.53), a following relation holds

$$\mathbf{C}_{\mathrm{M}} = \mathbf{C}_{\mathrm{M}}\left(D\right), \tag{4.55}$$

from where it is clear that the homogenized macrostructural stiffness is directly influenced by the damage growth observed at the microstructural level. Due to this degradation effect, capability of the proposed multiscale scheme in capturing the macrostructural localization of the deformation can be expected. Since only the classical stiffness tensor $\mathbf{C}_{\sigma\varepsilon}\left(D\right)$, that is independent of any choice of microstructural internal length scale and RVE size, is employed at the macrolevel due to $C^0$ continuity, a problems related to the regularization of strain localization could arise here, which will be tested in a numerical example in the following section. Presented $C^0$-$C^1$ macro-micro scheme is implemented in ABAQUS/Standard via user subroutines, as depicted in Figure 4.10. Numerical implementation of the proposed algorithm is similar to the one given for $C^1$-$C^0$ multiscale framework described lengthily in [11], and here only a basic algorithm of calculations at both structural levels is given in Table 4.1. Process can be briefly described as follows. Prior to multiscale analysis homogenization of the RVE constitutive behavior has to be performed for the purpose of initialization of values required for the macrostructural analysis. The subsequent multiscale analysis consists of UMAT subroutine at the macrolevel, where rectangular eight-node plane strain element with reduced integration (CPE8R) is used, and UEL subroutine at the microlevel, where the $C^1$ continuity triangular finite element for softening analysis is implemented. UMAT subroutine is here a main routine, where the RVE boundary conditions are formulated, and from where the UEL subroutine is initiated. During the computation of the microlevel BVP, macrolevel UMAT subroutine is paused. The computation resumes when the homogenized variables become available, after which the ABAQUS/Standard solver provides the solutions and checks for the convergence. The solving procedure of the presented multiscale scheme is completely parallelized between multiple CPU threads, which can be easily enabled through the UMAT subroutine. To every CPU thread one macrostructural finite element is assigned in every iteration, meaning that the calculations for particular Gauss integration points are done simultaneously for all “threaded” elements. Obviously, the parallelization procedure significantly accelerates the computation, which is always welcoming in usually very demanding multiscale calculations.

**Table 4.1** Solving algorithm of $C^0$-$C^1$ macro-micro scheme

| **MACRO** | **MICRO** |
|---|---|
| **1**. Start analysis<br>**2**. Apply new load increment<br>**3**. Apply new N.-R. iteration<br>**4**. Compute $\boldsymbol{\varepsilon}_M$ | |
| | **5**. Formulate RVE boundary conditions<br>**6**. Apply new load increment in terms of $\mathbf{u}_b$<br>**7**. Apply new N.-R. iteration<br>**8**. Solve RVE BVP<br>**9**. Convergence check:<br>Yes – go to **6**.<br>No – go to **7**.<br>Last increment - homogenize $\boldsymbol{\sigma}_M$ and $\mathbf{C}_M$ |
| **10**. Formulate macrostructural BVP<br>**11**. Solve macrostructural BVP<br>**12**. Convergence check:<br>Yes – go to **2**.<br>No – go to **3**. | |

### 4.2.2 Numerical example

In the following example plate with an imperfect zone subjected to tensile load, already analyzed in Chapter 3 for numerical testing of the one-scale damage model, is utilized for the damage analysis by employing the $C^0$-$C^1$ multiscale scheme, whereby the homogeneous microstructure is considered. By elimination of all effects resulting from the microstructural heterogeneities, a more clear conclusions can be made regarding the macrolevel structural response. Although the same numerical example is already described in previous chapter, all necessary computational data is given again for the clarity reasons. Computational model of the problem is shown in Figure 4.12, while three different discretizations for the $C^0$ continuous macrolevel are given in Figure 4.13. Homogeneous microlevel is taken as a rectangular MVE with uniform $C^1$ continuity discretization, as shown in Figure 4.14. Periodic boundary

conditions are considered at the MVE boundaries during the calculation. Since the term RVE is commonly reserved for description of the representative character of heterogeneous microstructure, MVE is used instead in this example.

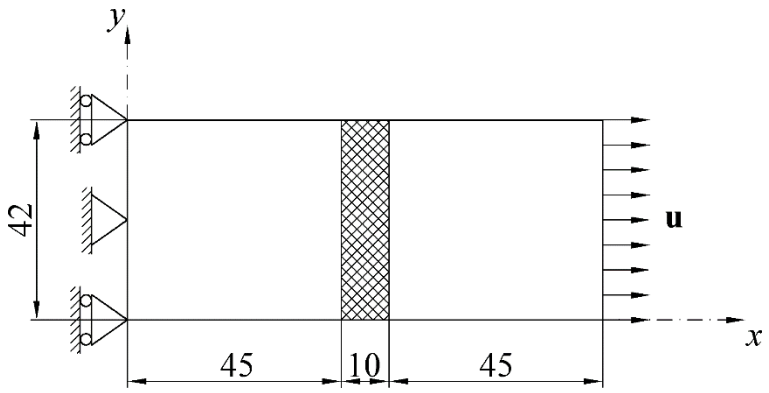


**Figure 4.12** Geometry and boundary conditions of the plate subjected to tensile load

Considering the softening characteristics, the Mazars' equivalent strain measure (2.8) is used together with the damage evolution governed by the linear softening law (2.6). The material data for the RVE matrix material are: the Young's modulus $E = 20000$ N/mm$^2$, the Poisson's ratio $\nu = 0.25$, the limit elastic strain $\kappa_0 = 0.0001$, the equivalent strain corresponding to the fully damaged state $\kappa_u = 0.0125$. The horizontal displacement of $u = 0.0325$ mm is prescribed at the right edge of the large scale model. In order to trigger localization, the Young's modulus is reduced by 10% in the 10 mm wide zone in the middle hatched area of the plate. Along the vertical edges the second-order derivatives of the displacement component in the normal direction, $u_{1,11}$ and $u_{1,22}$, together with the mixed derivatives, $u_{1,12}$ and $u_{2,12}$, are suppressed. The first-order derivatives associated with the shear deformation, $u_{1,2}$ and $u_{2,1}$, are also set to zero. These boundary conditions yield the straight vertical edges. Here, the indices 1 and 2 refer to the Cartesian coordinates *x* and *y*, respectively.

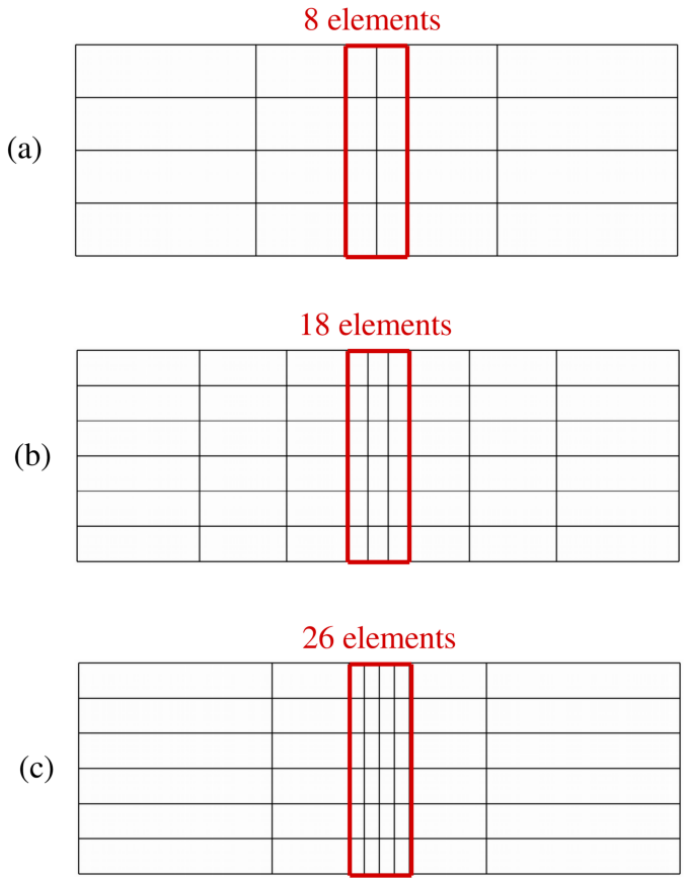


**Figure 4.13** Macrolevel discretization consisting of: (a) 24, (b) 54 and (c) 48 $C^0$ continuity rectangular finite elements (CPE8R)

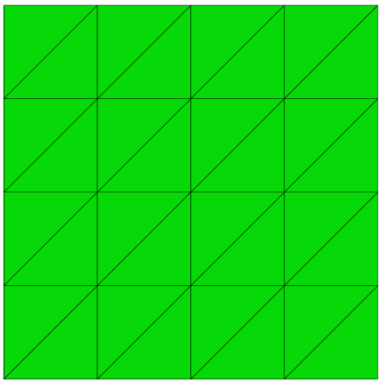

**Figure 4.14** Homogeneous MVE consisting of 32 $C^1$ continuity triangular finite elements

In order to make comparison with the results obtained by the one-scale damage model where the analysis of the microstructural evolution is excluded, the same macrostructural nonlocal parameter has to be employed both in multiscale and one-scale damage analyses. This is done by taking into account the relation for the calculation of the effective nonlocal behavior of the

macrostructure, derived in [73] by means of analytical $C^1$ continuous second-order computational homogenization and given by

$$l_{\text{eff}}^2 = \left(l_{\text{micro}}\right)^2 + \frac{L^2}{12}. \tag{4.56}$$

Relation (4.56) shows an approximate way to calculate the effective internal length scale at the macroscale, which is compounded out of the internal length scale at the microstructural level $l_{\text{micro}}$ and the contribution of the RVE side length $L$. From the physical point of view, RVE side length $L$ introduces the nonlocality in form of the size of the microstructural interaction domain, while $l_{\text{micro}}$ represents all nonlocal effects taking place at the length scales below microscale. Although this relation works only for the linear-elastic, isotropic and homogeneous material where no non-linear effects are observable, as there isn't any other alternative, it will be used in the following examples as a simple reference point in comparison of the multiscale analysis results with the results obtained by the one-scale damage model. In the following multiscale analyses, the effective macrostructural nonlocal parameter is taken as $l_{\text{eff}} = 1$ mm, which is obtained by using (4.56) and the microstructural nonlocal parameter of $l_{\text{micro}} = 0.6608$ mm at the MVE level, while the MVE size is taken as $L = 2.6$ mm. These particular values are chosen due to reason that they don't exhibit intense strain localization inside the MVE, which could happen if the ratio $l_{\text{micro}}/L$ is too small and which is undesirable in this case of homogeneous microstructure. The same numerical example is then calculated by the one-scale model based on the Aifantis theory of gradient elasticity where the $C^1$ continuity discretization is employed, while the Aifantis parameter is taken as $l = l_{\text{eff}} = 1$ mm. Structural responses for three different macroscale discretizations shown in Figure 4.13 and used in the $C^0$-$C^1$ multiscale scheme, together with the structural response obtained by the converged one-scale damage model are depicted in Figure 4.15. Obviously, three different mesh densities provide three different structural responses for $C^0$-$C^1$ multiscale scheme. Increase in the mesh density, i.e. decrease in the finite element width in the damage process zone where energy dissipation takes place, leads to more brittle reaction force response. Such behavior can be attributed to the local continuum model where the strain tends to localize in the smallest possible volume, or a narrowest band of finite elements in this case. With this example it is proven that with the employment of $C^0$ continuity at macrolevel, objective results in multiscale damage analysis cannot be provided.

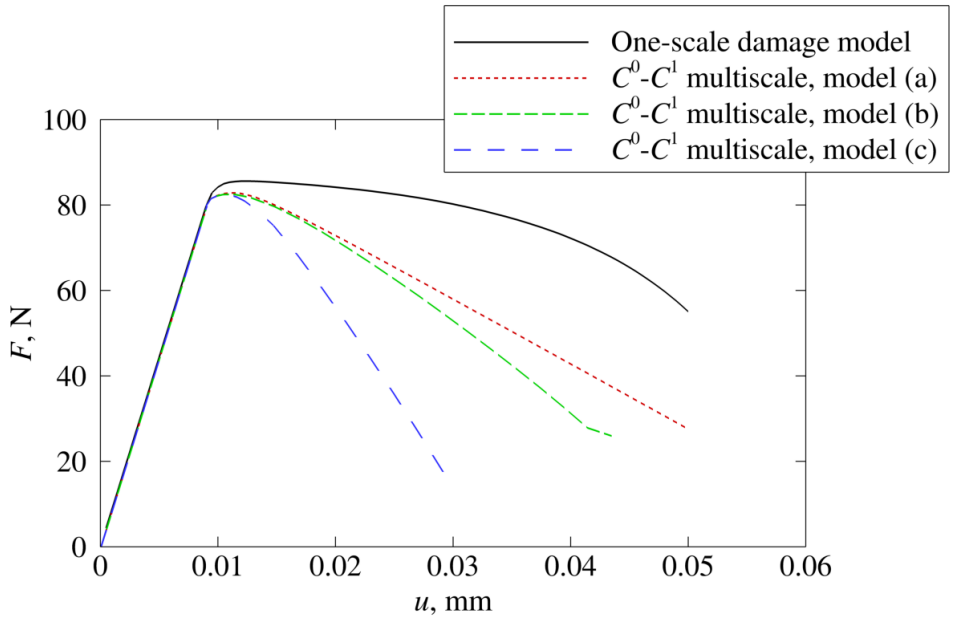


**Figure 4.15** Load-displacement diagrams obtained by three different macrolevel discretizations used in $C^0$-$C^1$ multiscale scheme and by one-scale damage model

# 4.3 $C^1$-$C^1$ multiscale scheme

## 4.3.1 $C^1$-$C^1$ macro-micro scale transition relations

Employment of the nonlocal continuum at the macrolevel instead of the classical one should be beneficial for two main reasons. First, since both strain and strain gradients are used in formulation of the RVE boundary conditions, a more complex and realistic RVE deformation modes can be obtained, and consequently a more realistic prediction of the damage growth can be made. The second reason is concerned with the regularization capabilities of the finite elements based on the strain gradient theory, which enables the transfer of the nonlocal parameters from the microstructure by homogenization of additional higher-order constitutive tensors. The $C^1$-$C^1$ multiscale scheme is shown in Figure 4.16, where few differences can be spotted in comparison with the $C^0$-$C^1$ multiscale scheme given in Figure 4.10. Due to employment of triangular finite elements that provide additional degrees of freedom, strain is accompanied by strain gradients in the calculation of the RVE boundary displacements. Regarding the homogenization process, besides classical constitutive tangent and Cauchy stress tensor, additional constitutive tangents as well as double stress tensor are required to be transferred back to macrolevel.

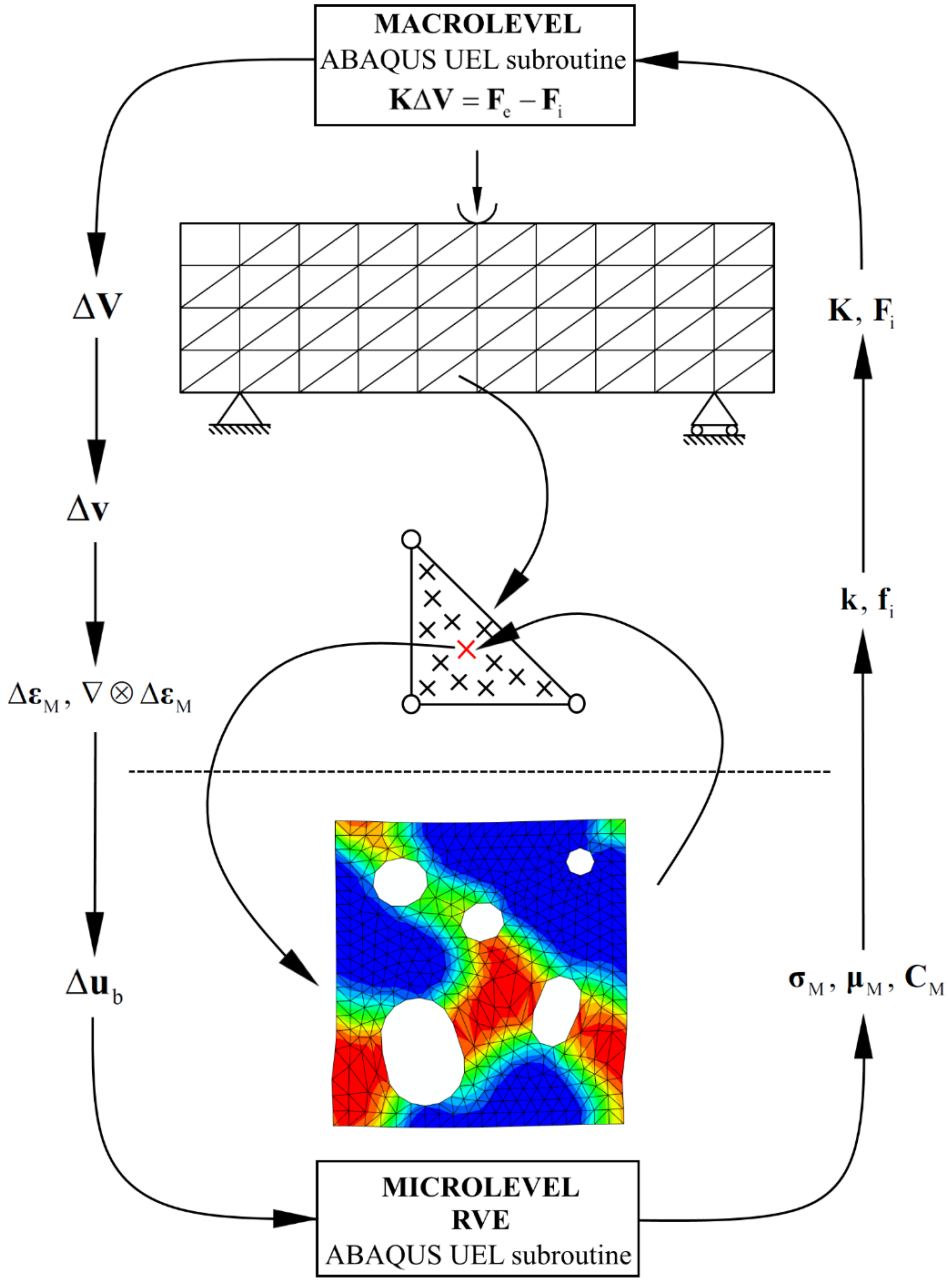


**Figure 4.16** Scheme of $C^1$-$C^1$ multiscale algorithm

The whole computational process is elaborated in [11, 73], so here only a brief explanation of basic scale transition relations is given. All relevant relations regarding the transition of variables from macro- to microscale are presented in Table 4.2. All that is previously said for macro-to-micro scale transitions in $C^0$-$C^1$ multiscale scheme basically holds for the $C^1$-$C^1$ multiscale scheme, with the main difference that in all relations the contribution of the macroscale strain gradient terms in now included. An additional constraint on the microfluctuation field (4.61) arises when the relation (4.59) is expressed in volume average terms. By using the same logic as described earlier, it can be easily shown that constraint (4.61)

completely satisfies both the displacement and the periodic boundary conditions. Coordinate matrices $\mathbf{H}_1$ and $\mathbf{H}_2$ are introduced to describe the dependency of strain gradient terms on the nodal position at the RVE boundary.

**Table 4.2** Macro-to-micro scale transition relations in $C^1$-$C^1$ multiscale scheme [11]

RVE boundary displacement field:

$$\mathbf{u}_{\mathrm{m}} = \boldsymbol{\varepsilon}_{\mathrm{M}} \cdot \mathbf{x} + \frac{1}{2}\left[\mathbf{x} \cdot \left(\nabla \otimes \boldsymbol{\varepsilon}_{\mathrm{M}}\right) \cdot \mathbf{x}\right] + \mathbf{r}\,. \tag{4.57}$$

Microlevel strain tensor:

$$\boldsymbol{\varepsilon}_{\mathrm{m}} = \boldsymbol{\varepsilon}_{\mathrm{M}} + \left(\nabla \otimes \boldsymbol{\varepsilon}_{\mathrm{M}}\right) + \nabla_{\mathbf{m}} \otimes \mathbf{r}\,. \tag{4.58}$$

Microlevel strain gradient tensor:

$$\nabla_{\mathbf{m}} \otimes \boldsymbol{\varepsilon}_{\mathrm{m}} = \nabla \otimes \boldsymbol{\varepsilon}_{\mathrm{M}} + \nabla_{\mathbf{m}} \otimes \left(\nabla_{\mathbf{m}} \otimes \mathbf{r}\right). \tag{4.59}$$

Constraints on the microfluctuation field:

$$\frac{1}{V}\int_V \left(\nabla_{\mathrm{m}} \otimes \mathbf{r}\right) \mathrm{d}V = \frac{1}{V}\int_A \left(\mathbf{n} \otimes \mathbf{r}\right) \mathrm{d}A = \mathbf{0}\,, \tag{4.60}$$

$$\frac{1}{V}\int_V \left[\nabla_{\mathrm{m}} \otimes \left(\nabla_{\mathrm{m}} \otimes \mathbf{r}\right)\right] \mathrm{d}V = \frac{1}{V}\int_A \left[\mathbf{n} \otimes \left(\nabla_{\mathrm{m}} \otimes \mathbf{r}\right)\right] \mathrm{d}A = \mathbf{0}\,. \tag{4.61}$$

RVE displacement of the *i*th node on the RVE boundary:

$$\mathbf{u}_i = \mathbf{D}_i^T \boldsymbol{\varepsilon}_{\mathrm{M}} + \left(\mathbf{H}_1^T\right)_i \left(\boldsymbol{\varepsilon}_{x_1}\right)_{\mathrm{M}} + \left(\mathbf{H}_2^T\right)_i \left(\boldsymbol{\varepsilon}_{x_2}\right)_{\mathrm{M}} + \mathbf{r}_i, \quad i = 1, ..., m\,. \tag{4.62}$$

Coordinate matrices:

$$\left(\mathbf{H}_1\right)_i = \begin{bmatrix} \frac{1}{2}x_1^2 & x_1 & 0 & 1 & 0 & 0 & 0 & 0 & 0 & 0 & 0 & 0 \\ -\frac{1}{2}x_2^2 & 0 & -x_2 & 0 & 0 & -1 & x_1x_2 & x_2 & x_1 & 0 & 1 & 0 \\ 0 & 0 & 0 & 0 & 0 & 0 & \frac{1}{2}x_1^2 & x_1 & 0 & 1 & 0 & 0 \end{bmatrix}, \tag{4.63}$$

$$\left(\mathbf{H}_2\right)_i = \begin{bmatrix} x_1x_2 & x_2 & x_1 & 0 & 1 & 0 & -\frac{1}{2}x_1^2 & -x_1 & 0 & -1 & 0 & 0 \\ 0 & 0 & 0 & 0 & 0 & 0 & \frac{1}{2}x_2^2 & 0 & x_2 & 0 & 0 & 1 \\ \frac{1}{2}x_2^2 & 0 & x_2 & 0 & 0 & 1 & 0 & 0 & 0 & 0 & 0 & 0 \end{bmatrix}. \tag{4.64}$$

Periodicity equations:

$$\mathbf{u}_{\mathrm{R}}-\mathbf{u}_{\mathrm{L}}=\left(\mathbf{D}_{\mathrm{R}}^{T}-\mathbf{D}_{\mathrm{L}}^{T}\right)\boldsymbol{\varepsilon}_{\mathrm{M}}+\left[\left(\mathbf{H}_{1}^{T}\right)_{\mathrm{R}}-\left(\mathbf{H}_{1}^{T}\right)_{\mathrm{L}}\right]\left(\boldsymbol{\varepsilon}_{x_1}\right)_{\mathrm{M}}+\left[\left(\mathbf{H}_{2}^{T}\right)_{\mathrm{R}}-\left(\mathbf{H}_{2}^{T}\right)_{\mathrm{L}}\right]\left(\boldsymbol{\varepsilon}_{x_2}\right)_{\mathrm{M}}, \quad (4.65)$$

$$\mathbf{u}_{\mathrm{T}}-\mathbf{u}_{\mathrm{B}}=\left(\mathbf{D}_{\mathrm{T}}^{T}-\mathbf{D}_{\mathrm{B}}^{T}\right)\boldsymbol{\varepsilon}_{\mathrm{M}}+\left[\left(\mathbf{H}_{1}^{T}\right)_{\mathrm{T}}-\left(\mathbf{H}_{1}^{T}\right)_{\mathrm{B}}\right]\left(\boldsymbol{\varepsilon}_{x_1}\right)_{\mathrm{M}}+\left[\left(\mathbf{H}_{2}^{T}\right)_{\mathrm{T}}-\left(\mathbf{H}_{2}^{T}\right)_{\mathrm{B}}\right]\left(\boldsymbol{\varepsilon}_{x_2}\right)_{\mathrm{M}}. \quad (4.66)$$

Microfluctuation integrals:

$$\int_{A_{\mathrm{L}}}\mathbf{u}_{\mathrm{L}}\mathrm{d}A=\left(\int_{A_{\mathrm{L}}}\mathbf{D}_{\mathrm{L}}^{T}\mathrm{d}A\right)\boldsymbol{\varepsilon}_{\mathrm{M}}+\left(\int_{A_{\mathrm{L}}}\left(\mathbf{H}_{1}^{T}\right)_{\mathrm{L}}\mathrm{d}A\right)\left(\boldsymbol{\varepsilon}_{,1}\right)_{\mathrm{M}}+\left(\int_{A_{\mathrm{L}}}\left(\mathbf{H}_{2}^{T}\right)_{\mathrm{L}}\mathrm{d}A\right)\left(\boldsymbol{\varepsilon}_{,2}\right)_{\mathrm{M}}, \quad (4.67)$$

$$\int_{A_{\mathrm{B}}}\mathbf{u}_{\mathrm{B}}\mathrm{d}A=\left(\int_{A_{\mathrm{B}}}\mathbf{D}_{\mathrm{B}}^{T}\mathrm{d}A\right)\boldsymbol{\varepsilon}_{\mathrm{M}}+\left(\int_{A_{\mathrm{B}}}\left(\mathbf{H}_{1}^{T}\right)_{\mathrm{B}}\mathrm{d}A\right)\left(\boldsymbol{\varepsilon}_{,1}\right)_{\mathrm{M}}+\left(\int_{A_{\mathrm{B}}}\left(\mathbf{H}_{2}^{T}\right)_{\mathrm{B}}\mathrm{d}A\right)\left(\boldsymbol{\varepsilon}_{,2}\right)_{\mathrm{M}}. \quad (4.68)$$

The most important relations and variables related to the homogenization process are given in Table 4.3. Once again, due to existence of the macrolevel strain gradients as a relevant degrees of freedom, Hill-Mandel energy condition is extended with second term on the right-hand side of (4.70), when compared with Hill-Mandel condition (4.46) in $C^0$-$C^1$ multiscale scheme. Regarding the homogenized double stress tensor (4.72), the second term under the integral represents contribution of the heterogeneities, as stated in [11]. Constitutive relations (4.73) - (4.75) are expanded with eight additional constitutive matrices, because the classical one cannot take into account the contribution of all the heterogeneities and the interactions taking place at the microstructural level. Since these additional constitutive tangents are dependent on the microstructure, a proper regularization of the damage effects at the macrolevel can be expected. Once again, tangent stiffness matrices (4.76) are formulated by the employment of only external RVE boundary nodes through the condensed stiffness matrix $\tilde{\mathbf{K}}_{\mathrm{bb}}$, together with the appropriate combination of two coordinate matrices. As already discussed for the $C^0$-$C^1$ multiscale scheme, when softening is observed at the microlevel, the homogenized macrostructural stiffness $\mathbf{C}_{\mathrm{M}}$ is through the condensed stiffness matrix $\tilde{\mathbf{K}}_{\mathrm{bb}}$ under a direct influence of the damage variable $D$. Considering this connection, the tangent stiffness matrices represented by relation (4.76) can be put in the following form

$$\mathbf{C}_{\sigma\varepsilon},\mathbf{C}_{\sigma\varepsilon_{x_1}},\mathbf{C}_{\sigma\varepsilon_{x_2}},\mathbf{C}_{\mu_{x_1}\varepsilon},\mathbf{C}_{\mu_{x_1}\varepsilon_{x_1}},\mathbf{C}_{\mu_{x_1}\varepsilon_{x_2}},\mathbf{C}_{\mu_{x_2}\varepsilon},\mathbf{C}_{\mu_{x_2}\varepsilon_{x_1}},\mathbf{C}_{\mu_{x_2}\varepsilon_{x_2}}=f\left(D\right). \quad (4.69)$$

**Table 4.3** Micro-to-macro scale transition relations in $C^1$-$C^1$ multiscale scheme [11]

Hill-Mandel energy condition:

$$\frac{1}{V}\int_V \left(\boldsymbol{\sigma}_{\mathrm{m}} : \delta\boldsymbol{\varepsilon}_{\mathrm{m}} + {}^3\boldsymbol{\mu}_{\mathrm{m}} \vdots \left(\nabla_{\mathrm{m}} \otimes \delta\boldsymbol{\varepsilon}_{\mathrm{m}}\right)\right) \mathrm{d}V = \boldsymbol{\sigma}_{\mathrm{M}} : \delta\boldsymbol{\varepsilon}_{\mathrm{M}} + {}^3\boldsymbol{\mu}_{\mathrm{M}} \vdots \left(\nabla \otimes \delta\boldsymbol{\varepsilon}_{\mathrm{M}}\right). \tag{4.70}$$

Homogenized stress tensors:

$$\boldsymbol{\sigma}_{\mathrm{M}} = \frac{1}{V}\int_V \boldsymbol{\sigma}_{\mathrm{m}} \, \mathrm{d}V, \tag{4.71}$$

$${}^3\boldsymbol{\mu}_{\mathrm{M}} = \frac{1}{V}\int_V \left({}^3\boldsymbol{\mu}_{\mathrm{m}} + \boldsymbol{\sigma}_{\mathrm{m}} \otimes \mathbf{x}\right) \mathrm{d}V. \tag{4.72}$$

Macroscopic constitutive relations:

$$\Delta\boldsymbol{\sigma} = {}^4\mathbf{C}_{\sigma\varepsilon} : \Delta\boldsymbol{\varepsilon} + {}^5\mathbf{C}_{\sigma\varepsilon_{x_1}} \vdots \Delta^3\boldsymbol{\varepsilon}_{x_1} + {}^5\mathbf{C}_{\sigma\varepsilon_{x_2}} \vdots \Delta^3\boldsymbol{\varepsilon}_{x_2}, \tag{4.73}$$

$$\Delta^3\boldsymbol{\mu}_{x_1} = {}^5\mathbf{C}_{\mu_{x_1}\varepsilon} : \Delta\boldsymbol{\varepsilon} + {}^6\mathbf{C}_{\mu_{x_1}\varepsilon_{x_1}} \vdots \Delta^3\boldsymbol{\varepsilon}_{x_1} + {}^6\mathbf{C}_{\mu_{x_1}\varepsilon_{x_2}} \vdots \Delta^3\boldsymbol{\varepsilon}_{x_2}, \tag{4.74}$$

$$\Delta^3\boldsymbol{\mu}_{x_2} = {}^5\mathbf{C}_{\mu_{x_2}\varepsilon} : \Delta\boldsymbol{\varepsilon} + {}^6\mathbf{C}_{\mu_{x_2}\varepsilon_{x_1}} \vdots \Delta^3\boldsymbol{\varepsilon}_{x_1} + {}^6\mathbf{C}_{\mu_{x_2}\varepsilon_{x_2}} \vdots \Delta^3\boldsymbol{\varepsilon}_{x_2}. \tag{4.75}$$

Tangent stiffness matrices:

$$\begin{aligned}
&\mathbf{C}_{\sigma\varepsilon} = \frac{1}{V}\mathbf{D}\tilde{\mathbf{K}}_{\mathrm{bb}}\mathbf{D}^T, \quad \mathbf{C}_{\sigma\varepsilon_{x_1}} = \frac{1}{V}\mathbf{D}\tilde{\mathbf{K}}_{\mathrm{bb}}\mathbf{H}_1^T, \quad \mathbf{C}_{\sigma\varepsilon_{x_2}} = \frac{1}{V}\mathbf{D}\tilde{\mathbf{K}}_{\mathrm{bb}}\mathbf{H}_2^T, \\
&\mathbf{C}_{\mu_{x_1}\varepsilon} = \frac{1}{V}\mathbf{H}_1\tilde{\mathbf{K}}_{\mathrm{bb}}\mathbf{D}^T, \quad \mathbf{C}_{\mu_{x_1}\varepsilon_{x_1}} = \frac{1}{V}\mathbf{H}_1\tilde{\mathbf{K}}_{\mathrm{bb}}\mathbf{H}_1^T, \quad \mathbf{C}_{\mu_{x_1}\varepsilon_{x_2}} = \frac{1}{V}\mathbf{H}_1\tilde{\mathbf{K}}_{\mathrm{bb}}\mathbf{H}_2^T, \\
&\mathbf{C}_{\mu_{x_2}\varepsilon} = \frac{1}{V}\mathbf{H}_2\tilde{\mathbf{K}}_{\mathrm{bb}}\mathbf{D}^T, \quad \mathbf{C}_{\mu_{x_2}\varepsilon_{x_1}} = \frac{1}{V}\mathbf{H}_2\tilde{\mathbf{K}}_{\mathrm{bb}}\mathbf{H}_1^T, \quad \mathbf{C}_{\mu_{x_2}\varepsilon_{x_2}} = \frac{1}{V}\mathbf{H}_2\tilde{\mathbf{K}}_{\mathrm{bb}}\mathbf{H}_2^T.
\end{aligned} \tag{4.76}$$

In contrast to the multiscale scheme with the $C^0$ continuity finite elements at the macrolevel, parallelization of the solving processes is not fully automated here since the UEL subroutine has to be used instead of UMAT, thus introducing some programming limitations. Still, the computing process is considerably accelerated by using a so-called "pseudo-parallelized" code, described in detail in [11]. Basically, all CPU power is at a time directed to the computations of only one finite element, where the RVEs for all Gauss integration points are considered simultaneously. Solving algorithm is fundamentally the same as presented in Table 4.1, where the only additions are needed in the context of the contributions of higher-order variables.

### 4.3.2 RVE failure conditions

With the formation of sharp localization zone inside the RVE, e.g. as depicted in Figure 4.17, the macrolevel material point represented by that particular RVE should not be able to carry the load anymore. The numerical model used so far considers that material remains the part of the continuum where in reality cracks should form, which is done by keeping the stiffness values close to zero by the application of the isotropic damage law. Basically, zero stiffness means that material in particular point does not provide any resistance to applied loading. When homogenization of the tangent stiffness is performed over the RVE, both the points inside and outside the localization zone are included in the calculation. When the localization zone is completely formed, there is practically no contribution to homogenized stiffness from this area, since the damage is maximum there. On the other hand, material points excluded from the localization zone still possess an intact or a slightly degraded stiffness, which makes a significant contribution to homogenized RVE stiffness tangents. In order to prevent this spurious contribution, a conditions used for the detection of the occurrence of fully formed localization zone are developed here and implemented in the UEL subroutines.

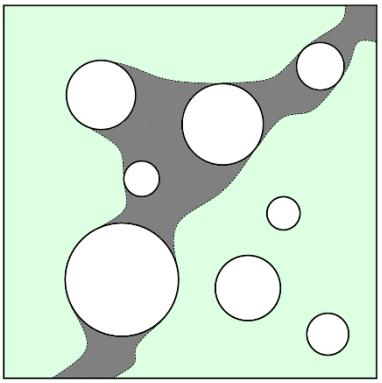

**Figure 4.17** Localization zone inside an RVE

First condition that has to be fulfilled is given as

$$\frac{A_d^{i-1}}{A_d} \approx 1, \tag{4.77}$$

where $A_d$ represents the localization area, i.e. area of all integration points which experienced the damage growth. If the ratio of the localization area from the last converged increment $A_d^{i-1}$ and the new converged value $A_d$ is close to the value of 1, it means that formation of the zone is most likely finished. Additionally, check over all integration points is performed to acquire

the maximum value of the damage variable $D^{\max}$ inside the localization zone, which leads to the second condition

$$D^{\max} > \alpha\,, \tag{4.78}$$

where $\alpha$ stands for a threshold value, usually taken very close to the critical value of damage. Two described conditions are necessary for the evaluation of the fully formed localization zone, since one without the other could provide the misleading information in some loading cases.

### 4.3.3 Numerical example

Considering the same numerical example analyzed by employment of the $C^0$-$C^1$ multiscale scheme, which computational model is depicted in Figure 4.12, elimination of the mesh dependency resulting from the discretization based on the local approach is achieved here by employing the $C^1$ continuity finite elements at the macrostructural level. Two different discretization densities are used, as shown in Figure 4.18. Material and model parameters remain the same as before, either at the micro- and macrolevel.

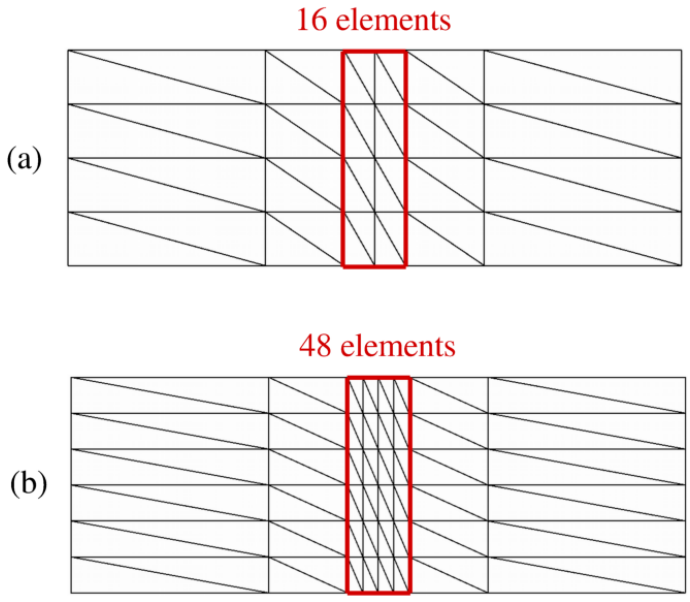


**Figure 4.18** Macrolevel discretization consisting of: (a) 48 and (b) 96 $C^1$ continuity triangular finite elements

Reaction force diagrams obtained by the two multiscale analyses with macroscale discretizations depicted above and by the one-scale damage model are given in Figure 4.19. Clearly, the results obtained by multiscale analyses are now basically identical, which confirms

that, generally, in the multiscale problems which involve the damage analysis at microlevel, macrolevel has to be discretized by numerical scheme that can regularize the strain localization phenomenon. A slight deviation from the results obtained by the one-scale damage model can be ascribed to the treatment of the nonlocality. While in one-scale model the initial nonlocal material behavior is degraded by the isotropic damage law as shown in (4.15) and (4.16), in multiscale analyses the nonlocality continuously changes with the evolution of the microstructure. It can be seen that the reaction forces are closest at the onset of softening and then start to deviate as the nonlinearity progresses, which confirms that the effective nonlocal parameter in the form of (4.56) is the most suited when linear material behavior is considered.

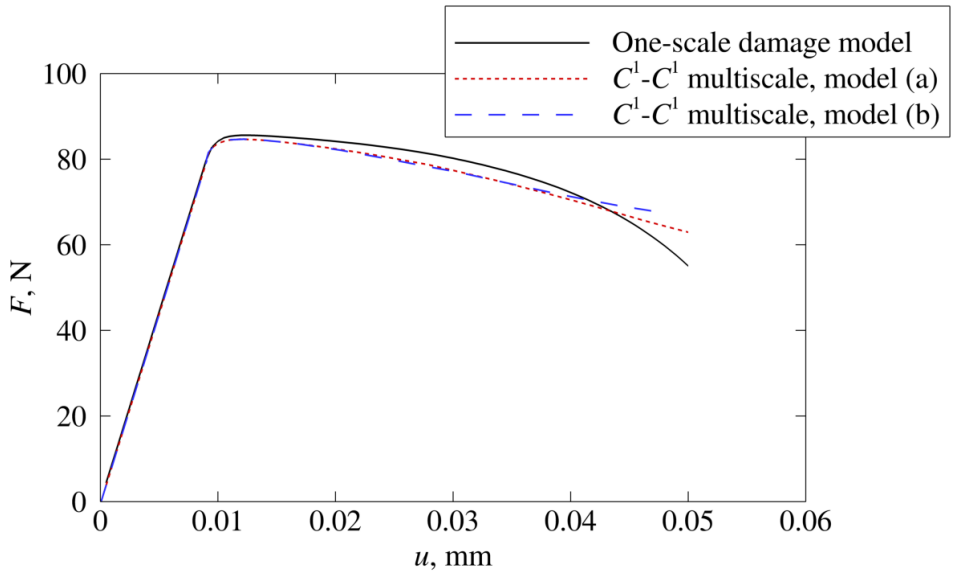


**Figure 4.19** Load-displacement diagrams obtained by two different macrolevel discretizations used in $C^1$-$C^1$ multiscale scheme and by one-scale damage model

# 4.4 Numerical examples

## 4.4.1 Rectangular plate subjected to tensile load

A rectangular plate subjected to tensile load, as depicted in Figure 4.20, is used for comparison of results obtained by one-scale and multiscale analyses of both homogeneous and heterogeneous materials. Horizontal displacement of $u = 0.05$ mm is applied, and both vertical edges are kept straight during the analyses by employment of the following boundary conditions: the second-order derivatives of the displacement component in the normal direction,

$u_{1,11}$ and $u_{1,22}$, mixed derivatives, $u_{1,12}$ and $u_{2,12}$ and the first-order derivatives associated with the shear deformation, $u_{1,2}$ and $u_{2,1}$, are set to zero. The indices 1 and 2 refer to the Cartesian coordinates *x* and *y*, respectively. Discretization of the plate is made very simple, by utilization of two $C^1$ continuous triangular finite elements, but considering the 13 integration points that each element has, acceptable accuracy is expected.

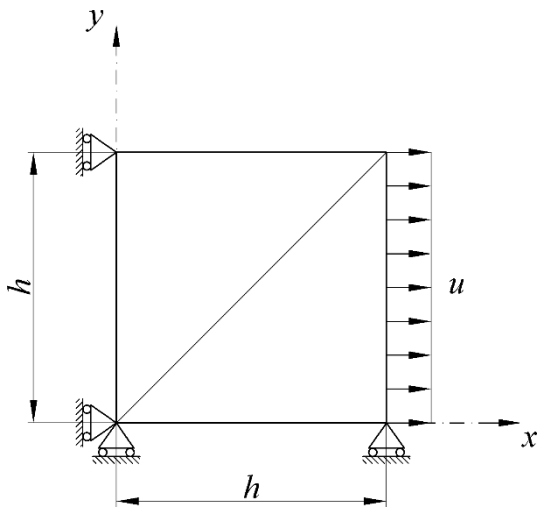


**Figure 4.20** Computational model of rectangular plate subjected to tensile load with $h$ = 10 mm

Material properties as well as the damage modeling characteristics, which include linear softening (2.6) and Mazars' equivalent elastic strain (2.8), are the same as in the previous example. Homogeneous MVE of the same dimensions and microstructural length scale is considered likewise, while the heterogeneous microstructure is modeled by the RVE shown in Figure 4.21. Basically, it is the same RVE as RVE_0 depicted in Figure 3.15, only the side length is now set to $L = 2.6$ mm, and the discretization is changed to $C^1$ continuity triangular finite elements. Presented RVE is utilized in two $C^1$-$C^1$ multiscale analyses where different microstructural length scale parameters are included. In order to induce only a mild strain localization, or a very diffused damage appearance over the RVE with no sharp gradients, the microstructural length scale of $l_{\text{micro}} = 0.6608$ mm is employed, which, together with the RVE size of $L = 2.6$ mm gives the effective macrostructural internal length scale of $l_{\text{eff}} = 1$ mm, according to (4.56). Diagram depicting the dependence of the reaction force at the right edge of the plate on the imposed displacement is shown in Figure 4.22. Distribution of the damage variable in several characteristic RVEs at the ending point of the analysis is presented in Figure 4.23. Considering the dispersed, non-localized distribution of the damage variable which has

reached the critical value in most of the RVEs, it can be concluded that the analysis reached the failure stage.

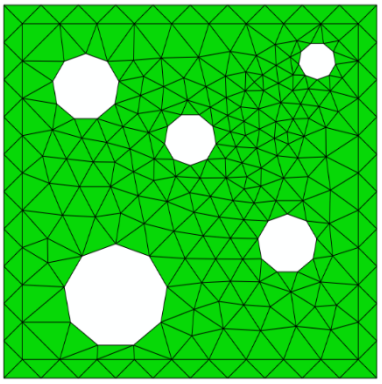

**Figure 4.21** RVE described by the size $L$ = 2.6 mm, average hole radius $r_{ave} = 0.559$ mm and porosity $e$ = 0.13

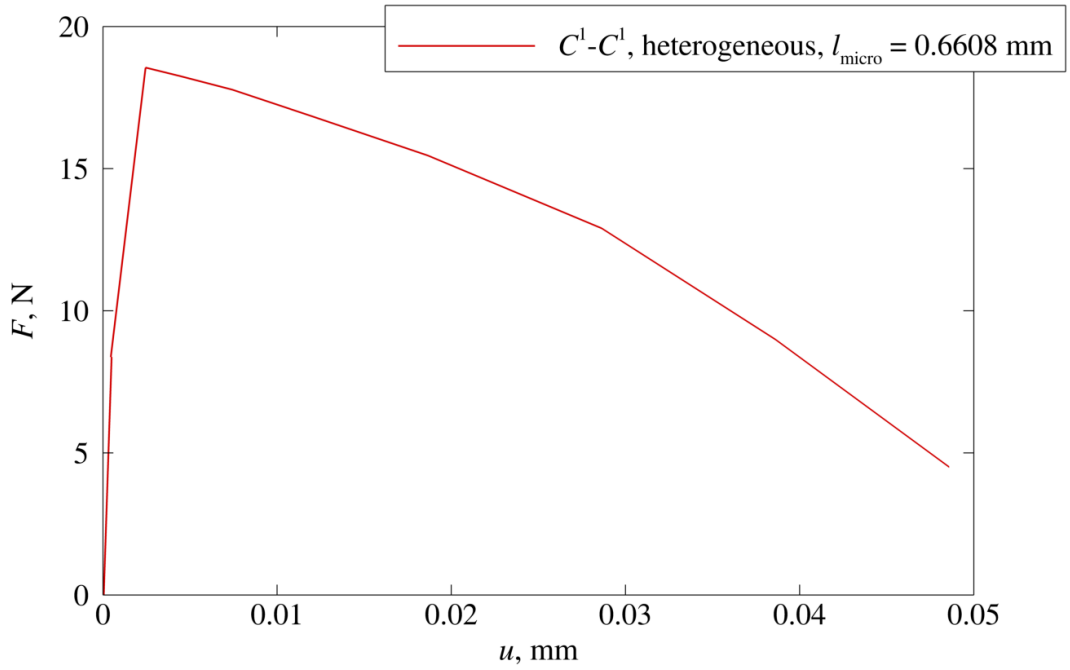


**Figure 4.22** Load-displacement diagram obtained by $C^1$-$C^1$ multiscale analysis for heterogeneous microstructure of internal length scale $l_{micro} = 0.6608$ mm

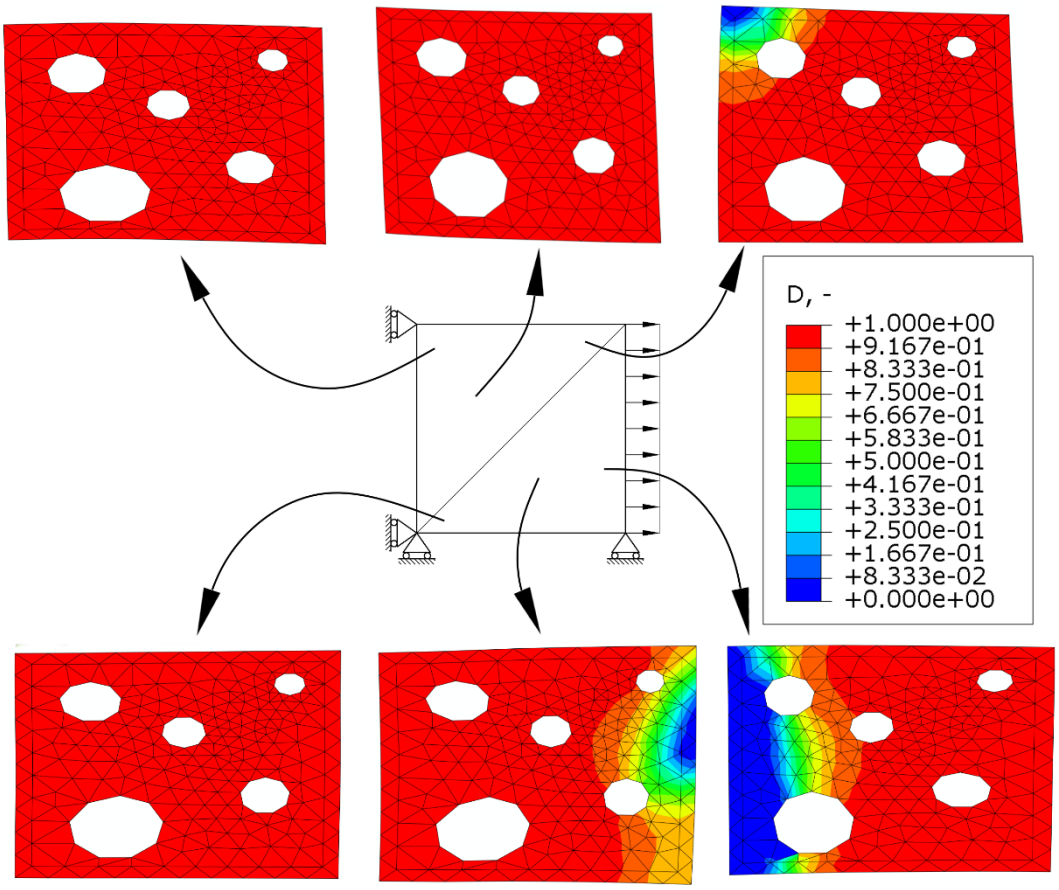


**Figure 4.23** Distribution of damage variable $D$ over some characteristic RVEs for $l_{\text{micro}} = 0.6608$ mm at failure stage

An additional multiscale analysis is made with a smaller microstructural internal length scale of $l_{\text{micro}} = 0.025$ mm, which leads to the formation of the sharp localization band over the RVE. Size of the RVE is left as $L = 2.6$ mm, which gives the effective internal length scale at the macrostructural level less than $l_{\text{eff}} = 1$ mm, but considering the nonlinear intricacy of the model, making the comparisons based on relation (4.56) might not lead to good conclusions anyway. Structural response of the analysis is given in Figure 4.24, and the distribution of the damage over some characteristic RVEs is depicted in Figure 4.25. Evidently, softening is now initiated at smaller value of the imposed displacement and lower reaction force level, which can be attributed to intense localizations obtained at the RVE level. The localization bands in the RVEs closer to the left boundary managed to stabilize, so it can be assumed that RVE failure conditions (4.77) and (4.78) have been satisfied there, and that the stiffness is accordingly degraded in appropriate macrostructural integration points in order to mimic the loss of material integrity. Growth of the damage at the RVE boundaries, as can be seen from Figure 4.25, is an effect of the enhanced compliance of the generalized periodic boundary conditions and can be

considered as spurious, but ultimately, it does not affect the formation of the localization zones. Overall, RVE responses show the physically acceptable behavior, which can be interpreted as follows. The localization is the most intense in the vicinity of the left edge of the computational model where microfuctuations are heavily influenced by the straight edge boundary conditions, allowing the RVEs to expand considerably only in the direction of the loading. By moving away from the left edge, localization gets milder until almost none can be noticed near the loaded right edge, where the material shows more compliancy in all directions, thus preventing the formation of the localization.

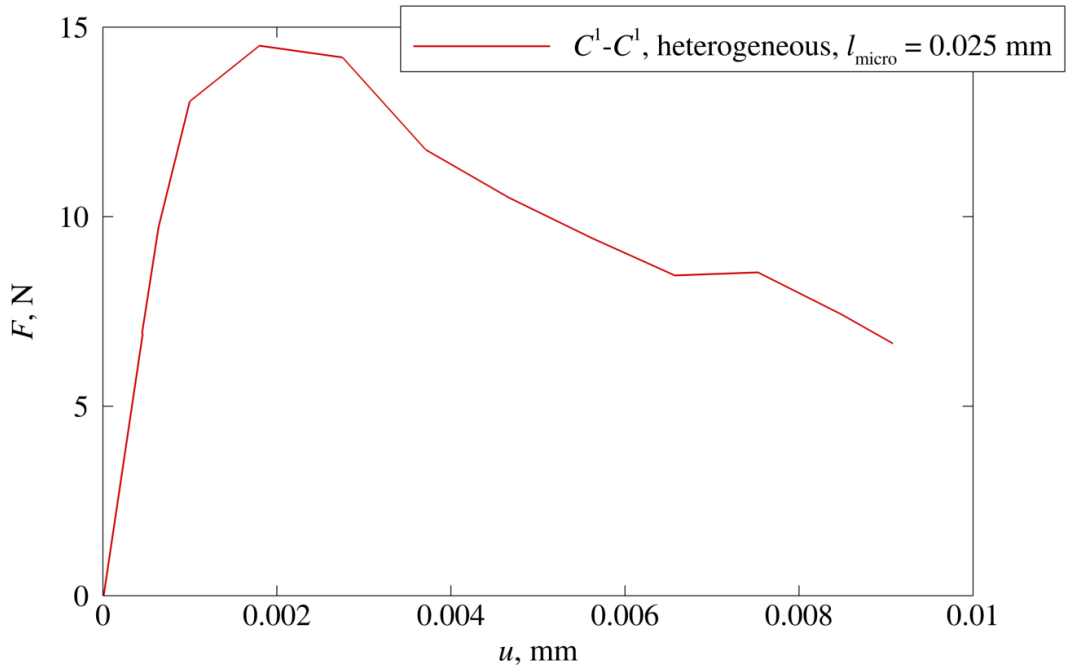


**Figure 4.24** Load-displacement diagram obtained by $C^1$-$C^1$ multiscale analysis for heterogeneous microstructure of internal length scale $l_{micro} = 0.025$ mm

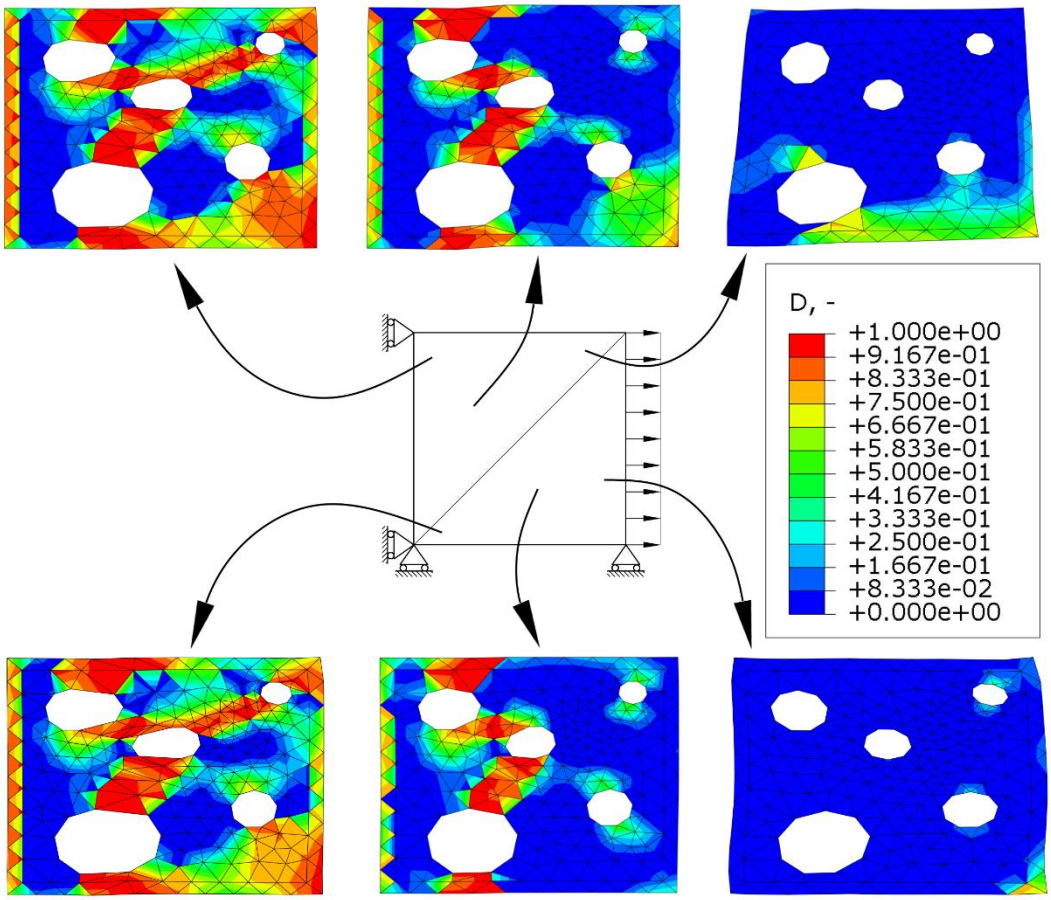


**Figure 4.25** Distribution of damage variable $D$ over some characteristic RVEs for $l_{\text{micro}} = 0.025$ mm at failure stage

Beside the multiscale analyses where heterogeneous microstructure is considered, multiscale analysis with the homogeneous microstructure is carried out, where the effective length scale of $l_{\text{eff}} = 1$ mm is modeled with the microstructural nonlocality of $l_{\text{micro}} = 0.6608$ mm and MVE side length of $L = 2.6$ mm. The comparison of the multiscale analyses results is made with solutions obtained by the one-scale damage model, where both the homogenous and the heterogeneous material are taken into consideration. One-scale damage analysis where homogeneous microstructure is considered is carried out by employing the Aifantis theory with $l = l_{\text{eff}} = 1$ mm, while in the case of heterogeneous microstructure damage model based on the strain gradient theory presented in Chapter 3 is used. Therein, the calculation of the tangent stiffness matrices is made on the RVE of the side length $L = 3.46$ mm, which can be obtained by relation (3.70) and considering that $l = 1$ mm. For the comparison purposes, it can be said that, through the damage constitutive model described by (3.28) and (3.29), the one-scale damage model assumes in a way an even distribution of the damage over an RVE, which

coincides more accurately with the assumption of no sharp localization zones, as presented in Figure 4.23. Structural responses of all conducted analyses are plotted in Figure 4.26.

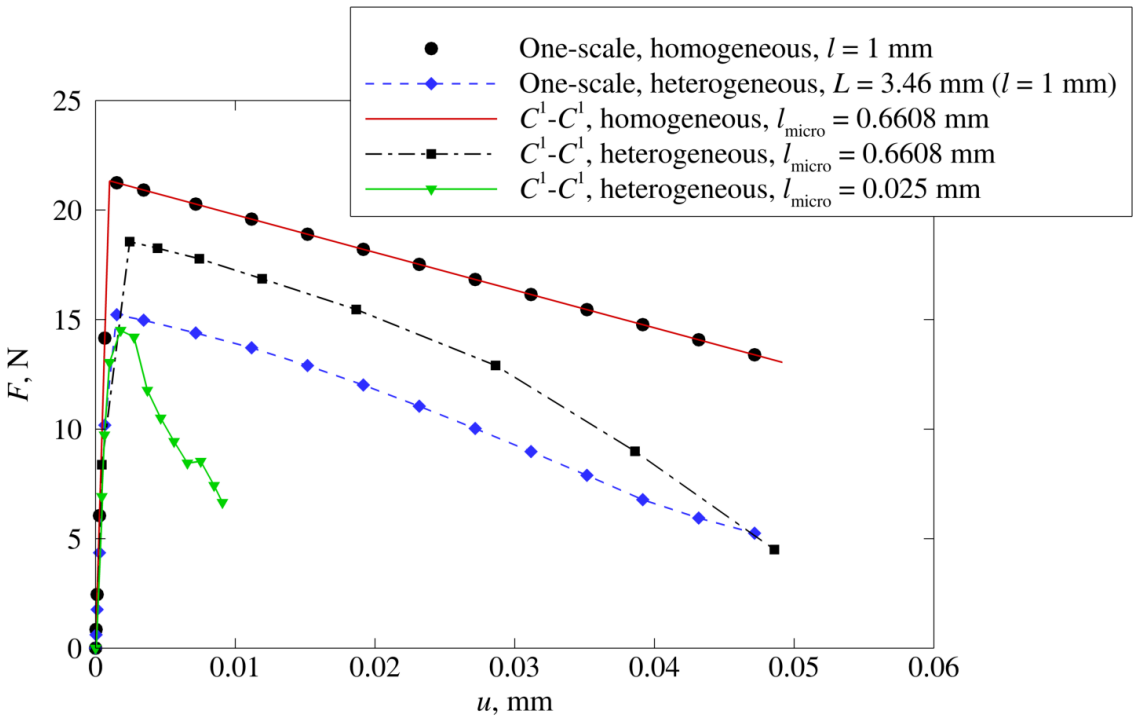


**Figure 4.26** Load-displacement diagrams obtained by one-scale damage models and $C^1$-$C^1$ multiscale scheme for materials consisting of homogeneous and heterogeneous microstructures

As can be seen from Figure 4.26, one-scale damage analysis and multiscale analysis for the homogeneous microstructure provide identical results, which is expected due to resulting constant macrolevel strain field and consequential absence of the strain gradients. For the one-scale and multiscale model where heterogeneous microstructure with $l_{\text{micro}} = 0.6608$ mm is considered, similar qualitative behaviors of the reaction forces can be noticed. Although the same macrostructural internal length scales are taken into account by employing the relations (3.70) and (4.56), in case of the one-scale damage model softening starts at a lower reaction force level than for the multiscale model. The reason for such response can be found in slightly different treatments of the nonlocal material behaviors, since the one scale damage model employs the strain gradient theory, and the multiscale model is based on the Aifantis theory. As presented above, multiscale analysis which includes the smaller microstructural internal length scale parameter of $l_{\text{micro}} = 0.025$ mm leads to the formation of the intense localization bands over the RVEs. Even though the bands itself occupy the smaller areas of the RVEs, due to very

abrupt rise of the damage inside the band, the homogenized results lead to more brittle macrostructural response.

### 4.4.2 Plate with an imperfect zone subjected to tensile load

Following example is already analyzed by both $C^0$-$C^1$ and $C^1$-$C^1$ multiscale procedures previously in this chapter, with the consideration of the homogeneous microstructure. Here the heterogeneous microstructure is included via the RVE presented in Figure 4.21. In order to get intense localization zones, similarly as in the previous example of rectangular palate, the microstructural internal length scale is taken as $l_{\text{micro}} = 0.025$ mm. The computational model of the macroscale analysis is shown in Figure 4.12, and all material parameters and softening characteristics are kept the same as described in Subsection 4.2.2. Discretization of the macrostructural model is made by employing 48 triangular finite elements, as it is shown previously in the thesis in Figure 4.18a. Considering that such finite element mesh density provided converged results in case of the homogenous microstructure, as can be seen from Figure 4.19, it can be assumed that accurate solutions will also be reached in case of the heterogeneous microstructure. Besides, a finer discretization would lead to a significant slowing down of the already very time consuming computational process. This is a consequence mainly of the computationally very expensive inverse calculation of the RVE structural matrix $\mathbf{K}_{\text{aa}}$, needed for the formation of the condensed stiffness matrix $\tilde{\mathbf{K}}_{\text{bb}}$, as given by (3.60). Load-displacement curve obtained by the presented model is depicted in Figure 4.27, where also the previously obtained structural response for the homogeneous microstructure is plotted for the comparison purpose. Obviously, the softening is initiated at a smaller reaction force level for the heterogeneous material. After the peak is reached, a very steep drop of the reaction force can be noticed. In the peak stage of the analysis, area of the localization zone is already formed at the macrostructural level, and few subsequent converged incremental steps lead only to the rise of the deformation level in the center of the zone. It should be mentioned that, in order to cross the peak, convergence criteria have to be relaxed slightly for the ABAQUS/Standard solver. However, the continuation of the analysis is not possible anymore at some point after the peak when the problems with the convergence increase, as shown in Figure 4.27. Deformed shape of the plate with the distribution of the strain tensor component in the direction of the $x$ Cartesian axis is depicted in Figure 4.28 for the final stage of the analysis. Due to very sparse mesh, smooth visualization of the variables at the macrolevel is difficult to obtain. Physically

acceptable localization of the deformation can clearly be seen from the figure, which indicates that, for the case of heterogeneous microstructure, the initiation of the damage and subsequent position of the macrocrack can successfully be captured by the proposed $C^1$-$C^1$ multiscale algorithm.

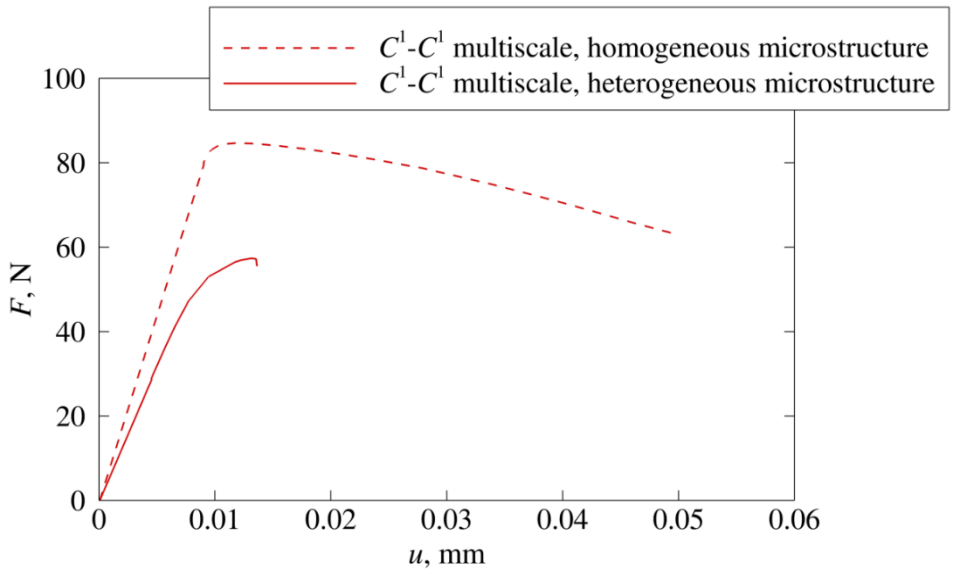


**Figure 4.27** Structural responses of the plate subjected to tensile load obtained by the $C^1$-$C^1$ multiscale scheme for homogeneous and heterogeneous microstructure

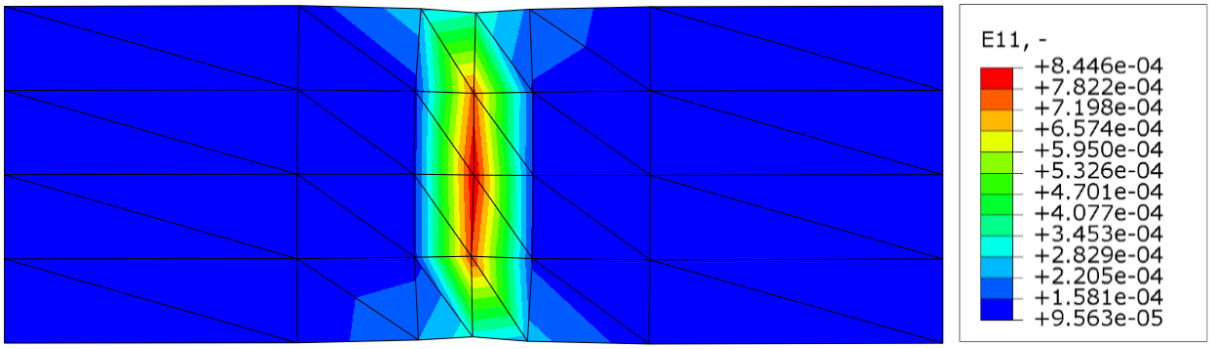


**Figure 4.28.** Deformed shape with the distribution of strain component $\varepsilon_{11}$ for heterogeneous microstructure with the internal length scale $l_{\text{micro}} = 0.025$ mm at final stage of the analysis

Distribution of the damage over several characteristic RVEs in the macrostructural localization zone is presented in Figure 4.29. It can be observed that the most intense damage bands are formed in the middle of the plate, where the localization of the deformation is the strongest. By moving away from the localization, damage bands at the microlevel are becoming milder, until they eventually become negligible and disappear. Obviously, material behavior can be interpreted as physical both at micro- and macrolevel.

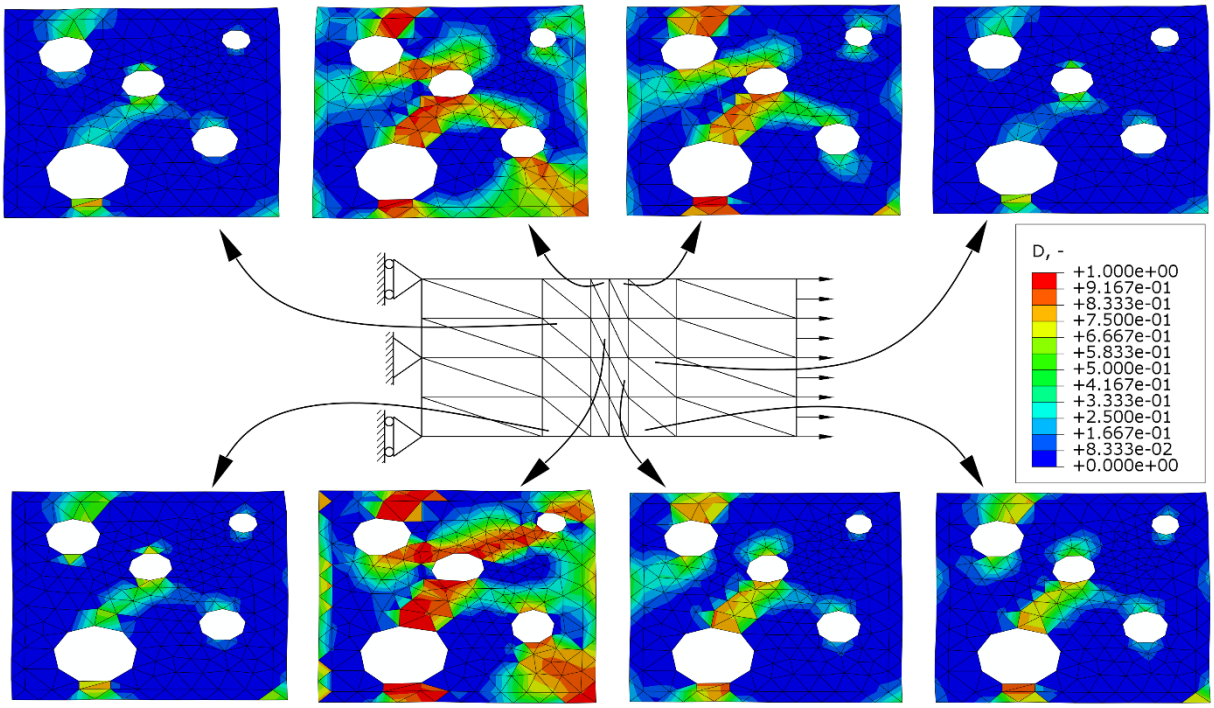


**Figure 4.29** Distribution of damage variable *D* over some characteristic RVEs for $l_{\text{micro}} = 0.025$ mm at final stage of the analysis

### 4.4.3 Shear band problem

In the final example $C^1$-$C^1$ multiscale scheme is employed for the analysis of the shear band problem, already considered in Chapter 3. Although most of the computational data is the same as for the one-scale analysis model, here it is displayed once again for the clarity reasons. Computational model for the analysis with the heterogeneous microstructure is given in Figure 4.30a. The compressive loading is prescribed both at top and bottom edge of the model using a direct displacement control, where the vertical displacement of $v = 0.08$ mm is imposed. Matrix material of the RVE is characterized by the Young's modulus $E = 20000$ N/mm$^2$ and the Poisson's ratio $\nu = 0.2$. For modeling of damage responses, the modified von Mises' equivalent elastic strain measure (2.10) together with the exponential softening law (2.7) is used, for which the parameters are set to: $\kappa_0 = 0.0001$, $\alpha = 0.99$ and $\beta = 300$. To induce localization, the reduced value of $\kappa_0 = 0.00005$ as a material imperfection is imposed on the small region of $h/10 \times h/10$ as shown in Fig. 24a. Since both the symmetry plane and the loaded edge have to remain straight during the analysis, the boundary conditions for the straight edge are enforced there. Herein, the second-order derivatives of the displacement component in the normal

direction, $u_{2,11}$ and $u_{2,22}$, the mixed derivatives, $u_{1,12}$ and $u_{2,12}$, and the first-order derivatives associated with the shear deformation, $u_{1,2}$ and $u_{2,1}$, are suppressed. The indices 1 and 2 refer to the Cartesian coordinates *x* and *y*, respectively.

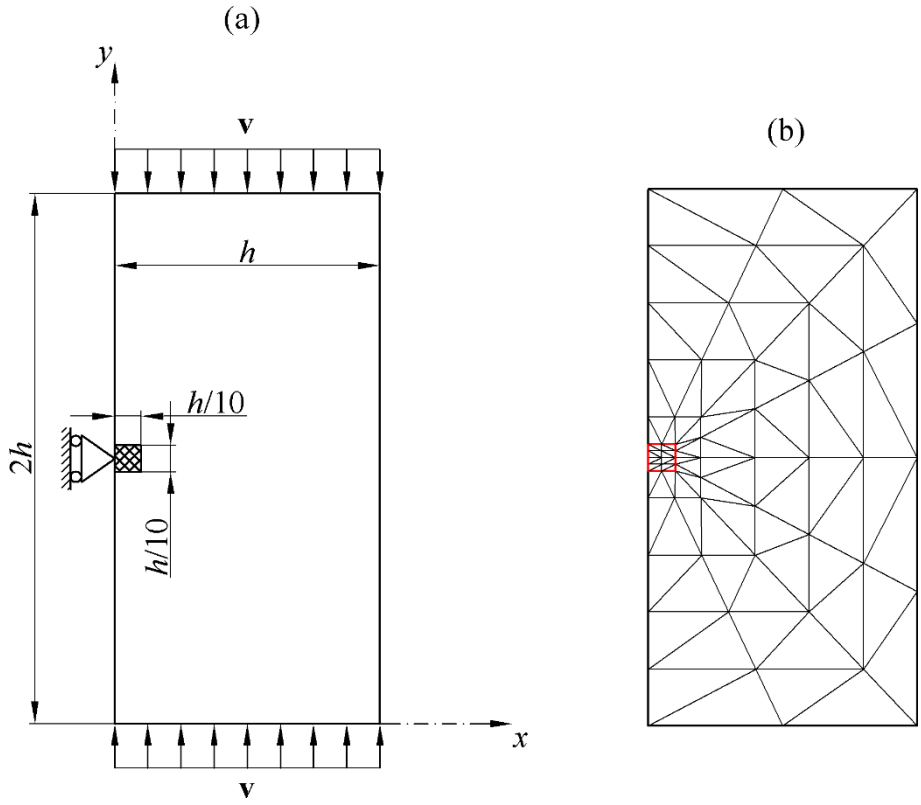


**Figure 4.30** (a) Geometry and boundary conditions of the plate with an imperfect zone subjected to compressive load (*h* = 60 mm) and (b) discretization consisting of 96 $C^1$ continuous triangular finite elements

Finite element mesh of the whole model is depicted in Figure 4.30b. Because the uniform mesh would lead to much higher number of finite elements, and therefore a more time-consuming computation, a non-uniform mesh is employed. Once again, finite elements might seem too large in order to obtain converged results, but considering the 13 integration points, this should not present the problem. Homogenous microstructure is modeled by the MVE of side length $L = 2.6$ mm, as presented in Figure 4.14, while the microstructural nonlocal behavior is described by the parameter $l_{\text{micro}} = 0.6608$, leading to an effective macrostructural internal length scale $l_{\text{eff}} = 1$ mm. On the other hand, for the modeling of heterogeneous microstructure RVE given in Figure 4.21 is used, where the same side length of $L = 2.6$ mm is considered, but the microstructural size of the nonlocal interactions is set to $l_{\text{micro}} = 0.025$ mm, similarly as in

previous example. Load-displacement curves for both homogeneous and heterogeneous microstructure are given in Figure 4.31, where again, a similar situation as in the previous example can be observed. Softening initiation happens at a smaller reaction force level for the heterogeneous material, while the subsequent drop, although pronounced, is very short due to emergence of convergence problems in the ABAQUS solver.

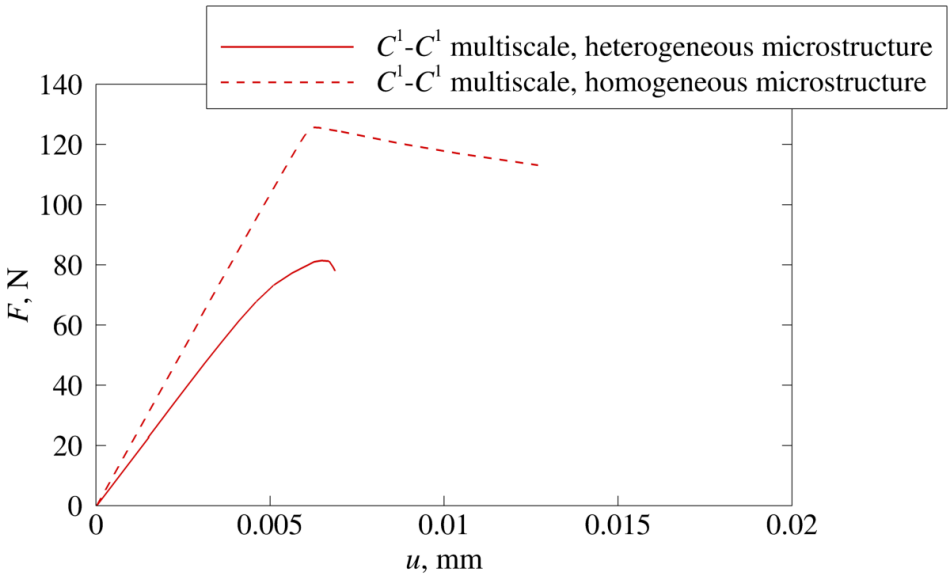


**Figure 4.31** Structural responses of the plate subjected to compressive load obtained by the $C^1$-$C^1$ multiscale scheme for homogeneous and heterogeneous microstructure

Distribution of the equivalent elastic strain at the onset of softening for heterogeneous material can be seen in Figure 4.32. Obviously, localization zones have started to develop as expected for the shear band problem.

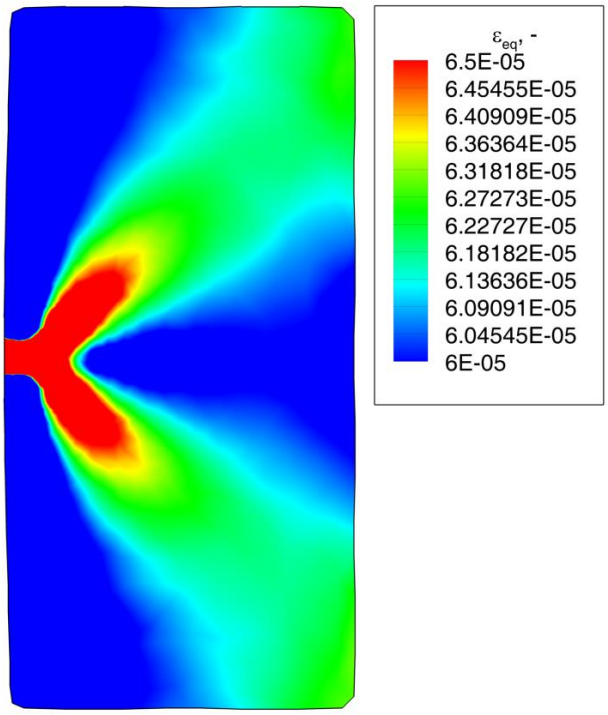


**Figure 4.32** Distribution of the equivalent elastic strain $\varepsilon_{\text{eq}}$ for heterogeneous microstructure with the internal length scale $l_{\text{micro}} = 0.025$ mm at the onset of softening

Distribution of damage over several characteristic RVEs in the macrostructural localization zone at the onset of softening is presented in Figure 4.33. By observing the small region where material parameters are decreased, it can be clearly seen that the developed damage zones are more intense in the RVEs in the lower part of the plate. Besides, direction in which the damage has evolved so far suggests that the lower shear band would eventually become dominant. Similar situation is already predicted by using the one-scale damage model where microstructural evolution is excluded from the analysis, as discussed in Chapter 3 and depicted in Figure 3.33. Although a more complex RVE is used in that analysis, a similar evolution of the microstructural localization zones as depicted in Figure 4.33 can be expected for that RVE case and employment of the true multiscale analysis presented in this chapter, but this has yet to be verified. If the verification turns out to be positive, it can be stated that the results obtained by the presented multiscale algorithm provide a strong confirmation of the applicability of the one-scale algorithm in problems where heterogeneous microstructure is observed.

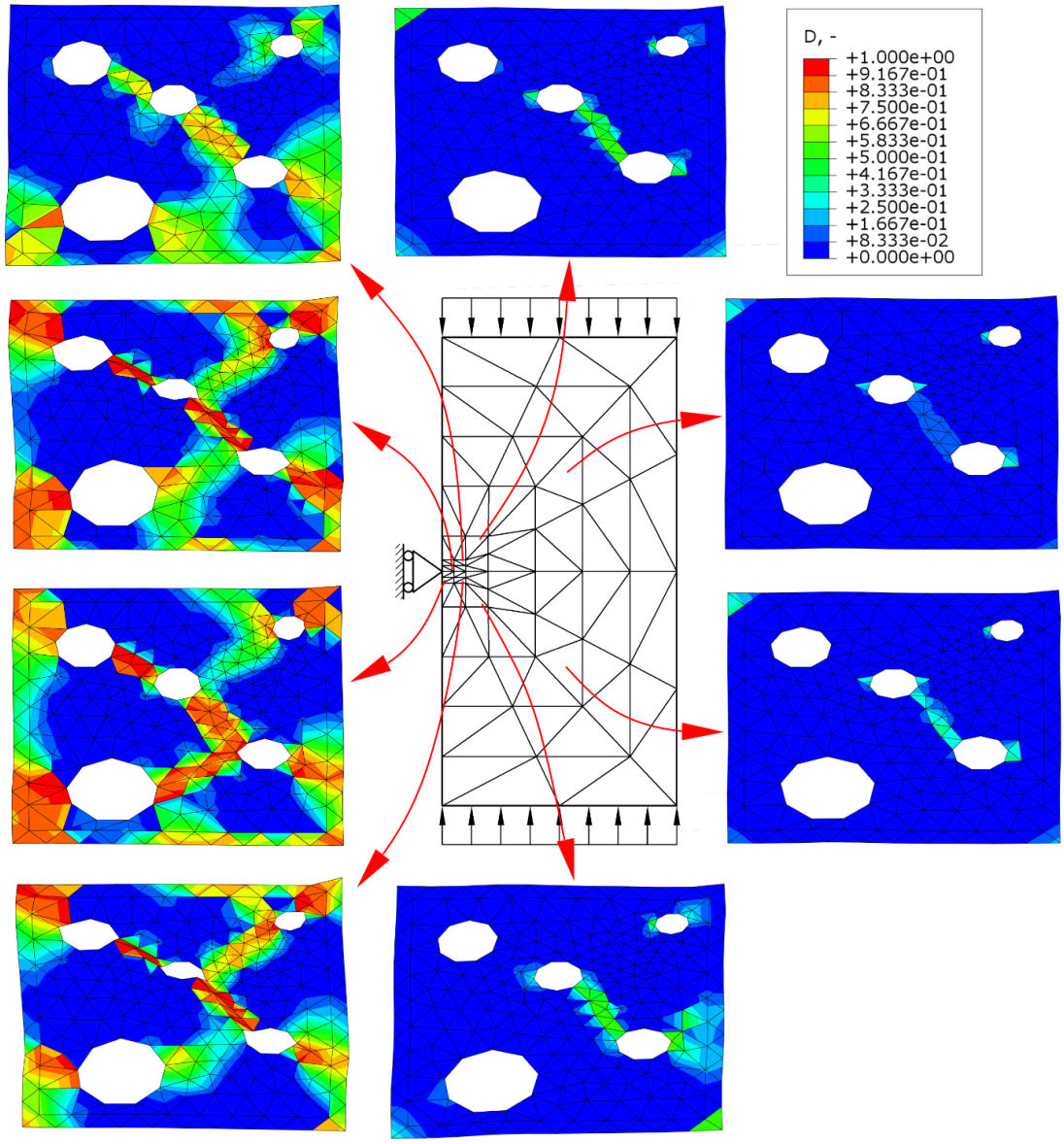


**Figure 4.33** Distribution of damage variable $D$ over some characteristic RVEs for $l_{\text{micro}} = 0.025$ mm at the onset of softening

### 4.4.4 Discussion

As obvious from the results of the considered numerical examples, $C^1$-$C^1$ multiscale scheme is able to successfully predict the initiation of the localization at the macrostructural level. By taking into account that the constitutive behavior of the macrostructure is obtained directly from the analysis of the evolving heterogeneous microstructure, it can be said that such algorithm represents a step forward with respect to the one-scale damage model presented in Chapter 3. Although the structural responses can be qualitatively interpreted as physically acceptable, additional comparison with the experimental results is needed to confirm the quantitative

validity of the obtained numerical results. Considering that the localized deformation is transformed into a diffused deformation field over an RVE by the application of homogenization, it is questionable if the homogenized constitutive response can accurately describe the softening process at the macrolevel after the initiation of the localization. Albeit the macrostructural load-displacement curves might be different than in reality, the compensation comes in form of the ability of the algorithm to capture the RVE failure and incorporate it in the macrostructural constitutive behavior, which should bring the final loss of mechanical integrity closer to the actual solution. It should also be stressed that, once the formation of the initial localization zone at the macrolevel is reached, some convergence issues can be noticed in the computational process, and in order for the analysis to continue, appropriate convergence criteria have to be relaxed slightly. It is not yet clear why this happens, and further research is needed to reach some reasonable conclusions. One of the possible explanations for such behavior could be that there is a too large difference in the initial stiffness between the region where material is purposely degraded and rest of the material, which causes extremely high spatial gradients of the variables at the interface. This in turn causes a very intense softening, as suggested by reaction force diagrams in Figure 4.27 and Figure 4.31, which cannot be resolved by ABAQUS solver. In addition, due to a very large difference between the values in the global stiffness matrix once the softening is initiated, the problems connected with the ill-posedness possibly arise. Hence, effect of the increase of the appropriate initial material parameters in the degraded regions should be investigated in more detail.

Furthermore, a discussion should be made regarding the principle of the scale separation, which is, from the purely physical point of view, undoubtedly violated in the numerical examples presented above where strong localizations are observed at the microlevel. Generally, by the formation of the computational model, all numerical methods necessarily include some degree of approximation and simplification of the real life problems. While it is desirable to mathematically describe the real physics as accurately as possible, sometimes, primarily due to shortage of the available computational resources, a higher degree of approximation is needed in order to obtain specific results. And the beauty of the numerical methods lies in the fact that the substantial simplification of the problem does not automatically yield inaccurate results. On the contrary, sometimes the simpler, more elegant modeling solutions tend to be more efficient than ones where every possible physical aspect is included. Whether this is the case with the proposed multiscale approach where the fulfillment of the principle of scale separation is not considered crucial, it has yet to be demonstrated. Numerical

results obtained in the examples above by all means make sense from the physical perspective, which is definitely an encouraging fact.

However, presented multiscale algorithm could potentially be employed without the violation of the scale separation principle. The key is to eliminate the sharp fluctuations of the strain field over the RVE, which could be done by decreasing the size of the RVE and increasing the microstructural length scale parameter, thus resulting in a diffused damage appearance over the RVE. In such way a physically more realistic situation could be obtained, where the consistency of the strain fields between the scales would be preserved. Numerical example of the rectangular plate, where the heterogeneous microstructure with larger microstructural parameter $l_{\text{micro}} = 0.6608$ mm is considered leading to results depicted in Figure 4.22 and Figure 4.23, might be observed as such a case.

Theoretically, the violation of the principle could also be avoided by development of the order of the computational homogenization higher than two, where continuum of the same order would be used at the macrolevel. By doing so, the strain state of the RVE where sharp localization is present could be transferred at the macrostructural level more consistently. Likewise, the RVE boundary conditions could be described more precisely. Thereby, the higher number of the Taylor order terms corresponding to the higher number of the macrostructural degrees of freedom could easily model the sharp distributions of the RVE boundary displacements. Of course, it is questionable whether this could be done in the finite element framework, due to significant complication of the computational problem with the increase of the macrolevel continuity order. However, it is known that some of the available numerical methods can model the higher-order continuity much easily than finite element method, like meshless numerical schemes for example, which could definitely be one of the possible research directions in multiscale damage analysis in order to preserve the scale separation.

# 5 Conclusions

The first and the main objective of the research presented in this thesis was a development of a mathematically consistent continuum model that could realistically describe the initiation and subsequent growth of the damage. When it comes to classical continuum theory, the principal problem in modeling of the localization of the deformation, which is always associated with the damage phenomenon, is that it cannot be objectively described due to mathematical inconsistencies that can arise at the onset of the softening. Namely, loss of positive-definiteness of the tangent stiffness matrix is induced as a result of material instabilities, which eventually leads to the loss of ellipticity of the equilibrium rate equations and consequentially to loss of the well-posedness of the rate boundary value problem. Displacement discontinuities can arise in such circumstances leading to an unstable development of the damage which cannot be uniquely described anymore, thus yielding a non-physical material behavior. In the framework of the finite element solution scheme, numerical results become strongly dependent on the fineness and orientation of the spatial discretization, where the damage localizes in the smallest possible finite element or a narrowest band of the finite elements, whereby an objective convergence cannot be achieved.

In order to eliminate the nonphysical material responses associated with the employment of the damage models based on the classical continuum mechanics, which relies on the local approach, a nonlocal constitutive behavior may be introduced. In that way the stress state of the material point is, in addition to its own deformation state, governed by the deformation state of the neighboring material as well. Size of the material domain which participates in the interaction is defined by the internal length scale parameter that has to be related to the microstructure of the material, and which acts as a localization limiter, thus preventing the displacement discontinuities and ensuring a smooth damage field. In this thesis, the strain gradient continuum theory is employed for the description of the nonlocal material behavior, where the internal length scale is introduced in the model through the constitutive higher-order tensors. The nonlocal action is due to continuity of the displacement field carried out by the strain gradient terms which, although local quantities in the mathematical sense, include the information about the deformation of the surrounding material.

With the strain gradient theory as a foundation, a computational approach for the modeling of quasi-brittle damage phenomena is proposed. The model is based on the isotropic damage law so that right-hand side of the constitutive relations are pre-multiplied by the same term governing the damage process. The growth of the damage causes this term to decrease, which not only ensures the softening of the material by reducing the values of the constitutive tensors, but it also affects the size of the microstructural interaction domain in the same way. The latter is mandatory for the correct description of the final localized deformation band, i.e. a macrocrack, which comes into existence from the scattered network of microcracks at the onset of the softening, when the size of microstructural interaction domain is the largest. While the physical formation of the cracks is not considered by the model, they are represented virtually by the integration points where all the stiffness is lost, i.e. where the damage variable is close to the critical value. The highly non-linear softening model is embedded into the triangular $C^1$ finite element and implemented into the FE software ABAQUS/Standard via UEL subroutine.

The capabilities of the proposed computational strategy to simulate the strain localization are demonstrated in several benchmark examples in which the verification of the derived algorithm is performed by comparison with the available solutions from the literature. Both homogeneous and heterogeneous materials are considered by employing the second-order homogenization to obtain the required material stiffness matrices, a procedure which is mainly used in the multiscale computational approach. It is observed that the damage response depends on the RVE size, porosity and average hole radius of the heterogeneous material. Furthermore, constitutive behavior resulting from the heterogeneous microstructure evokes the structural anisotropy in the macrostructural computational model, which can be observed in some numerical examples as an asymmetrical evolution of the damage zone. The structural responses clearly indicate that heterogeneous material has a much lower load-carrying capacity, as expected. In addition, reaction forces rarely drop to values close to zero, which would be expected when the fully formed localization zone crosses the computational model. Explanation for such behavior can be found in the definition of the damage variable, which is a function only of the elastic strain tensor. Since the damage variable in the constitutive model degrades the classical and higher-order material tensors by the same intensity, improvement could probably be made by adding in the definition of the damage variable the dependency on strain gradient terms as well.

In contrast to the results obtained in the literature, where the conventional implicit gradient damage formulation is adopted, the proposed damage algorithm yields a fully localized

deformation band without any notice of spurious damage growth. The conducted analyses demonstrate that the proposed damage model based on the strain gradient continuum theory is able to successfully predict the initiation of the damage growth as well as to describe the subsequent localization of the deformation into a macroscopic crack, meaning that a complete regularization of the mathematical model of the material failure behavior can be achieved.

The second part of the thesis is concerned with the multiscale modeling of the materials exhibiting the strain localization phenomena, whereby the evolution of damage is observed at the microstructural level described by an RVE. Regarding the employment of the computational homogenization approach in multiscale analysis of damage, several key issues need to be addressed here when the sharp localization bands form at the RVE level. Objectivity of the macrolevel results cannot be achieved by using the local continuum approach, which can be remedied by the application of the second-order computational homogenization, where higher-order continuum is employed instead of the classical one. Furthermore, for the increasing size of the RVE, which generally should not have an effect on the homogenized material behavior due to representative character of the RVE, increased brittleness of the macrostructural response can be noticed, compromising in this way the objectivity of the numerical results. The last issue is of the physical nature, and it is concerned with the violation of the principle of separation of the scales when the localization is obtained at the microlevel. Since the RVE represents an actual portion of the material around the macrolevel integration point, it is believed that the occurrence of localization phenomenon across the RVE would actually mean that a localization zone of the same dimensions should be present in the macromodel. Representativeness of the RVE comes in the question then, and so does its ability to describe the strain state of the locally surrounding material. All of the problems listed here can be solved to some extent by introducing the effective discontinuities and traction-separation laws at the macrolevel, which can be calculated from the localization bands that occur across the RVEs. However, an efficient solving procedure still has to be developed, and therefore the applicability of the second-order computational homogenization to the localization problems is examined in more detail in this thesis.

In order to simplify the problem at the microscale, continuum theory based on modified case of Mindlin's form II strain energy density is employed, in which only a classical constitutive tensor exists and the size of the nonlocal interaction zone is explicitly assigned by the internal length scale parameter. Triangular $C^1$ finite element for softening analysis is derived in the same manner as is the case with strain gradient theory, by the application of the isotropic damage law to the constitutive relations of the gradient elasticity theory. Applicability of the

finite element is tested on the RVE example where several loading conditions are applied, and the results show the expected material behavior. It is found that change in the size of the nonlocal interaction zone leads to the formation of completely different localization paths.

Next, the $C^0$-$C^1$ macro-micro multiscale scheme with the appropriate scale transitions is derived, in order to examine the influence of the classical continuum at the macrolevel. The multiscale procedure is implemented into the FE software ABAQUS/Standard by using the UMAT subroutine for the macrolevel, and UEL subroutine for the microlevel. As expected, the results are dependent on the discretization and the convergence to physically acceptable solution cannot be reached. In contrast, $C^1$-$C^1$ multiscale scheme developed in [73] and applied to considered damage problem shows almost identical structural responses for different finite element mesh densities, and the results are comparable with the one-scale damage model solution. RVE failure conditions used for the assessment of the complete formation of the localization zone across the RVE are derived. The stiffness of the macrostructural integration point is then manually updated to the value of zero, which emulates the formation of the crack. An example is considered where no formation of the localization at the macrolevel is expected due to absence of the localization triggering mechanisms, and comparison is made between the macrostructural responses for several different RVE cases. When a larger microstructural length scale is used, damage is spread more even across the RVE and the results are then qualitatively comparable to the one-scale damage model. For the smaller length scale which induces a significant localization at the microlevel, much brittle macrostructural material behavior is obtained. Additionally, two examples which include the localization of the deformation at the macrostructural level are considered, where it is shown that the presented multiscale damage model can successfully describe the initiation of the localization.

# Životopis

Filip Putar rođen je 2. veljače 1991. godine u Varaždinu. Osnovnu školu pohađao je u Ivancu, gdje je 2004. godine upisao opću gimnaziju. Nakon završene srednje škole, upisuje studij strojarstva na Fakultetu strojarstva i brodogradnje Sveučilišta u Zagrebu, a kao smjer odabire Inženjersko modeliranje i računalne simulacije. Akademski naziv magistra inženjera strojarstva stekao je 2014. godine obranom diplomskog rada pod naslovom „Numerička analiza zaostalih naprezanja i deformacija kod zavarivanja“ pod mentorstvom prof. dr. sc. Zdenka Tonkovića. Završetkom preddiplomskog i diplomskog studija nagrađen je medaljom fakulteta za najbolje studente. Od 2015. godine zaposlen je na Fakultetu strojarstva i brodogradnje na Zavodu za tehničku mehaniku kao asistent na HRZZ projektu „Višerazinsko numeričko modeliranje deformiranja materijala od makro do nanorazine“. Iste akademske godine upisuje i poslijediplomski doktorski studij, smjer Numerička mehanika. Tijekom istraživanja dva se puta po mjesec dana znanstveno usavršavao na Tehničkom sveučilištu u Eindhovenu u Nizozemskoj. Kao autor ili koautor objavio je 11 znanstvenih radova od kojih je jedan objavljen u CC znanstvenom časopisu.

# Biography

Filip Putar was born on February 02, 1991 in Varaždin, Croatia. He attended primary school in Ivanec, where he also enrolled in grammar school in 2004. Afterwards, he enrolled in graduate studies at the Faculty of Mechanical Engineering and Naval Architecture, University of Zagreb. In 2014 he graduated with the thesis on the theme "Numerical Analysis of Welding Residual Stresses and Deformations", and received Mag. Ing. Mech. degree. He has been rewarded by the Medal of the Faculty for the best students, both after the undergraduate and the graduate studies. Since 2015, he has been employed as a research assistant in scope of the project financed by the Croatian Science Foundation, named "Multiscale Numerical Modeling of Material Deformation Responses from Macro- to Nanolevel". In the same academic year he enrolled in postgraduate studies in Numerical Mechanics. During the research, he visited Technical University of Eindhoven in Netherlands twice for the period of one month, where he acquired specific scientific knowledge in the field of multiscale and damage modeling of heterogeneous materials. He is the author of 11 scientific publications, including one contribution published in CC scientific journal.

# Bibliography

[1] D. Broek, Elementary engineering fracture mechanics, 1 ed., Springer, Dordrecht, Netherlands, 1982.
[2] J.L. Chaboche, Continuum Damage Mechanics: Part I—General Concepts, Journal of Applied Mechanics, 55 (1988) 59-64.
[3] J. Lemaitre, A Course on Damage Mechanics, 2 ed., Springer, Berlin, 1992.
[4] S. Murakami, Continuum damage mechanics, Springer, Berlin, 2012.
[5] J.L. Chaboche, Continuum Damage Mechanics: Part II—Damage Growth, Crack Initiation, and Crack Growth, Journal of Applied Mechanics, 55 (1988) 65-72.
[6] R.H.J. Peerlings, Enhanced damage modeling for fracture and fatigue, in, Eindhoven University of Technology, Eindhoven, The Netherlands, 1999.
[7] J. Lemaitre, Local approach of fracture, Engineering Fracture Mechanics, 25 (1986) 523-537.
[8] G. Pijaudier-Cabot, Z.P. Bažant, Nonlocal damage theory, J. Eng. Mech., 113 (1987) 1512-1533.
[9] D.J. Luscher, A hierarchical framework for the multiscale modeling of microstructure evolution in heterogeneous materials, in, Georgia Institue of Technology, Springfield, USA, 2010.
[10] V. Kouznetsova, Computational homogenization for the multi-scale analysis of multiscale materials, in, Technical University Eindhoven, Eindhoven, Netherlands, 2002.
[11] T. Lesičar, Multiscale modeling of heterogeneous materials using second-order homogenization, in, Faculty of Mechanical Engineering and Naval Architecture, Zagreb, Croatia, 2015.
[12] I.M. Gitman, H. Askes, L.J. Sluys, Representative volume: Existence and size determination, Engineering Fracture Mechanics, 74 (2007) 2518-2534.
[13] V.G. Kouznetsova, M. Geers, W.A.M. Brekelmans, Size of a Representative Volume Element in a Second-Order Computational Homogenization Framework, 2 (2004) 24.
[14] T. Kanit, S. Forest, I. Galliet, V. Mounoury, D. Jeulin, Determination of the size of the representative volume element for random composites: statistical and numerical approach, International Journal of Solids and Structures, 40 (2003) 3647-3679.
[15] V.D. Nguyen, G. Becker, L. Noels, Multiscale computational homogenization methods with a gradient enhanced scheme based on the discontinuous Galerkin formulation, Computer Methods in Applied Mechanics and Engineering, 260 (2013) 63-77.
[16] Ł. Kaczmarczyk, C.J. Pearce, N. Bićanić, Studies of microstructural size effect and higher-order deformation in second-order computational homogenization, Computers & Structures, 88 (2010) 1383-1390.
[17] T. Lesičar, Z. Tonković, J. Sorić, A second-order two-scale homogenization procedure using C1 macrolevel discretization, Computational Mechanics, 54 (2014) 425-441.
[18] V.G. Kouznetsova, M.G.D. Geers, W.A.M. Brekelmans, Multi-scale second-order computational homogenization of multi-phase materials: a nested finite element solution strategy, Computer Methods in Applied Mechanics and Engineering, 193 (2004) 5525-5550.
[19] E.W.C. Coenen, Multi-scale modelling of damage and fracture, in, Eindhoven University of Technology, Eindhoven, The Netherlands, 2012.
[20] V.P. Nguyen, Multiscale failure modelling of quasi-brittle materials, in, Delft University of Technology, Delft, The Netherlands, 2011.

[21] R.H.J. Peerlings, R. De Borst, W.A.M. Brekelmans, J.H.P. De Vree, Gradient enhanced damage for quai-brittle materials, International Journal for Numerical Methods in Engineering, 39 (1996) 3391-3403.
[22] R. de Borst, L.J. Sluys, H.B. Muhlhaus, J. Pamin, Fundamental issues in finite element analysis of localization of deformation, Engineering Computations, 10 (1993) 99-121.
[23] S. Chang Ching, L. Ma, Modeling of Discrete Granulates as Micropolar Continua, Journal of Engineering Mechanics, 116 (1990) 2703-2721.
[24] L.J. Sluys, R. de Borst, Wave propagation and localization in a rate-dependent cracked medium—model formulation and one-dimensional examples, International Journal of Solids and Structures, 29 (1992) 2945-2958.
[25] S. Pietruszczak, Z. Mróz, Finite element analysis of deformation of strain softening materials, Int. J. Num. Meth. Eng., 17 (1981) 327-334.
[26] Z.P. Bažant, B.H. Oh, Crack band theory for fracture of concrete, Mater. Struct., 16 (1983) 155-177.
[27] P. Bažant Zdeněk, Why Continuum Damage is Nonlocal: Micromechanics Arguments, Journal of Engineering Mechanics, 117 (1991) 1070-1087.
[28] Z.P. Bažant, T.B. Belytschko, T.P. Chang, Continuum theory for strain-softening, J. Eng. Mech. Trans. ASCE, 110 (1984) 1666-1692.
[29] R.H.J. Peerlings, R. de Borst, W.A.M. Brekelmans, M.G.D. Geers, Gradient-enhanced damage modelling of concrete fracture, Mechanics of Cohesive-frictional Materials, 3 (1998) 323-342.
[30] R. De Borst, H.-B. Mühlhaus, Gradient-dependent plasticity: Formulation and algorithmic aspects, International Journal for Numerical Methods in Engineering, 35 (1992) 521-539.
[31] R.A.B. Engelen, M.G.D. Geers, F.P.T. Baaijens, Nonlocal implicit gradient-enhanced elasto-plasticity for the modelling of softening behaviour, International Journal of Plasticity, 19 (2003) 403-433.
[32] L.J. Sluys, R. de Borst, H.B. Mühlhaus, Wave propagation, localization and dispersion in a gradient-dependent medium, International Journal of Solids and Structures, 30 (1993) 1153-1171.
[33] A. Simone, H. Askes, L.J. Sluys, Incorrect initiation and propagation of failure in non-local and gradient-enhanced media, International Journal of Solids and Structures, 41 (2004) 351-363.
[34] L.H. Poh, G. Sun, Localizing gradient damage model with decreasing interactions, International Journal for Numerical Methods in Engineering, 110 (2016) 503-522.
[35] G. Pijaudier-Cabot, K. Haidar, J.-F. Dubé, Non-local damage model with evolving internal length, International Journal for Numerical and Analytical Methods in Geomechanics, 28 (2004) 633-652.
[36] G.D. Nguyen, A damage model with evolving nonlocal interactions, International Journal of Solids and Structures, 48 (2011) 1544-1559.
[37] A. Triantafyllou, C. Perdikaris Philip, E. Giannakopoulos Antonios, Gradient Elastodamage Model for Quasi-Brittle Materials with an Evolving Internal Length, Journal of Engineering Mechanics, 141 (2015) 04014139.
[38] M. Ambati, T. Gerasimov, L. De Lorenzis, A review on phase-field models of brittle fracture and a new fast hybrid formulation, Computational Mechanics, 55 (2015) 383-405.
[39] M. Ambati, R. Kruse, L. De Lorenzis, A phase-field model for ductile fracture at finite strains and its experimental verification, Computational Mechanics, 57 (2016) 149-167.
[40] K. Seleš, T. Lesičar, Z. Tonković, J. Sorić, A Residual Control Staggered Solution Scheme for the Phase-Field Modeling of Brittle Fracture, Engineering Fracture Mechanics, 205 (2019) 370-386.

[41] M.J. Borden, C.V. Verhoosel, M.A. Scott, T.J.R. Hughes, C.M. Landis, A phase-field description of dynamic brittle fracture, Computer Methods in Applied Mechanics and Engineering, 217-220 (2012) 77-95.
[42] R. de Borst, C.V. Verhoosel, Gradient damage vs phase-field approaches for fracture: Similarities and differences, Computer Methods in Applied Mechanics and Engineering, 312 (2016) 78-94.
[43] R.D. Mindlin, N.N. Eshel, On first strain-gradient theories in linear elasticity, International Journal of Solids and Structures, 4 (1968) 109-124.
[44] C.S. Chang, H. Askes, L.J. Sluys, Higher-order strain/higher-order stress gradient models derived from a discrete microstructure, with application to fracture, Engineering Fracture Mechanics, 69 (2002) 1907-1924.
[45] Y. Yang, A. Misra, Higher-Order Stress-Strain Theory for Damage Modeling Implemented in an Element-free Galerkin Formulation, CMES-Computer Modeling in Engineering & Sciences, 64 (2010) 1-36.
[46] Ł. Kaczmarczyk, C.J. Pearce, N. Bićanić, Scale transition and enforcement of RVE boundary conditions in second-order computational homogenization, International Journal for Numerical Methods in Engineering, 74 (2007) 506-522.
[47] J. Li, A micromechanics-based strain gradient damage model for fracture prediction of brittle materials – Part I: Homogenization methodology and constitutive relations, International Journal of Solids and Structures, 48 (2011) 3336-3345.
[48] J. Li, X.-B. Zhang, A numerical approach for the establishment of strain gradient constitutive relations in periodic heterogeneous materials, European Journal of Mechanics - A/Solids, 41 (2013) 70-85.
[49] S. Forest, D.K. Trinh, Generalized continua and non-homogeneous boundary conditions in homogenisation methods, ZAMM - Journal of Applied Mathematics and Mechanics / Zeitschrift für Angewandte Mathematik und Mechanik, 91 (2010) 90-109.
[50] V. Kouznetsova, M.G.D. Geers, W.A.M. Brekelmans, Multi-scale constitutive modelling of heterogeneous materials with a gradient-enhanced computational homogenization scheme, International Journal for Numerical Methods in Engineering, 54 (2002) 1235-1260.
[51] L. Zybell, U. Mühlich, M. Kuna, Constitutive equations for porous plane-strain gradient elasticity obtained by homogenization, Archive of Applied Mechanics, 79 (2008) 359.
[52] A. Zervos, S.A. Papanicolopulos, I. Vardoulakis, Two Finite-Element Discretizations for Gradient Elasticity, Journal of Engineering Mechanics, 135 (2009) 203-213.
[53] S. Akarapu, H.M. Zbib, Numerical analysis of plane cracks in strain-gradient elastic materials, International Journal of Fracture, 141 (2006) 403-430.
[54] P. Fischer, J. Mergheim, P. Steinmann, On the C1 continuous discretization of non-linear gradient elasticity: A comparison of NEM and FEM based on Bernstein–Bézier patches, International Journal for Numerical Methods in Engineering, 82 (2009) 1282-1307.
[55] I.M. Gitman, H. Askes, L.J. Sluys, Coupled-volume multi-scale modelling of quasi-brittle material, European Journal of Mechanics - A/Solids, 27 (2008) 302-327.
[56] S. Loehnert, T. Belytschko, A multiscale projection method for macro/microcrack simulations, International Journal for Numerical Methods in Engineering, 71 (2007) 1466-1482.
[57] T. Zohdi, P. Wriggers, A domain decomposition method for bodies with heterogeneous microstructure basedon material regularization, International Journal of Solids and Structures, 36 (1999) 2507-2525.
[58] P.A. Guidault, O. Allix, L. Champaney, C. Cornuault, A multiscale extended finite element method for crack propagation, Computer Methods in Applied Mechanics and Engineering, 197 (2008) 381-399.

[59] V. Kouznetsova, W.A.M. Brekelmans, F.P.T. Baaijens, An approach to micro-macro modeling of heterogeneous materials, Computational Mechanics, 27 (2001) 37-48.
[60] I. Temizer, T.I. Zohdi, A numerical method for homogenization in non-linear elasticity, Computational Mechanics, 40 (2007) 281-298.
[61] C. Miehe, A. Koch, Computational micro-to-macro transitions of discretized microstructures undergoing small strains, Archive of Applied Mechanics, 72 (2002) 300-317.
[62] I.M. Gitman, Representative volumes and multi-scale modelling of quasi-brittle materials, in, Delft University of Technology, Delft, The Netherlands, 2006.
[63] M.G.D. Geers, V.G. Kouznetsova, W.A.M. Brekelmans, Multi-scale computational homogenization: Trends and challenges, Journal of Computational and Applied Mathematics, 234 (2010) 2175-2182.
[64] E.W.C. Coenen, V.G. Kouznetsova, M.G.D. Geers, Enabling microstructure-based damage and localization analyses and upscaling, Modelling and Simulation in Materials Science and Engineering, 19 (2011) 074008.
[65] T.J. Massart, R.H.J. Peerlings, M.G.D. Geers, An enhanced multi-scale approach for masonry wall computations with localization of damage, International Journal for Numerical Methods in Engineering, 69 (2006) 1022-1059.
[66] V.P. Nguyen, O. Lloberas-Valls, M. Stroeven, L.J. Sluys, Homogenization-based multiscale crack modelling: From micro-diffusive damage to macro-cracks, Computer Methods in Applied Mechanics and Engineering, 200 (2011) 1220-1236.
[67] T. Belytschko, S. Loehnert, J.-H. Song, Multiscale aggregating discontinuities: A method for circumventing loss of material stability, International Journal for Numerical Methods in Engineering, 73 (2007) 869-894.
[68] V.P. Nguyen, M. Stroeven, L.J. Sluys, An enhanced continuous–discontinuous multiscale method for modeling mode-I cohesive failure in random heterogeneous quasi-brittle materials, Engineering Fracture Mechanics, 79 (2012) 78-102.
[69] E.W.C. Coenen, V.G. Kouznetsova, M.G.D. Geers, Multi-scale continuous–discontinuous framework for computational-homogenization–localization, Journal of the Mechanics and Physics of Solids, 60 (2012) 1486-1507.
[70] V.P. Nguyen, O. Lloberas-Valls, M. Stroeven, L.J. Sluys, Computational homogenization for multiscale crack modeling. Implementational and computational aspects, International Journal for Numerical Methods in Engineering, 89 (2011) 192-226.
[71] C.V. Verhoosel, J.J.C. Remmers, M.A. Gutiérrez, A partition of unity-based multiscale approach for modelling fracture in piezoelectric ceramics, International Journal for Numerical Methods in Engineering, 82 (2009) 966-994.
[72] V.P. Nguyen, O. Lloberas-Valls, M. Stroeven, L. Johannes Sluys, On the existence of representative volumes for softening quasi-brittle materials – A failure zone averaging scheme, Computer Methods in Applied Mechanics and Engineering, 199 (2010) 3028-3038.
[73] T. Lesičar, Z. Tonković, J. Sorić, Two-scale computational approach using strain gradient theory at microlevel, International Journal of Mechanical Sciences, 126 (2017) 67-78.
[74] F. Putar, J. Sorić, T. Lesičar, Z. Tonković, Damage modeling employing strain gradient continuum theory, International Journal of Solids and Structures, 120 (2017) 171-185.
[75] M.G.D. Geers, R. de Borst, W.A.M. Brekelmans, R.H.J. Peerlings, Strain-based transient-gradient damage model for failure analyses, Computer Methods in Applied Mechanics and Engineering, 160 (1998) 133-153.
[76] D. Krajcinovic, Continuum damage mechanics, Appl. Mech. Rev., 37 (1984) 1-6.
[77] J. Lemaitre, J.-L. Chaboche, Mechanics of Solid Materials, Cambridge University Press, Cambridge, 1990.
[78] R. Hill, Elastic properties of reinforced solids: some theoretical principles, J. Mech. Phys. Solids, 11 (1963) 357-372.

[79] D. Krajcinovic, G.U. Fonseka, The continuous damage theory of brittle materials. Part I: General theory, J. Appl. Mech., 48 (1981) 809-815.
[80] L.M. Kachanov, On the Time Failure Under Creep Conditions, (1958) 26-31.
[81] K. Otsuka, H. Date, Fracture process zone in concrete tension specimen, Engineering Fracture Mechanics, 65 (2000) 111-131.
[82] P. Grassl, M. Jirásek, Meso-scale approach to modelling the fracture process zone of concrete subjected to uniaxial tension, International Journal of Solids and Structures, 47 (2010) 957-968.
[83] J. Mazars, G. Pijaudier-Cabot, Continuum damage theory – application to concrete, J. Eng. Mech., 115 (1989) 345-365.
[84] J.H.P. de Vree, W.A.M. Brekelmans, M.A.J. van Gils, Comparison of nonlocal approaches in continuum damage mechanics, Comp. Struct., 55 (1995) 581-588.
[85] M.G.D. Geers, Experimental analysis and computational modelling of damage and fracture, in, Eindhoven University of Technology, Eindhoven, The Netherlands, 1997.
[86] S. Murakami, Y. Liu, Local approach to fracture based on continuum damage mechanics and related problems, Mat. Sci. Res. Int., 2 (1996) 131-142.
[87] Z.P. Bažant, G. Pijaudier-Cabot, Nonlocal continuum damage, localization instability and convergence, J. Appl. Mech. Trans. ASCE, 109 (1988) 1119-1149.
[88] J.C. Simo, Strain softening and dissipation: a unification of approaches, in: J. Mazars, Bažant, Z.P. (Ed.) Cracking and Damage, Strain Localization and Size Effect. Proc. France-US Workshop, Elsevier, 1989, pp. 440-461.
[89] R. Hill, A general theory of uniqueness and stability in elastic-plastic solids, J. Mech. Phys. Solids, 6 (1958) 161-176.
[90] A. Benallal, R. Billardon, G. Geymonat, Some mathematical aspects of the damage softening rate problem, in: J. Mazars, Z.P. Bažant (Eds.) Cracking and damage, Taylor & Francis, 1989.
[91] N.S. Ottosen, K. Runesson, Properties of discontinuous bifurcation solutions in elasto-plasticity, International Journal of Solids and Structures, 27 (1991) 401-421.
[92] A. Benallal, R. Billardon, G. Geymonat, Bifurcation and Localization in Rate-Independent Materials. Some General Considerations, in: Q.S. Nguyen (Ed.) Bifurcation and Stability of Dissipative Systems, Springer Vienna, Vienna, 1993, pp. 1-44.
[93] G. Pijaudier-Cabot, A. Benallal, Strain localization and bifurcation in a nonlocal continuum, International Journal of Solids and Structures, 30 (1993) 1761-1775.
[94] R. de Borst, Stability and uniqueness in numerical modelling of concrete structures, IABSE Rep., 54 (1987) 161-176.
[95] P.H. Feenstra, R. de Borst, J.G. Rots, Numerical study on crack dilatancy. I: Models and stability analysis, ASCE J. Eng. Mech., 117 (1991) 733-753.
[96] B.A. Bilby, I.C. Howard, Z.H. Li, Mesh independent cell models for continuum damage theory, Fatigue. Fract. Eng. Mater. Struct., 17 (1994) 1221-1233.
[97] A. Needleman, Material rate dependence and mesh sensitivity in localization problems, Computer Methods in Applied Mechanics and Engineering, 67 (1988) 69-85.
[98] L.J. Sluys, R. de Borst, Dispersive properties of gradient-dependent and rate-dependent media, Mechanics of Materials, 18 (1994) 131-149.
[99] P. Steinmann, An improved FE expansion for micropolar localization analysis, Communications in Numerical Methods in Engineering, 10 (1994) 1005-1012.
[100] C.S. Chang, T.K. Wang, L.J. Sluys, J.G.M. van Mier, Fracture modeling using a micro-structural mechanics approach—I. Theory and formulation, Engineering Fracture Mechanics, 69 (2002) 1941-1958.

[101] C.S. Chang, T.K. Wang, L.J. Sluys, J.G.M. van Mier, Fracture modeling using a microstructural mechanics approach—II. Finite element analysis, Engineering Fracture Mechanics, 69 (2002) 1959-1976.
[102] L. Srinivasa Mohan, K. Kesava Rao, P.R. Nott, A frictional Cosserat model for the slow shearing of granular materials, Journal of Fluid Mechanics, 457 (2002) 377-409.
[103] J. Pamin, Gradient-dependent plasticity in numerical simulation of localization phenomena, in, Delft University of Technology, Netherlands, 1994.
[104] Z.P. Bažant, M. Jirásek, Nonlocal integral formulations of plasticity and damage: survey of progress, J. Eng. Mech. Trans. ASCE, 128 (2002) 1119-1149.
[105] A.C. Eringen, D.G.B. Edelen, On nonlocal elasticity, Int. J. Eng. Sci., 10 (1972) 233-248.
[106] G. Di Luzio, Z.P. Bažant, Spectral analysis of localization in nonlocal and over-nonlocal materials with softening plasticity or damage, International Journal of Solids and Structures, 42 (2005) 6071-6100.
[107] H.S. Hosseini, M. Horák, P.K. Zysset, M. Jirásek, An over-nonlocal implicit gradient-enhanced damage-plastic model for trabecular bone under large compressive strains, International Journal for Numerical Methods in Biomedical Engineering, 31 (2015).
[108] M.G.D. Geers, R.H.J. Peerlings, W.A.M. Brekelmans, R. de Borst, Phenomenological nonlocal approaches based on implicit gradient-enhanced damage, Acta Mechanica, 144 (2000) 1-15.
[109] Y. Yang, W.Y. Ching, A. Misra, Higher-Order Continuum Theory Applied to Fracture Simulation of Nanoscale Intergranular Glassy Film, Journal of Nanomechanics and Micromechanics, 1 (2011) 60-71.
[110] Y. Yang, A. Misra, Micromechanics based second gradient continuum theory for shear band modeling in cohesive granular materials following damage elasticity, International Journal of Solids and Structures, 49 (2012) 2500-2514.
[111] E. Amanatidou, N. Aravas, Mixed finite element formulations of strain-gradient elasticity problems, Computer Methods in Applied Mechanics and Engineering, 191 (2002) 1723-1751.
[112] J.Y. Shu, W.E. King, N.A. Fleck, Finite elements for materials with strain gradient effects, International Journal for Numerical Methods in Engineering, 44 (1999) 373-391.
[113] N. Kirchner, P. Steinmann, A unifying treatise on variational principles for gradient and micromorphic continua, Philosophical Magazine, 85 (2005) 3875-3895.
[114] S.A. Papanicolopulos, A. Zervos, I. Vardoulakis, A three-dimensional C1 finite element for gradient elasticity, International Journal for Numerical Methods in Engineering, 77 (2008) 1396-1415.
[115] R.H.J. Peerlings, W.A.M. Brekelmans, R. de Borst, M.G.D. Geers, Gradient-enhanced damage modelling of high-cycle fatigue, International Journal for Numerical Methods in Engineering, 49 (2000) 1547-1569.
[116] S. Forest, Micromorphic Approach for Gradient Elasticity, Viscoplasticity, and Damage, Journal of Engineering Mechanics, 135 (2009) 117-131.
[117] K. Saanouni, M. Hamed, Micromorphic approach for finite gradient-elastoplasticity fully coupled with ductile damage: Formulation and computational aspects, International Journal of Solids and Structures, 50 (2013) 2289-2309.
[118] H. Askes, J. Pamin, R. de Borst, Dispersion analysis and element-free Galerkin solutions of second- and fourth-order gradient-enhanced damage models, International Journal for Numerical Methods in Engineering, 49 (2000) 811-832.
[119] J. Pamin, H. Askes, R. de Borst, Two gradient plasticity theories discretized with the element-free Galerkin method, Computer Methods in Applied Mechanics and Engineering, 192 (2003) 2377-2403.
[120] H. Li, S.S. Mulay, Meshless Methods and Their Numerical Properties, CRC Press Boca Raton, USA, 2013.

[121] Z.P. Bažant, Size effect on structural strength: a review, Archive of Applied Mechanics, 69 (1999) 703-725.
[122] E.M.P. Cosserat, F. Cosserat, Théorie des Corps déformables, Nature, 81 (1909) 67.
[123] R.D. Mindlin, H.F. Tiersten, Effects of couple-stresses in linear elasticity, Archive for Rational Mechanics and Analysis, 11 (1962) 415-448.
[124] R.D. Mindlin, Influence of couple-stresses on stress concentrations, Experimental Mechanics, 3 (1963) 1-7.
[125] R.A. Toupin, Elastic materials with couple-stresses, Archive for Rational Mechanics and Analysis, 11 (1962) 385-414.
[126] A.C. Eringen, E.S. Suhubi, Nonlinear theory of simple micro-elastic solids—I, International Journal of Engineering Science, 2 (1964) 189-203.
[127] R.D. Mindlin, Second gradient of strain and surface-tension in linear elasticity, International Journal of Solids and Structures, 1 (1965) 417-438.
[128] P. Germain, The Method of Virtual Power in Continuum Mechanics. Part 2: Microstructure, SIAM Journal on Applied Mathematics, 25 (1973) 556–575.
[129] R.D. Mindlin, Micro-structure in linear elasticity, Archive for Rational Mechanics and Analysis, 16 (1964) 51-78.
[130] N.A. Fleck, J.W. Hutchinson, A phenomenological theory for strain gradient effects in plasticity, Journal of the Mechanics and Physics of Solids, 41 (1993) 1825-1857.
[131] R. de Borst, J. Pamin, M.G.D. Geers, On coupled gradient-dependent plasticity and damage theories with a view to localization analysis, European Journal of Mechanics - A/Solids, 18 (1999) 939-962.
[132] G.A. Maugin, A.V. Metrikine, Mechanics of Generalized Continua, Springer, 2010.
[133] S.B. Altan, E.C. Aifantis, On the structure of the mode III crack-tip in gradient elasticity, Scripta Metallurgica et Materialia, 26 (1992) 319-324.
[134] C.Q. Ru, E.C. Aifantis, A simple approach to solve boundary-value problems in gradient elasticity, Acta Mechanica, 101 (1993) 59-68.
[135] G.E. Exadaktylos, E.C. Aifantis, Two and Three-Dimentsional Crack Problems in Gradient Elasticity, in: Journal of the Mechanical Behavior of Materials, 1996, pp. 93.
[136] Abaqus/Standard 6.13.4., in, Dassault Systemes, Simulia, 2013.
[137] ABAQUS Documentation, in, Dassault Systemes, Simulia, 2013.
[138] A. Alshibli Khalid, S. Sture, Shear Band Formation in Plane Strain Experiments of Sand, Journal of Geotechnical and Geoenvironmental Engineering, 126 (2000) 495-503.
[139] J.G.M. van Mier, Fracture Processes of Concrete, CRC Press, Boca Raton, Florida, 1997.
[140] K. Vučković, Fatigue crack initiation in the tooth root of thin-rimmed gears, in, University of Zagreb, Faculty of Mechanical Engineering and Naval Architecture, Croatia, 2009.
[141] E. Buckingham, Analytical Mechanics of Gears, Dover Publications, Inc, New York, USA, 1949.
[142] S. Pehan, T.K. Hellen, J. Flasker, S. Glodez, Numerical methods for determining stress intensity factors vs crack depth in gear tooth roots, International Journal of Fatigue, 19 (1997) 677-685.
[143] Y. Pandya, A. Parey, Simulation of crack propagation in spur gear tooth for different gear parameter and its influence on mesh stiffness, Engineering Failure Analysis, 30 (2013) 124-137.
[144] T. Lesičar, J. Sorić, Z. Tonković, Large strain, two-scale computational approach using C1 continuity finite element employing a second gradient theory, Computer Methods in Applied Mechanics and Engineering, 298 (2016) 303-324.
[145] I. Özdemir, W.A.M. Brekelmans, M.G.D. Geers, Computational homogenization for heat conduction in heterogeneous solids, International Journal for Numerical Methods in Engineering, 73 (2007) 185-204.

[146] C.B. Hirschberger, N. Sukumar, P. Steinmann, Computational homogenization of material layers with micromorphic mesostructure, Philosophical Magazine, 88 (2008) 3603-3631.
[147] E.W.C. Coenen, V.G. Kouznetsova, M.G.D. Geers, Computational homogenization for heterogeneous thin sheets, International Journal for Numerical Methods in Engineering, 83 (2010) 1180-1205.
[148] H.M. Inglis, P.H. Geubelle, K. Matouš, Boundary condition effects on multiscale analysis of damage localization, Philosophical Magazine, 88 (2008) 2373-2397.